Structural trends and phase relations in off-stoichiometric kesterite type compound semiconductors

Dissertation zur Erlangung des akademischen Grades
Doktor der Naturwissenschaften (Dr. rer. nat.)

vorgelegt von
Kai Neldner

Freie Universität Berlin

HZB Helmholtz Zentrum Berlin

Eingereicht am Fachbereich Geowissenschaften
der Freien Universität Berlin

Angefertigt am Helmholtz-Zentrum Berlin für Materialien und Energie
Abteilung Struktur und Dynamik von Energiematerialien (EM-ASD)
und im Rahmen der Graduiertenschule Materials for Solar Energy Conversion

Die Arbeit ist in englischer Sprache verfasst

Berlin, August 2016

Erstgutachter: Prof. Dr. Susan Schorr

Zweitgutachter: Dr. Ralf Milke

eingereicht von: Kai Neldner

Matrikelnummer: 4142760

Tag der Disputation: Montag, 05.12.2016

Zusammenfassung

Begrenzte Reserven von fossilen Brennstoffen, Sicherheitsbedenken von Atomkraftwerken sowie die Endlagerung atomarer Abfälle haben die Bedeutung erneuerbarer Energien wie z. B. Wind- und Sonnenkraft gesteigert. Photovoltaik hat in den letzten Jahren bedeutsame Entwicklungen erlebt, wodurch sich besonders bei den Dünnschichtsolarzellen mehrere neue Absorbermaterialien sowie Technologien etabliert haben. In kurzer Zeit wurde eine Effizienz von Dünnschichtsolarzellen basierend auf CZTS von 12.6 % [97] erreicht. Die Vorteile der Dünnschichttechnologie liegen besonders in den schnellen (teils vakuumfreien) Herstellungsverfahren, dem geringen Rohstoffbedarf und den daraus resultierend gesunkenen Herstellungskosten. Um die Effizienz von CZTS Dünnschichtsolarzellen weiter zu steigern, ist es wichtig die limitierenden Faktoren des Materials zu verstehen, um eine vergleichbare Effizienz wie bei CIGS mit 22.6 % [8] zu erreichen und gleichzeitig den Einsatz von giftigen und seltenen Elementen wie Cd oder In zu vermeiden.

In dieser Arbeit wird eine systematische und grundlegende Untersuchung über die strukturellen Variationen und chemischen Trends in nichtstöchiometrischen Kesterit-Halbeitern durchgeführt. Dafür werden Pulverproben mittels Festkörpersynthese hergestellt und deren chemische Zusammensetzung mittels WDX-Analysen bestimmt. Außerdem werden mehrere Diffraktionsmethoden wie die Röntgenbeugung, anomale Röntgenstreuung und Neutronenbeugung eingesetzt, um die Gitterkonstanten und Platzbesetzungen der Wyckoff Positionen zu bestimmen. Das Ziel ist die detaillierte Analyse der intrinsischen Punktdefekte und der entsprechenden Defektkonzentrationen in Zusammenhang mit den unterschiedlichen nichtstöchiometrischen Kesterit-Typen.

Insgesamt kann zwischen sechs unterschiedliche nichtstöchiometrische Kesterit-Typen unterschieden werden. Neben den bereits bekannten A-, B-, C- und D-Typ [45] werden der E- [29] und F-Typ [96] neu eingeführt. Die chemische Charakterisierung der Pulver ergibt, dass einphasige Proben mit B-Typ Chemismus mit Anteilen von A- und F-Typ bevorzugt gebildet werden (Cu-arm / Zn-reich). Die Ergebnisse der Röntgenbeugung zeigen, dass CZTS die Hauptphase in allen Proben ist, auch wenn Sekundärphasen entdeckt wurden. Außerdem zeigt die tetragonale Deformation und das Einheitszellenvolumen eine starke Abhängigkeit vom Cu- und Zn-Anteil der Proben. Die tetragonale Deformation und das Einheitszellenvolumen verringern sich von Cu-armen / Zn-reichen zu Cu-reichen / Zn-armen Bedingungen (keine tetragonale Deformation = 1).

Des Weiteren hängen die Defektkomplexe und -konzentrationen, die mittels Neutronenbeugung und der durchschnittlichen Neutronenstreulänge bestimmt wurden, von der chemischen Zusammensetzung ab und stimmen mit den vorgeschlagenen Kesterit-Typen überein. Außerdem wird die Cu-Zn-Unordnung untersucht, die unabhängig von den Kesterit-Typen und der Stöchiometrie auftritt und den dominierenden Defektkomplex in den meisten Proben darstellt.

Abstract

The finite resources of fossil fuels, the security risk of atomic power plants and the absence of a permanent repository for nuclear waste have greatly increased the importance of renewable energies like wind power and solar energy.

Photovoltaic materials have seen a rapid development in the recent years. Especially in the thin film solar cell research multiple new technologies and absorber materials have emerged. In a short period of time the efficiency of the thin films based on CZTS have reached a record efficiency of 12.6 % [97]. The main advantages of thin film solar cells are fast (vacuum free) fabrication processes, fewer material usage and therefore lower fabrication costs.

To further increase the efficiency of CZTS based thin film solar cells it is important to understand the limiting factors of the material system to reach similar efficiency as the CIGS system of 22.6 % [8] by avoiding the use of toxic and scarce elements like Cd and In.

This work presents a systematic and fundamental study on the structural variations and chemical trends in off-stoichiometric CZTS type compound semiconductors. Therefore CZTS powder samples are synthesized by solid state reaction and the chemical composition is determined by WDX analyses at an electron micro probe analyzer. Several advanced diffraction techniques like X-ray diffraction, anomalous X-ray diffraction and neutron diffraction are used to obtain lattice parameters and site occupations of the Wyckoff positions. The goal is to study intrinsic point defects and the corresponding defect concentration in relation to the distinct off-stoichiometric CZTS types.

In total six different off-stoichiometric types are identified by introducing the E- [29], F-type [96] to the already postulated A-, B-, C- and D-type [45]. The chemical characterization of the CZTS powders shows that single-phase samples are formed preferably in the off-stoichiometric B-type region, with mixtures of A- and F-type, which correspond mainly to Cu-poor / Zn-rich conditions. X-ray diffraction results show that CZTS is the main phase in all samples even if secondary phases like copper, zinc and tin sulfides are present. Furthermore the evaluation of the tetragonal deformation and unit cell volume show a strong relation to the Cu and Zn content of the samples. The tetragonal deformation and unit cell volume decrease from Cu-poor / Zn-rich to Cu-rich / Zn-poor conditions (no tetragonal deformation = 1).

Also the intrinsic point defects, defect complexes and defect concentrations determined by neutron diffraction in combination with the average neutron scattering length method, change by chemical composition and correspond to the proposed off-stoichiometric CZTS types. Furthermore the analyzed Cu-Zn disorder is independent of the off-stoichiometric CZTS types and is the dominating defect complex in the majority of samples.

Contents

List of Figures

List of Tables

List of Equations

List of Abbreviations

Θ	....	diffraction angle
η	....	efficiency
λ	....	wavelength
Å	....	Ångström
cm	....	centimeter
°C	....	degree Celsius
fm	....	femtometer
mbar	....	millibar
a_B	....	Bohr radius
A	....	ampere
AZO	....	aluminum doped zinc oxide
ca.	....	circa
C	....	calculated weight
CdS	....	cadmium sulfide
CIGS	....	$Cu(In,Ga)Se_2$
const.	....	constant
Cu	....	copper
CZTS	....	Cu_2ZnSnS_4
CZTSe	....	$Cu_2ZnSnSe_4$
CZTSSe	....	$Cu_2ZnSnS_xSe_{4-x}$
EDX	....	energy-dispersive X-ray spectroscopy
EMPA	....	electron micro probe analyzer
err	....	error
FF	....	fill factor
FWHM	....	full width at a half maximum
h	....	hour
I_{mp}	....	current at max power
I_{SC}	....	short-circuit current
ICSD	....	Inorganic Crystal Structure Database
ITO	....	indium tin oxides
KCN	....	potassium cyanide
K	....	kelvin
MIT	....	metal-insulator transition

M .... measured weight

N_c .... critical acceptor concentration

NIST .... National Institute of Standards and Technology

NREL .... National Renewable Energy Laboratory

Occ .... occupation

p_1 .... a value influenced by Θ, channel and further parameters of the Time of flight experiment per data point

P_{In} .... input power

P_{max} .... maximum power

PDT .... post-deposition treatment

PVD .... physical vapor deposition

Q .... reciprocal space

Se .... selenium

Sn .... tin

SNS .... Spallation Neutron Source

S .... sulfur

tof .... time of flight data in µs

UAM .... University Autonoma of Madrid

V_{mp} .... voltage at max power

V_{OC} .... open-circuit voltage

WDX .... wavelength dispersive X-ray spectroscopy

XRPD .... X-ray powder diffraction

ZnO .... zinc oxide

Zn .... zinc

1 Introduction

1.1 Motivation

In recent years thin film solar cells based on chalcogenide compound semiconductors as absorber layer, like copper indium gallium selenide (CIGS), had a big impact on the thin film solar cell market due to their high efficiency of 22.6 % [8]. In comparison to crystalline silicon (c-Si) with 25.6 % efficiency [20] thin film solar cells are very cost-effective due to low material consumption and fast production processes. Amorphous silicon (a-Si) thin film solar cells with 13.6 % [20] efficiency have the same advantages as CIGS chalcopyrite type thin film solar cells but possess lower efficiencies.

Several new solar cell material systems, as copper zinc tin sulfide/selenide (CZTSSe) with an efficiency of 12.6 % [97], have emerged to overcome the disadvantages of CIGS thin film solar cells like the use of toxic and scarce elements. To overcome the difference in efficiency between CIGS and CZTSSe, a deeper understanding of the absorber material is important. The CZTSSe and also CZTS absorber material, which was investigated in detail in this study, crystallize in the tetragonal kesterite type structure (space group I$\bar{4}$) [32, 74].

The flexibility of the crystal structure under off-stoichiometric conditions and the occurring intrinsic point defects are of great importance because the CIGS absorber material used in highly efficient thin film solar cells show off-stoichiometric compositions with a Cu deficiency by maintaining the chalcopyrite type structure [4, 77, 79, 88]. By inducing this Cu deficiency copper vacancies (V_{Cu}) are formed in the CIGS absorber layer which are important for the electronic properties and efficient solar cell devices [4, 79, 88]. Chalcopyrite type absorbers are well characterized and the flexibility of the crystal structure and intrinsic point defects were examined deeply and thoroughly. Therefore intensive research on off-stoichiometric CZTS compounds and the occurring intrinsic point defects is necessary to understand the influence of off-stoichiometry on the crystal structure.

Some fundamental research was conducted by several groups on the kesterite type absorber material [9, 40, 45, 57, 75] but the quaternary CZTS material is far more complex, regarding the different cation substitution processes induced by off-stoichiometry in comparison to the ternary chalcopyrite type absorbers. Lafond et al. [45] and Choubrac et al. [14] introduced four cation substitution processes balancing the crystal structure when off-stoichiometric CZTS compounds are formed. Especially in relation to intrinsic point defects mostly theoretical work was conducted by Chen et al. [9, 11, 12]

and Huang & Persson [38] and off-stoichiometric compounds were only analyzed in a narrow chemical region.

Only few experimental investigations on the flexibility of the CZTS crystal structure under off-stoichiometric conditions were conducted and there exist no systematic and detailed study analyzing the cation distribution, intrinsic point defects and defect concentrations of off-stoichiometric CZTS compounds.

The aim of this work is to proof that CZTS type absorber compounds possess a high structural flexibility, to analyze intrinsic point defects and to verify if the experimental results correspond to the postulated defect complexes by Lafond et al. [45]. The most important tools used in this study are chemical characterization by WDX spectroscopy (electron micro probe analyzer) and structural characterization by X-ray powder diffraction and neutron diffraction. The diffraction data are processed by a full pattern Rietveld refinement in combination with the average neutron scattering length method [73].

These tools give a unique possibility to gain a deeper understanding of the CZTS type absorber material and can identify certain efficiency limiting factors, like the off-stoichiometric chemical composition, which can either produce harmful intrinsic point defects or defect complexes which enhance the electronic properties of the devices.

1.2 Insight in the Cu–Zn–Sn–S system

The kesterite type material studied in this work consists of Cu, Zn, Sn and S with the formula Cu_2ZnSnS_4 and is often referred as CZTS. The quaternary compound CZTS is analog to the natural mineral kesterite.
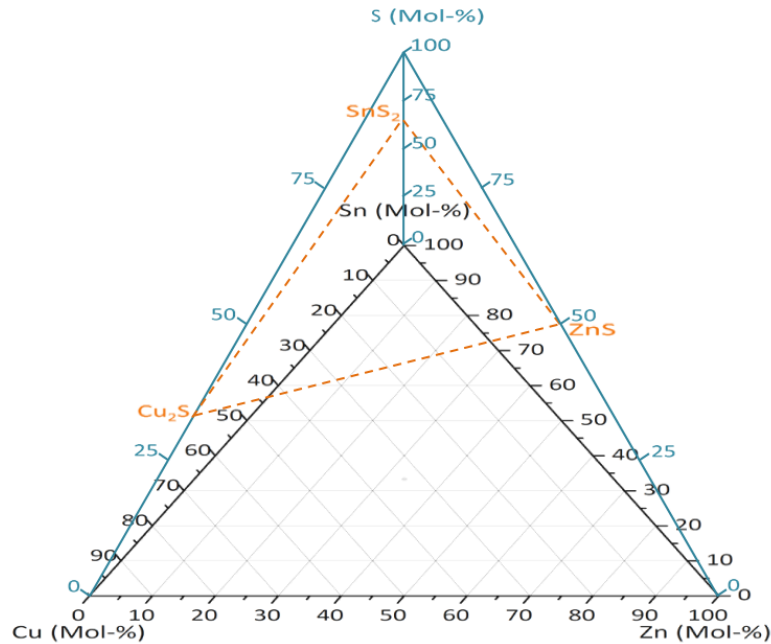
Figure 1.1: Quaternary Cu–Zn–Sn S diagram including pseudo ternary Cu_2S–ZnS–SnS_2 cut which is shown in more detail in Figure 1.2.

In Figure 1.1 the quaternary Cu–Zn–Sn–S system is shown. To gain an overview and especially to see where CZTS is situated in the phase diagram this illustration is far to complicated. To simplify the illustration a ternary cut is introduced. This quasi-ternary diagram cuts the quaternary diagram at SnS_2 (66.6 % sulfur and 33.3 % tin), Cu_2S (66.6 % copper and 33.3 % sulfur) and ZnS (50 % zinc and 50 % sulfur).

The quasi-ternary diagram at 397 °C was partially investigated by Olekseyuk et al. [57] and can be seen in Figure 1.2a). CZTS can be found in this quasi-ternary system at 33.3 % of each binary compound. Olekseyuk et al. [57] postulates a narrow stability region for CZTS. This is supported by Figure 1.2b) where a binary cut of Cu_2SnS_3–ZnS is investigated and single-phase CZTS forms only on one line at 50 % Cu_2SnS_3 and 50 % ZnS. Already a slightly shift from the line seems to introduce secondary phases.

CZTS is formed by a peritectic reaction at 980 °C [57] and this agrees well with the forming temperature postulated by Matsushita et al. [51] at 990 °C. This complex system also leads to a lot of possible secondary phases like CuS (covellite), $Cu_{1.8}S$

(digenite), Cu_2S (chalcocite), ZnS (sphalerite), SnS (herzenbergite) and some ternary compounds like Cu_2SnS_3.

a)

b)
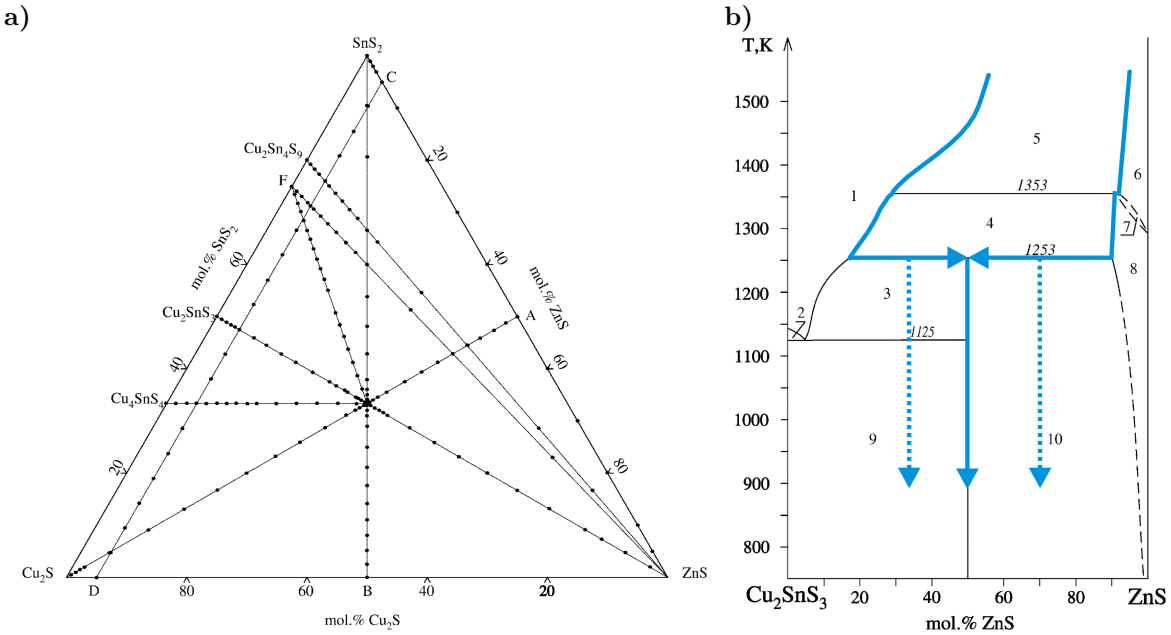
Figure 1.2: a) showing the ternary Cu_2S–ZnS–SnS_2 diagram and b) showing the pseudo-binary Cu_2SnS_3–ZnS cut by Olekseyuk et al. [57]. The blue solid line shows the path and stability region of the CZTS phase and the dashed lines represent the paths where additional secondary phases may occur.
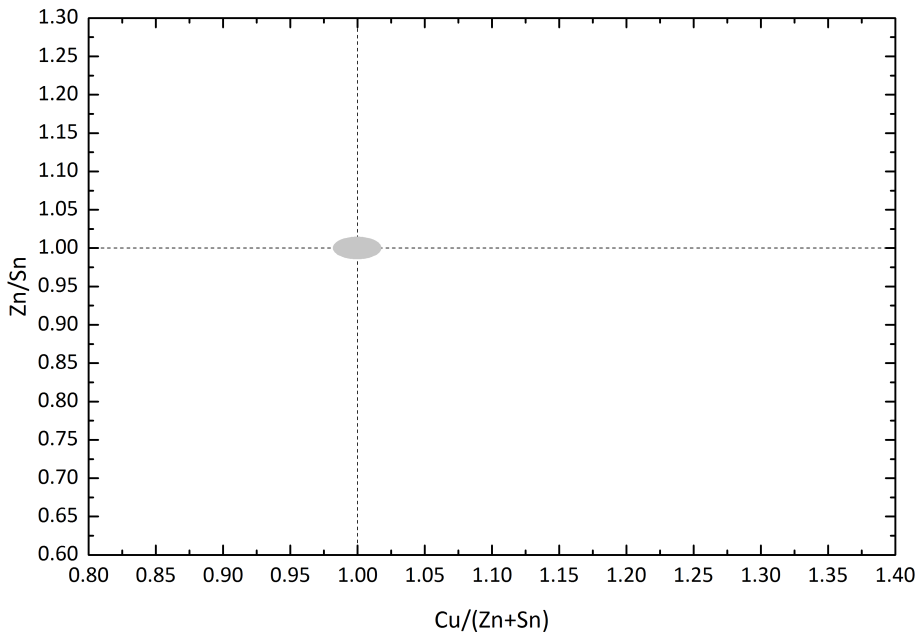
Figure 1.3: Cation ratio plot of Zn / Sn vs. Cu / (Zn + Sn). At the intersection of Zn / Sn = 1 and Cu / (Zn + Sn) = 1 stoichiometric CZTS is situated, marked by a light gray field including the error of the electron micro probe analyzer.

Although the secondary phases are important, the main focus of this study lies on CZTS. To further simplify the illustration and to increase the usability the cation ratio plot of Zn / Sn vs. $Cu / (Zn + Sn)$ is introduced (see Figure 1.3). It allows a better focus of the kesterite type stability field and a good separation between stoichiometry and off-stoichiometry CZTS phases.

In Figure 1.3 the cation ratio plot is presented. At the intersection of $Zn / Sn = 1$ and $Cu / (Zn + Sn) = 1$ stoichiometric CZTS is located. This area is highlighted by a light gray circle and includes the error of the electron micro probe analyzer measurements (see Chapter 2.1.2, page 16).

1.3 Kesterite type crystal structure of the CZTS absorber material
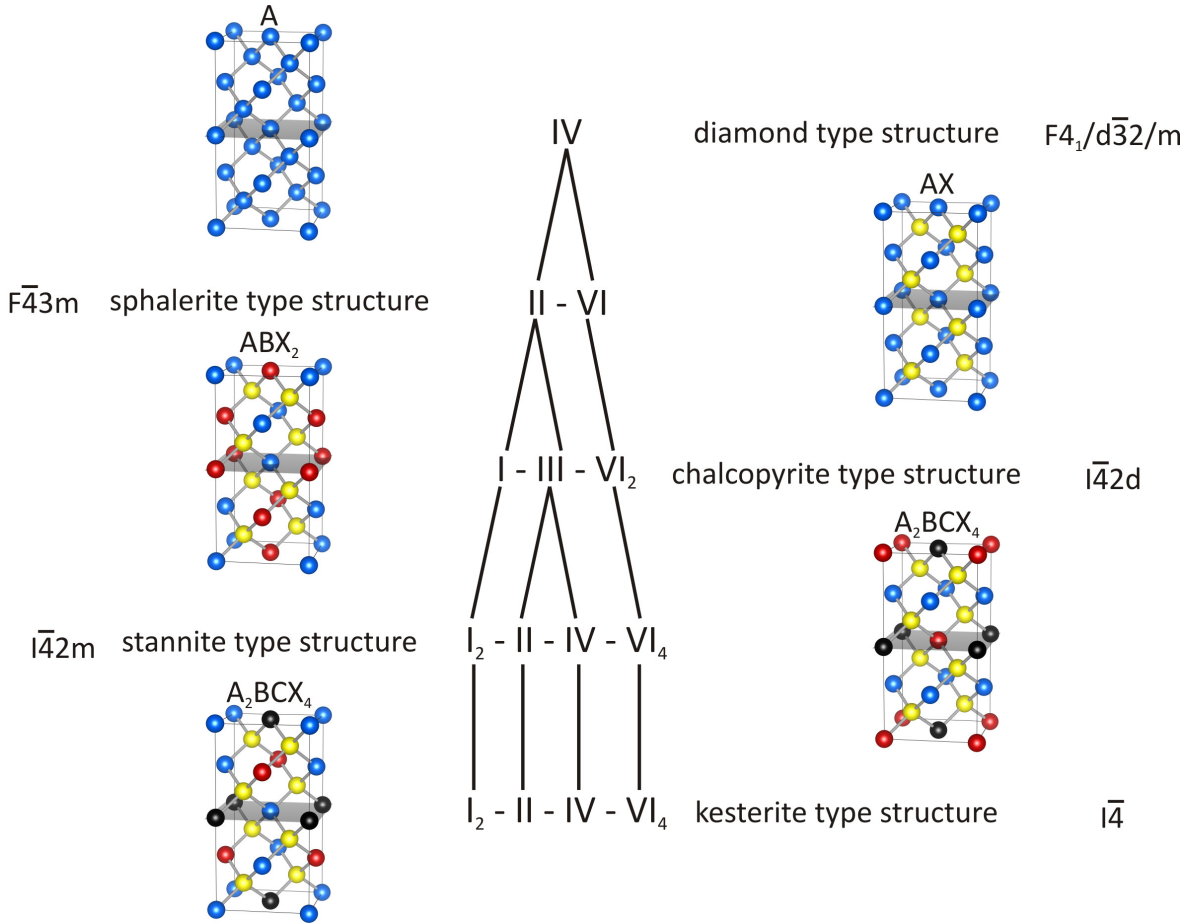
Figure 1.4: The derivation of the kesterite type structure I$\bar{4}$ is illustrated from the diamond structure by incorporating more elements and as a result reducing the symmetry.

CZTS belongs to the $A_2^I B^{II} C^{IV} X_4^{VI}$ compound family and crystallizes in the tetragonal kesterite type structure [32, 74]. It can be derived from the diamond type structure with the space group $F4_1/d\bar{3}2/m$ as shown in Figure 1.4 which is build by only one element (A). The sphalerite type structure (space group F$\bar{4}$3m) introduces a second element (AX). To reach the chalcopyrite type structure (space group I$\bar{4}$2d) the unit cell of the sphalerite type structure needs to be doubled in c-direction and a third element (ABX$_2$) is incorporated. All these transformations lead to a structure with lower symmetry. The stannite type structure (space group I$\bar{4}$2m) incorporates a fourth element (A$_2$BCX$_4$). The difference of the kesterite type structure (space group I$\bar{4}$) is induced by a different occupation of the Wyckoff positions.

In the kesterite type structure copper occupies the 2a (0, 0, 0) and 2c (0, ½, ¼) position whereas Zn is situated on the 2d (0, ½, ¾) and Sn on the 2b (½, ½, 0) position (see Figure 1.5). Thus leads to alternating Cu–Sn, Cu–Zn, Cu–Sn and Cu–Zn cation layers at z = 0, ¼, ½ and ¾. The anion, in this case sulfur, can be found on the 8g (x, y, z)

position. The lattice parameters and Wyckoff positions result in the tetragonal crystal structure with the space group $I\bar{4}$ for CZTS [32, 74].
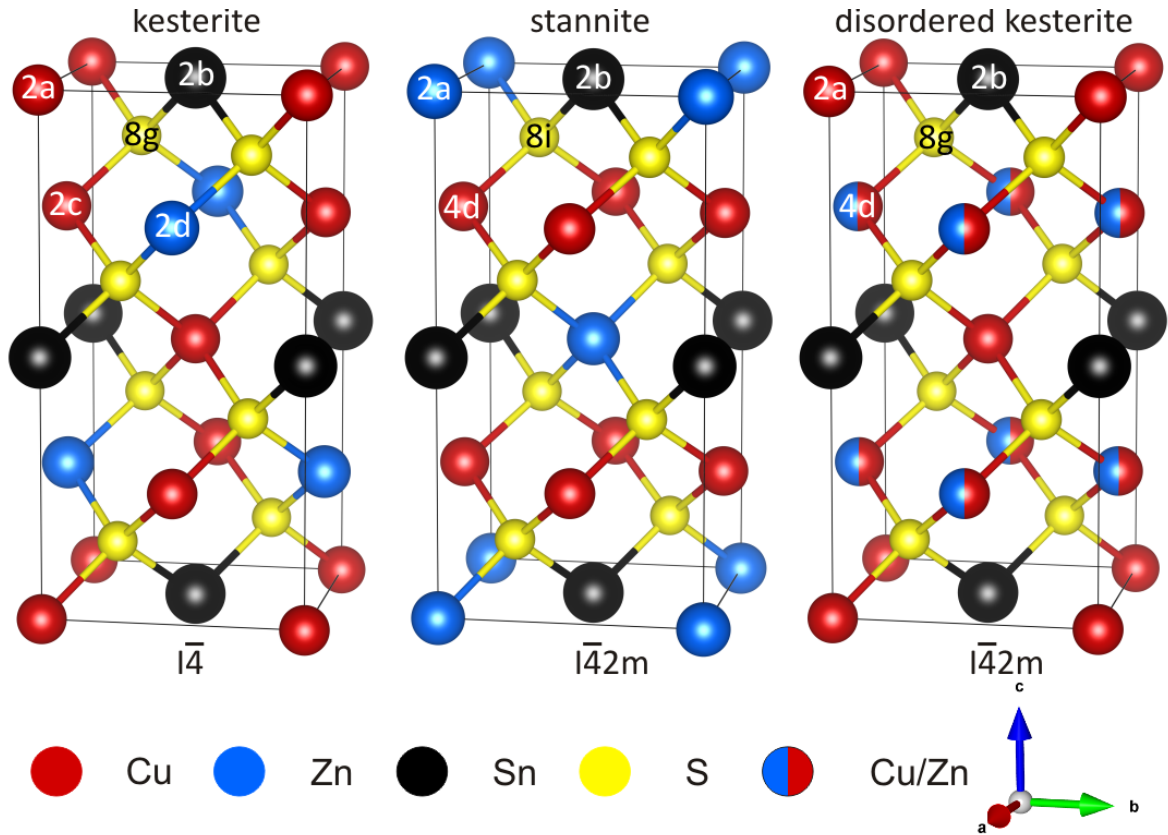
Figure 1.5: Kesterite, stannite and disordered kesterite type structure. The different Wyckoff positions and the elements occupying these positions are highlighted: Cu = red, Zn = blue, Sn = black, S = yellow and Cu / Zn shared = blue / red.

In the stannite structure Zn is on the 2a (0, 0, 0) and Cu on the 4d (0, ½, ¼) position. This leads to alternating Zn–Sn, Cu–Cu, Zn–Sn, Cu–Cu layers at z = 0, ¼, ½ and ¾ which is shown in Figure 1.5. Also S is now located on the 8i (x, x, z) position where the anion coordinates x and y are equal. These structural changes induce a higher symmetry leading to the space group $I\bar{4}2m$ [32, 74]. If the anion position (x,y,z) stays the same also disordered kesterite has the same space group but there again Cu is occupying the 2a (0, 0, 0) position and Cu and Zn are randomly distributed on the 4d (0, ½, ¼) position [75, 76].

The main difference between stannite and kesterite type structure is the splitting of Wyckoff position 4d in the Wyckoff positions 2c and 2d. Due to the similarity of the Cu on 2c and Zn on 2d Wyckoff positions and elements the formation of Cu_{Zn} and Zn_{Cu} antisites is easily possible without changing the chemical composition [10, 78]. These Cu_{Zn} and Zn_{Cu} antisites will be referred to as Cu-Zn disorder and can be found in stoichiometric CZTS. The strongest influence on the Cu-Zn disorder has the applied temperature profile. Scragg et al. [81] described that at high temperatures ordered CZTS ($I\bar{4}$) cannot exist and instead only a disordered kesterite phase (space group

I$\bar{4}$2m) will form [76, 95]. The ordering starts when the temperature drops below the critical temperature $T_c = (260 \pm 10)\,°C$ [67, 81, 93].

The introduction of changes to the chemical composition and the resulting formation of off-stoichiometry CZTS increase the complexity of this quaternary compound further.

1.3.1 The influence of off-stoichiometry on the CZTS structure

One of the main reason of the success of the chalcopyrite type structure in thin film solar cells is the high structural flexibility of the crystal structure which is needed to balance local inhomogeneities during the growth process of thin films. The flexibility of the kesterite type structure and the ability to deviate from stoichiometry were partly studied by Lafond et al. [45].

a)

b)
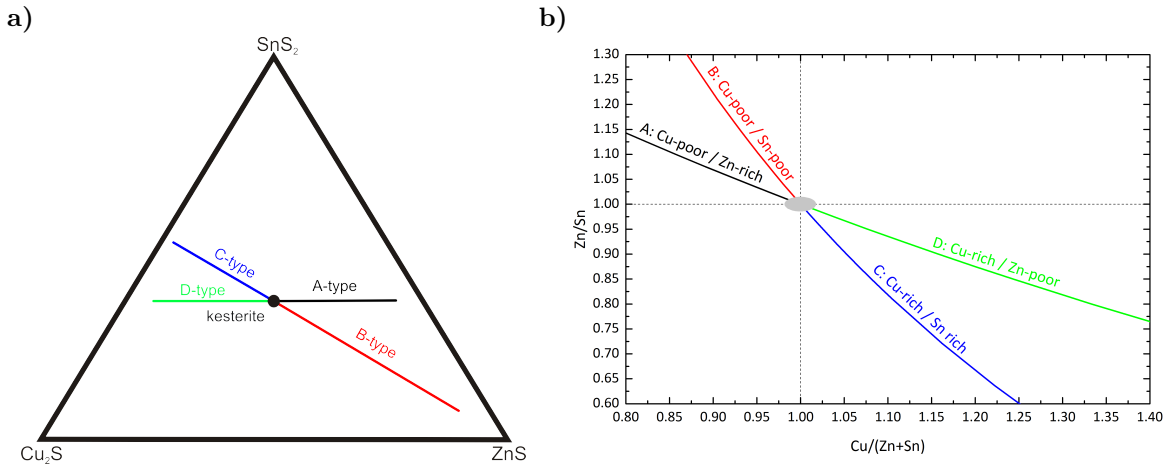
Figure 1.6: Postulated types by Lafond et al. [45] plotted in a ternary and cation ratio plot: A-type = black, B-type = red, C-type = blue and D-type = green. The cation ratio plot will be favorably used because of a better accessibility and scalability.

Lafond et al. [45] proposed cation substitution processes and their related intrinsic point defect complex formations by considering the charge balance must be given. This led to four off-stoichiometry types (see Figure 1.6 and Table 1.1): A-type Cu-poor / Zn-rich where copper is substituted by Zn forming a copper vacancy (V_{Cu}) and a zinc on copper antisite (Zn_{Cu}), B-type Cu-poor / Zn-rich where copper and tin are substituted by zinc forming zinc on copper (Zn_{Cu}) and zinc on tin (Zn_{Sn}), C-type Cu-rich / Zn-poor with zinc substituted by copper and tin forming copper (Cu_{Zn}) and tin (Sn_{Zn}) on zinc antisites and D-type Cu-rich / Zn-poor where copper substitutes zinc forming a copper on zinc antisite (Cu_{Zn}) and an additional copper interstitial (Cu_i). All those cation substitutions are illustrated in Table 1.1 and summarized in Figure 1.7 [45].

Furthermore Figure 1.6 shows the progression of these types in the ternary Cu_2S–ZnS–SnS_2 (Figure 1.6a) and Zn / Sn vs. Cu / (Zn + Sn) cation ratio plot (Figure 1.6b). The progression of the different off-stoichiometry types in the cation ratio plot is mirrored

Table 1.1: Four off-stoichiometry kesterite types proposed by Lafond et al. [45]: A-type, B-type, C-type and D-type. Their chemical composition and the corresponding cation substitution reaction and related intrinsic point defects are presented. Furthermore the formulae representing the type line.

Type	Composition	Cation substitution reaction	Intrinsic point defects
A	Cu-poor / Zn-rich / Sn-const.	$2\text{Cu}^+ \rightarrow \text{Zn}^{2+}$	$\text{V}_{\text{Cu}} + \text{Zn}_{\text{Cu}}$
B	Cu-poor / Zn-rich / Sn-poor	$2\text{Cu}^+ + \text{Sn}^{4+} \rightarrow 3\text{Zn}^{2+}$	$2\text{Zn}_{\text{Cu}} + \text{Zn}_{\text{Sn}}$
C	Cu-rich / Zn-poor / Sn-rich	$3\text{Zn}^{2+} \rightarrow 2\text{Cu}^+ + \text{Sn}^{4+}$	$2\text{Cu}_{\text{Zn}} + \text{Sn}_{\text{Zn}}$
D	Cu-rich / Zn-poor / Sn-const.	$\text{Zn}^{2+} \rightarrow 2\text{Cu}^+$	$\text{Cu}_{\text{Zn}} + \text{Cu}_{\text{i}}$

in comparison to the ternary plot. Due to the better scalability and accessibility the cation ratio plot will be preferably used.
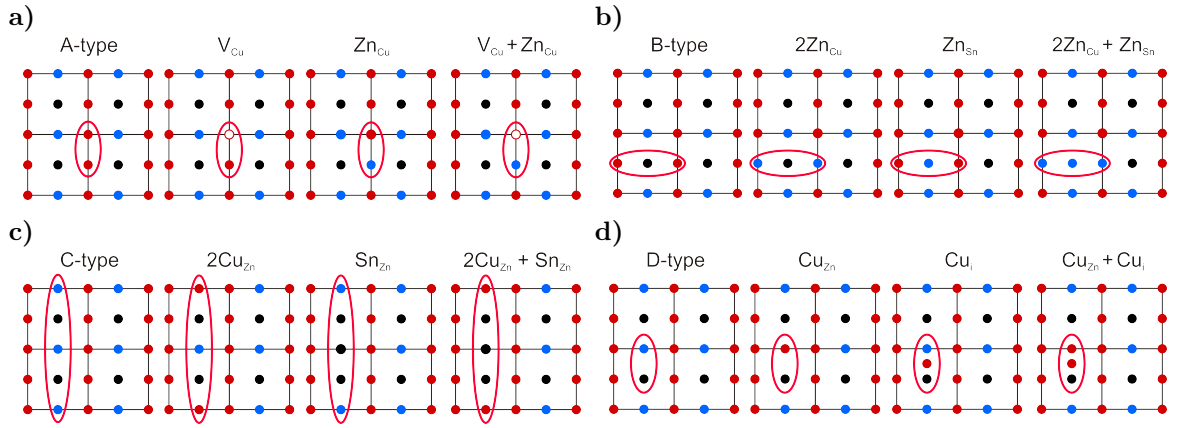
Figure 1.7: Overview of the structural impact of the different off-stoichiometric types postulated by Lafond et al. [45]. Four unit cell along the *c*-axes for a) A-type, b) B-type, c) C-type and d) D-type are shown: Cu = red, Zn = blue and Sn = black.

In Figure 1.7 the different off-stoichiometry types are explained by a two-dimensional structure. Four unit cells perpendicular to the *c*-axes were plotted and the changes of the defect complexes are highlighted in the structure. These changes in the structure can also be expressed as formulae as shown in Table 1.1.

1.4 Kesterite type semiconductor thin film solar cells

Quaternary chalcogenide absorber layers have seen rapid development in recent years leading to a world record efficiency for thin film solar cells based on $Cu_2ZnSn(S,Se)_4$ (CZTSSe) of 12.6 % [97]. The adjustable optical band gap energy is located between 1 eV to 1.5 eV [2, 13, 23, 24, 50, 59, 91] and an optical absorption coefficient of $10^4 \, cm^{-1}$ [41] proved that CZTS is a promising absorber material for thin film solar cells. Efficiencies for the endmembers CZTSe and CZTS solar cells are lower with 11.6 % [46] and 9.2 % [89] respectively. Furthermore CZTS thin film solar cells consist mostly of abundant and non-toxic elements like Cu, Zn, Sn and S.
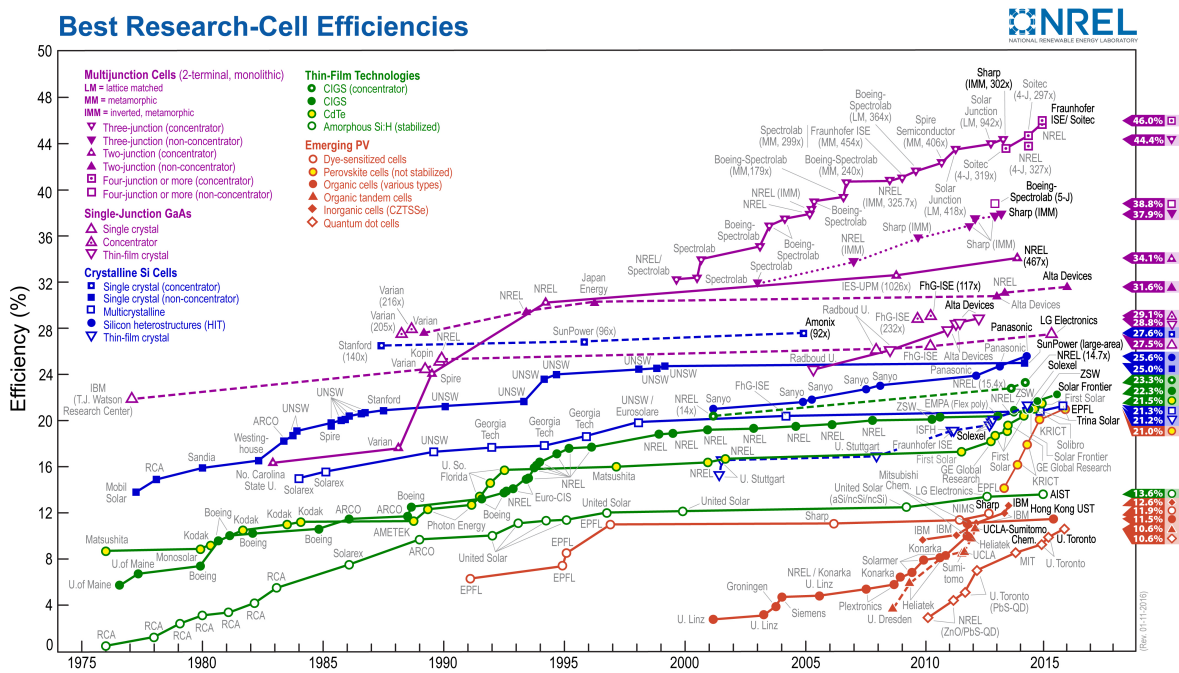
Figure 1.8: Overview of research cell efficiency records of different solar cell systems updated and maintained by the National Renewable Energy Laboratory [55]. Kesterite type solar cells are listed under „Engineering PV" inorganic cells (CZTSSe) as a single junction cell.

Figure 1.8 presents an overview of different solar cells systems and their achieved maximum efficiency under laboratory conditions. This means solar cells fabricated and sold by industry probably achieve lower efficiency. This chart is regularly updated by the National Renewable Energy Laboratory (NREL).

CZTSSe thin film solar cells were listed first 2010 with an efficiency of 9 %. The record efficiency by Wang et al. [97] dates from 2014. In comparison to other solar cells systems CZTSSe has only a short research history but already a decent efficiency. This is an effect of the close relation between CIGS and CZTSSe thin film solar cells because many techniques and processes from CIGS can be applied for CZTSSe. On the other hand this close relation creates some problems because the used techniques and processes from CIGS led to decent thin film solar cells but probably they are not the best solutions for the CZTSSe thin film solar cells and could be a limiting factor.

With the current record efficiency of 12.6 % [97] the question of the maximum efficiency of solar cells and their limiting factors arises. The Shockley–Queisser limit [86] describes the theoretical maximum efficiency under the assumption of one sun with the spectrum ASTM G173 AM1.5GT at 298 K and it can be calculated for different solar cell systems [40, 44, 64, 98]. Ki & Hillhouse [44] calculated the maximum efficiency of single junction CZTS thin film solar cells of $\eta = 32.4\,\%$ and for CZTSe devices $\eta = 31\,\%$. In Figure 1.9 the maximum efficiency over the band gap is plotted and this describes the Shockley–Queisser limit [86]. CZTSe with 1 eV and CZTS with 1.5 eV have almost an ideal band gap [2, 13, 23, 24, 50, 59, 91].
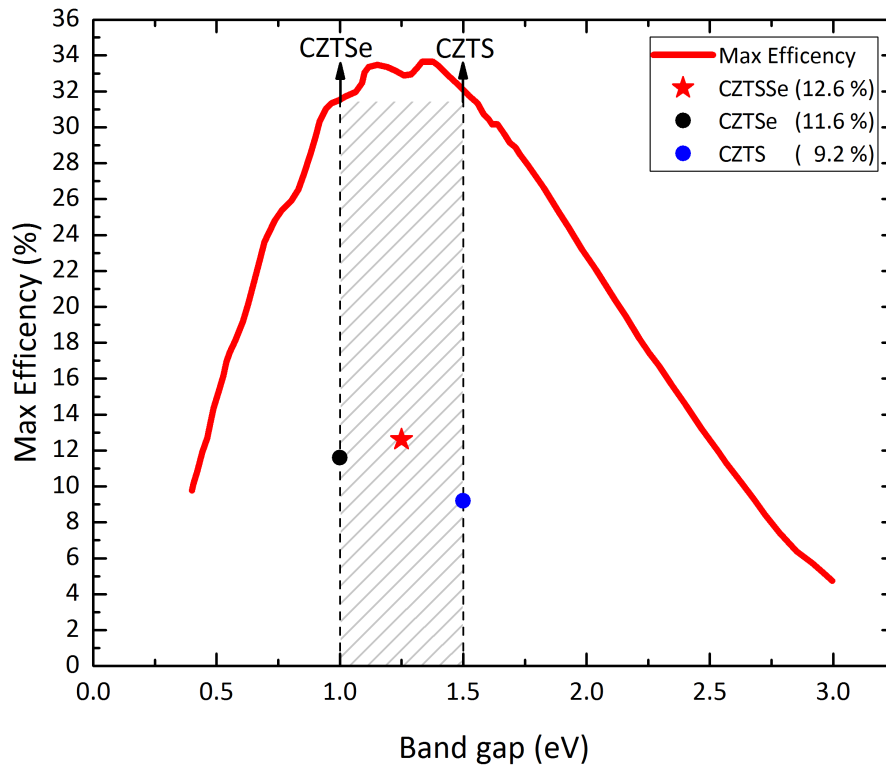
Figure 1.9: Theoretical maximum efficiency of thin film solar cells based on CZTSe, CZTS and CZTSSe [44, 86]. Furthermore the corresponding record efficiencies 11.6 % [46], 9.2 % [89] and 12.6 % [97] of single junction solar cells.

Only a certain percentage of power is extractable and there are processes responsible for the loss of around ⅔ of the energy. In CZTS the main loss processes are [44]:

1. photons which are not absorbed by the material (37.5 %)

2. thermalization of the carriers (18.6 %)

3. thermodynamic losses (10.5 %)

4. radiative recombination (1 %)

In the CZTSe system the processes are the same but the amount of loss they induce is different. Further details can be found in Ki & Hillhouse [44].

a)

b)
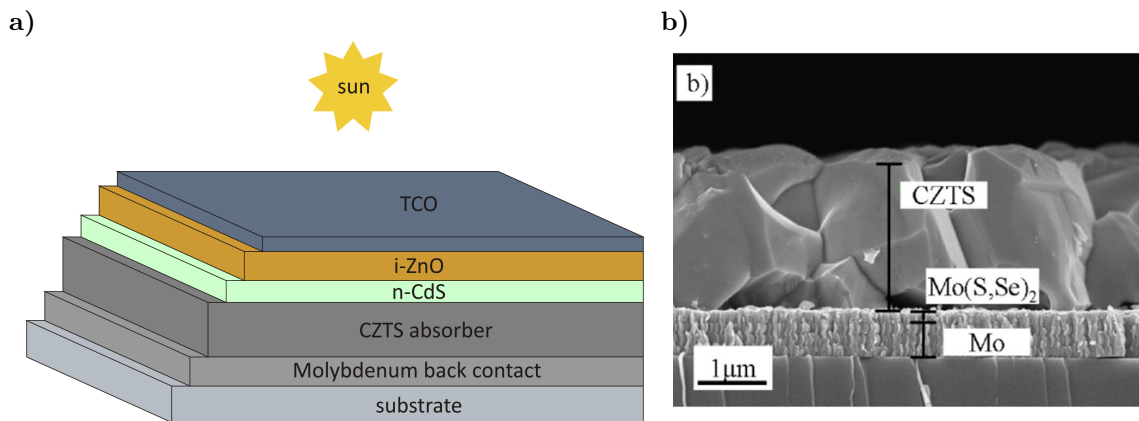
Figure 1.10: Schematic layout of a CZTS thin film solar cell [64] and a corresponding SEM image of the CZTS absorber layer deposited on a Molybdenum back contact on a substrate [97].

For a working solar cell only an absorber layer is not enough. Additional layers are necessary to convert sunlight into energy which can be extracted and used. Figure 1.10a) shows a schematic overview of a thin film solar cell and Figure 1.10b) a SEM picture of the substrate how Molybdenum and the CZTS absorber look like [97]. The foundation of a solar cell builds the substrate which is normally soda-lime glass. Also elastic foils and metals can be used. On the substrate a back contact needs to be deposited. Sputtering is the standard method to apply the Molybdenum back contact on the substrate and often a preferred orientation can be observed. The back contact is also an important link because it influences how good the absorber material adheres and ultimately impacts the stability of the thin film solar cell. The deposition of the absorber material in this case CZTS can be conducted by various vacuum or non-vacuum processes [1, 5, 30, 36, 58, 80, 100, 101]. Between the i-ZnO front contact and the p-type absorber layer a n-type buffer layer is necessary which also improves the interface between these materials and completes the p-n-junction. Normally CdS is used but because of the toxicity of Cd alternatives like Zn(O,S) are tested [37]. In the last step a transparent conductive oxide layer is added which reduces the reflectivity of the thin film solar cell and enhances the amount of sunlight reaching the absorber layer.

Comparing different solar cells and their properties is essential for a deeper understanding of the processes influencing the efficiency. Therefore several parameters can be extracted from an I–V curve measured under verifiable conditions [47]. An example is shown in Figure 1.11 and the most important parameters are:

I_{SC} The short circuit current is the maximum current when the voltage is zero.

V_{OC} The open circuit voltage is the maximum voltage when the current is zero.

FF The Fill Factor determines the maximum power from a solar cell.

η The efficiency of a solar cell is defined as the ratio of energy output to input energy

The I_{SC} and V_{OC} can be extracted as shown in Figure 1.11. Both parameters are necessary to calculate the FF (see Equation 1.1) which is the area of the largest rectangle to fit below the I–V curve. Also the I_{mp} (current at max power) and the V_{mp} (voltage at max power) are needed for the calculation:

$$FF = \frac{Imp \cdot Vmp}{I_{SC} \cdot V_{OC}} = \frac{areaA}{areaB} \tag{1.1}$$

With these three parameters it is possible to calculate P_{max} (maximum power) and the efficiency η.

$$P_{max} = I_{SC} \cdot V_{OC} \cdot FF \tag{1.2}$$

$$\eta = \frac{I_{SC} \cdot V_{OC} \cdot FF}{P_{In}} \tag{1.3}$$
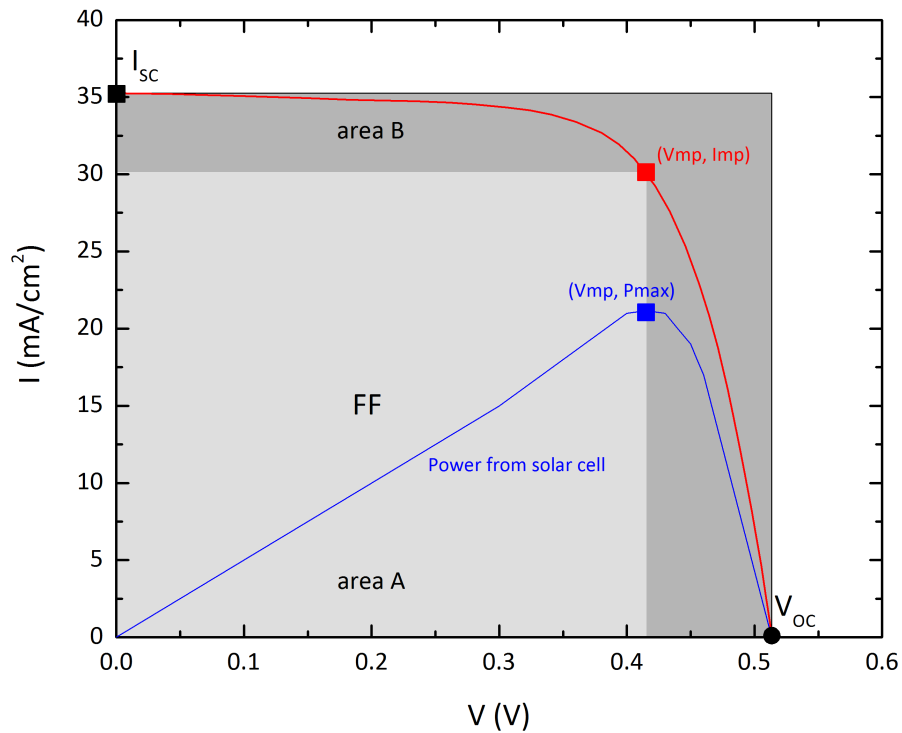
Figure 1.11: I–V curve and explanation of the most important splar cell parameters: I_{SC}, V_{OC} and FF [47, 97].

In order to compare solar cell efficiencies the measurement conditions must be carefully controlled. Typical conditions use the spectrum ASTM G173 AM1.5GT at 298 K. This is equal to the input power $P_{In} = 10\,\mathrm{W}$ for a $100\,\mathrm{mm}^2 \times 100\,\mathrm{mm}^2$ cell.

2 Experimental

2.1 Preparation and chemical analysis of off-stoichiometric CZTS samples

2.1.1 Synthesis by solid state reaction

Solid state reaction was used to synthesize off-stoichiometric CZTS powder samples. It is a well controllable and adjustable method to produce sizable quantities of powder samples for further characterizations.

The composition of the first samples synthesized was chosen by the knowledge of the average composition of high efficient CZTSSe thin film solar cells [1, 43, 97]. High efficient solar cells have an average composition which corresponds to A-type Cu-poor / Zn-rich composition [97]. The goal was to synthesize all off-stoichiometric types introduced by Lafond et al. [45] which were shown in Table 1.1 (page 9) and Figure 1.7 (page 9). For the calculation of the amount of elements for the synthesis a formula is needed. This formula was derived from the cation substitution reaction and the corresponding intrinsic point defects presented in Table 1.1.

Table 2.1: Four off-stoichiometric kesterite types including the formulae: A-type, B-type, C-type and D-type proposed by Lafond et al. [45]. Their chemical composition and the corresponding cation substitution reaction, related intrinsic point defects and formulae are presented.

Type	Composition	Cation substitution reaction	Intrinsic point defects	Formulae
A	Cu-poor / Zn-rich / Sn-const.	$2Cu^+ \rightarrow Zn^{2+}$	$V_{Cu} + Zn_{Cu}$	$Cu_{2-2x}Zn_{1+x}SnS_4$
B	Cu-poor / Zn-rich / Sn-poor	$2Cu^+ + Sn^{4+} \rightarrow 3Zn^{2+}$	$2Zn_{Cu} + Zn_{Sn}$	$Cu_{2-2y}Zn_{1+3y}Sn_{1-y}S_4$
C	Cu-rich / Zn-poor / Sn-rich	$3Zn^{2+} \rightarrow 2Cu^+ + Sn^{4+}$	$2Cu_{Zn} + Sn_{Zn}$	$Cu_{2+2z}Zn_{1-3z}Sn_{1+z}S_4$
D	Cu-rich / Zn-poor / Sn-const.	$Zn^{2+} \rightarrow 2Cu^+$	$Cu_{Zn} + Cu_i$	$Cu_{2+2m}Zn_{1-m}SnS_4$

The formulae presented in Table 2.1 and the Molar mass were used to calculate the amount of Cu ($63.546\,\mathrm{g\,mol^{-1}}$), Zn ($65.409\,\mathrm{g\,mol^{-1}}$), Sn ($118.71\,\mathrm{g\,mol^{-1}}$) and S ($32.065\,\mathrm{g\,mol^{-1}}$) needed to form the CZTS compound and to produce samples with a final weight of $3\,\mathrm{g}$ to $5\,\mathrm{g}$.

Therefore the pure elements Cu, Zn, S ($99.999\,\%$ purity) and Sn ($99.9999\,\%$ purity) are placed inside a pyrolytic graphite boat. Furthermore for most samples a sulfur excess

of 10 % was added to ensure the reaction of all cations. All elements were weighed out with an accuracy of ± 0.0003 g.

a)   **b)**
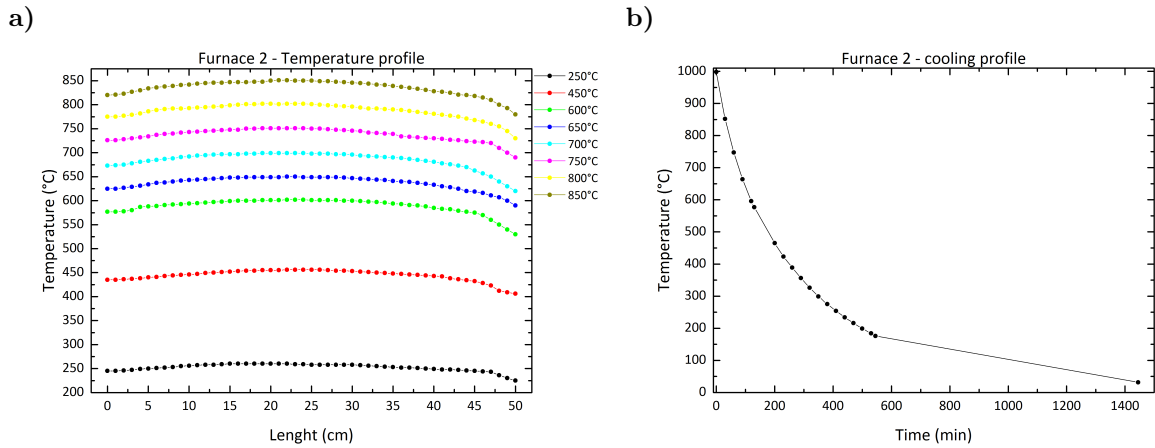
Figure 2.1: a) Temperature profile over the length of the single zone furnace at 250 °C, 450 °C, 600 °C, 650 °C, 700 °C, 750 °C, 800 °C and 850 °C. b) showing the measured cooling profile of switched off furnace.

The pyrolytic graphite boat was then carefully placed inside a quartz ampule, evacuated to 10^{-5} mbar and sealed with an oxyhydrogen torch. During the sealing it is important to prevent the evaporation of S. Hence for the cooling liquid nitrogen was used. Also the reaction room was limited to 8 cm by using a quartz plug. Afterwards the sealed ampules were placed inside a single zone furnace. The temperature profile over the length of the furnace and the uncontrolled cooling by just switching off the furnace were measured and are presented in Figure 2.1. The temperature profile over the length of the furnace was used to figure out the optimal position for the sealed ampules regarding the temperature stability.

Afterwards the synthesis was started by applying a temperature program. The temperature program was steadily improved over different syntheses and led to the following optimized temperature program (see Table 2.2, page 16). During the 1st reaction step the temperature was raised by $10 \, \mathrm{K \, h^{-1}}$ to 250 °C, 450 °C, 600 °C and 820 °C and held for 48 h and 240 h at the final temperature stage. These different temperature stages were necessary to prevent the ampule from exploding because of the S excess and the resulting high vapor pressure.

After the 1st reaction step the homogenization step followed where the material was ground and some extra S was added. The powders were then pressed to pellets and again placed in sealed silica ampules.

Now the 2nd reaction step starts and this time no additional temperature stages are needed and a heating rate of $50 \, \mathrm{K \, h^{-1}}$ to the final temperature stage of 750 °C was applied. This temperature was held for 240 h. After these 240 h a cooling rate of $50 \, \mathrm{K \, h^{-1}}$ was applied but because it was no active furnace the cooling rate below 250 °C is equivalent to the cooling profile of the switched off furnace(see Figure 2.1). The temperature program in Table 2.2 was used for most of the samples [96].

Table 2.2: Optimized temperature program showing the procedure of the synthesis of homogeneous CZTS powder material [96].

Step	Stage	Temperature
1st reaction step	1st heating stage	250 °C heating rate 10 K h^{-1} hold for 48 h
	2nd heating stage	450 °C heating rate 10 K h^{-1} hold for 48 h
	3rd heating stage	600 °C heating rate 10 K h^{-1} hold for 48 h
	Final heating stage	820 °C, which is 170 °C below the CZTS melting point [51, 57] heating rate 10 K h^{-1} hold for 240 h
	Cooling	50 °C heating rate 50 K h^{-1} to 250 °C; below 250 °C slower cooling rate to room temperature
Homogenization step		Grinding of the material pressed to pellets which are placed in sealed silica tubes
2nd reaction step	1st heating stage	750 °C heating rate 50 K h^{-1} hold for 240 h
	Cooling	50 K h^{-1} to 250 °C; below 250 °C slower cooling rate to room temperature

2.1.2 Electron micro probe analysis by wavelength dispersive X-ray spectroscopy

The chemical composition of the synthesized powder samples needs to be known as precise as possible for the latter analyses. Therefore the determination of the phase content and chemical composition of the synthesized powder samples was performed on an electron micro probe analyzer (JEOL–JXA 8200) equipped with a wavelength dispersive X-ray spectroscopy unit (WDX). In order to obtain precise results from the WDX measurements the calibration of the system was done by using elemental standards for Cu, Zn, Sn and a mineral standard (chalcopyrite) for S. Figure 2.2 shows a schematic setup of an electron micro probe analyzer [66].

Furthermore well polished and prepared samples are needed. These are produced by embedding portions of the synthesized sample powder in epoxy and polish them mechanically till a clean surface was achieved. The grain size of the powder should be between 10 μm to 150 μm to be able to measure accurate results with a beam diameter of around 1 μm. After all this preparation the chemical composition can be obtained with a relative error of 1 %.

To obtain a reliable chemical composition of the powder samples 30-60 grains and 10-15 points on each grain were measured. These measurements points were set as line measurements to ensure that the grains are homogeneous and have no chemical gradient. Furthermore 5-10 backscattered electron micrographs were saved per sample. To distinguish the secondary phases from the quaternary phase EDX (energy dispersive X-ray spectroscopy), backscattered electron micrographs and the optical microscope

were used. Also WDX measurements were executed to obtain the chemical composition of the secondary phases.
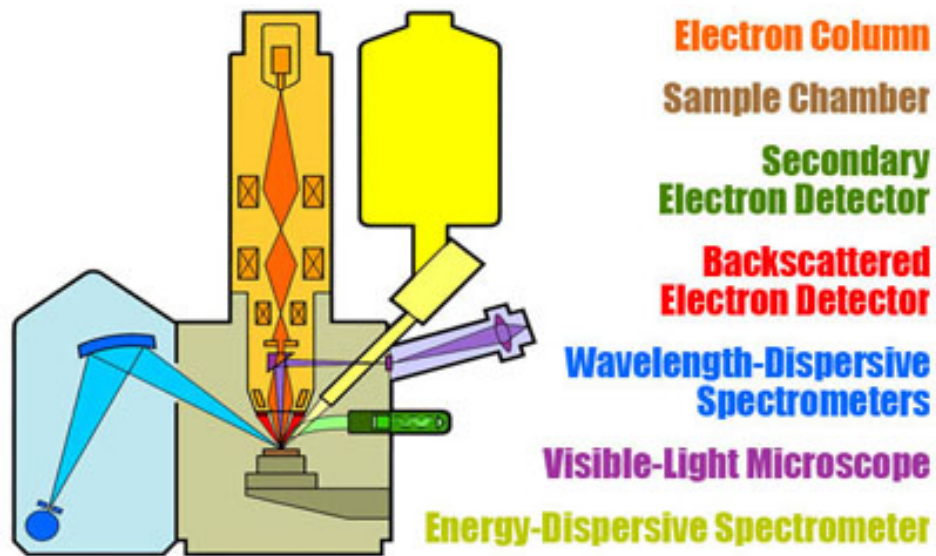
Figure 2.2: Schematic overview and components of an electron micro probe analyzer used for the chemical characterization of the samples [39].

After the measurements the obtained data needs to be processed and analyzed. First the 10-15 points per grain were average if the deviation of the composition was smaller than the error of the electron micro probe analyzer. Afterwards the chemical compositions of the grains were average if the deviation was smaller than 1%. To evaluate the deviation elemental plots for Cu, Zn, Sn and S vs. grains and ratio plots $\mathrm{Cu}\,/\,(\mathrm{Zn}+\mathrm{Sn})$, $\mathrm{Zn}\,/\,\mathrm{Sn}$ and Cation$\,/\,$Anion were prepared to evaluate the homogeneity of the grains. If all quality standards were fulfilled all points and grains of one sample and one phase are average to get the chemical composition of the phases present inside of the powder sample. Only points and grains with the same composition were averaged.

From the average data the $\mathrm{Cu}\,/\,(\mathrm{Zn}+\mathrm{Sn})$ and $\mathrm{Zn}\,/\,\mathrm{Sn}$ ratios were deduced. These are the most important values for further analysis because they show to which off-stoichiometry type the sample belongs and which defect complexes can be expected.

2.2 Diffraction techniques and data treatment

2.2.1 X-ray powder diffraction

X-ray powder diffraction and full pattern Rietveld refinement [68] (see Chapter 2.2.4, page 25) were applied to attain basic structural parameters as a function of the chemical composition. Furthermore quantitative fractions of the present phases were obtained. X-ray powder diffraction and neutron diffraction are following the same diffraction principle described in Spieß et al. [87]. To obtain a powder pattern, reflexes must be measured and therefore Bragg's law (see Equation 2.1, page 18) must be fulfilled for constructive interference.

$$n \cdot \lambda = 2 \cdot d_{hkl} \cdot \sin \Theta \qquad (2.1)$$

With n = the order of reflection or diffraction, λ = wavelength, d_{hkl} = lattice plane spacing and Θ = diffraction angle.

A PANalytical X'Pert PRO MRD diffractometer with Bragg-Brentano geometry and a sample spinner stage was utilized. The powder was placed on a zero background sample holder and measured in a 2Θ range of 10° to 130° with a step size of 0.013 13°. The collected X-ray patterns were further processed by a Rietveld refinement using the FullProf Suite software package [72].
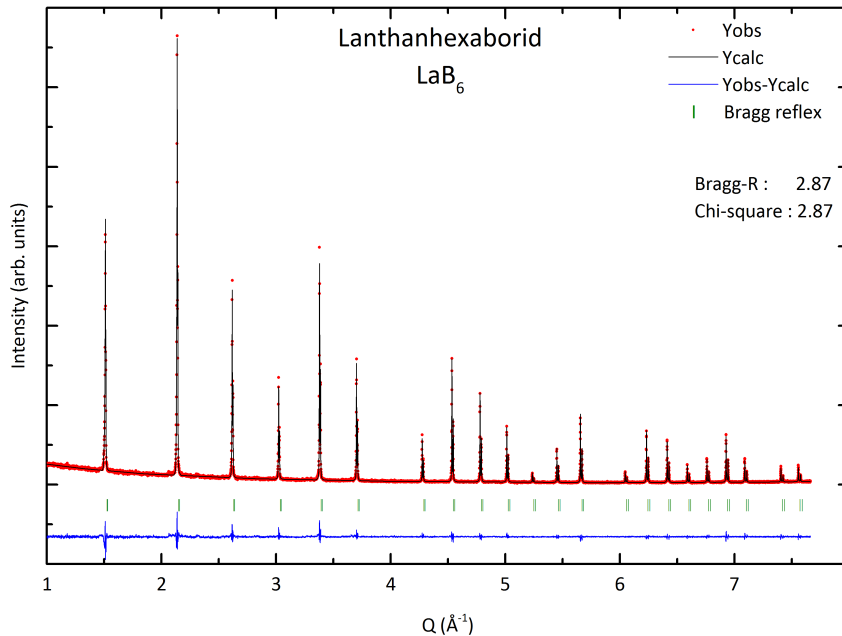
Figure 2.3: X-ray powder diffraction and Rietveld analysis of LaB_6 standard used as calibration for the CZTS measurements.

For the described measurement setup an instrument resolution function was created. Therefore a standard with well known lattice parameters and sharp, strong reflexes was

analyzed (see Figure 2.3, page 18). The standard Lanthanhexaborid (LaB$_6$) provided by NIST has a cubic crystal structure and certified lattice parameters $0.415\,682(8)\,\text{nm}$ at $22.5\,°\text{C}$.

Out of this Rietveld refinement the profile parameters and the asymmetry parameters were extracted which are representing the peak shape of the instrument. These parameters are used as starting parameters for every Rietveld refinement. The standard measurement must be repeated every time when the instrument is maintained or the X-ray tube is exchanged. A more detailed explanation of the profile and asymmetry parameters can be found in Chapter 2.2.4.
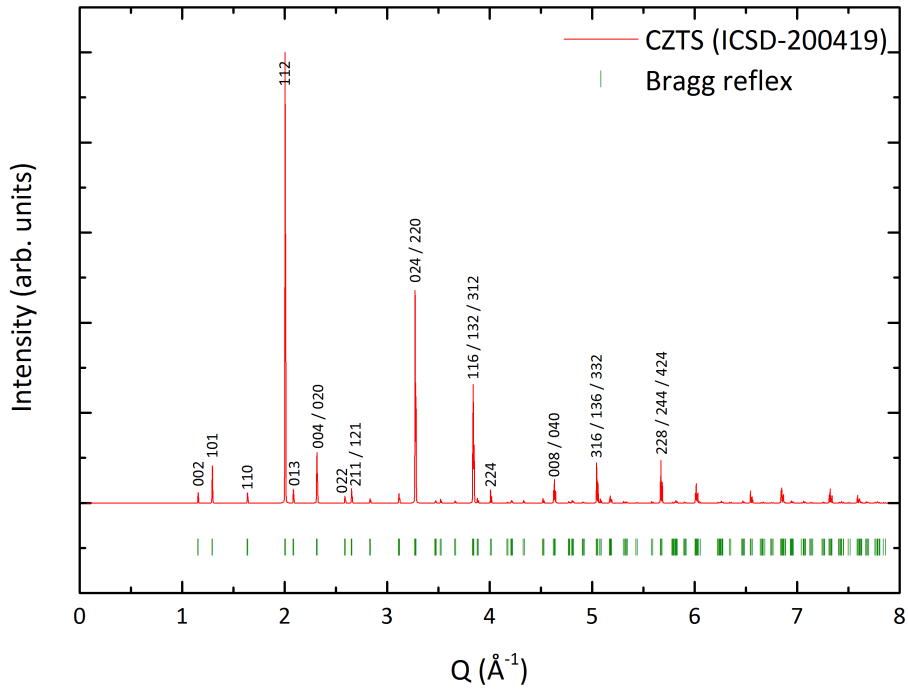
Figure 2.4: Simulated CZTS X-ray powder diffraction pattern and the most important Bragg reflexes highlighted [32].

A simulated X-ray powder pattern of CZTS with kesterite type structure (space group I$\bar{4}$) is presented in Figure 2.4. In contrast to the usually used $2\,\Theta$ [°] the Q space [Å^{-1}] will be used for all patterns. Q space offers an easier way to compare patterns measured at different wavelengths / energies because the values are wavelength corrected. The calculation for the conversion from different x spaces follows:

$$Q = 4 \cdot \pi \cdot \frac{sin\Theta}{\lambda} = \frac{2 \cdot \pi}{d} \quad \text{for constant wavelength}$$

$$Q = \frac{2 \cdot \pi}{tof} \cdot p_1 \quad \text{for time of flight}$$

(2.2)

With λ = wavelength, d_{hkl} = lattice plane spacing and Θ = diffraction angle, tof = time of flight dat in µs and p_1 = a value influenced by Θ, channel and further parameters of the time of flight experiment per data point.

Also the most important Bragg reflexes are highlighted. The experimental data will show the same Bragg reflexes but some may have lower intensities or are hidden in the background noise and the peak shape will differ from the simulated pattern. Also additional Bragg reflexes will be visible if secondary phases are present. The strongest Bragg reflex is *112* but the most important are *002*, *101* and *110* to distinguish kesterite type phases from ZnS. A separation between kesterite and stannite type structure would be possible if the experimental and simulated data would have the same quality but the small intensity differences of the Bragg reflexes are not distinguishable in the experimental data due to the instrument resolution function and inability to distinguish isoelectronic elements.
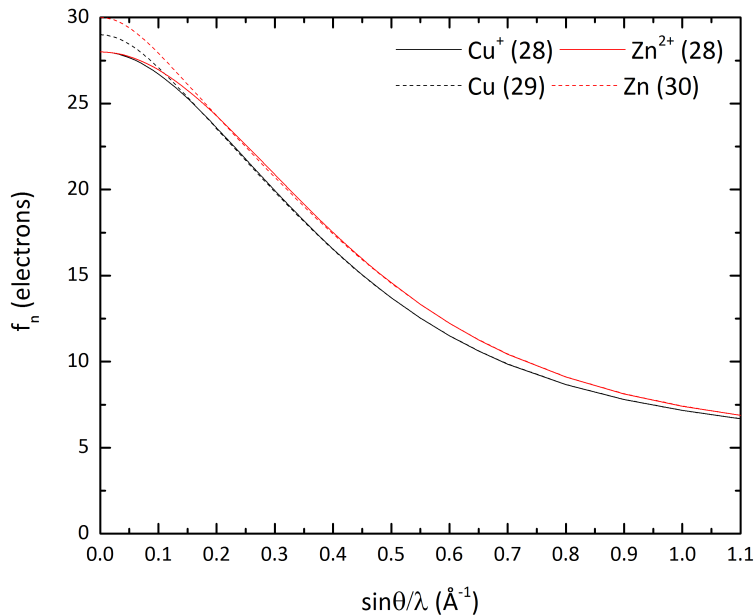
Figure 2.5: Atomic scattering factor f_n of Cu^+ and Zn^{2+} over the range of a standard X-ray measurement [7].

There are limits to the parameters which can be extracted out of X-ray powder diffraction patterns. X-ray radiation interacts with the electron shell of an atom. Due to the same numbers of electrons of Cu^+ and Zn^{2+} (28 in total) they are isoelectronic cations. This results in a similar atomic scattering factor f_n as shown in Figure 2.5 and Equation 2.3, so the determination of the cation distribution is not possible by X-ray powder diffraction. Furthermore the atomic scattering factor decreases with increasing scattering angle and the shorter the wavelength, the faster the atomic scattering factor drops with the scattering angle. More details can be found elsewhere [34, 87].

$$F_{hkl} = \sum_{1}^{N} \cdot f_n \cdot e^{2 \cdot \pi \cdot i \cdot (hx_n + ky_n + lz_n)} \tag{2.3}$$

Where F_{hkl} is the structure factor for the hkl reflection, N is the total number of atoms or ions belonging to the unit cell, f_n is the atomic scattering factor of the nth atom or ion in the unit cell and the coordinates (x_n, y_n, z_n) give the location of the nth atom or ion in the unit cell [34].

The solution to overcome this limitation is neutron diffraction. Neutrons interact with the nucleus of atoms and so the neutron scattering length of the elements is different (b_c for Cu = 7.718 fm, Zn = 5.680 fm and Sn = 6.225 fm [84]) to the atomic scattering factor.

2.2.2 Neutron powder diffraction

Neutron diffraction experiments were conducted at the Fine Resolution Powder Diffractometer (FIREPOD) at BERII at the Helmholtz-Zentrum Berlin and at the POWGEN beam line at SNS in Oak Ridge in USA. All neutron experiments were conducted at room temperature.
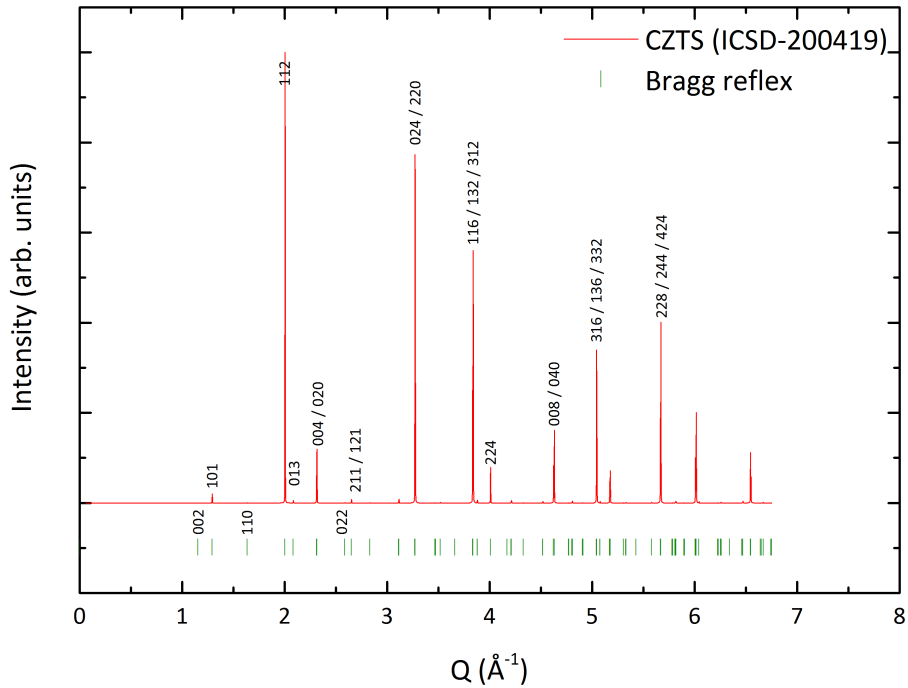
Figure 2.6: Simulated neutron diffraction pattern of CZTS (wavelength = 1.7978 Å)

A simulated neutron diffraction pattern of CZTS with a wavelength of 1.7978 Å can be seen in Figure 2.6. Due to the different scattering center the neutron diffraction patterns have some deviations from X-ray diffraction patterns. The general order of the Bragg reflexes remains. Similar to X-ray powder diffraction the simulated neutron

pattern in Figure 2.6 exhibit sharper Bragg reflexes and no background noise in contrast to the experimental results.

At the Fine Resolution Powder Diffractometer most of the CZTS powder samples were measured. The neutrons are produced by a reactor source with a continuous flux of 2×10^{14} neutrons/cm^{2}s in the core and 10^5 neutrons/cm^{2}s at the Fine Resolution Powder Diffractometer with a neutron wavelength of $1.7978\,\text{Å}$. The samples were placed in cylindrical vanadium containers of $6\,\text{mm}$ diameter and mounted at a $10\times$ sample changer. Good reflex statistics were important for further data processing so an average measurement time of $6\,\text{h}$ was applied which led to 10^4 counts in the strongest Bragg reflex.

Some samples were measured at the TOF (Time of Flight) instrument POWGEN in Oak Ridge. Here pulsed neutrons from a spallation source are used in a TOF setup. Due to the higher neutron output shorter measurement times can be achieved but because of the TOF setup data processing was more difficult.
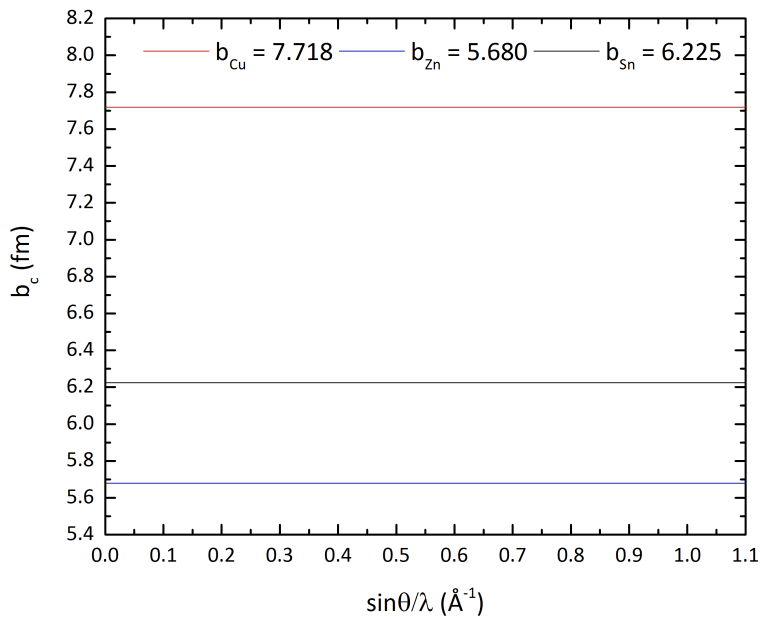
Figure 2.7: Neutron scattering factor b_c of Cu = red ($7.718\,\text{fm}$), Zn = blue ($5.680\,\text{fm}$) and Sn = black ($6.225\,\text{fm}$) [84].

Neutron powder diffraction made it possible to distinguish the isoelectronic Cu$^+$ and Zn^{2+} because the neutron scattering length is different for these atoms [84]. Similar successful experiments were conducted by Gurieva et al. [29], Schorr [74] and Schorr et al. [76]. Furthermore the neutron scattering length is not decreasing with higher scattering angles (see Figure 2.7) like the atomic scattering factor (see Figure 2.5, page 20).

This has a direct impact on the powder patterns measured by neutron diffraction. The Bragg reflex intensity is much stronger in higher Q space range than in X-ray powder
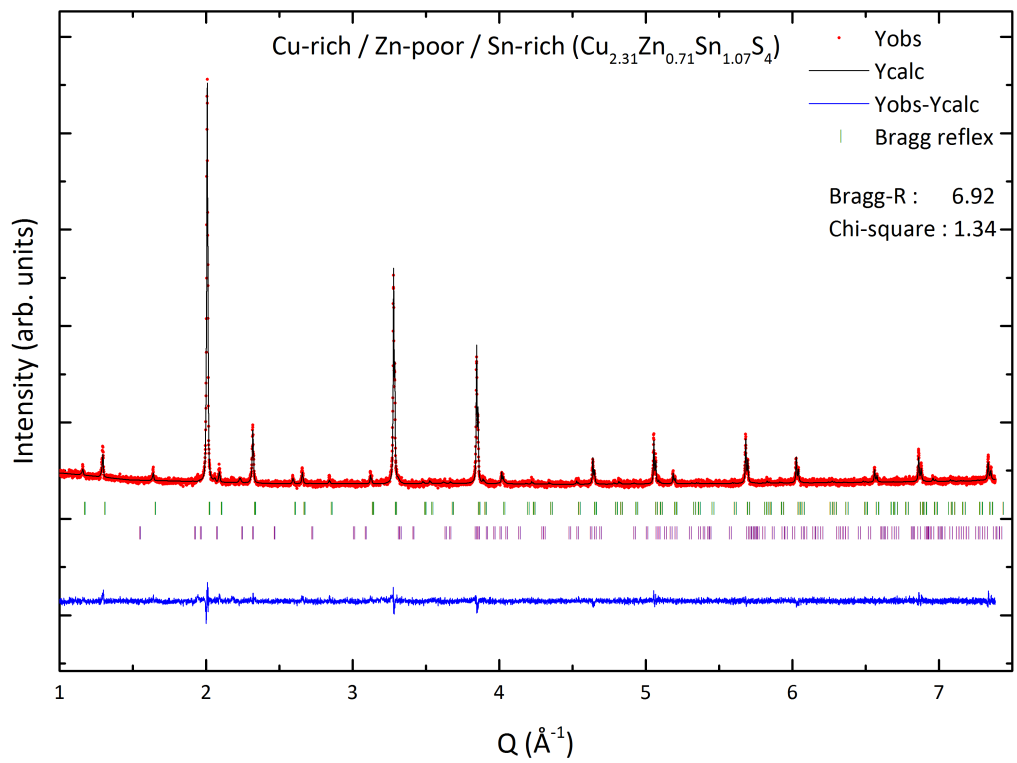
Figure 2.8: Comparison of X-ray and neutron diffraction pattern (below) to highlight the increased intensities of neutron diffraction at higher Q.
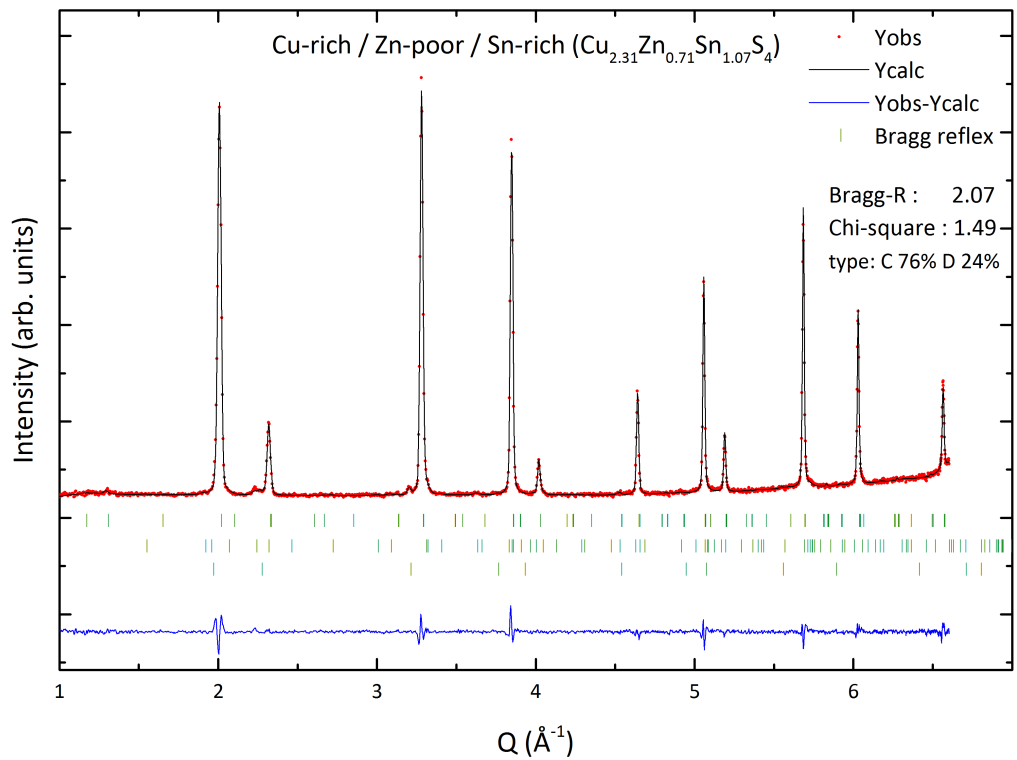
Figure 2.9: Comparison of X-ray (above) and neutron diffraction pattern to highlight the increased intensities of neutron diffraction at higher Q.

diffraction. A comparison between a X-ray powder diffraction and neutron diffraction pattern of the same sample can be seen in Figure 2.8 and Figure 2.9. The intensity of the strongest reflex is similar but the reflexes at higher Q space have increased intensities.

2.2.3 Anomalous X-ray diffraction

The limitation of conventional X-ray diffraction patterns to distinguish isoelectronic Cu^+ and Zn^{2+} can also be overcome by the use of anomalous X-ray diffraction. Anomalous X-ray diffraction was applied as an alternative to distinguish the Cu-Zn disorder by neutron powder diffraction. Hereby anomalous X-ray diffraction utilizes the energy / wavelength dependence of the dispersion factor (f') and phase shift (f''), described in Equation 2.4, especially at the absorption edges of Cu and Zn (see Figure 2.10). If the occupation of the lattice plane contributing to a Bragg reflex changes intensity changes are induced. This approach is not trivial as the definition of the atomic form factor is complicated:

$$f_n = f_0 + f' + i \cdot f'' \tag{2.4}$$
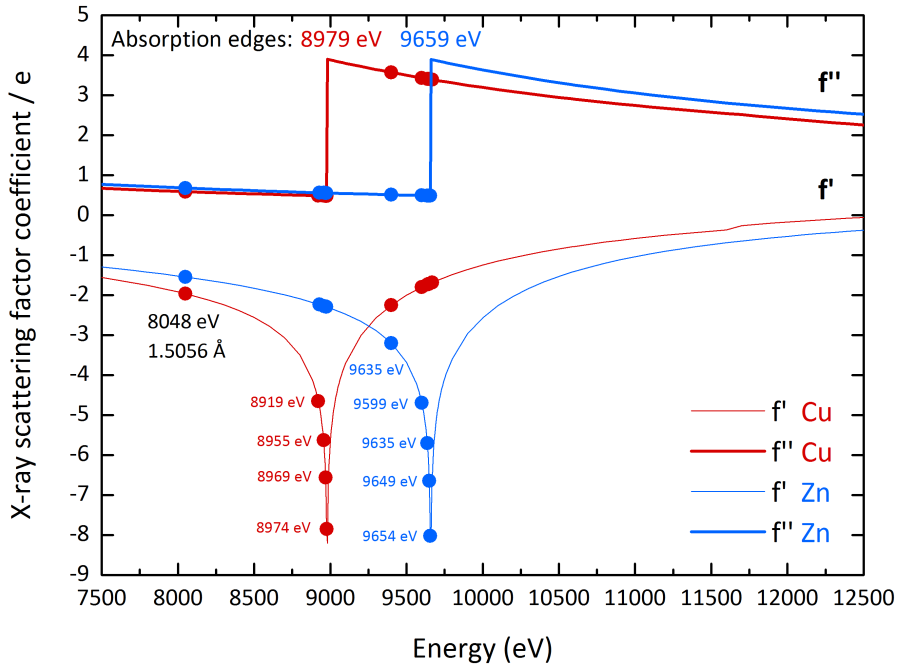
Figure 2.10: f' and f'' in dependence of the energy / wavelength and absorption edges of Cu and Zn [16, 17]. Also all ten energies measured during the experiment are highlighted.

The atomic form factor f_n is described by the dispersion factor f' and the f'' phase shift which is a complex function. Both f' and f'' are energy / wavelength dependent.

The base component f_0 is a function of the diffraction angle. However it was shown by Többens et al. [92] that the simple approximation $f_n \approx f_0 + f'$ can be used if a properly adjusted f_0 is chosen. The correct value for f_0 was derived from simulated powder patterns and further details can be found in Többens et al. [92].

This approximation led to the following equation in the case of only two elements:

$$Occ^{calc}(A) = Occ(B) \cdot \frac{f(B)}{f(A)} + Occ(A) \tag{2.5}$$

The result is a linear plot of $Occ^{calc}(A)$ over $f(B)/f(A)$ with $Occ(B)$ as slope and $Occ(A)$ as zero intercept. The site occupation of $Occ(A) + Occ(B)$ at $f(B)/f(A) = 1$ [92].

For the calculation several values are needed, especially f' for Zn and Cu. Luckily various tabulated values of all components of the atomic form factor exist. The wavelength independent part of f_0 was considered by the analytic 9-parameter approximation stored in FullProf for neutral atoms [72]. f' and f'' were taken from the dataset by Merritt [52]. This data was calculated by using the subroutine library by Brennan & Cowan [6] and the theoretical approximation developed by Cromer & Liberman [17]. Linear interpolation was used for all data between the tabulated values [92].

Nevertheless some corrections were necessary and in order to get a significant result in total ten different energies / wavelengths were measured. Further details can be found in Többens et al. [92].

To achieve accurate results a setup is needed which allows energy / wavelength dependent measurements. The diffraction station at the KMC-2 beam line at BESSY II fulfills all these conditions. Synchrotron measurements near the absorption edges of Cu (8979 eV) and Zn (9659 eV) with energies of 8048 eV, 8919 eV, 8955 eV, 8969 eV, 8974 eV, 9376 eV, 9599 eV, 9635 eV, 9649 eV and 9654 eV were possible.

Finally the sample preparation is very important to obtain reliable results. Because intensity changes in reflexes with low intensities are important, a well ground homogeneous sample is needed. Some larger crystallites can influence these intensities and have a huge impact on the results.

After the measurements the data needs to be evaluated. Therefore the FullProf Suite by Rodríguez-Carvajal [72] was used.

2.2.4 The Rietveld method

In order to process the X-ray and neutrons diffraction patterns and obtain structural parameters, full pattern Rietveld refinement has been applied [68, 69, 102]. The free FullProf Suite software package by Juan Rodríguez-Carvajal was used [72].

The Rietveld refinement is a complex minimization method on the basis of the least square approach [68, 69, 102]. It is a structure refinement and not a structure solution

method where an unknown structure is solved. So some previous knowledge about the structure and good starting parameters are prerequisite for a successful Rietveld analysis.

An important parameter is the peak shape (full width at a half maximum = FWHM) which is shown in Equation 2.6 and depends on two factors. First the instrument resolution which is taken into account by measuring a standard and creating an irf-file out of the Rietveld analysis (see Figure 2.3, page 18) and second the influence of the crystal structure and crystallinity of the measured samples.

$$(FWHM)_k = U \cdot \tan^2 \cdot \Theta_k + V \cdot \tan \cdot \Theta_k + W \tag{2.6}$$

Important for the peak shape is also the profile function selected for the refinements. The Thompson-Cox-Hastings pseudo-Voigt function convoluted with axial divergence asymmetry function [19, 90] was used for all X-ray powder diffraction and neutron diffraction patterns. Further details about Rietveld refinement can be found elsewhere [68, 69, 72, 102].

In case of the investigated samples for the quaternary compounds the kesterite type structure was used as a starting model [32, 74]. If secondary phases were present the structure was added if additional Bragg reflexes were detected and an improvement of the refinement observed. The free parameters for the refinements are global parameters: scale factor, background, zero shift, profile parameters (U, V, W, X, Y), asymmetry ($S\_$-L, D_L) and structural parameters: lattice parameters (a, b, c), anion position (x, y, z), site occupation (Occ) of Wyckoff positions, isotropic temperature factors (Biso) of Wyckoff positions.

Also the order of the refined parameters is very important for the Rietveld analysis because a wrong refinement order of parameters could lead to wrong results. So it does not make sense refining the occupation at the beginning because the Rietveld fit is inaccurate and produces huge errors. The following order has been applied for most of the neutron Rietveld refinements and was converging:

1. global parameters are refined like the scale factor, zero shift and the manually selected background points (ca. 20)

2. lattice parameters *a, b, c*

3. profile parameters: *U* and *Y* (*V,W,X* only if improvement for refinement)

4. anion position (x, y, z)

5. asymmetry (S_L, D_L) → coupled and damped

6. isotropic temperature factors (Biso) → starting values of single crystal measurements by Choubrac et al. [14]. If values become unreasonable strongly correlated Wyckoff positions 2a, 2b and 2c, 2d were coupled

7. isotropic temperature factors (Biso), asymmetry (S_L, D_L) and anion position (x, y, z) fixed → refine occupation (*Occ*)

The refinement procedure for the anomalous X-ray diffraction differs from the neutron procedure slightly:

1. LeBail refinement of pattern at $8048\,\text{eV}$ [3]

    a) global parameters are refined like the scale factor, zero shift and the manually selected background points (ca. 20)

    b) lattice parameters *a, b, c*

    c) profile parameters: *U* and *Y* (*V,W,X* only if improvement for refinement)

2. Rietveld refinement of pattern at $8048\,\text{eV}$ [68]

    a) global parameters are refined like the scale factor, zero shift and the manually selected background points (ca. 20)

    b) lattice parameters *a, b, c*

    c) profile parameters: *U* and *Y* (*V,W,X* only if improvement for refinement)

    d) anion position (*x, y, z*) $\rightarrow$ used for all energies

3. Rietveld refinement of all energies [68]

    a) global parameters are refined like the scale factor, zero shift and the manually selected background points (ca. 20)

    b) lattice parameters *a, b, c*

    c) profile parameters: *U* and *Y* (*V,W,X* only if improvement for refinement)

    d) isotropic temperature factor (Bov) $\rightarrow$ starting values of single crystal measurements by Choubrac et al. [14].

    e) preferred Orientation if necessary

    f) refine occupation (*Occ*)

There is also a need of an indicator to interpret the quality of the Rietveld analysis. In Equation 2.9 and 2.10 the two most important numerical indicators of a Rietveld analysis are given. If χ^2 (chi square) (see Equation 2.9, page 28), which is calculated by R_{wp}/R_{exp} (see Equation 2.7, page 28), is approaching one the Rietveld refinement has a very good quality. Also higher values are possible because χ^2 is strongly coupled with the measurement statistics. R_{Bragg} indicates the quality of the Rietveld refinement. If it approaches zero R_{Bragg} has the best compliance. Also higher values are acceptable if the refinement and difference plot look reasonable.

$$R_{wp} = 100 \cdot \left[\frac{\sum\limits_{i=1,n} w_i |y_i - y_{c,i}|^2}{\sum\limits_{i=1,n} w_i y_i^2} \right]^{1/2} \tag{2.7}$$

$$R_{exp} = 100 \cdot \left[\frac{n - p}{\sum\limits_{i} w_i y_i^2} \right]^{1/2} \tag{2.8}$$

$$\chi^2 = \left[\frac{R_{wp}}{R_{exp}} \right]^2 = S^2 \tag{2.9}$$

$$R_{Bragg} = 100 \cdot \frac{\sum\limits_{h} |I_{obs,h} - I_{cal,h}|}{\sum\limits_{h} |I_{obs,h}|} \tag{2.10}$$

2.2.5 The average neutron scattering length method

To combine the knowledge of the electron micro probe analyzer measurements and Rietveld analysis of the neutron data the average neutron scattering length method by Schorr [73] was used [21, 64]. By this approach it is possible to gain information about the cation distribution and intrinsic point defects of the different Wyckoff positions. Furthermore after the cation distribution is known the defect concentrations of the kesterite phase can be calculated.

Therefore it is necessary to extract site occupation parameters Occ_x *(x = 2a, 2c, 2d, 2b)* of the different Wyckoff positions of the refined neutron data (see Chapter 2.2.4, page 25). These site occupations were then multiplied with the neutron scattering length of the element b_c *(c = Cu, Zn, Sn)* occupying the Wyckoff position in the fully ordered crystal structure leading to the experimental neutron scattering length $\bar{b}_x^{RR}$ *(x = 2a, 2c, 2d, 2b)* presented in Equation 2.11.

$$\begin{aligned} \bar{b}_{2a}^{RR} &= Occ_{2a} \cdot b_{Cu} \\ \bar{b}_{2c}^{RR} &= Occ_{2c} \cdot b_{Cu} \\ \bar{b}_{2d}^{RR} &= Occ_{2d} \cdot b_{Zn} \\ \bar{b}_{2b}^{RR} &= Occ_{2b} \cdot b_{Sn} \end{aligned} \tag{2.11}$$

Conditions:

$Occ(Cu)_x^{calc} + Occ(Zn)_x^{calc} + Occ(Sn)_x^{calc} + Occ(V)_x^{calc} = 1$

$\sum_x Occ(Cu)_x^{calc} = Cu^{WDX}, \sum_x Occ(Zn)_x^{calc} = Zn^{WDX}, \sum_x Occ(Sn)_x^{calc} = Sn^{WDX}$

Only the amounts of Cu, Zn and Sn measured by WDX can be distributed.

Now the experimental neutron scattering length $\bar{b}_x^{RR}$ *(x = 2a, 2c, 2d, 2b)* has to be correlated with the chemical composition obtained by WDX measurements at the electron micro probe analyzer. Therefore elements measured by WDX are distributed fulfilling certain conditions: the sum of elements cannot exceed one and the elements distributed on the different Wyckoff positions cannot exceed the amount of the elements measured by WDX.

Out of this cation distribution considering the mentioned conditions the average neutron scattering length for the different Wyckoff positions can be calculated which corresponds to $\bar{b}_x^{calc}$ in Equation 2.12. The goal is to converge the experimental neutron scattering length ($\bar{b}_x^{RR}$) and the calculated average neutron scattering length ($\bar{b}_x^{calc}$) by varying the site occupation under the given conditions.

$$\bar{b}_x^{calc} = Occ(Cu)_x^{calc} \cdot b_{Cu} + Occ(Zn)_x^{calc} \cdot b_{Zn} + Occ(Sn)_x^{calc} \cdot b_{Sn} \qquad (2.12)$$

Therefore the elements occupying a Wyckoff site have to be multiplied with their respective neutron scattering length ($b_{Cu} = 7.718\,\mathrm{fm}$, $b_{Zn} = 5.680\,\mathrm{fm}$, $b_{Sn} = 6.225\,\mathrm{fm}$) and then summed up to the calculated average neutron scattering length ($\bar{b}_x^{calc}$) as shown in Equation 2.12. By the variation of the atoms (Cu, Zn, Sn) on a Wyckoff site, taking into account a reasonable contribution regarding the defect complexes and their correlating intrinsic point defects, b_x^{calc} *(x = 2a, 2c, 2d, 2b)* was calculated. In the best case $\bar{b}_x^{RR}$ is equal to b_x^{calc} but also a result inside the error bar of $\bar{b}_x^{RR}$ is in very good agreement.

2.3 Temperature dependent resistivity measurements

In collaboration with the Institute of Applied Physics at the Academy of Sciences of Moldova in the IRSES PVICOKEST 269167 project temperature dependent electrical resistivity and conductivity measurements were conducted to characterize electronic properties of the CZTS absorber material [18, 31, 54]. The Van der Pauw method and a four-terminal sensing setup illustrated in Figure 2.11 was used for the analysis [60]. Therefore off-stoichiometry CZTS powders were pressed as pellets and four silver paste contacts were applied. Two contacts were connected to a voltmeter and on the other two the ammeter was connected and a current I was forced through the sample. The resistivity ρ of the sample can be calculated:

$$\rho = \frac{V \cdot w \cdot h}{I \cdot length} \tag{2.13}$$

a)

b)
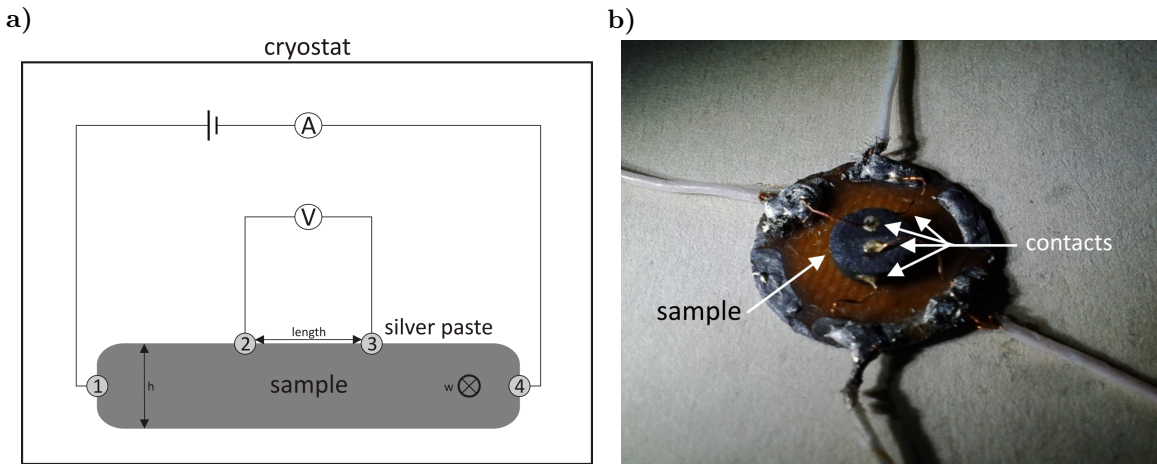
Figure 2.11: Setup of the temperature dependent resistivity measurements: a) schematic overview b) actual setup at CZTS sample.

Furthermore by adding a cryostat the samples were measured in temperature range of $12\,\mathrm{K}$ to $300\,\mathrm{K}$. This was repeated twice (cooling and heating) for each sample. Similar experiments were already conducted elsewhere [25, 26, 48, 49].

For the data analysis and fitting the following universal law will be used:

$$\rho(T) = AT^{1/x} \exp[(\frac{T_0}{T})^{1/x}] \tag{2.14}$$

The factor x can be substituted by a constant of one of the three common models which are used to describe the electron processes and by fitting the results the dominating process can be found out:

1. Miller-Abrahams or nearest neighbor hopping (NNH) (x = 1) [53]

2. Mott variable range hopping (M-VRH)(x = 4) [54]

3. Shklovski-Efros variable Range hopping (SE-VRH) (x = 2) [18]

If the data obtained from temperature dependent resistivity measurements can be fitted by one of the presented models further parameters concerning the charge carriers can be determined. There exists no advantage of any of the presented models over another. Different materials can require a distinct model and if none of the given models applies the carrier process is allocated to intergrain diffusion which is inferior to the various hopping mechanisms.

2.4 Absorber layer processing by rapid thermal evaporation

The thin film fabrication by thermal evaporation and the analyses were conducted as part of the INTERKEST 57050358 project where R. Caballero and R. Gunder performed most of the experiments [22].

In order to produce thin films off-stoichiometric CZTS powder was used as an evaporation precursor material. The thin films were deposited onto Molybdenum coated glass substrates by thermal evaporation and subsequent thermal treatment in an Ar + S atmosphere. The crucible containing the powder was heated until the total evaporation of the precursor at around 1200 °C. The substrate was heated to a temperature of 250 °C and the whole deposition of the thin films was achieved in around 12 min. This resulted in CZTS thin films with an average thickness of 1.5 µm to 2 µm. All these steps are conducted inside of a vacuum chamber with a pressure of 10^{-5} mbar. This method can be classified as a form of physical vapor deposition (PVD) and a schematic overview of the setup can be seen in Figure 2.12.
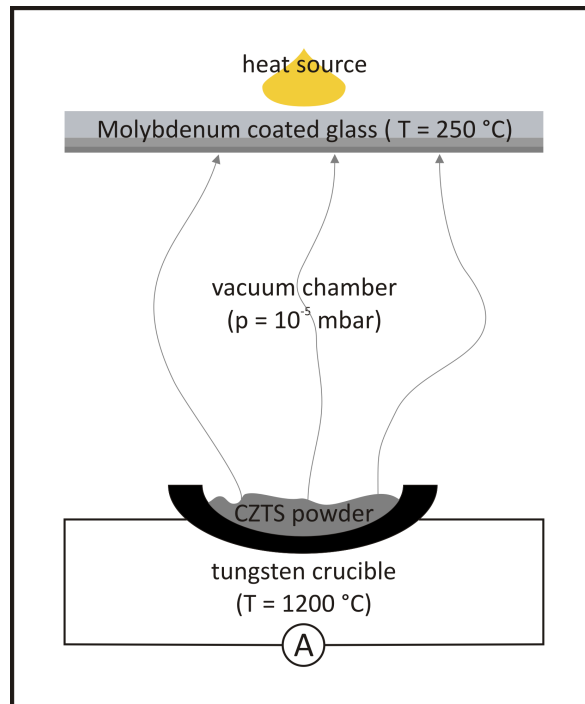
Figure 2.12: Schematic overview of the thermal evaporation setup where the thin film solar cells were prepared.

Afterwards different thermal treatments were applied and chemical etchings with KCN or $(NH_4)_2S$ conducted to reduce the presence of secondary phases. At last solar cells were fabricated by deposition of a CdS or Zn(O,S) buffer and ZnO / ITO or i-ZnO / AZO layers. The efficiency of the fabricated solar cells was measured with a ASTM G173 AM1.5GT spectrum at 298 K in a solar simulator. Further details can be found in Garcia-Llamas et al. [22].

3 Results and discussion

3.1 Phase content and chemical composition of the Cu$_2$S–ZnS–SnS$_2$ system

Kesterite type semiconductors have achieved a rapid development in recent years leading to a world record thin film solar cell efficiency of 12.6 % [97]. Even so the understanding of defect complexes and influence of secondary phases are still not well known. Also the optical and electronic properties of the absorber material are strongly influenced by compositional changes which have a direct impact on the structure and intrinsic point defects. The most efficient kesterite type solar cells exhibit A-type composition (Cu-poor / Zn-rich) (see Table 1.1, page 9) but in solar cells only an integral composition can be measured. So in principle it is possible that in solar cells multiple kesterite type phases are present which prevents a deeper understanding of the structure and the occurring intrinsic point defects.

This limitation can be overcome with the use of homogeneous powder samples. To achieve accurate results for further investigations like cation distribution and defect concentrations it is of major importance to know the chemical composition as exact as possible. Therefore all samples were studied by:

1. backscattered electron micrographs produced by an electron micro probe analyzer (see Chapter 2.1.2, page 16) → identification of secondary phases

2. optical microscope included in the electron micro probe analyzer → identification of secondary phases

3. wavelength dispersive X-ray spectroscopy (WDX) to determine the chemical composition of the occurring phases

4. X-ray powder diffraction for qualitative phases identification and quantitative phase contents [35]

Some of the following results were already published and can be found in Valle Rios et al. [96].

3.1.1 Chemical characterization of intermediate and annealed off-stoichiometric CZTS samples of the first synthesis

The synthesis was started by weighting elements for CZTS exhibiting an A-type composition. Therefore the formula for A-type composition presented in Table 1.1 was used with x = 0, 0.025, 0.050, 0.100 and 0.125. An overview of the weighed elements of the described samples can be seen in Table 3.1. The synthesis routine by Schorr [74] was used but the cooling rate was adjusted. The final temperature where the samples were held for $240\,h$ was $750\,°C$ and a S excess of $3\,\%$ was chosen.

Table 3.1: A-type synthesis: overview of calculated weights and needed elements.

x	Name	$\dfrac{Cu}{Zn + Sn}$	$\dfrac{Zn}{Sn}$	Cu_{2-2x}	Zn_{1+x}	Sn_1	S_4		Cu (g)	Zn (g)	Sn (g)	S (g)
0.000	A0000	1	1	2	1	1	4	C	1.44597	0.74418	1.35060	1.45925
								M	1.44567	0.74410	1.35076	1.45956
0.025	A0025	0.963	1.025	1.95	1.025	1	4	C	1.41478	0.76547	1.35536	1.46439
								M	1.41485	0.76544	1.35555	1.46451
0.050	A0050	0.9268	1.05	1.85	1.075	1	4	C	1.38338	0.78691	1.36015	1.46957
								M	1.38322	0.78692	1.36014	1.46968
0.100	A0100	0.8571	1.1	1.6	1.2	1	4	C	1.31989	0.83025	1.36983	1.48003
								M	1.31994	0.83035	1.36963	1.48028
0.125	A0125	0.8235	1.125	1.4	1.3	1	4	C	1.28781	0.85215	1.37472	1.48531
								M	1.28771	0.85220	1.37482	1.48552

To gain a better understanding of the synthesis the first samples were also characterized between the 1st and 2nd reaction step. The results of the WDX analysis of these intermediate samples have shown that a quaternary compound was already formed, but the chemical variation of the grains was significant and the quaternary phase was not homogeneous throughout the samples. Also multiple binary and ternary phases were present. These phases have shown a limited solubility of Cu and Sn in ZnS, Zn and Sn in CuS as well as some Zn in Cu_2SnS_3 was determined. Furthermore the fraction of secondary phases was equal to the amount of the quaternary compound. These results have been assistant to understand the growth process of CZTS and to improve the solid state synthesis procedure.

In Figure 3.1 $Cu\,/\,(Zn + Sn)$ and $Zn\,/\,Sn$ ratios of the corresponding weighted elements ($\star$) are presented together with the measured chemical composition of the electron micro probe analyzer analyses after the 2nd reaction step ($\square$). Secondary phases are represented by squares filled with colors according to the identified secondary phases in the sample:

single-phase CZTS	pure single-phase CZTS = 🔴
copper sulfides	CuS (covellite), $Cu_{1.8}S$ (digenite) and Cu_2S (chalcocite) = 🟦
zinc sulfide	ZnS (sphalerite) = 🟪
tin sulfides	SnS (herzenbergite) and SnS_2 (berndtite) = 🟩
copper-tin compounds	Cu-Sn-S = ⬛
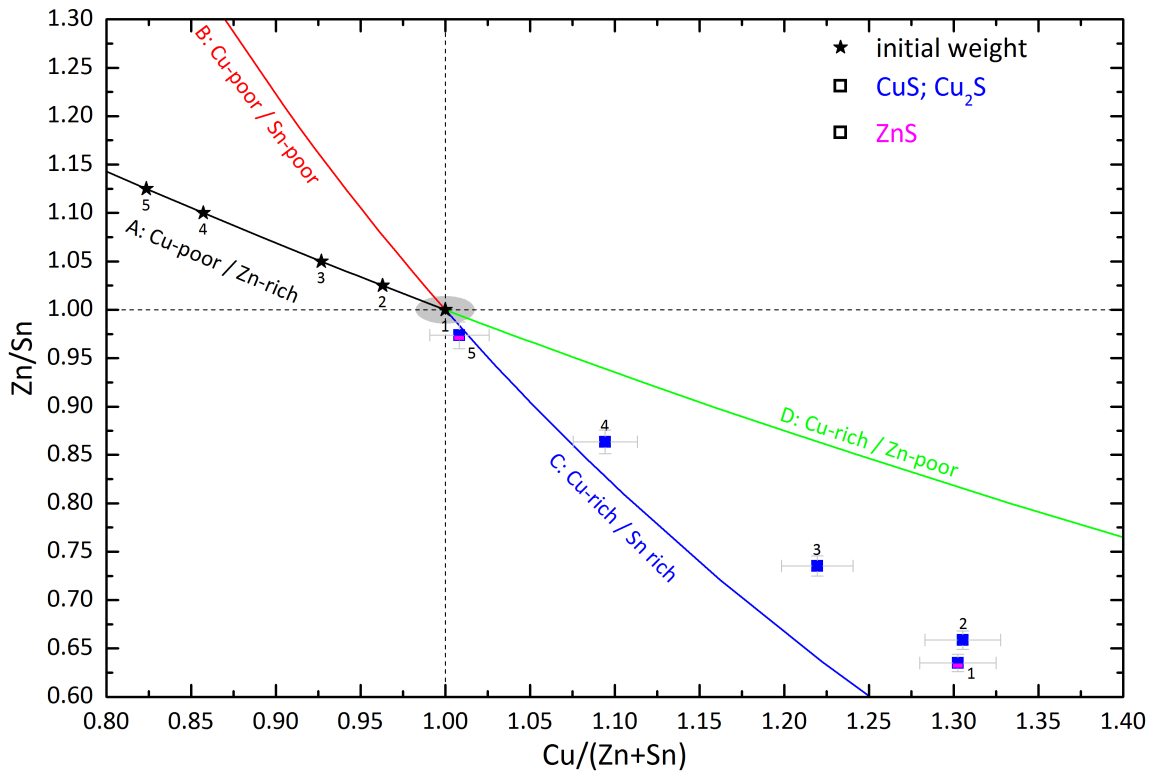
Figure 3.1: Results of the chemical characterization of the CZTS phases of the finished first A-type synthesis and the corresponding initial weighed composition. The colors of the rectangles represent single-phase = red and different secondary phases: copper sulfides = blue, zinc sulfides = magenta and star = initially weighed composition.
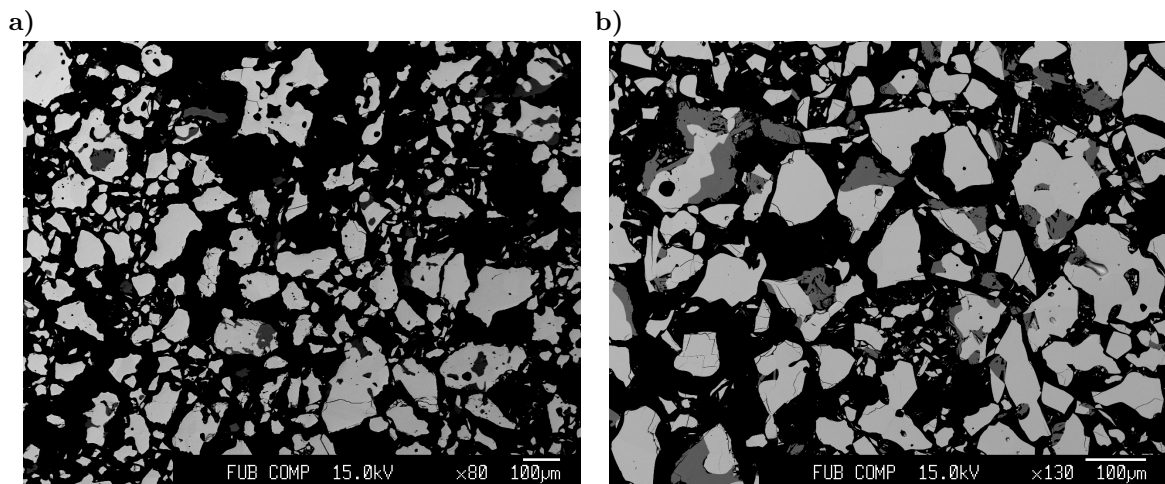
Figure 3.2: BSE micrographs of two samples of the first A-type synthesis: a) almost stoichiometric sample with Cu / (Zn + Sn) = 1.008(17) and Zn / Sn = 0.974(14) b) off-stoichiometric sample with Cu / (Zn + Sn) = 1.305 and Zn / Sn = 0.659. In both samples secondary phases are present: dark gray = copper sulfide.

During the electron micro probe analyzer measurements also backscattered micrographs were produced and an example can be seen in Figure 3.2. CZTS can normally be separated from the secondary phases due to a different gray tone, and covellite can be distinguished in the optical microscope which is attached to the electron micro probe analyzer. Some secondary phases, like mohite Cu_2SnS_3, can only be distinguished from CZTS by applying WDX measurements.

In comparison to the analysis after the 1st reaction step the amount of secondary phases was greatly reduced and ternary phases have completely disappeared and were probably transformed to CZTS. The comparison of the results after the 1st and 2nd reaction step has shown that at least two reaction steps are prerequisite for the successful synthesis of homogeneous powder samples.

a)

b)
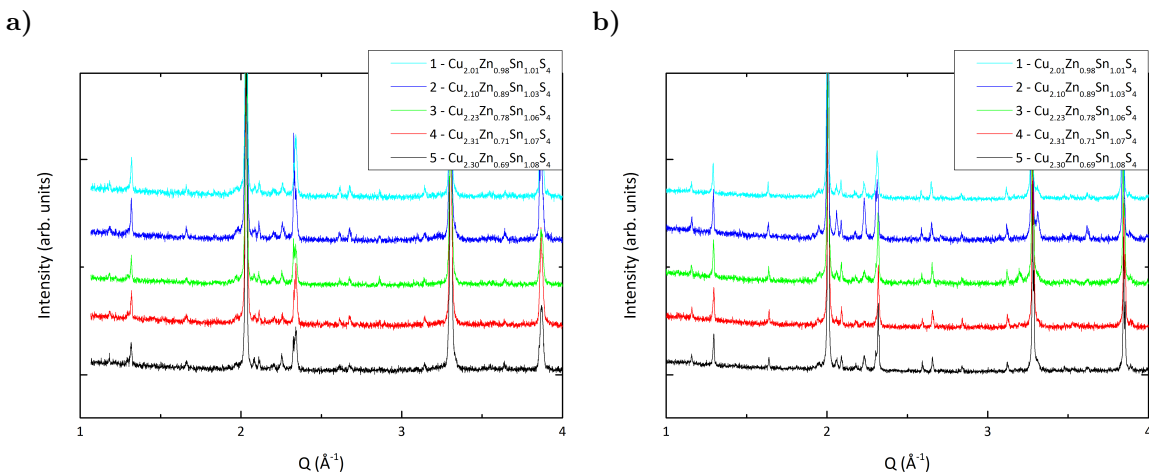
Figure 3.3: Comparison of the diffraction patterns of the intermediate and final samples.

A strong shift of the chemical composition can be observed from the intended composition (see Figure 3.1, page 35). This shift was mainly caused by non-reacted metals which moved the composition from Cu-poor / Zn-rich to Cu-rich / Zn-poor. The consequence of non-reacted metals discovered after the synthesis was an increase of the final temperature to 820 °C and S excess to 10 % for the following syntheses. The leftover metals had no negative influence on the homogeneity of the powder samples which is also a proof of the stability and flexibility of the CZTS compound.

The identified secondary phases are still in agreement with the chemical trend of the samples. Mostly copper sulfides were detected as secondary phase which can be expected if the samples exhibit a Cu-rich / Zn-poor composition. Also a small amount of ZnS was identified and a limited solubility of Cu and Sn in the binary compound was observed. In contrast the copper sulfides identified as covellite and digenite show no solubility of Zn or Sn although the compounds were slightly copper poor (x = 0, $Cu_{0.92}S$). Overall the solubility of elements in the secondary phases decreased in comparison to the intermediate samples.

Complementary to the EMPA measurements X-ray powder diffraction was performed to gain information about the lattice parameters of the CZTS compounds and to estimate the amount of the identified phases by quantitative analysis. Due to the limited
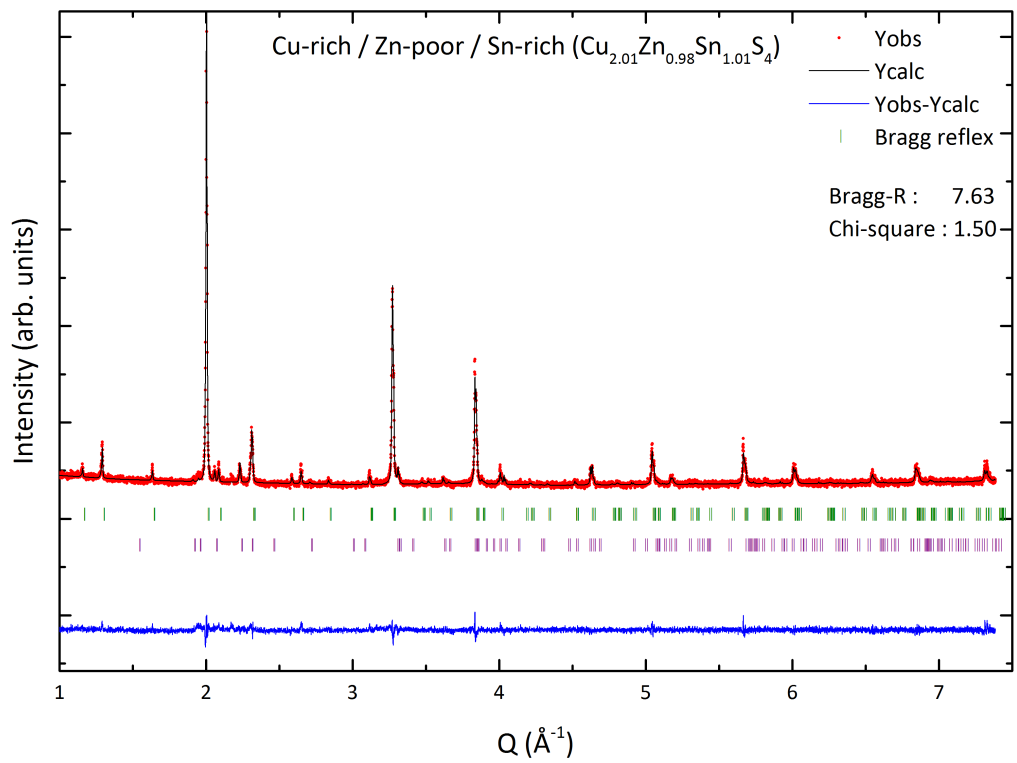
Figure 3.4: Refined X-ray patterns of almost stoichiometric sample with $Cu/(Zn+Sn)$ = 1.008(17) and $Zn/Sn = 0.974(14)$.
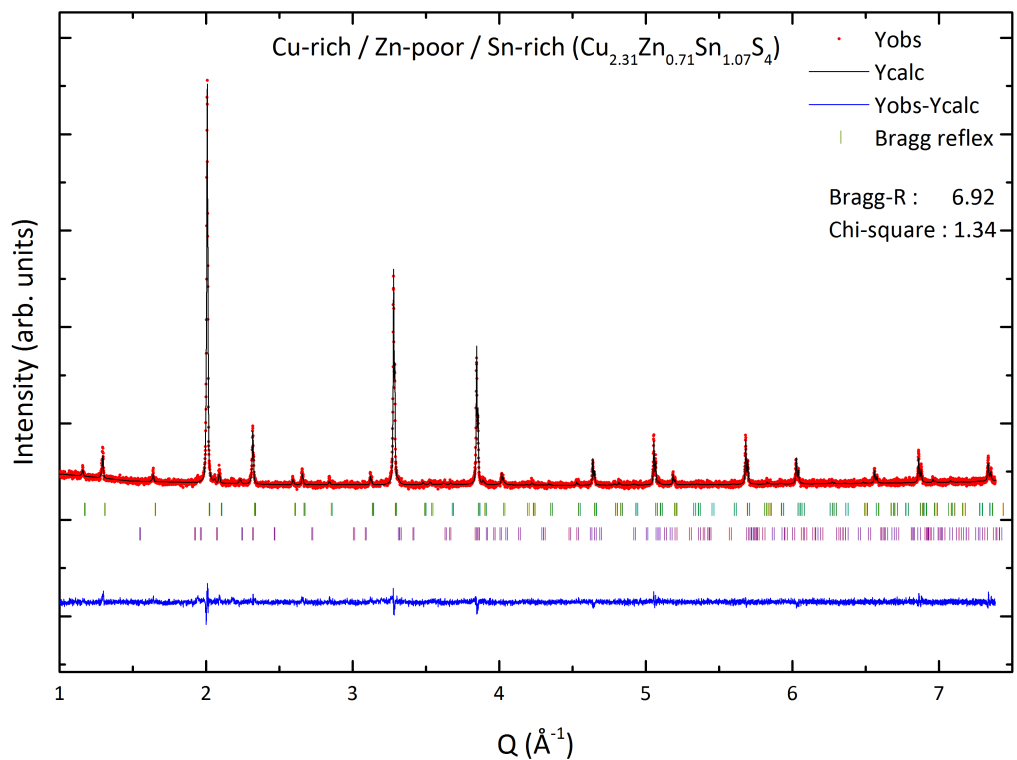
Figure 3.5: Refined X-ray patterns of off-stoichiometric C-type sample with $Cu/(Zn+Sn)$ = 1.305(22) and $Zn/Sn = 0.659(10)$.

volume used for the X-ray diffraction analyses compared to the neutron diffraction the results of the quantitative analysis from X-rays are inferior, but still offer a good representation of the phase fractions. Therefore only the quantitative results of the neutron diffraction will be used and are presented in Table A.1.

The diffraction patterns presented in Figure 3.3 are supporting the results of the EMPA measurements of more homogeneous samples and an increased crystallinity after the 2nd reaction step. Overall the Bragg reflexes are sharper in the final samples and not as broad at higher angles as in the intermediate sample X-ray patterns. Furthermore in all diffraction patterns some additional Bragg reflexes were identified which could be assigned to secondary phases.

In Figure 3.4 and Figure 3.5 two refined diffraction patterns are presented which exhibit distinct chemical compositions (Cu-rich / Zn-poor). Figure 3.4 shows an almost stoichiometric sample with $Cu / (Zn + Sn) = 1.008(17)$ and $Zn / Sn = 0.974(14)$ and Figure 3.5 an off-stoichiometric C-D-type sample with $Cu / (Zn + Sn) = 1.305(22)$ and $Zn / Sn = 0.659(10)$. Both samples can also be found in Figure 3.3, but unrefined X-ray patterns only offer limited evaluation of the data. Both refined X-ray patterns are very similar because CZTS is the dominating phase and all Bragg reflexes could be assigned accordingly. Furthermore the copper sulfide measured by the electron micro probe analyzer could be identified as covellite. Furthermore digenite was later identified by neutron diffraction.

The ZnS found by WDX in the almost stoichiometric sample could not be assigned to any Bragg reflexes in the X-ray pattern which indicates ZnS corresponds to sphalerite because the Bragg reflexes with high intensity of CZTS and sphalerite tend to overlap. Since no Bragg reflexes of ZnS were detected in the diffraction pattern it could also indicate that the phase content of ZnS is below the X-ray powder diffraction detection limit. In that case ZnS could also have wurtzite structure. This is very unlikely because wurtzite is the high temperature phase of sphalerite. The small observed differences of the two X-ray diffraction patterns are mainly caused by different secondary phases.

3.1.2 New off-stoichiometry CZTS types and the calculation routine of the chemical composition

Except the difficulties regarding reactivity during the first synthesis some additional problems were revealed:

1. Lafond et al. [45] suggested four cation substitution types but these cannot explain all synthesized chemical compositions.

2. Unknown fraction of the different off-stoichiometric types especially in a mixture composition which are the majority of samples.

3. Chemical formulae derived from the electron micro probe analyzer measurements do not consider some intrinsic point defects like V_{Cu} and Cu_i due to the internal normalization of the instrument.
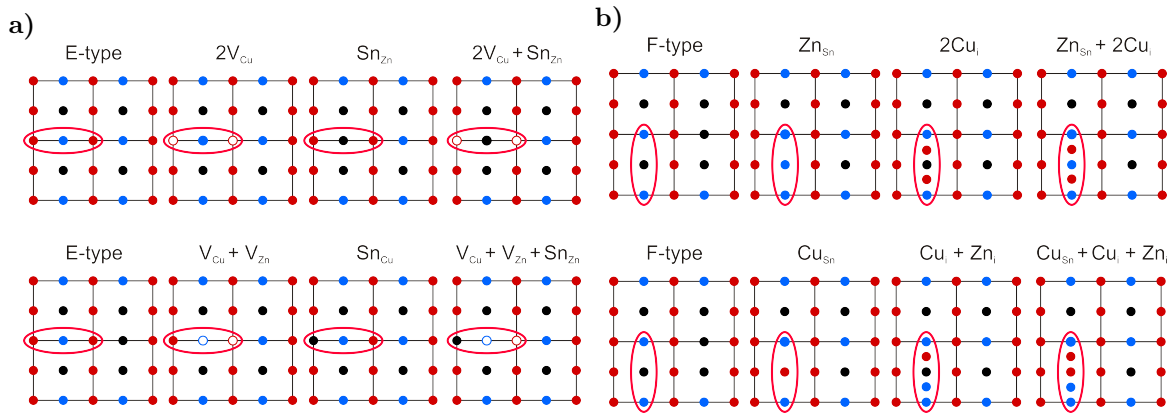
Figure 3.6: Two additional off-stoichiometric types: a) E-type = Cu-poor / Zn-poor / Sn-rich and b) F-type = Cu-rich / Zn-rich / Sn-poor postulated by our group EM-ASD [29, 96]. Four unit cell along the c-axes: Cu = red, Zn = blue and Sn = black.

The first problem was introduced because of the sample located near the stoichiometry point but situated between the C- and A-type with Cu / (Zn + Sn) = 1.008(17) and Zn / Sn = 0.974(14) (see Figure 3.1, page 35). The opposing chemistry of the A- and C-type makes a mixture impossible. Also further samples have shown that an extra type needs to be introduced [29]. Therefore the E-type was introduced and in contrast to the four existing types two different defect complexes are possible:

E-type: $2\mathrm{Cu}^+ + \mathrm{Zn}^{2+} \rightarrow 2\mathrm{V}_{\mathrm{Cu}} + \mathrm{Sn}_{\mathrm{Zn}}$ or $2\mathrm{Cu}^+ + \mathrm{Zn}^{2+} \rightarrow \mathrm{V}_{\mathrm{Cu}} + \mathrm{V}_{\mathrm{Zn}} + \mathrm{Sn}_{\mathrm{Cu}}$ [29]
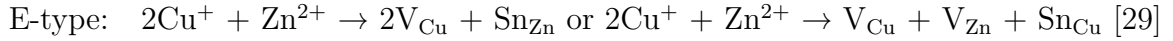
Furthermore similar to the other type pairs (A-C-type and B-D-type) a further type could be introduced prolonging the line of the E-type from the Cu-poor / Zn-poor / Sn-rich to the Cu-rich / Zn-rich / Sn-poor composition. This type was named F-type which also can be described by two different defect complexes:

F-type: $\mathrm{Sn}^{4+} \rightarrow \mathrm{Zn}_{\mathrm{Sn}} + 2\mathrm{Cu}_{\mathrm{i}}$ or $\mathrm{Sn}^{4+} \rightarrow \mathrm{Cu}_{\mathrm{Sn}} + \mathrm{Cu}_{\mathrm{i}} + \mathrm{Zn}_{\mathrm{i}}$ [96]
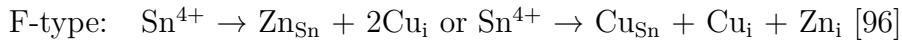
An overview of the E- and F-type defect complexes and how they are balanced by the crystal structure can be seen in Figure 3.6.

In total now six off-stoichiometric kesterite types exist leading to the updated Table 3.2, ternary plot and cation ratio plot Figure 3.7a) and b).

The problem to obtain the type fractions was solved by using the lever rule which is a graphical solution well known in science. Therefore a horizontal or vertical line is drawn through the measured data point. This line cuts two type lines. The fraction of the left intersected type line correspond to the length from the point to the right intersected type line and for the right intersected line vice versa. An example can be seen in Figure 3.8. Except this graphical approach it is also possible to calculate the type fractions with the foundation of the lever rule and offers a reliable solution of the second problem (type fractions of mixture types).

Table 3.2: Six off-stoichiometric kesterite types: A-type, B-type, C-type and D-type proposed by Lafond et al. [45] and E-type Gurieva et al. [29] and F-type Valle Rios et al. [96]. Their chemical composition and the corresponding cation substitution reaction and related intrinsic point defects are presented.

Type	Composition	Cation substitution reaction	Intrinsic point defects	Formulae
A	Cu-poor / Zn-rich / Sn-const.	$2Cu^+ \rightarrow Zn^{2+}$	$V_{Cu} + Zn_{Cu}$	$Cu_{2-x}Zn_{1+x}SnS_4$
B	Cu-poor / Zn-rich / Sn-poor	$2Cu^+ + Sn^{4+} \rightarrow 3Zn^{2+}$	$2Zn_{Cu} + Zn_{Sn}$	$Cu_{2-2y}Zn_{1+3y}Sn_{1-y}S_4$
C	Cu-rich / Zn-poor / Sn-rich	$3Zn^{2+} \rightarrow 2Cu^+ + Sn^{4+}$	$2Cu_{Zn} + Sn_{Zn}$	$Cu_{2+2z}Zn_{1-3z}Sn_{1+z}S_4$
D	Cu-rich / Zn-poor / Sn-const.	$Zn^{2+} \rightarrow 2Cu^+$	$Cu_{Zn} + Cu_i$	$Cu_{2+2m}Zn_{1-m}SnS_4$
E	Cu-poor / Zn-poor / Sn-rich	$2Cu^+ + Zn^{2+} \rightarrow Sn^{4+}$	$2V_{Cu} + Sn_{Zn}$ $Sn_{Zn} + V_{Cu} + V_{Zn}$	$Cu_{2-2w}Zn_{1-w}Sn_{1+w}S_4$
F	Cu-rich / Zn-rich / Sn-poor	$Sn^{4+} \rightarrow 2Cu^+ + Zn^{2+}$	$Zn_{Sn} + 2Cu_i$ $Cu_{Sn} + Zn_i + Cu_i$	$Cu_{2(2-k)}Zn_{2-k}Sn_kS_4$

a)

b)
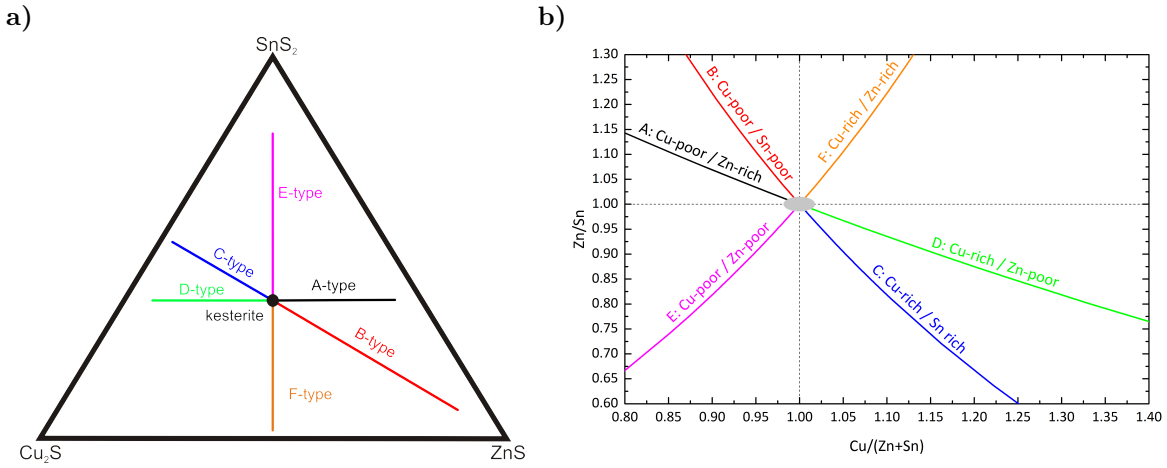
Figure 3.7: a) ternary and b) cation ratio plot of Zn / Sn vs. Cu / (Zn + Sn) containing all six off-stoichiometric kesterite types.

Furthermore from this simple graphical approach and the calculation of the type fractions the final chemical formulae considering the defect complexes of the CZTS compounds could be derived. Figure 3.8 shows the basic procedure of the calculation for a F-D-type and in more detail for an A-B-type sample. This solves the third problem and a calculation of the chemical composition regarding the defect complexes is possible. An example calculation of A-type ($Cu_{2-2x}Zn_{1+x}SnS_4$) and B-type ($Cu_{2-2y}Zn_{1+3y}Sn_{1-y}S_4$) mixture follows (see also Figure 3.8):

$$\frac{Zn}{Sn} = \frac{1+x}{1} \qquad\qquad \frac{Zn}{Sn} = \frac{1+3y}{1-y} \qquad (3.1)$$

$$x = \frac{Zn}{Sn} - 1 \qquad\qquad y = \frac{\frac{Zn}{Sn}-1}{3+c} \qquad (3.2)$$
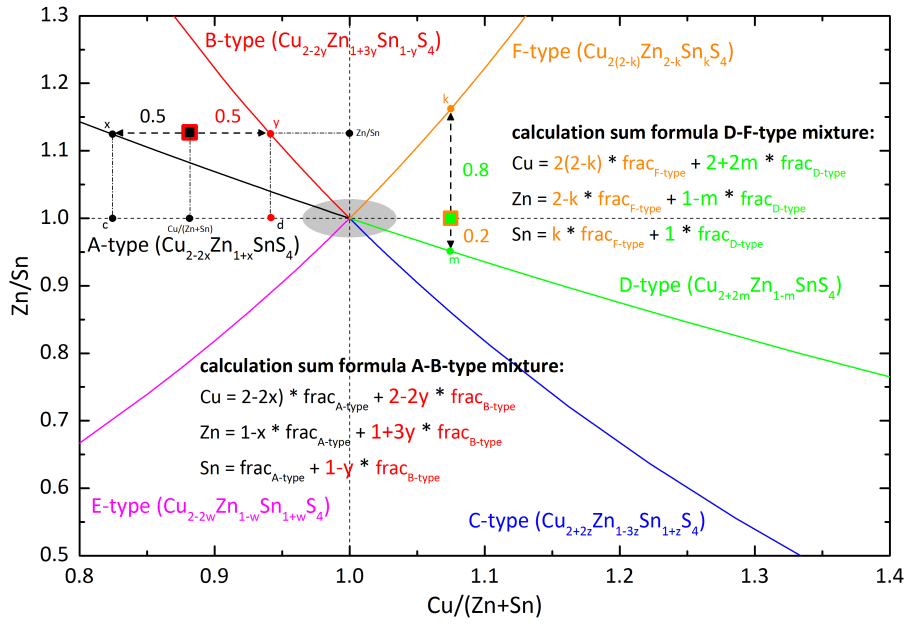
Figure 3.8: Calculations of type fractions and chemical formulae by applying the Lever rule.

x and y correspond to x and y in the A- and B-type formulae

$$c = \frac{2 - 2x}{2 + x} \qquad\qquad d = \frac{2 - 2y}{2 + y} \qquad (3.3)$$

$$(3.4)$$

c and d correspond to the points c and d in Figure 3.8

$$fract._{A-type} = \frac{d - \frac{Cu}{Zn+Sn}}{d - c} \qquad\qquad fract._{B-type} = \frac{\frac{Cu}{Zn+Sn} - c}{d - c} \qquad (3.5)$$

The values of Equation 3.2 and Equation 3.5 allow the calculation of the final chemical composition:

$$Cu_\nu Zn_\nu Sn_\nu S_4 \begin{cases} Cu_\nu = (2 - 2x) \cdot fract._{A-type} + (2 - 2y) \cdot fract._{B-type} \\ Zn_\nu = (1 + x) \cdot fract._{A-type} + (1 + 3y) \cdot fract._{B-type} \\ Sn_\nu = 1 \cdot fract._{A-type} + (1 - y) \cdot fract._{B-type} \end{cases} \qquad (3.6)$$

3.1.3 Improved synthesis of initially weighed off-stoichiometry A-type CZTS

The knowledge gained from the results in Chapter 3.1.1 was used to improve the solid state synthesis and new A-type samples were synthesized with the optimized
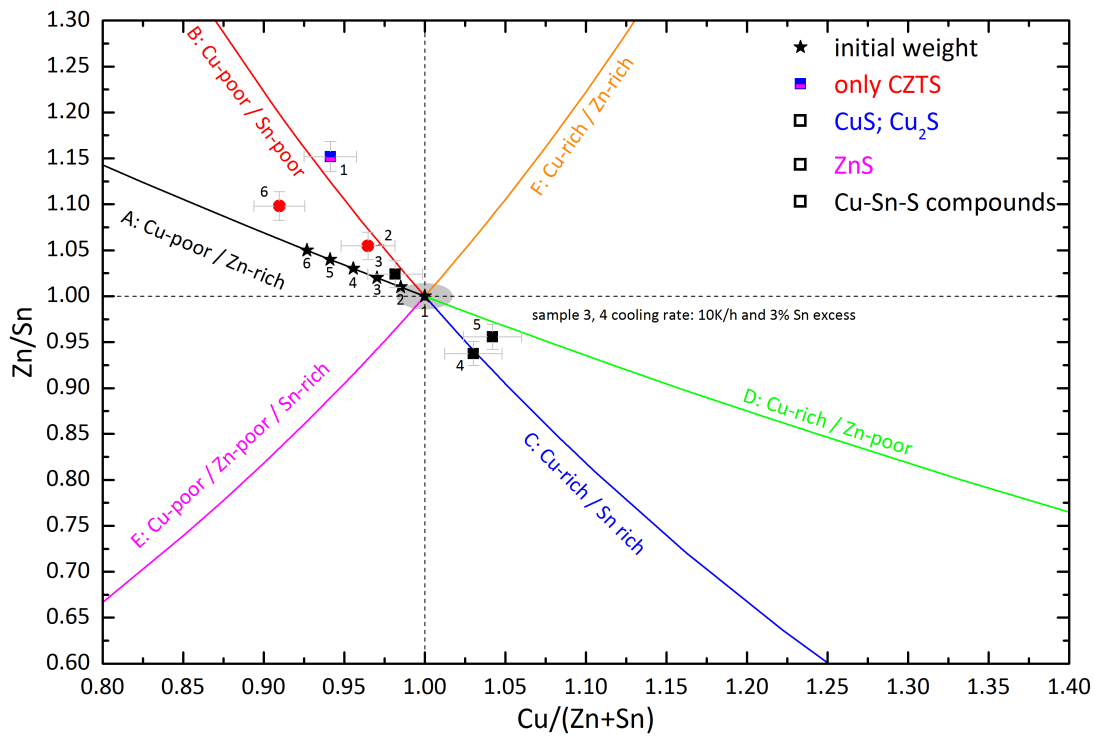
Figure 3.9: Results of the WDX analysis of the improved synthesis of the initial weighed A-type CZTS part 2: single-phase = red, copper sulfides = blue, zinc sulfides = magenta and Cu-Sn-S-compound = black.
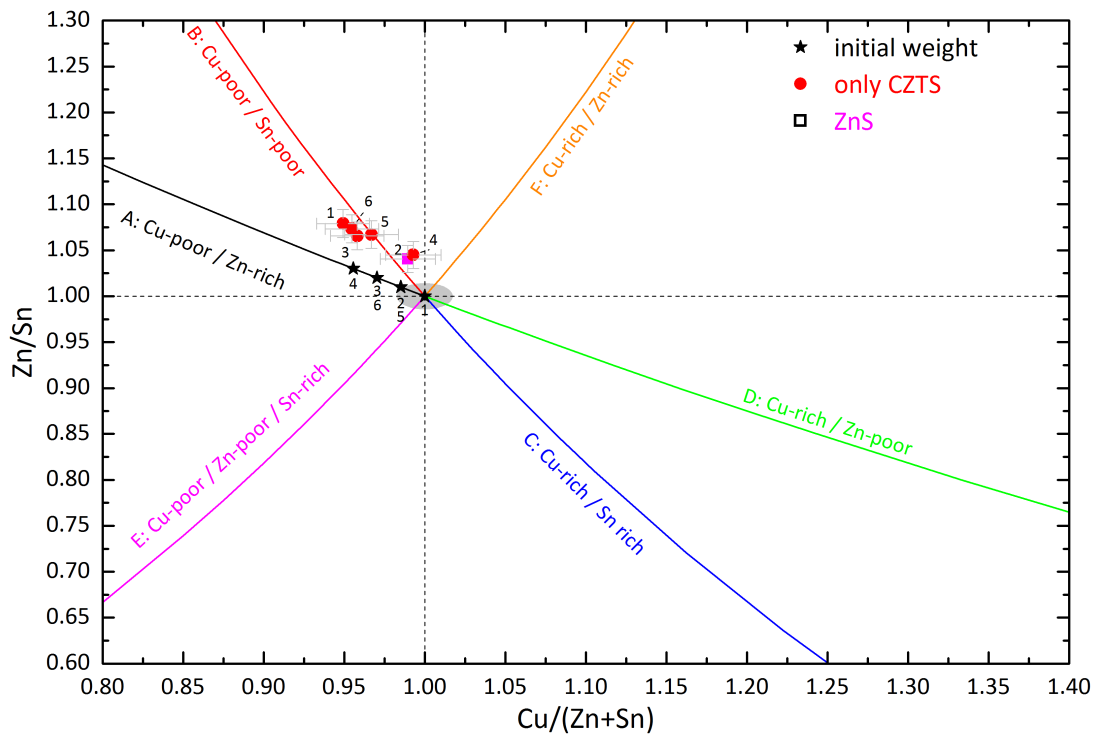
Figure 3.10: Chemical characterization of the improved synthesis and the initial weighed A-type CZTS part 3: single-phase = red and zinc sulfides = magenta.

temperature program presented in Table 2.2. Furthermore the new types introduced in the previous chapter will be included in all graphs and formulae.

Figure 3.9 and Figure 3.10 show the obtained cation ratios of these 12 CZTS compounds which were separated in two graphs to increase the overview. Furthermore it has to be mentioned that the CZTS phases in one graph must not represent the synthesis order and can originate from different sample batches.

The major advance over the first synthesis (Chapter 3.1.1) due to the improved temperature program was that all metals have reacted. Even so the chemical composition still shifts from the initial weighted composition. For some CZTS compounds this shift is stronger than for others. This can be explained by the slightly different temperature profile inside the furnace because the sealed ampules have to be stacked to be able to synthesize six together. These slightly varying conditions have led to different element losses at the ampule glass during the synthesis and to the formation of varying amounts of secondary phases in the samples.

a)   b)

c)   d)
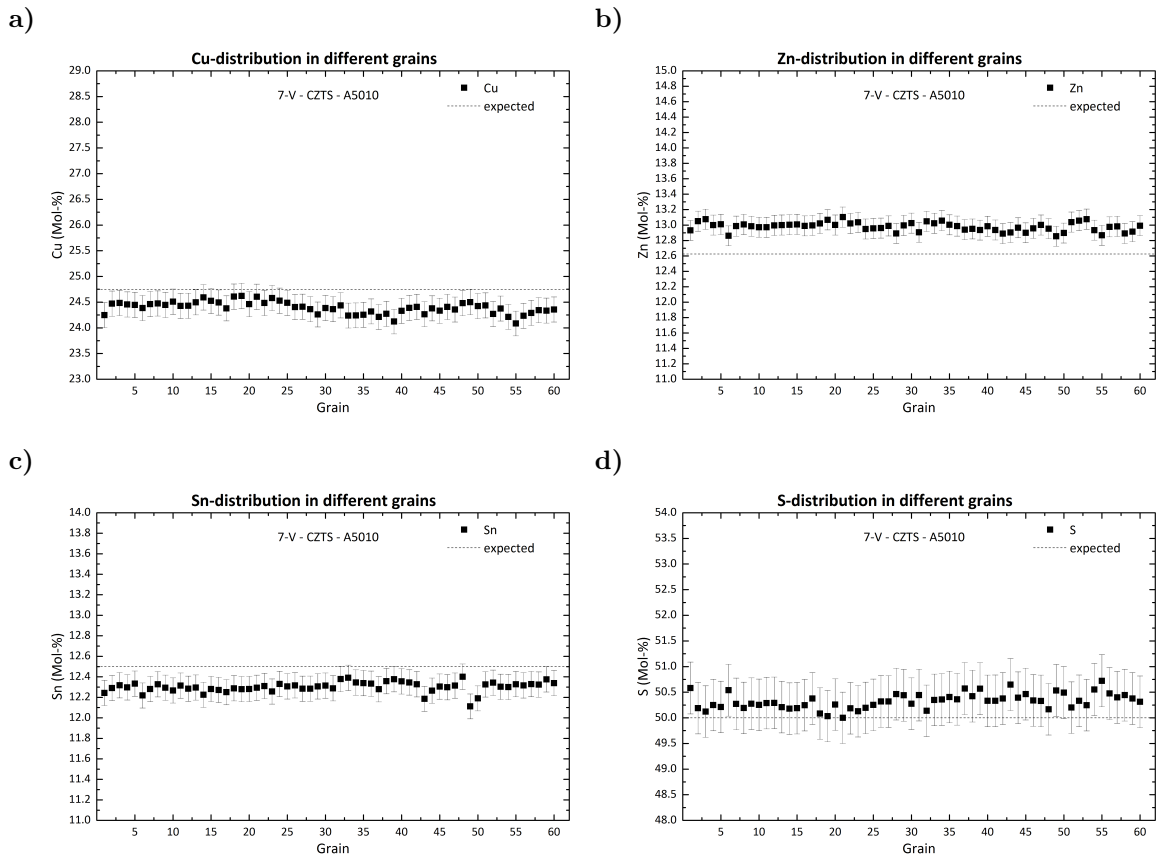
Figure 3.11: WDX spectroscopy results of a single-phase sample and how the homogeneity of CZTS was checked. If the measured Cu, Zn, Sn and S content are equal inside the EMPA error, the grains will be averaged leading to the cation ratios $Cu / (Zn + Sn) = 0.965(17)$ and $Zn / Sn = 1.055(15)$.

All these factors have not influenced the homogeneity of the quaternary CZTS phase, only the formation of different secondary phases. The homogeneity was tested by

comparing the measured mol % of the elements of all grains by taking into account the relative error of 1 % from the electron micro probe analyzer as shown in Figure 3.11. The CZTS presented has an average Cu / (Zn + Sn) and Zn / Sn ratio of 0.965(17) and 1.055(15) and this was deduced out of the 60 grains measured at the electron micro probe analyzer. The initial weighted amount of the given elements was include in Figure 3.11 by a dashed line. This method represents a reliable and fast way to check the homogeneity of the analyzed CZTS compounds. The Cu and Sn mole percent in Figure 3.11 are slightly lower and the Zn content is clearly higher in comparison to the weighted elements whereas the S content complies with initial amount.

In Figure 3.9 two CZTS compounds change from Cu-poor / Zn-rich to Cu-rich / Zn-poor composition. One corresponds to almost pure C-type and the other to a C-D-type mixture composition. The biggest distinction between these samples was the difference in the cooling rate applied with $10 \, \text{K h}^{-1}$ and $50 \, \text{K h}^{-1}$ but it seems to have no influence on the final compound. In both samples a Cu-Sn-S-compound was identified which also had a limited solubility of Zn. An additional sample with the same secondary phase was identified where the deviation from the initial weight is almost neglectable, but the CZTS phase of this sample corresponds to an A-B-type composition with Cu / (Zn + Sn) and Zn / Sn ratio of 0.982(17) and 1.024(14). Furthermore a cooling rate of only $10 \, \text{K h}^{-1}$ was applied. The initial stoichiometry sample shows the most pronounced change in chemistry due to the formation of copper, zinc and tin sulfides. ZnS with some incorporated Cu and Sn, SnS with Cu and Zn and $Cu_{1.85}S$ were identified by EMPA measurements. The sample possesses a Cu-poor / Zn-rich / Sn-poor composition which leads to the first B-F-type mixture CZTS. By X-ray diffraction SnS could be identified as herzenbergite and $Cu_{1.85}S$ as the low temperature phase of chalcocite.

a)   b)
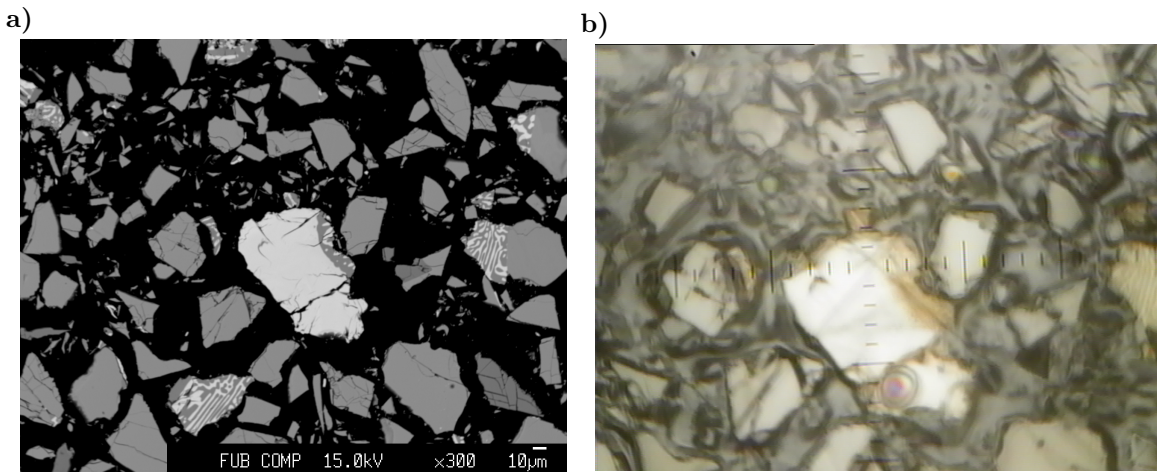
Figure 3.12: a) BSE micrograph and b) optical microscope image of CZTS with Cu / (Zn + Sn) = 0.941(16) and Zn / Sn = 1.152(16) and secondary phases SnS (light) and $Cu_{1.85}S$ (dark gray).

Also these secondary phases are clearly visible in the BSE micrograph in Figure 3.12a). The big white grains correspond to herzenbergite and the darker grains to chalcocite. Furthermore some grains show an intergrowth between herzenbergite and chalcocite.

These structures were identified in further samples. The same excerpt shown in Figure 3.12a) can be seen in Figure 3.12b), this time the built-in optical microscope of the electron micro probe analyzer was used and also there the different phases of the sample can be distinguished. The Cu-Sn-S-compound detected in some samples could not be structural identified by X-ray powder diffraction due to low phase content inside the sample and the resulting weak Bragg reflexes which were mostly disappearing in the background noise.

Two more samples are pure CZTS without any secondary phases within the detection limit of the used instruments. Even these single-phase CZTS samples show a chemical shift from A-type to A-B-type mixture composition. The initial Cu-poor / Zn-rich chemistry remained unchanged or was even slightly increased.

Figure 3.10 (page 42) presents the last samples with an initial A-type composition. The strongest chemical change was conducted by the initial stoichiometric sample, but still only CZTS was detected. This is also an indicator that elements are lost before the actual formation of CZTS. Two more samples changed to B-F-type CZTS. ZnS with some Cu solubility was formed in one of these samples while the other stayed pure-phase CZTS. Another sample changed from A-type to B-type composition with a $Cu / (Zn + Sn)$ and Zn / Sn ratio of CZTS of 0.967(17) and 1.067(15). The last two samples were weighed with the same initial chemical composition and shifted to CZTS with A-B-type mixture and the same chemical composition inside the error. Both samples are single-phase CZTS and proof that reproducible results by using the solid state reaction method are possible if the formation of secondary phases can be avoided. The fact that both samples originate from different synthesis batches supports this assertion.

Despite the vast amount of initial A-type weighed samples pure Cu-poor / Zn-rich / Sn-const. CZTS compounds were never successfully synthesized because their composition always shifts to B-type conditions (Sn-poor) and so only A-B-type mixtures were synthesized. The chemical shift shows always a change to Sn-poor composition. Even a Sn excess of 3 % and a variation of the S excess did not increase the Sn incorporation neither could a decrease of the cooling temperature to $10 \, \mathrm{K \, h^{-1}}$ shift the chemistry to a pure A-type composition.

3.1.4 Phase content and composition of initially weighed off-stoichiometric CZTS B-type samples

In total six Cu-poor / Zn-rich / Sn-poor samples were attempted to synthesize which correspond to B-type composition (see Figure 3.13, page 46). To further check the reproducibility of the synthesis routine only three different compositions were used, but they were weighed two times. Because of that only three initially weighted points are present in Figure 3.13. Furthermore it was necessary to press two pellets during the homogenization step because of the limited capacity of the pressing tool. These pellets were also separately prepared and analyzed and have shown exactly the same chemical composition and in both samples ZnS was identified. Hence only one data

point with all the average grains of these CZTS phases will be presented in the cation ratio plot.
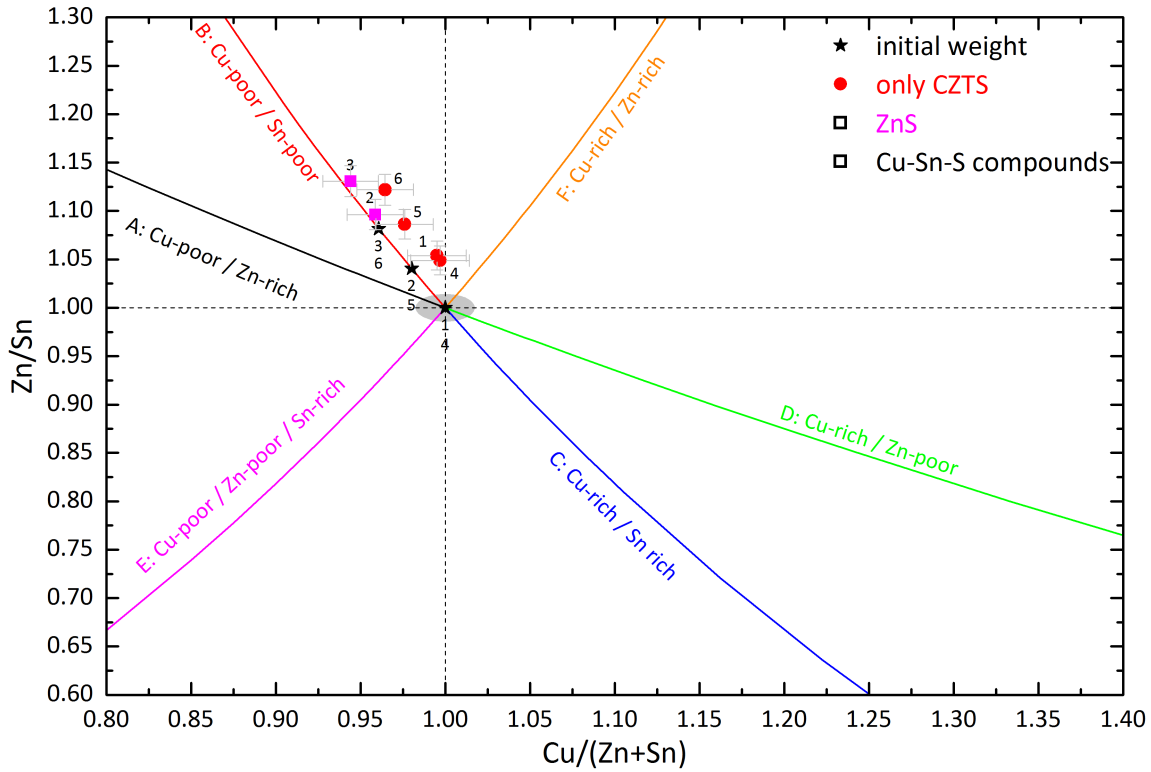
Figure 3.13: Results of the chemical characterization of the improved synthesis and the initial weighed B-type composition: single-phase = red, copper sulfides = blue, zinc sulfides = magenta, tin sulfides = green and Cu-Sn-S-compound = black.

This further proofs the reliability of the solid state reaction and indicate that the problems with the synthesis mostly seem to be connected with Sn content. The assumption is supported by the small chemical deviations of the Sn-poor B-type CZTS which is mainly caused by the formation of secondary phases. Also in the CZTS with a $Cu / (Zn + Sn)$ ratio of $0.959(17)$ and Zn / Sn ratio of $1.096(16)$ almost no ZnS was found during the EMPA analysis whereas in the CZTS $Cu / (Zn + Sn) = 0.944(16)$ and $Zn / Sn = 1.131(16)$ multiple ZnS grains were found (see Figure 3.14a). These two samples containing ZnS still have almost pure B-type composition which indicates only minor fractions of secondary phases.

The two initially weighed stoichiometric samples moved slightly up to Zn-rich CZTS retaining the initial Cu content and a $Cu / (Zn + Sn)$ ratio of $0.997(17)$ and $0.995(17)$ and a Zn / Sn ratio of $1.049(15)$ and $1.054(15)$. Furthermore the samples are single-phase CZTS and have the same chemical composition. In Figure 3.14b) CZTS with $Cu / (Zn + Sn)$ ratio of $0.995(17)$ and a Zn / Sn ratio of $1.054(15)$ can be seen. Also the last two samples are pure CZTS with a similar chemical shift to a Zn-rich composition. Overall all synthesized B-type CZTS compounds have a low deviation from their initially weighted composition keeping their B-type characteristics.

a)   b)
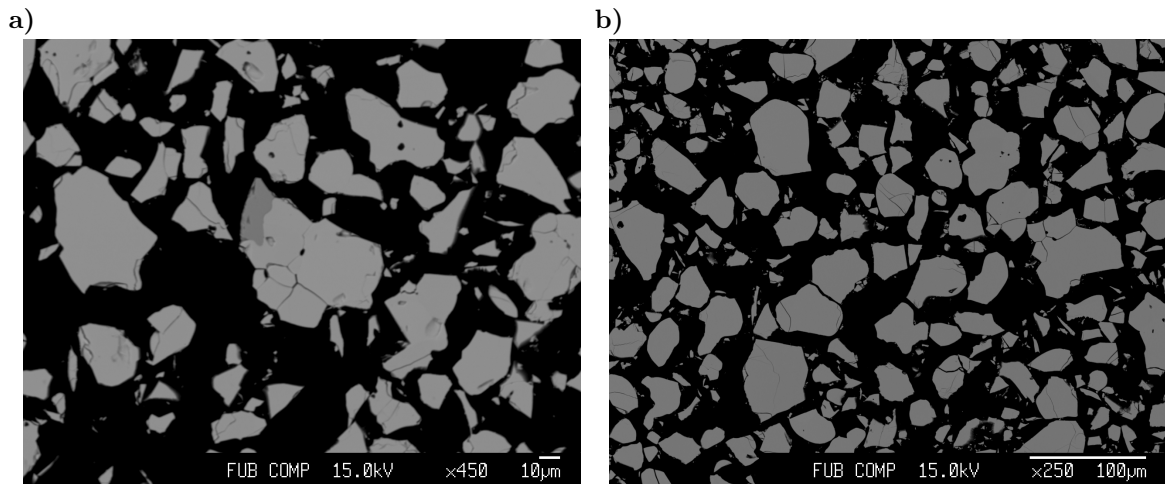
Figure 3.14: The sample a) CZTS with Cu / (Zn + Sn) = 0.944(16) and Zn / Sn = 1.131(16) and ZnS. During the analysis multiple ZnS grains were identified. b) shows the initial stoichiometric weighted sample with the measured Cu / (Zn + Sn) ratio of 0.995(17) and Zn / Sn ratio of 1.054(15) of CZTS and retaining single-phase composition.

3.1.5 C- and D-type synthesis and their chemical characterization

In Figure 3.15 the initial weighted Cu-rich CZTS compounds are plotted comprising in total one C- and six D-type CZTS compounds. The C-type CZTS experienced a strong chemical change from Cu-rich / Zn-poor to Cu-poor / Zn-rich composition with Cu / (Zn + Sn) = 0.943(16) and Zn / Sn = 1.147(16) due to the formation of secondary phases like ZnS, SnS and Cu$_{1.86}$S. These secondary phases also show a solubility of further elements. In the micrograph in Figure 3.16a) the intergrowth of SnS and Cu$_{1.86}$S is shown which were identified by X-ray powder diffraction (see Figure 3.16b) as herzenbergite and the low temperature phase of chalcocite. The refinement of the diffraction data shows that CZTS is still the dominating phase with a fraction over 50 %. Due to the vast amount of secondary phases, the low symmetry of the chalcocite phase and the resulting peak overlap the refinement has a lower quality in comparison to other CZTS refinements. However this was the sample with the highest amount of secondary phases. A similar sample initially weighed stoichiometric from Chapter 3.1.3 and CZTS with Cu / (Zn + Sn) = 0.941(16) and Zn / Sn = 1.152(16) showed exactly the same secondary phases in lower quantity and was successfully refined.

Two samples of intended D-type composition also change to a similar chemistry and formed similar secondary phases like the C-type sample. One of these samples exhibit again almost pure B-type composition while the other has a stronger influence of F-type. On the Cu / (Zn + Sn) = 1 line an additional sample is located, possessing slightly Zn-rich composition, and the formed secondary phases SnS and Cu$_{1.84}$S are in agreement with the chemical shift from Sn-const. to Sn-poor and Cu-rich to Cu-poor composition.
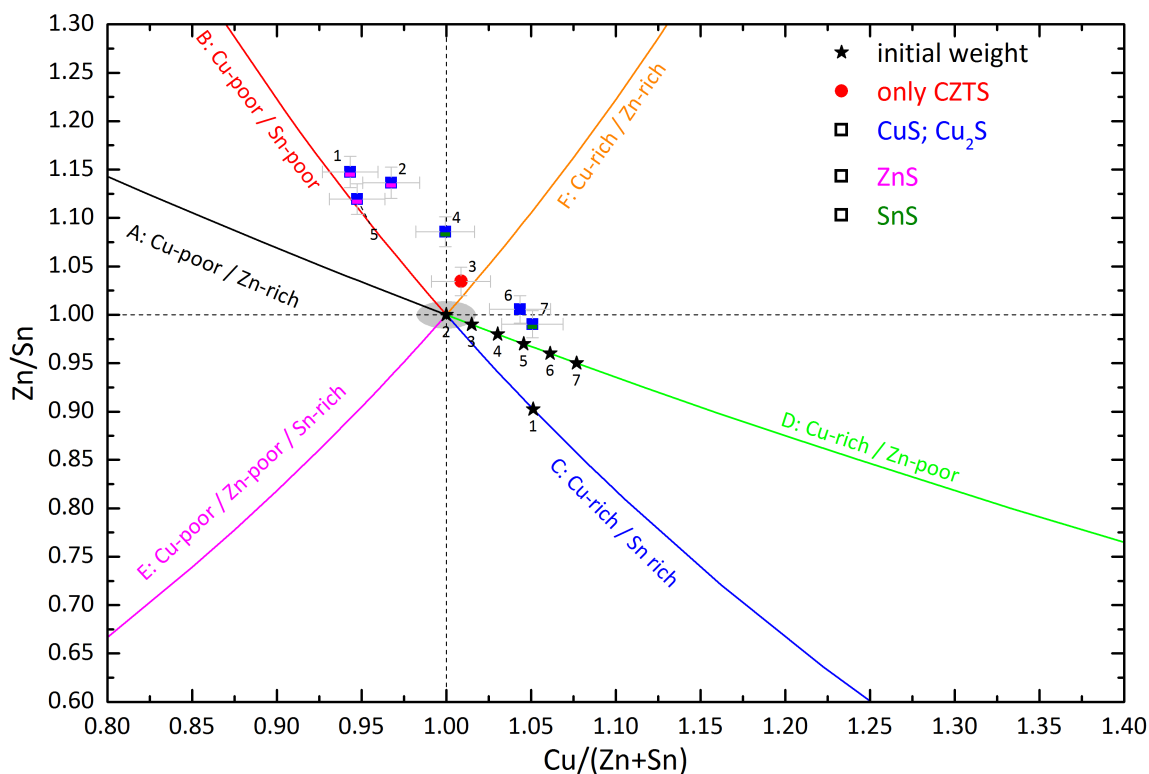
Figure 3.15: Results of the chemical characterization of the improved synthesis and the initial weighed C-D-type composition: single-phase = red, copper sulfides = blue, zinc sulfides = magenta, tin sulfides = green and Cu-Sn-S-compound = black.
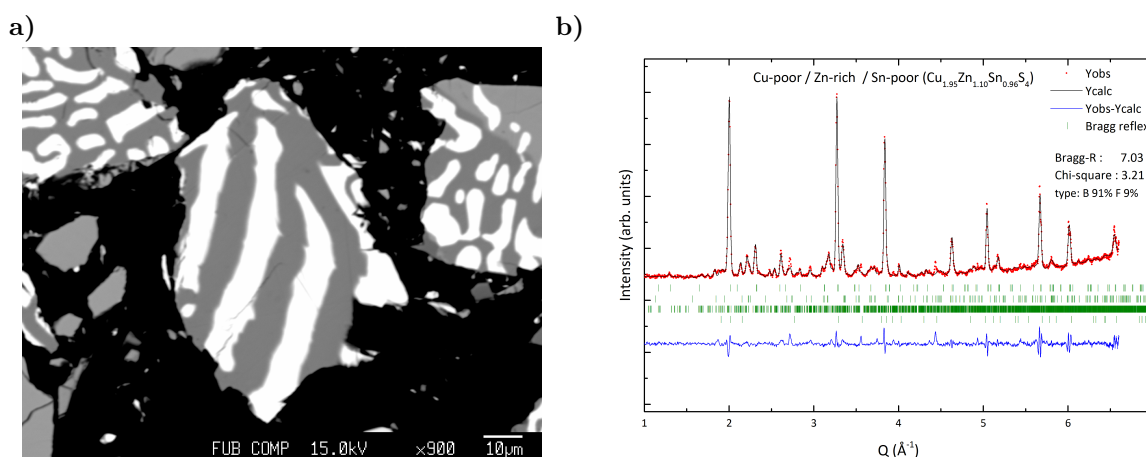
Figure 3.16: BSE micrograph and neutron pattern of B-F-type sample with $Cu/(Zn+Sn)$ = 0.943(16) and Zn/Sn = 1.147(16) of CZTS. a) showing the intergrowth of SnS and $Cu_{1.86}S$ (herzenbergite and chalcocite) and b) the refined neutron diffraction pattern.

The last three samples have experienced smaller chemical changes whereby one sample retained a single-phase CZTS composition while in the other two samples secondary phases were formed. In both samples CuS was identified and in the stronger off-stoichiometric sample SnS was additionally found. By X-ray powder diffraction these secondary phases are corresponding to the minerals covellite and herzenbergite.

3.1.6 Synthesis of newly introduced off-stoichiometric CZTS E-type samples
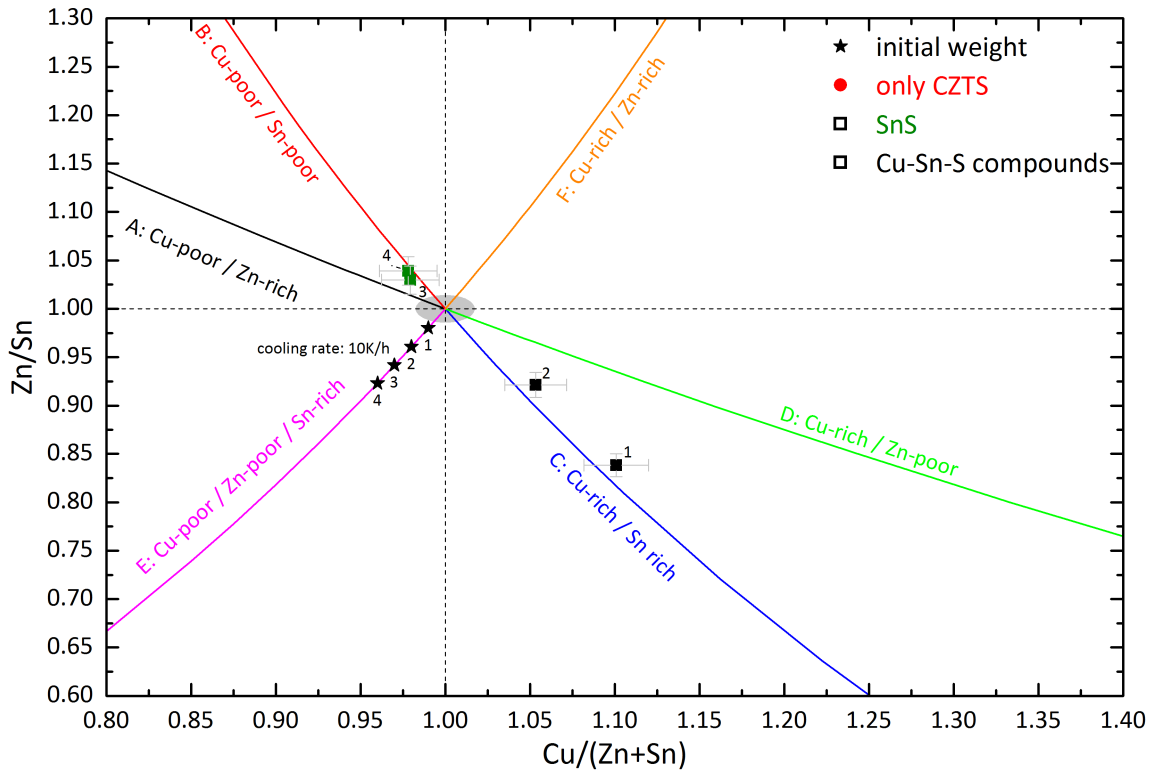
Figure 3.17: Results of the chemical characterization of the improved synthesis and the initial weighed E-type composition: single-phase = red, copper sulfides = blue, zinc sulfides = magenta, tin sulfides = green and Cu-Sn-S-compound = black.

The last samples synthesized were initially E-type CZTS which correspond to a Cu-poor / Zn-poor / Sn-rich composition (see Figure 3.17). The E-type was first introduced by Gurieva et al. [29]. All four samples were cooled down with $10 \, \text{K} \, \text{h}^{-1}$. The two stronger off-stoichiometric samples changed from Cu-poor / Zn-poor / Sn-rich to Cu-poor / Zn-rich / Sn-poor composition. This was mainly caused by the formation of tin sulfides with $\text{Sn}_{0.97}(\text{Cu}_{0.04}\text{Z}_{0.02})\text{S}_2$ and $\text{Sn}_{2.82}(\text{Cu}_{0.08}\text{Z}_{0.05})\text{S}_4$. Both secondary phases were only observed in these two samples. The first corresponds to berndtite and the second could not be identified and seems to be a compound formed of elements which could not be incorporated in CZTS.

In the other two samples again the Cu-Sn-S-compound was identified with a limited solubility of Zn. These samples moved from an E-type CZTS composition to a Cu-rich / Zn-poor / Sn-rich C-type CZTS composition. In Figure 3.18 two backscattered micrographs are presented were a) shows an overview of a typical prepared powder used for analysis and b) a magnified area where the grains of the analysis were selected.

a)

b)
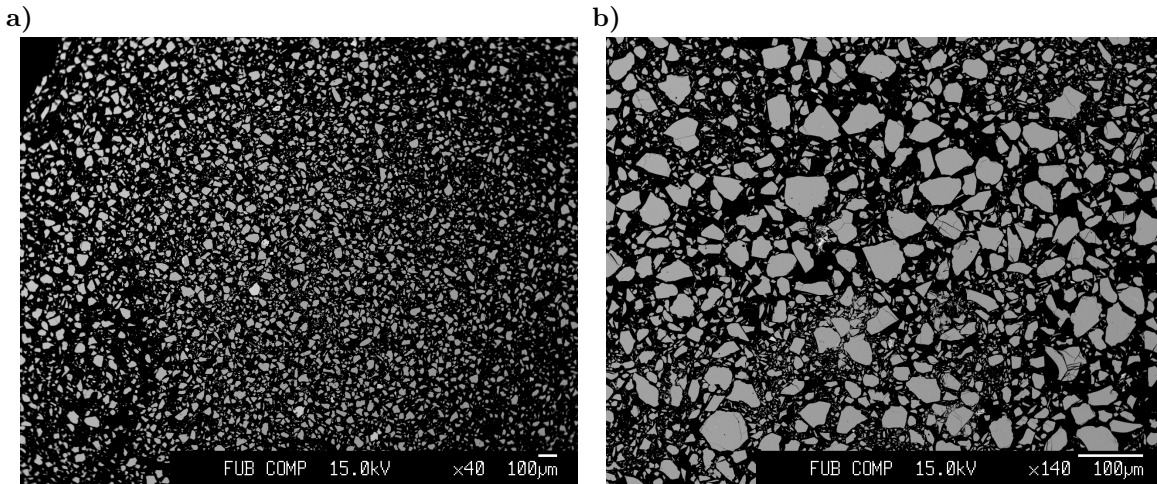
Figure 3.18: BSE micrographs of weighed E-type CZTS a) $Cu / (Zn + Sn) = 1.101(19)$ and $Zn / Sn = 0.838(12)$ with Cu-Sn-S-compound and showing the amount of grains available for reliable statistics and b) $Cu / (Zn + Sn) = 0.979(17)$ and $Zn / Sn = 1.030(15)$ with tin sulfide.

Due to the very low amount of secondary phases identified by the electron micro probe analyzer also the identification by X-ray powder diffraction was not possible because of weak Bragg reflexes.

3.1.7 Conclusion of the chemical characterization

In total 34 samples with a homogeneous CZTS phase were successfully synthesized. Furthermore 12 of these samples were single-phase CZTS because no secondary phases were identified by applying electron micro probe analyzer measurements by WDX, X-ray powder diffraction and neutron diffraction. An overview of the chemical composition and type fraction is given in Table 3.3. Figure 3.19 summarizes all analyzed samples in one graph to distinguish further trends regarding all CZTS compounds. The numbers assigned in Table 3.3 will be used in further figures if necessary. Furthermore more details of the CZTS compounds and a summary of the secondary phases can be found in the appendix in Chapter A.2 and Table A.1.

The synthesis of CZTS was essentially improved and it was possible to synthesize homogeneous single-phase CZTS samples in a quantity necessary to apply neutron diffraction. The region of single-phase CZTS samples seem to be limited to the vicinity of the B-type in the A-B and B-F-types mixture region. A similar region of single-phase samples was observed for the CZTSe compounds [96] where the same synthesis

Table 3.3: Overview of all CZTS phases and their most important values obtained by WDX spectroscopy.

No.	sample	$\frac{\text{Cu}}{\text{Zn} + \text{Sn}}$	err	$\frac{\text{Zn}}{\text{Sn}}$	err	type fraction				CZTS phase			
										Cu	Zn	Sn	S
1	A0125	1.008	0.017	0.974	0.014	C	81%	E	19%	2.006	0.981	1.008	4
2	A0100	1.094	0.019	0.864	0.012	D	14%	C	86%	2.100	0.890	1.030	4
3	A0050	1.220	0.021	0.735	0.010	D	22%	C	78%	2.227	0.776	1.055	4
4	A0025	1.305	0.022	0.659	0.010	D	24%	C	76%	2.307	0.705	1.071	4
5	A0000	1.303	0.023	0.635	0.009	D	18%	C	82%	2.295	0.687	1.083	4
6	A5010	0.965	0.017	1.055	0.015	A	16%	B	84%	1.960	1.043	0.989	4
7	A3010	0.967	0.017	1.067	0.015	A	1%	B	99%	1.966	1.050	0.984	4
8	A3020	0.955	0.017	1.073	0.015	A	14%	B	86%	1.949	1.057	0.985	4
9	B1010	0.959	0.017	1.096	0.016	B	95%	F	5%	1.956	1.069	0.976	4
10	B1020	0.944	0.016	1.131	0.016	B	95%	F	5%	1.946	1.094	0.966	4
11	A2000	0.941	0.016	1.152	0.016	B	91%	F	9%	1.946	1.106	0.960	4
12	C0025	0.943	0.016	1.147	0.016	B	91%	F	9%	1.948	1.103	0.961	4
13	B2000	0.997	0.017	1.049	0.015	B	57%	F	43%	2.007	1.031	0.983	4
14	B2010	0.976	0.017	1.086	0.015	B	79%	F	21%	1.984	1.059	0.975	4
15	B2020	0.964	0.017	1.122	0.016	B	81%	F	19%	1.974	1.083	0.965	4
16	B1000	0.995	0.017	1.054	0.015	B	59%	F	41%	2.005	1.034	0.981	4
17	D0010	1.009	0.017	1.034	0.015	B	24%	F	76%	2.021	1.019	0.985	4
18	D0040	1.044	0.018	1.006	0.014	F	29%	D	71%	2.066	0.992	0.988	4
19	D0050	1.051	0.018	0.990	0.014	F	17%	D	83%	2.072	0.981	0.991	4
20	D0020	0.999	0.017	1.086	0.015	B	51%	F	49%	2.019	1.052	0.969	4
21	D0000	0.967	0.017	1.136	0.016	B	76%	F	24%	1.981	1.090	0.959	4
22	A4000	0.949	0.016	1.079	0.015	A	17%	B	83%	1.941	1.062	0.984	4
23	A4010	0.989	0.017	1.041	0.015	B	76%	F	24%	1.994	1.028	0.988	4
24	A4030	0.993	0.017	1.045	0.015	B	66%	F	34%	2.000	1.030	0.985	4
25	A4040	1.042	0.018	0.956	0.014	D	43%	C	57%	2.051	0.962	1.006	4
26	A4050	0.958	0.017	1.066	0.015	A	16%	B	84%	1.952	1.051	0.986	4
27	E0010	1.101	0.019	0.838	0.012	D	7%	C	93%	2.102	0.871	1.039	4
28	E0020	1.053	0.018	0.921	0.013	D	15%	C	85%	2.058	0.937	1.017	4
29	E0030	0.979	0.017	1.030	0.015	A	21%	B	79%	1.976	1.024	0.994	4
30	E0040	0.978	0.017	1.039	0.015	A	7%	B	93%	1.977	1.030	0.991	4
31	A6020	0.982	0.017	1.024	0.014	A	27%	B	73%	1.978	1.020	0.996	4
32	A6030	1.030	0.018	0.938	0.013	C	97%	E	3%	2.029	0.953	1.016	4
33	A4020	0.910	0.016	1.098	0.016	A	47%	B	53%	1.883	1.084	0.987	4
34	D0030	0.947	0.016	1.120	0.016	B	97%	F	3%	1.948	1.086	0.970	4
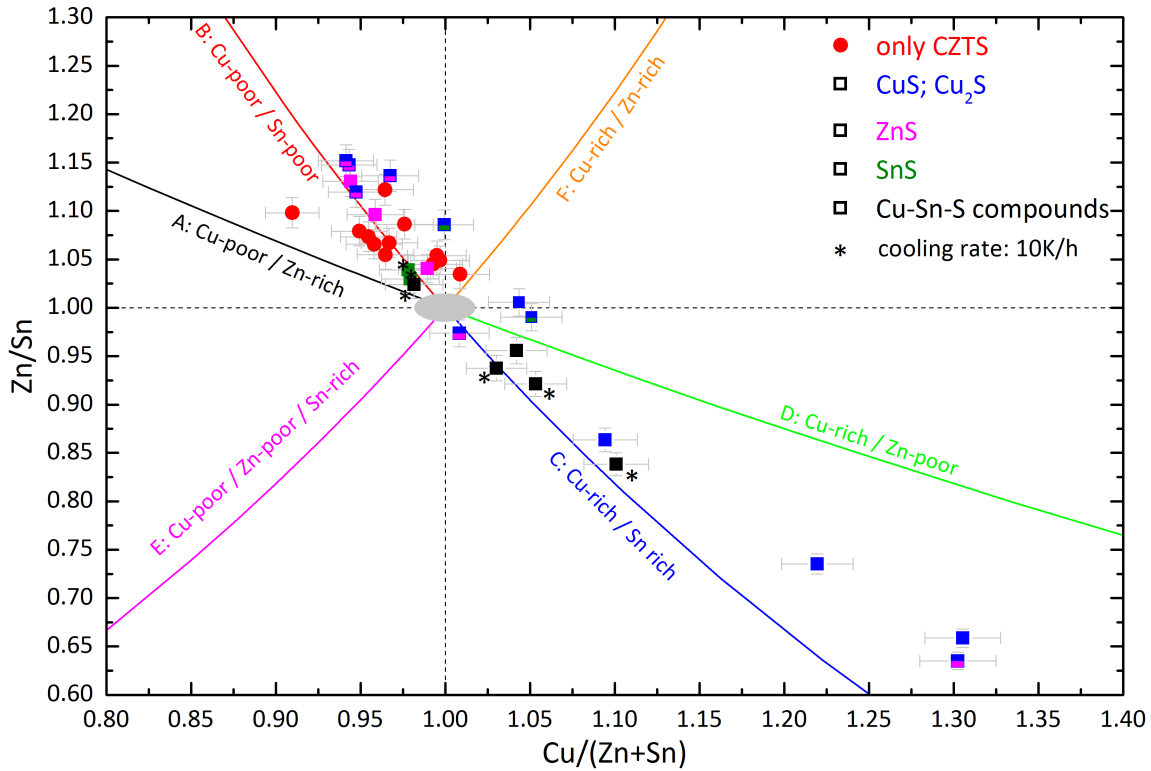
Figure 3.19: Cation ratio plot of all 34 CZTS samples and the results of the chemical characterization: single-phase = red, copper sulfides = blue, zinc sulfides = magenta, tin sulfides = green and Cu-Sn-S-compound = black.

routine, with a slightly different final temperature, was used. Furthermore in other studies single-phase CZTS was located in similar regions, and also single-phase CZTS with a Cu-rich / Zn-poor composition was synthesized, therefore a mechanochemical synthesis routine [70, 71] was used and fewer CZTS material produced [45].

Furthermore the concentration of CZTS along the B-C-type lines is noticeable with only small deviations. Especially in the direction of E-type Cu-poor / Zn-poor / Sn-rich composition only two CZTS compounds with a minor influence of the E-type were synthesized and these were not intended E-type samples. All initially weighed E-type samples changed to different compositions due to the formation of secondary phases. And mostly tin dominated secondary phases were formed which led to a shift from Sn-rich to Sn-poor composition. The lack of Sn incorporation in the CZTS crystal structure is also the obstacle of forming a pure A-type CZTS. This deficiency of Sn could not be overcome by improving the synthesis by adding excess Sn or cutting the Sn in smaller metal pieces.

The problem of the Sn loss is described in literature [40, 62, 65, 82, 83] and shown in Figure 3.20. The Sn loss is directly connected to CZTS equilibrium and vapor pressure of the gas phases. The majority of results [40, 62, 65, 82, 83] are discussed in connection with the fabrication of CZTS thin films. The observation can be transferred to our solid state reaction routine because the conditions during the synthesis are similar inside the

ampule. The following equilibrium reaction was proposed for CZTS and details can be found in Redinger et al. [65]:

$$Cu_2S_{(s)} + ZnS_{(s)} + SnS_{(g)} + {}^1\!/\!{}_2 S_{2(g)} \Longleftrightarrow CZTS_{(s)} \tag{3.7}$$
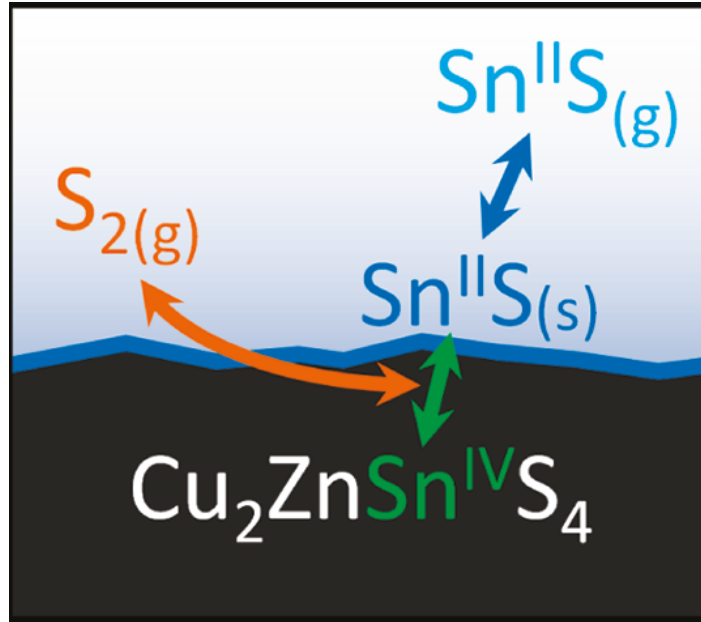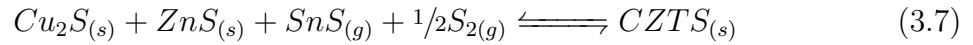
Figure 3.20: Sn-loss process of the absorber layer which can also be assigned to the solid state reaction [83].

Especially sulfur and tin sulfide are very volatile at the temperature used for syntheses whereas copper and zinc sulfides are quite stable. This is also supported by the observations during the synthesis of the off-stoichiometric CZTS samples where mostly Sn and S were the limiting factors of a successful synthesis. By adding excess S (10 %) the synthesis was improved but the Sn loss could not be overcome by adding (3 %) Sn excess. Probably by increasing the Sn excess or the binary phase SnS the Sn loss can be prevented.

There do not exist initially weighed F-type Cu-rich / Zn-rich / Sn-poor CZTS compounds but still more CZTS phases have a F-type than an E-type component. There exists only one CZTS compound where the F-type dominates (76 %). Normally the F-type fraction of the CZTS compounds is below 50 %. The fact of more F-type than E-type CZTS compounds is directly connected to the Sn-poor composition of the F-type in contrast to the Sn-rich E-type. Similar to the F-type there are many A-B-type CZTS compounds but the A-type is never the dominating off-stoichiometric type. In most CZTS phases the A-type fraction is restricted below 30 % with only one exception of the strongest off-stoichiometric A-B-type CZTS where the fractions of A- and B-type are equal. Only in the Cu-poor / Zn-rich CZTS it seems that the Sn-rich C-type is preferred over the Sn-const. D-type. In the C-D type Cu-rich / Zn-poor CZTS compounds the D-type fraction is limited below 30 % in the majority of samples and

only one exception near stoichiometry can be observed. The D-type dominates in the two B-F-type CZTS compounds with a fraction above of 70 %.

Due to the large possibilities of secondary phases it is hard to predict and control the chemical composition of the CZTS phase. It is possible to reproduce samples like shown in Chapter 3.1.4 where two samples had the same initial composition and despite a slight chemical shift the same final single-phase CZTS composition. Even if the synthesized sample exhibits a single-phase composition a chemical shift was often observed. This was accounted to the precipitation of elements or phases at the ampule glass. An example of such precipitation can be found in Figure 3.21.

a)   b)
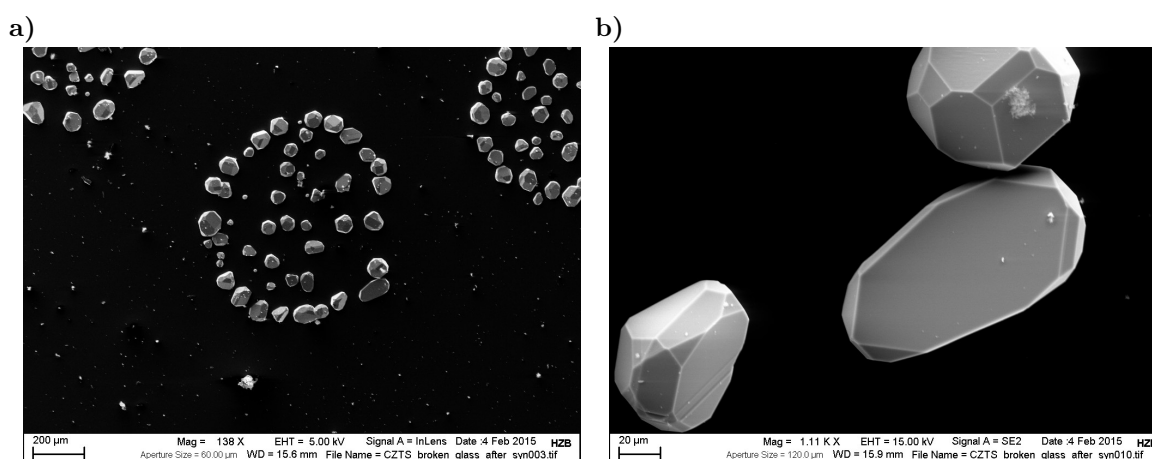
Figure 3.21: SEM images of crystals growing at the ampule glass: a) extensive structures b) magnified view where even crystal surfaces can be identified.

SEM measurements which are working similar as electron micro probe analyzer analyses just without the quantitative WDX measurements were conducted to create Figure 3.21. The precipitations turned out to be tiny crystals with a maximum size of 100 µm. These tiny crystals and also some S precipitations were only found after the 1st reaction step of the synthesis and the element content was qualitative determined by EDX measurements. The results of these measurements have shown that Cu, Zn, Sn and S were present. So it seems that small amounts of quaternary CZTS are formed at the ampule glass. Further analyses are necessary to approve the results of the qualitative EDX measurements. Due to the SEM analysis it could be proven that element losses were occurring already in early stages of the synthesis.

A lot of knowledge of the CZTS system was gained and occurring secondary phases were identified. To gain a deeper understanding of CZTS, structural parameters are necessary. The structural characterization was conducted by X-ray powder diffraction and neutron diffraction described in Chapter 2.2.1 and Chapter 2.2.2. It is important to understand if the chemical flexibility of the CZTS compound has a direct impact on the structural parameters.

3.2 Structural trends in kesterite type compound semiconductors

Structural parameters like the lattice parameters are important to obtain a deeper understanding of changes in the crystal structure caused by chemical changes. Due to sharper Bragg reflexes of the X-ray diffraction patterns, and the well known wavelength of the Cu X-ray tube in contrast to the experimental determined neutron wavelength, the X-ray lattice parameters were preferred over values obtained by neutron diffraction.

Unfortunately it is not possible to learn much about intrinsic point defects from X-ray powder diffraction because of the restrictions mentioned in Chapter 2.2.1. The lattice parameters were obtained after a successful Rietveld analysis but FullProf is underestimating the errors of the values. To deduce values with more than three decimal places a constant temperature must be guaranteed otherwise the changes of the lattice parameters are preventing more precise measurements.

The extracted lattice parameters are a reliable parameter to compare results of synthesized CZTS compounds and CZTS produced by different synthesis routines. Of course differences should be expected because of different process conditions due to various existing fabrication processes.

3.2.1 Influence of off-stoichiometric types on the lattice parameters

In Figure 3.22 the lattice parameters a and c were plotted vs. the $Cu/(Zn+Sn)$ and Zn/Sn ratios. Also the secondary phases are highlighted by different colors. To be able to compare the lattice parameters a and c more easily $c/2$ will be used instead of c.

These figures give an overview of the contribution of the lattice parameters in combination with the chemical composition. The first recognizable features are two distinct point clouds for a and c in the Cu-poor/Zn-rich region. These dense point clouds are not surprising regarding the small chemical deviation between the CZTS compounds. Also most of the single-phase CZTS samples are located in the Cu-poor/Zn-rich region but also samples containing secondary phases are located in-between. The samples containing ZnS, CuS and SnS as secondary phases have similar lattice parameters as the single-phase CZTS samples with the same chemical composition. Only the samples with the Cu-Sn-S-compound show a different trend and especially the lattice parameter c is increasing whereas all other samples show decreasing values in Cu-rich/Zn-poor direction. Overall the results support the reliability of the derived CZTS lattice parameters as long as it is the main phase and no significant deviation is caused by secondary phases.

To compare the lattice parameters as reference points the values of off-stoichiometric CZTS by Lafond et al. [45] were introduced in Figure 3.22. The literature values of c are
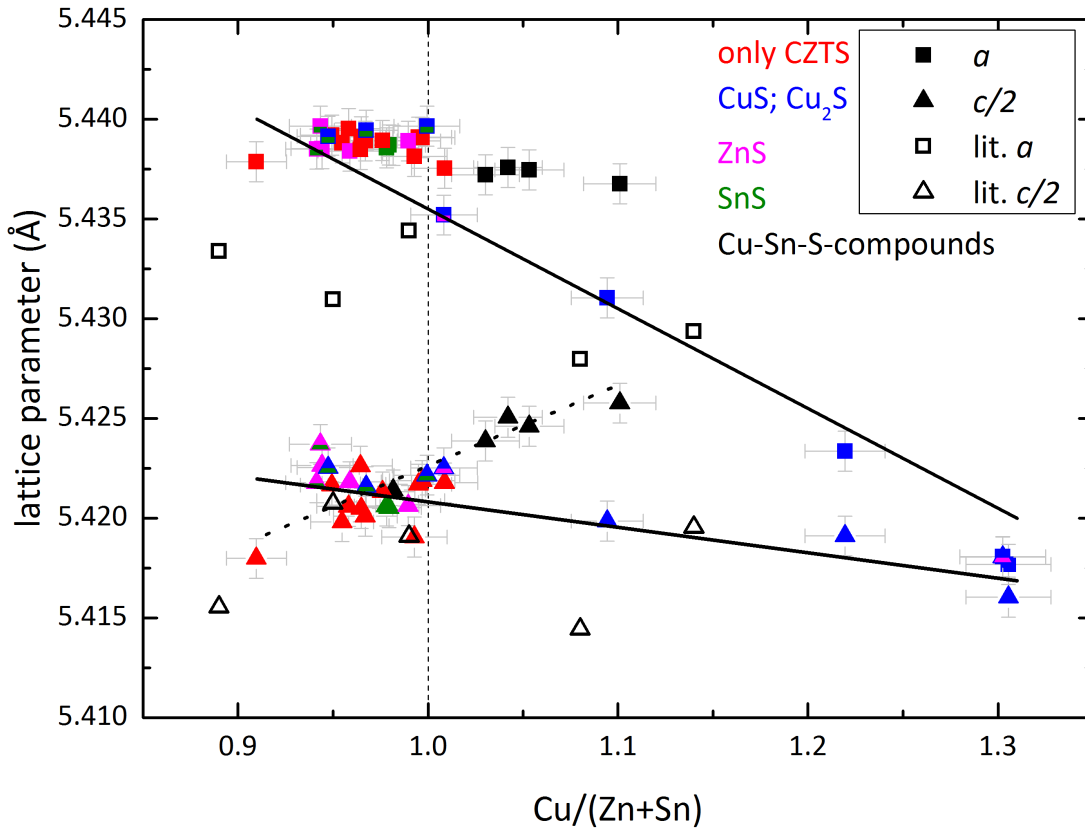
Figure 3.22: Lattice parameters vs. Cu / (Zn + Sn): single-phase = red, copper sulfides = blue, zinc sulfides = magenta, tin sulfides = green, Cu-Sn-S-compound = black, rectangle = a, triangle = $c/2$ and open symbols = literature [45].

in good agreement with the analyzed samples. The lattice parameters a by Lafond et al. [45] are distinctly smaller compared to the experimental values. This deviation can have several origins. The literature values were derived from a different X-ray instrument and evaluated by a different software. Furthermore different synthesis parameters and especially varying gas pressures could have influenced the lattice parameters and lead to the observed deviation. The trend of the literature and experimental lattice parameters is similar. Both lattice parameters a and c decrease from Cu-poor to Cu-rich conditions.

The more Cu-rich / Zn-poor the composition becomes the more the lattice parameters a and c seem to be decreasing. The exceptions are samples containing the Cu-Sn-S-compound as secondary phase and this trend his highlighted by a dotted line for lattice parameter c. Probably the altered chemical environment caused by the Cu-Sn-S-compound influences the lattice parameters because in these samples a and c are slightly higher. All Cu-rich / Zn-poor samples containing copper sulfides as secondary phases follow the trend of decreasing a and c.

Unfortunately not so many off-stoichiometric samples in the Cu-poor / Zn-rich as in the Cu-rich / Zn-poor region were synthesized to confirm the trend of decreasing a and

c. Furthermore it seems that the chemical changes have a stronger structural influence on the *a* parameter. The stronger decrease of *a* compared to *c* leads to similar values of *a* and *c/2* in the strongest off-stoichiometric CZTS compounds.

The Cu / (Zn + Sn) ratio is preferred to compare A-B- and C-D-type CZTS compounds but for B-F-type CZTS phases the Zn / Sn ratio offers a better overview. Therefore in Figure 3.23 and Figure 3.24 the cation ratio plot was used and the lattice parameters are introduced as the z-coordinate. Furthermore a transparent contour plot overlaps the data to be able to identify more easily structural trends.

Figure 3.23 shows the lattice parameter *a*. The measured data reaches from 5.417 Å to 5.440 Å. The contour plot indicates a clear trend with decreasing lattice parameters from Cu-poor / Zn-rich to Cu-rich / Zn-poor composition. The samples marked by a star indicate that a slower cooling rate was applied. This seems to have no impact on the lattice parameter *a* because the lattice parameters are in the same magnitude as the surrounding samples.

Also in the Cu-poor / Zn-rich region the amount of CZTS compounds is higher and all CZTS phases show similar lattice constants which confirms reliability and reproducibility of the X-ray results. In the Cu-rich / Zn-poor region less samples were synthesized leaving more room for interpretation. The three strongest off-stoichiometric C-D-type CZTS compounds show similar lattice parameters and these are clearly smaller than the lattice parameters in the Cu-poor / Zn-rich region. The C-D type CZTS phases near stoichiometry show only slightly lower lattice parameters than the A-B-type CZTS compounds in the vicinity of stoichiometry. In the E- and F-type directing no statements can be made due to lack of strong off-stoichiometric CZTS compounds. The cause of this decrease could be the slightly smaller cation radius of Cu^+ (0.635 Å) over Zn^{2+} (0.640 Å) [85]. In an unit cell multiple layers of atoms are present and so the lattice parameters become higher or lower if more Cu^+ or Zn^{2+} is incorporated in the structure which can be measured by X-ray powder diffraction. This also explains why a decrease is only observed in the Cu-rich / Zn-poor region (C-D-type). This would also implicate an increase in the Cu-poor / Zn-rich region due to the increasing Zn content but it seems the vacancy defect of the A-type counteracts this progress.

Figure 3.22 shows that the changes of lattice parameters *a* are stronger than for lattice parameters *c* which is presented in Figure 3.24. Because of the combined information of Cu / (Zn + Sn) and Zn / Sn some additional observations could be made. The results of lattice parameters *c* are not showing the same correlation as the lattice parameters of *a* and no clear trend with increasing or decreasing lattice parameters can be observed. But in detail it is apparent that the strongest Cu-poor / Zn-rich A-B mixture CZTS and the two most off-stoichiometric Cu-rich / Zn-poor C-D mixture CZTS compounds show the lowest values of lattice parameter *c*. This supports the assumption that the substitution of Cu^+ for Zn^{2+} decreases the lattice parameters. Furthermore it could indicate that the V_{Cu} are not only counteracting the increasing lattice parameters due to the Zn^{2+} incorporation for Cu^+ but shrink the lattice parameters for off-stoichiometric A-B-type CZTS compounds. Therefore it seems a minimum amount of A-type is needed because with dominating B-type composition the lattice parameters are increasing due
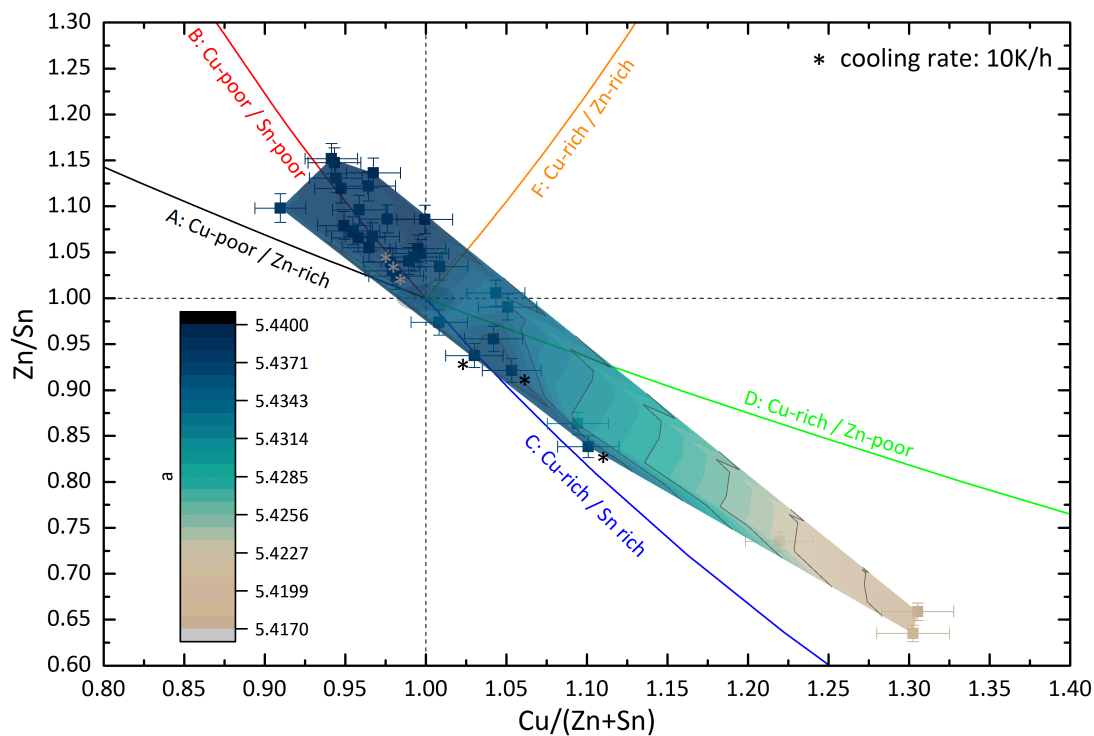
Figure 3.23: Lattice parameter a vs. the Cu / (Zn + Sn) and Zn / Sn cation ratio including a contour plot.
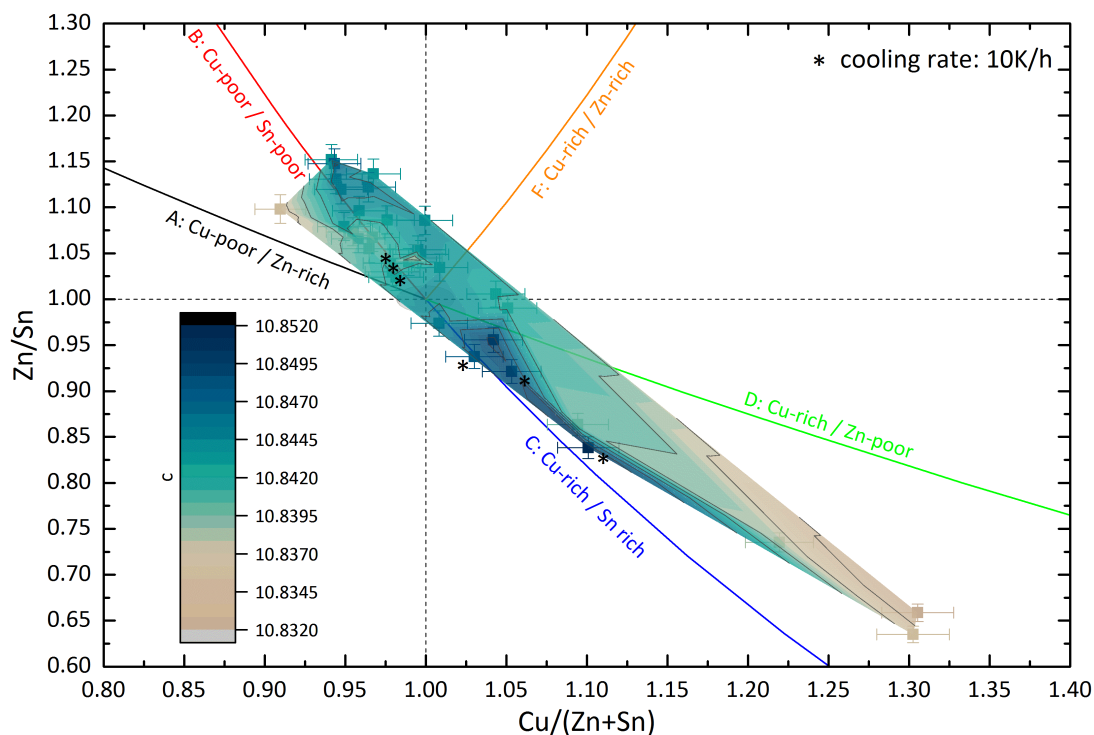
Figure 3.24: Lattice parameter c vs. the Cu / (Zn + Sn) and Zn / Sn cation ratio including a contour plot.

to the declining amount of V_{Cu}. The highest values for the c parameter was measured in the slightly off-stoichiometric C-D-type and B-F-type CZTS compounds.

Until now only separated a and c values were evaluated. In Figure 3.25 a combination of the lattice parameters is presented also known as the tetragonal deformation. If the value of the tetragonal deformation is equal to one, no deformation is present, which correspond to $2 \cdot a = c$. If the value is < 1 or > 1 Bragg reflex splitting can be observed in a powder pattern. No values above $c/2 \cdot a > 1$ were observed.
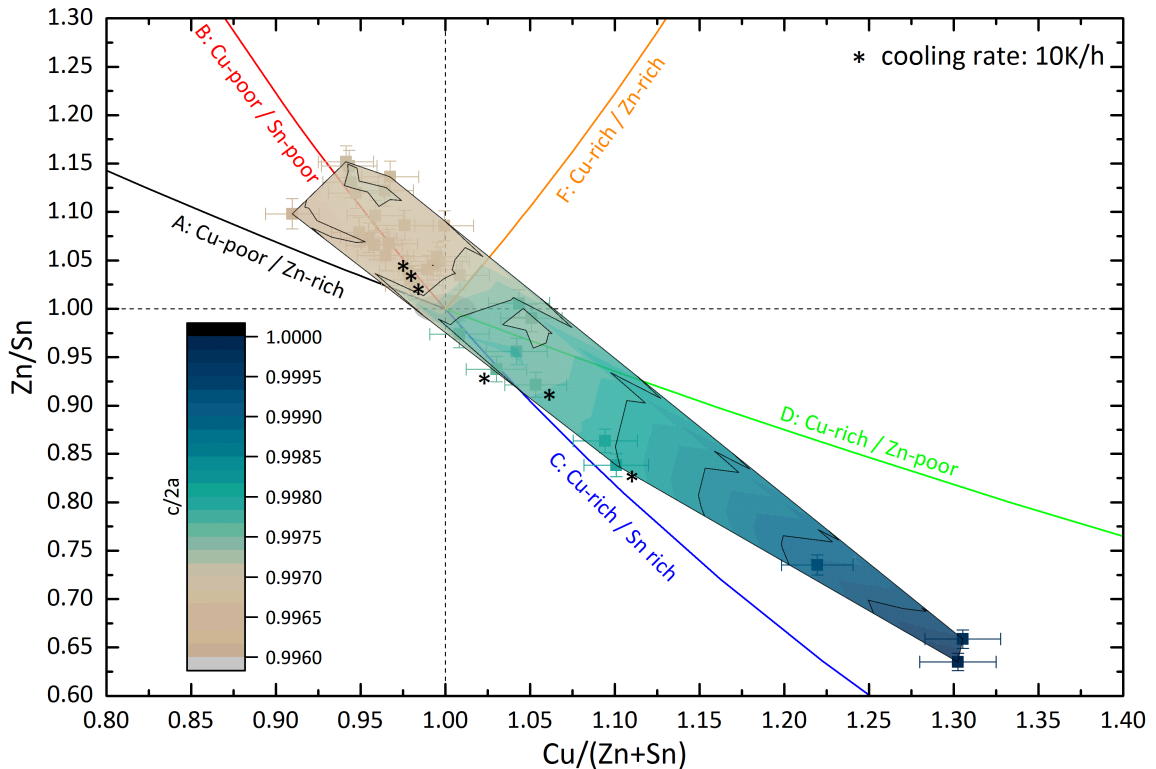
Figure 3.25: Tetragonal deformation of CZTS vs. the cation ratio plot.

In the Cu-poor / Zn-rich region the values of the tetragonal deformation are lowest and increase incremental to Cu-rich / Zn-poor conditions. From the Cu-poor / Zn-rich to the Cu-rich / Zn-poor composition a distinct trend can be determined and no tetragonal deformation was observed in the strongest off-stoichiometric Cu-rich / Zn-poor CZTS compounds. The values of the tetragonal deformation decrease with increasing Zn content reaching the minimum in the Cu-poor / Zn-rich region. Similar observations, but not with such a strong difference between Cu-poor / Zn-rich and Cu-rich / Zn-poor composition, were made for CZTSe [96] and also the CZTS compounds by Lafond et al. [45] show this trend.

Furthermore the unit cell volume was included (see Figure 3.26) and it supports the assumptions made from the results of the lattice parameters and tetragonal deformation. The cell volume gradually decreases from Cu-poor / Zn-rich composition to Cu-rich / Zn-poor conditions by incorporating Cu^+ for Zn^{2+}. Furthermore also in the strongest off-stoichiometric Cu-poor / Zn-rich CZTS with the highest A-type fraction,
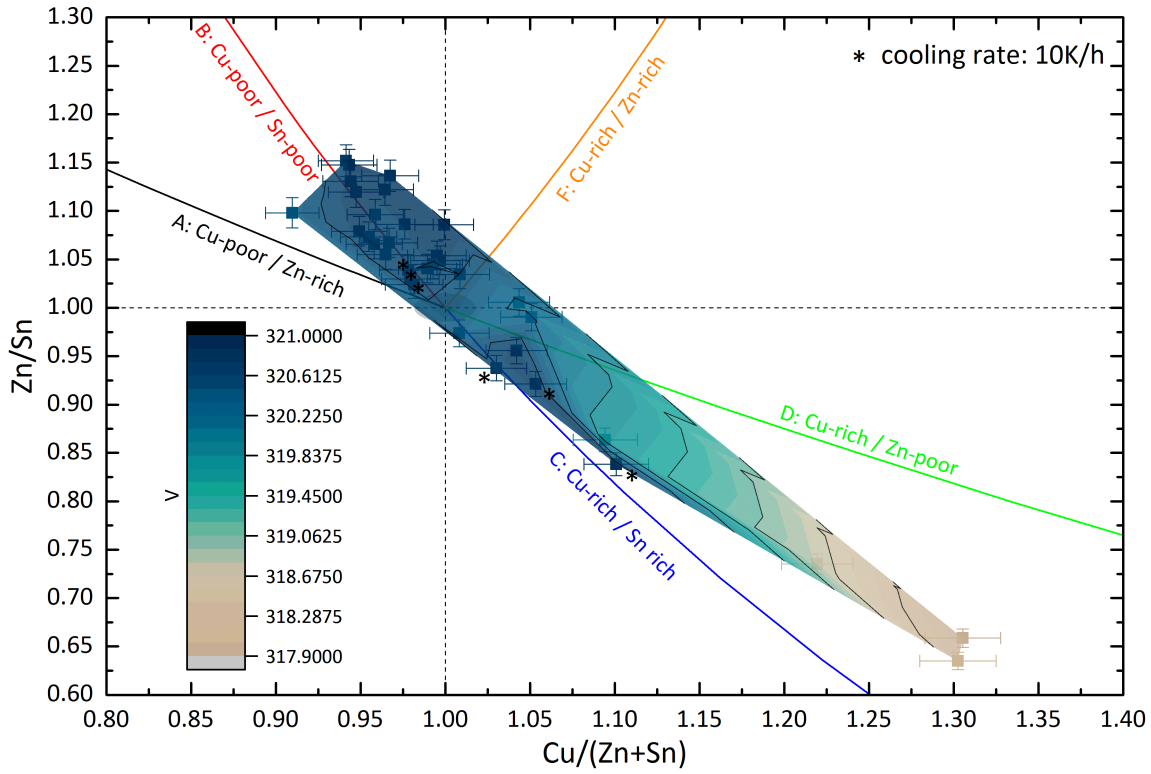
Figure 3.26: Overview of the unit cell volume of CZTS vs. chemical composition.

a slightly lower cell volume in contrast to the B-type dominated CZTS compounds can be observed which supports the influence of the V_{Cu} counteracting the increase of the cell volume from the rising Zn content.

3.2.2 Conclusion

The lattice parameters, tetragonal deformation and unit cell volume are strongly influenced by changing Cu- and Zn-content. In the Cu-rich / Zn-poor region the impact of the chemistry on the lattice parameters is stronger pronounced than in the Cu-poor / Zn-rich region due to more off-stoichiometric CZTS samples. Also the most off-stoichiometric Cu-poor / Zn-rich CZTS shows a slight trend to decreasing lattice parameters. The change of lattice parameter a is stronger compared to lattice parameter c. Decreasing lattice constants induce a shrinking unit cell with increasing Cu-rich / Zn-poor conditions. This was supported by the plot of the unit volume which exhibit the lowest volume in the Cu-rich / Zn-poor region.

Furthermore the tetragonal deformation ($c/2a$)was analyzed and an increase from Cu-rich / Zn-poor to Cu-poor / Zn-rich conditions was observed whereas in the most off-stoichiometric Cu-rich / Zn-poor CZTS phases no tetragonal deformation was observed ($c/2a = 1$). These results were also observed for CZTS compounds synthesized by Lafond et al. [45]. Moreover CZTSe powders show the same lattice parameter trends, but in a smaller magnitude than CZTS [96].

3.3 Cation distribution and intrinsic point defects

The main focus of this study was the analysis of the cation distribution in different off-stoichiometric CZTS samples and the identification of the intrinsic point defects and if the defect complexes are in agreement with the postulated substitution processes and their corresponding defect complexes.

The analysis of the intrinsic point defects was conducted by applying neutron diffraction to distinguish reliable Cu^+ and Zn^{2+}. Furthermore neutron diffraction was also necessary to determine if the crystal structure of CZTS correspond to kesterite or stannite structure which was shown in detail by Schorr [74].

3.3.1 Characterization of single-phase CZTS: Cu-poor / Zn-rich

The first sample characterized by neutron diffraction was a very well studied slightly Cu-poor / Zn-rich homogeneous CZTS with $Cu / (Zn + Sn) = 0.965(17)$ and $Zn / Sn = 1.055(15)$. The Rietveld analysis of the neutron data can be seen in Figure 3.27a) which shows the experimental and refined results in a very good agreement. The difference curve and also the quality factors R_{Bragg} and χ^2 described in Chapter 2.2.4 confirm a high quality Rietveld refinement. A list of the quality factors of the refinement parameters can be found in Table A.3.

a)   b)
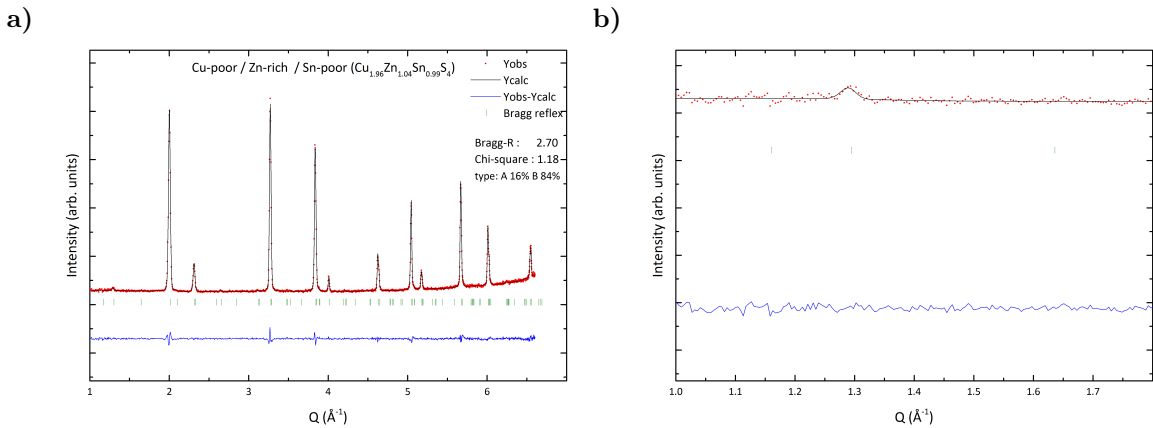
Figure 3.27: Refinement of A-B-type CZTS with $Cu / (Zn + Sn) = 0.965(17)$ and $Zn / Sn = 1.055(15)$ a) showing the whole Q-space and b) the magnified area of the first three kesterite reflexes.

Neutron powder data with a high resolution and good signal to noise ratio are vital for an accurate and reliable Rietveld analysis. Only high quality neutron data guarantees dependable evaluations of the measurement data, which are very important for the cation distribution analyses, because fine changes can greatly impact the results. In Figure 3.27b) the area of the *002*, *110* and *101* reflexes of the CZTS phase are magnified because they have an important role for the distinction between kesterite and stannite structure described in Chapter 3.3.2 and which was already solved by Schorr [74] for

stoichiometric CZTS. Therefore it is important to check the structure of the newly synthesized off-stoichiometric CZTS phases.

a)

b)
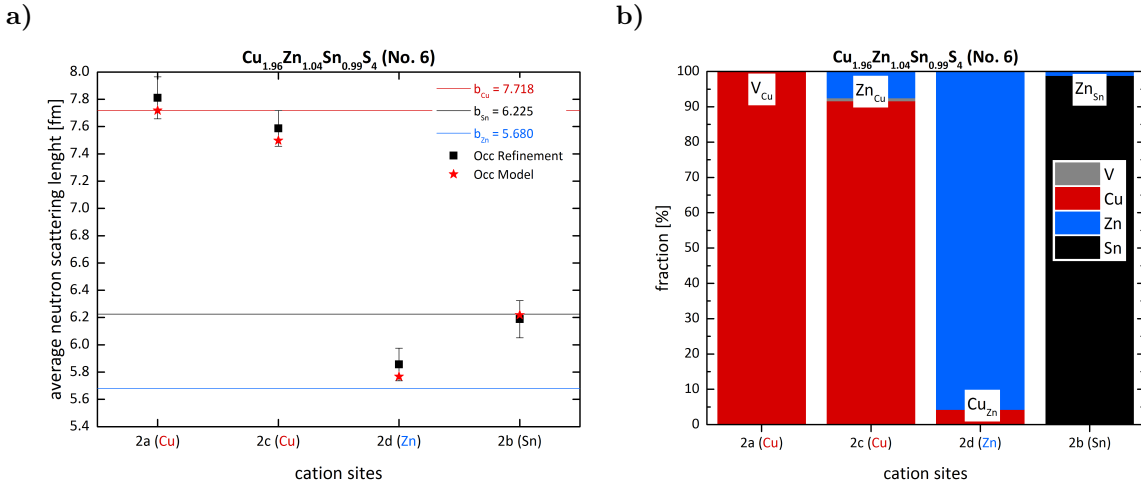
Figure 3.28: Cation distribution of A-B-type CZTS with $Cu/(Zn+Sn) = 0.965(17)$ and $Zn/Sn = 1.055(15)$ a) showing the average neutron scattering length and b) the resulting cation distribution in %.

Figure 3.28 shows the results of the Rietveld analysis and the evaluation by the use of the average neutron scattering length method described in Chapter 2.2.4. In Figure 3.28a) the black rectangles represent the average neutron scattering length of the Wyckoff positions $(\bar{b}_x^{RR})$ derived from the refined site occupations multiplied by the neutron scattering length of the element occupying the Wyckoff position in a fully ordered kesterite type structure. Also the corresponding error was included. The red stars belong to the data modeled $(\bar{b}_x^{calc})$ which should conform to the black rectangle $(\bar{b}_x^{RR})$ by including the results of the electron micro probe analyzer. A more detailed description of the method can be found in Chapter 2.2.5.

The 2a(Cu) position seems to be fully occupied by Cu because the black rectangle $(\bar{b}_{2a}^{RR})$ overlaps with neutron scattering length of Cu from literature [84]. Furthermore it seems also the 2b(Sn) position mostly contains Sn because of the overlapping of the calculated average neutron scattering length (black rectangle) with the literature value of Sn [84]. The average neutron scattering length of the 2c(Cu) position is located slightly below the average neutron scattering length of Cu (b_{Cu}) and 2d(Zn) experimental data lies slightly above the neutron scattering length of Zn (b_{Zn}). The deviation from the neutron scattering length of a pure Cu position indicate that, except Cu, additional elements with a lower average neutron scattering length or vacancies are incorporated on the 2c(Cu) position. In contrast to the 2c(Cu) position on the 2d(Zn) a cations with a higher average neutron scattering length than Zn must be incorporated.

The $Cu/(Zn+Sn) = 0.965(17)$ and $Zn/Sn = 1.055(15)$ ratios correspond to a A-B-type off-stoichiometric CZTS composition with a dominating B-type fraction of 84 % and only 16 % A-type fraction. In Table 3.2 (page 40) the intrinsic point defects of A-type and B-type are presented. V_{Cu} and Zn_{Cu} are possible for A-type as well as Zn_{Cu}
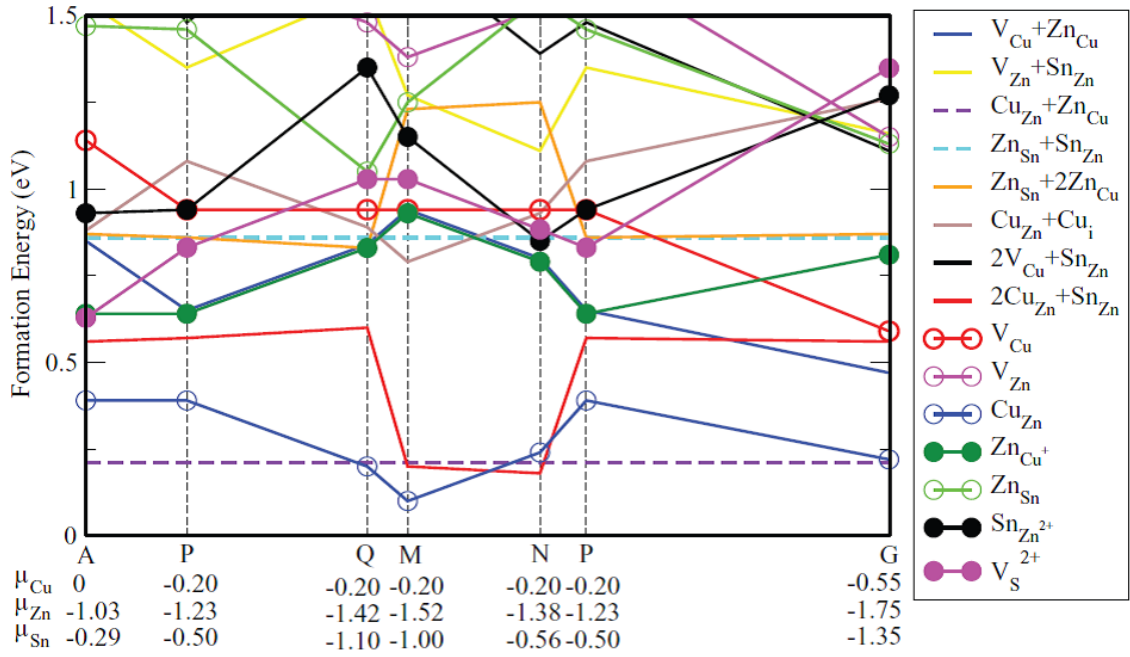
Figure 3.29: Overview of the formation energy of CZTS intrinsic point defects [9].
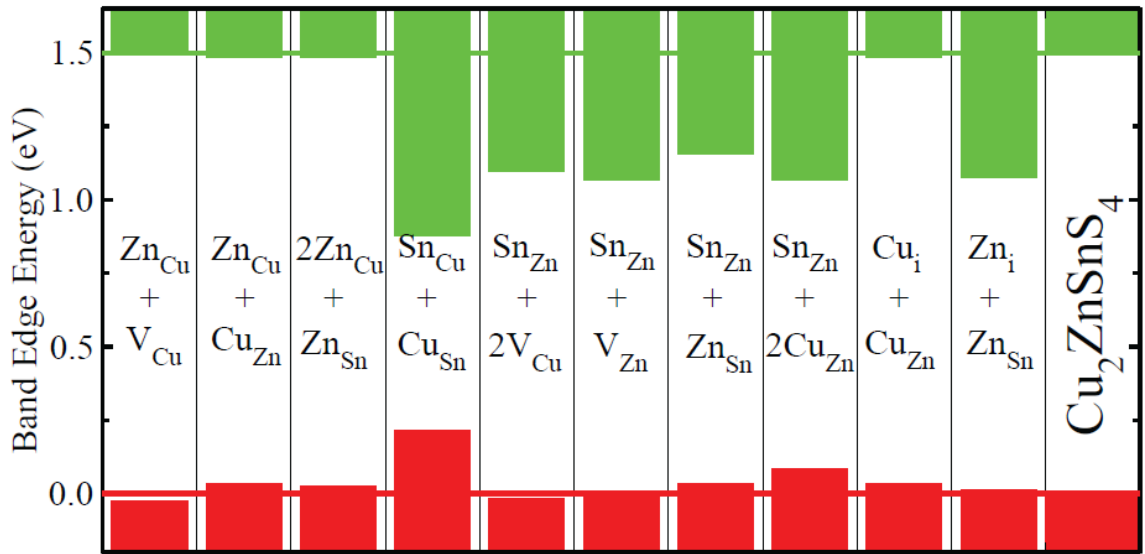
Figure 3.30: Overview of the CZTS defect complexes and their influence on the band gap [9].

and Zn_{Sn} for B-type. Furthermore Cu_{Zn} and Zn_{Cu} as part of the Cu-Zn disorder are possible. The challenging question is how to decide which defect and elements occur on which position if multiple possibilities exist. Several groups conducted simulations of the formation energies of different intrinsic point defects and defect complexes [9, 10, 33, 38, 63, 99]. This data provides indications and evidences which intrinsic point defects form more favorable under the given conditions.

Several defect formation energy calculations and their impact on the band gap were conducted [9, 10, 33, 38, 63, 99]. If multiple cation distributions were possible, the intrinsic point defect or defect complex with the lowest formation energy in relation to the electron micro probe analyzer results was chosen. Figure 3.29 and Figure 3.30 show an overview of formation energies of the intrinsic point defects and their influence on the band gap by Chen et al. [9]. Defect complexes can be harmful for the band gap and should be avoided like most of the Sn related defects which reduce the band gap and would lower the efficiency of a thin film solar cell. On the other hand the defect complex $Zn_{Cu} + V_{Cu}$ expands the band gap which supports highly efficient devices. The influence of the defect complexes on the band gap can be altered by the occurrence of secondary phases.

3.3.2 Test of the structural model used for Rietveld refinement

Ahead of the Rietveld refinement of the neutron data a check of the structural model used for the analyses was conducted. It was described by Schorr [74] that CZTS crystallizes in kesterite and not stannite type structure. To highlight differences in these two crystal structures, simulations of neutron patterns of kesterite and stannite type structure were conducted by using the FullProf Suite. Also a Rietveld analysis of a sample was evaluated by applying both structures. Therefore the well characterized single-phase A-B-type CZTS with $Cu / (Zn + Sn) = 0.965(17)$ and $Zn / Sn = 1.055(15)$ ratio was used.

The main difference between the two simulated patterns is that in the kesterite structure model in Figure 3.31 the *101* reflex has intensity whereas the *002* and *110* reflexes have such a low intensity that it seems like their extinct. In contrast in the stannite structure it is exactly opposite. Here the *101* reflex has almost no intensity but the *002* and *110* reflexes have higher intensities. Also more Bragg reflexes show differences. These are mostly smaller and result only in intensity changes which are lost in the background noise of real experimental data. Furthermore no differences are observed in high intensity reflexes which emphasizes the similarity of the two structures. In the experimental data the differences of *101*, *002* and *110* are distinguishable and therefore high quality measurement results are necessary. In the appendix separate figures of simulated patterns using the kesterite and stannite type structure are included (see Figure A.71, page 170).

Now the analysis of experimental data with the two different structures follows. The Rietveld analysis of the chosen A-B-type CZTS using the kesterite type structure was already shown in Figure 3.27. In Figure 3.32 the refinement using the stannite type
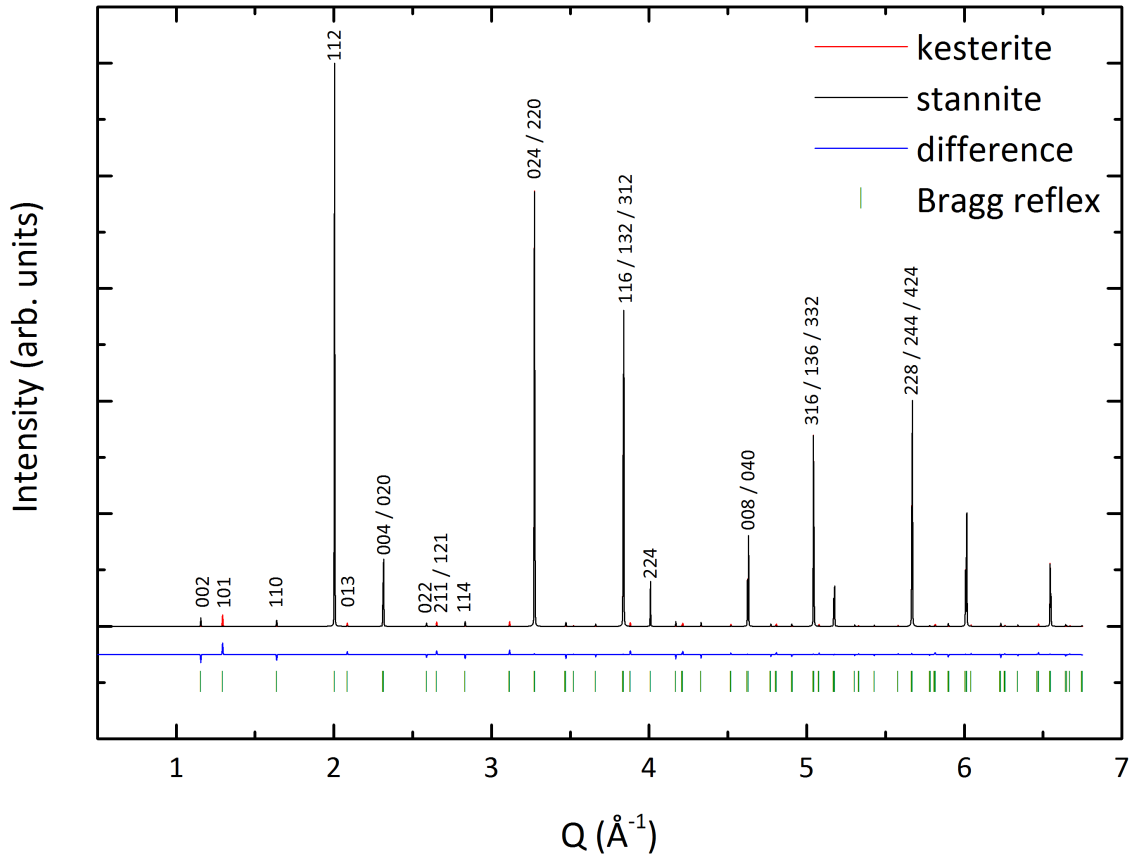
Figure 3.31: A comparison of simulated kesterite and stannite structure neutron patterns and their difference plot. A stronger magnified pattern can be found in Figure A.70.

structure can be seen where figure a) and c) as well as b) and d) belong together. Figure 3.32a) and c) show the neutron pattern before and b) and d) the patterns after the occupation refinement.

Without the refinement of the site occupation parameter the calculated model (red line) of the Rietveld refinement (Figure 3.32) corresponds well with the simulated stannite pattern in Figure 3.31. The experimental data in Figure 3.32 is not so well matched. Especially the reflexes *002* and *110*, which were calculated by the model were not observed in the experimental data. After the refinement of the site occupation parameter, the refined model changes, the reflexes *002* and *110* disappear from the model and the Bragg reflex *101* fits the reflex measured in the experimental data. Furthermore the refinement using the kesterite and stannite type structure have almost the same R_{Bragg} and χ^2 values. These observations support also the kesterite type structure as the preferable model for the Rietveld refinement because the *002* and *110* reflexes of the stannite structure disappear during the refinement as they are not needed to fit the experimental data.

Additionally the average neutron scattering length method was used to compare the cation distribution results of the refinement conducted with the kesterite and stannite

type structure. In contrast to the kesterite type structure in the stannite structure, Zn should be located on the 2a(Zn) position and Cu on the 4d(Cu) position (see Figure 1.5, page 7). In the kesterite type structure the 2c(Cu) and 2d(Zn) positions comply to the 4d(Cu) in stannite structure.

a)

b)

c)

d)
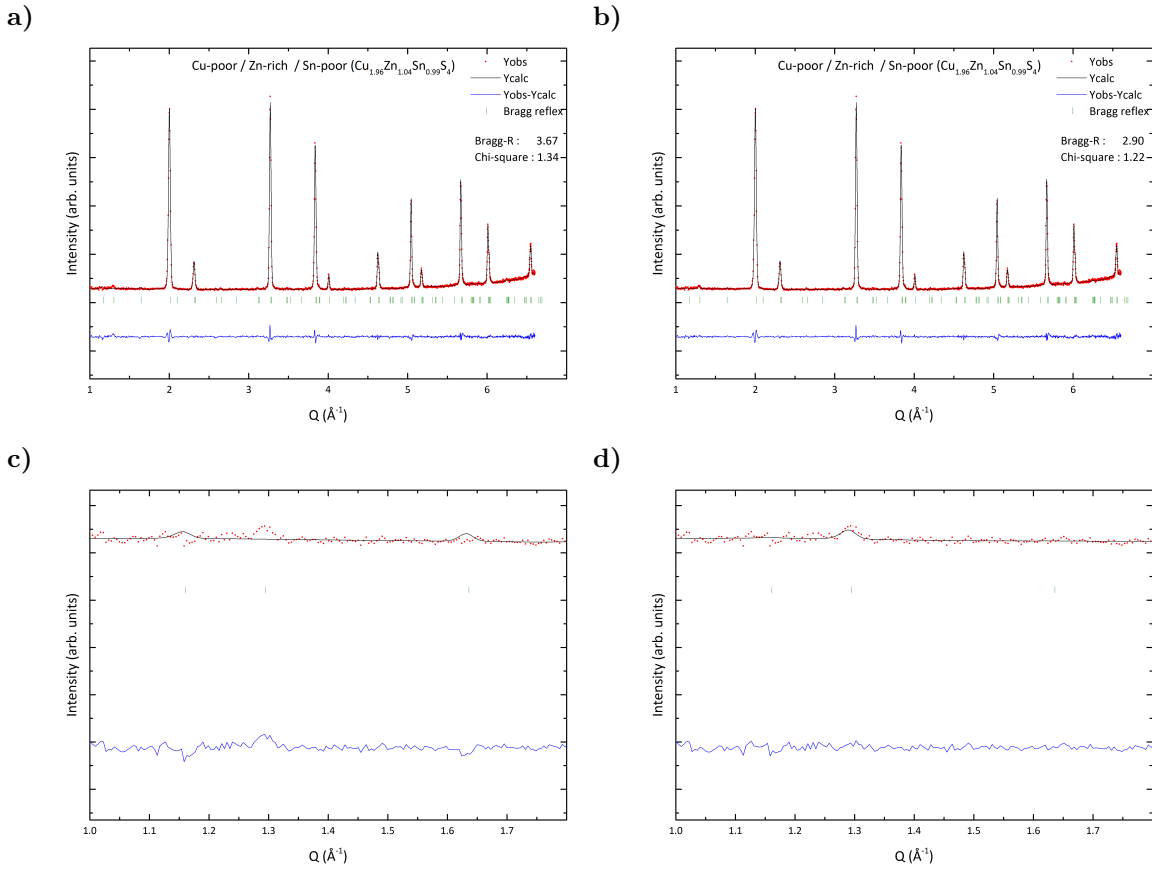
Figure 3.32: Rietveld analysis of A-B-type CZTS $(\mathrm{Cu}\,/\,(\mathrm{Zn}+\mathrm{Sn}) = 0.965(17)$ and $\mathrm{Zn}\,/\,\mathrm{Sn} = 1.055(15))$ by using the stannite structure: a) refinement without site occupation parameter, b) after refining the site occupation parameter and c, d) a zoom of the first three stannite Bragg reflexes.

Figure 3.33 presents a comparison of the average neutron scattering length results $(\bar{b}_x^{calc})$ by refining the neutron pattern using the kesterite and stannite type structure and the average neutron scattering length of a fully ordered kesterite and stannite structure as a reference. The refinement with kesterite type structure shows a fully Cu occupied 2a(Cu) position and also the 2c(Cu) position is almost fully occupied by Cu with only small amounts of lower scattering elements or vacancies. On the 2d(Zn) position mostly Zn is located with higher scattering elements lifting the point slightly above the ideal average neutron scattering length of Zn. The 2b(Sn) position is mostly occupied by Sn. Next to the experimental results also the average neutron scattering length of a fully ordered kesterite and stannite type structure is presented, marked by open symbols. This should facilitate the evaluation of the differences of the refined to the fully ordered average neutron scattering length.

The stannite type structure should have a fully Zn occupied 2a(Zn) position but the average neutron scattering length shows a fully Cu occupied position which corresponds to kesterite type structure. Furthermore the 4d(Cu) position should only be occupied by Cu but the average neutron scattering length is located on a line at 50 % Cu and Zn occupation with a average neutron scattering length of 6.699 fm which corresponds to a separated 2c(Cu) and 2d(Zn) position. Also the average neutron scattering length of the experimental data confirms the formation of kesterite type structure in off-stoichiometric CZTS which is in agreement with the result by Schorr [74].
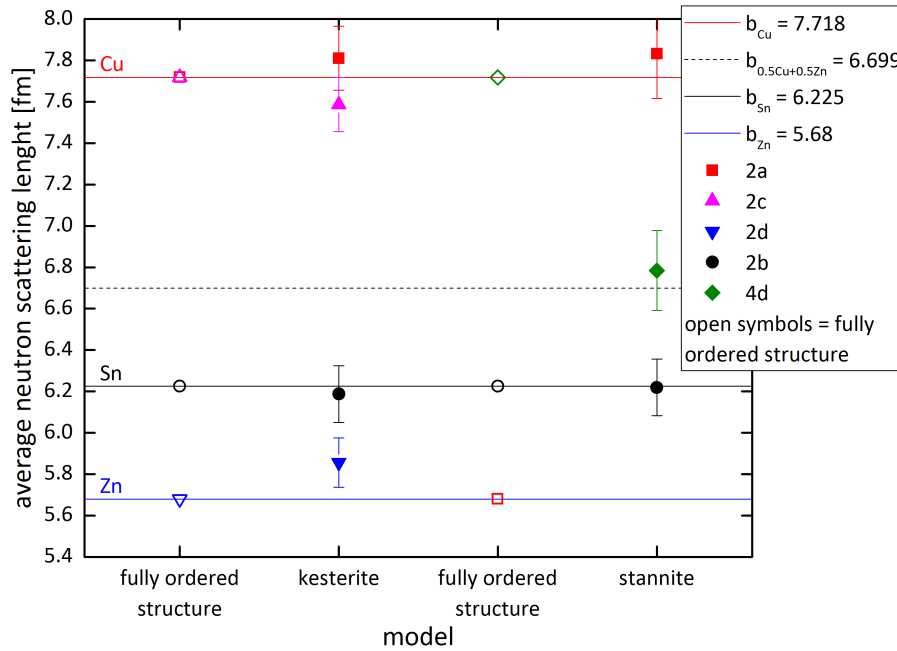
Figure 3.33: Average neutron scattering length of Cu-poor / Zn-rich CZTS (Cu / (Zn + Sn) = 0.965(17) and Zn / Sn = 1.055(15)) refined with the kesterite and stannite type structure. The open symbols show the average neutron scattering length of a fully ordered kesterite and stannite type structure and the closed symbols the average neutron scattering length of the refined experimental neutron data.

The slight deviation of a fully occupied 2c(Cu) and 2d(Zn) position (see Figure 3.28, page 62) can be explained by induced intrinsic point defects due to the off-stoichiometric Cu-poor / Zn-rich chemical characteristics. Because of the Cu-poor / Zn-rich composition the missing Cu is exchanged by the excess Zn. This substitution corresponds to the Zn_{Cu} defect which is part of the A- and B-type defect complex and is in good agreement with the postulated cation substitution processes and defect complexes [45]. Also some V_{Cu} were identified on the 2c(Cu) position completing the A-type defect complex $2Cu^+ \rightarrow V_{Cu} + Zn_{Sn}$. Furthermore some Zn was identified on the 2b(Sn) position because not enough Sn was incorporated in the structure to fully occupy the position (WDX results: Sn < 1). These observations correspond well with the B-type defect complex $2Cu^+ + Sn^{4+} \rightarrow 2Zn_{Cu} + Zn_{Sn}$ and are in good agreement with the calculated formation energies [9]. Furthermore some Cu_{Zn} was observed which contributes to the always present Cu-Zn disorder. The same amount of Cu on 2d(Zn) has to be subtracted from the Zn on 2c(Cu) and the remaining Zn_{Cu} belongs to the

intrinsic point defect. A small fraction of Cu-Zn disorder is almost unavoidable due to the lowest average formation energy of the defect complex (see Figure 3.29, page 63).

3.3.3 Cation distribution of single off-stoichiometric type CZTS

In total 34 samples were synthesized and many are located near a pure off-stoichiometric type line similar to the sample in the previous chapter but have still minor amounts of a second type. For the identification of single type samples the error of 5 % of the type fraction was considered. In this chapter the CZTS phases located on a type line and with an amount of the second type below 5 % were selected and analyzed (Figure 3.34).
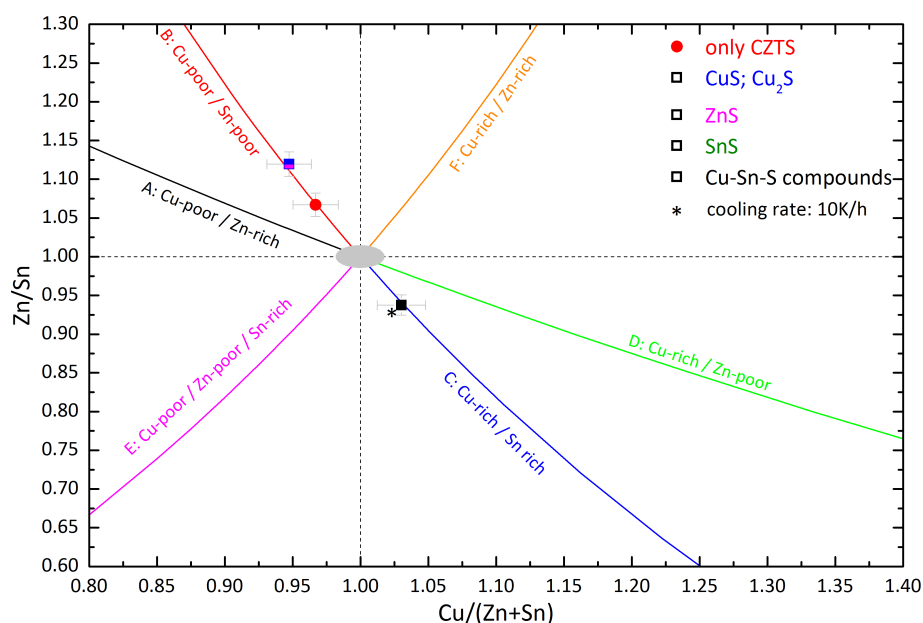
Figure 3.34: Cation ratio of three single type phases located on the B- and C-type line: single-phase = red, copper sulfides = blue, zinc sulfides = magenta, tin sulfides = green and Cu-Sn-S-compound = black.

In total three CZTS phases fulfill these criteria and are regarded as a single off-stoichiometry type CZTS. Two of them have a B-type composition. The single-phase CZTS has a $\mathrm{Cu}\,/\,(\mathrm{Zn}+\mathrm{Sn}) = 0.967(17)$ and $\mathrm{Zn}\,/\,\mathrm{Sn} = 1.067(15)$ ratio. The more Cu-poor B-type CZTS has a $\mathrm{Cu}\,/\,(\mathrm{Zn}+\mathrm{Sn}) = 0.947(16)$ and $\mathrm{Zn}\,/\,\mathrm{Sn} = 1.120(16)$ ratio. The third CZTS has a C-type Cu-rich / Zn-poor composition with $\mathrm{Cu}\,/\,(\mathrm{Zn}+\mathrm{Sn}) = 1.030(18)$ and $\mathrm{Zn}\,/\,\mathrm{Sn} = 0.938(13)$.

Furthermore several secondary phases were identified in the C- and in one of the B-type samples. Copper sulfide, tin sulfide and zinc sulfide were observed in the stronger off-stoichiometric B-type sample and a Cu-Sn-S compound in the C-type sample. Also a lower cooling rate of $10\,\mathrm{K\,h^{-1}}$ instead of $50\,\mathrm{K\,h^{-1}}$ was applied for the C-type sample. All this information was summarized in Figure 3.34.

It is noticeable hat these samples are located on a line from Cu-poor / Zn-rich / Sn-poor to Cu-rich / Zn-poor / Sn-rich composition and also the majority of type mixture samples are located in the vicinity of these two off-stoichiometric type lines. B- and C-type complement each other.
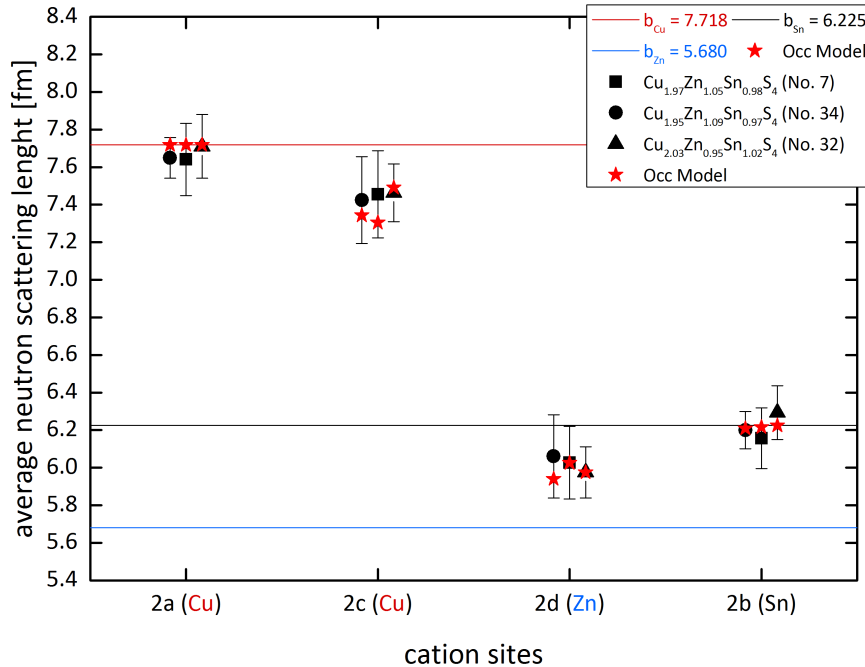
Figure 3.35: Overview of the average neutron scattering length vs. the Wyckoff positions of single type CZTS: black symbols = average neutron scattering length calculated from the refinement ($\bar{b}_x^{RR}$), red star = calculated average neutron scattering length ($\bar{b}_x^{calc}$), colored lines = neutron scattering length of Cu, Sn and Zn.

In Figure 3.35 the results of the cation distribution are presented and Figure 3.36 shows the results of the cation distribution in a more accessible bar diagram. The black symbols, which represent the average neutron scattering length ($\bar{b}_x^{calc}$), show a fully Cu occupied 2a(Cu) and a fully Sn occupied 2b(Sn) position. The B-type CZTS phases are slightly Sn-poor and the small amount of Zn on the 2b(Sn) position has a neglectable impact on the average neutron scattering length of the experimental and modeled data. In Figure 3.36 the small fraction of Zn_{Sn} can be seen because in the defect complexes of B- and C-type no vacancies are present and also the average neutron scattering length data suggests a fully occupied 2b(Sn) position. There are no striking differences between the experimental data of the B- and C-type CZTS compounds. Also the calculated average neutron scattering lengths based on the cation distribution models (red stars) are very similar. This emphasizes the importance of the measured chemical composition by the electron micro probe analyzer. Without this data cation distribution analyses would not be possible.

Significant changes can be observed on the 2c(Cu) and 2d(Zn) position because both are shifted from the neutron scattering length of the fully ordered kesterite type structure.
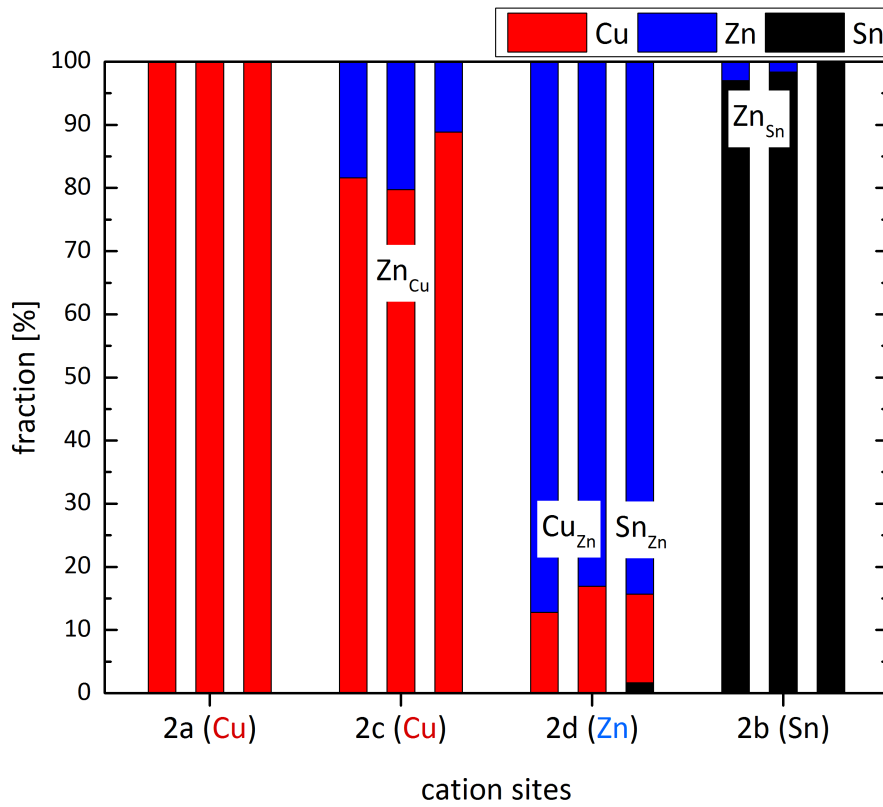
Figure 3.36: Cation distribution of the Wyckoff positions extracted from the average neutron scattering length model in %: vacancies = gray, copper = red, zinc = blue and tin = black.

The 2c(Cu) position scatters slightly lower and the 2d(Zn) position slightly higher. The difference between the average neutron scattering length of the 2c(Cu) and 2d(Zn) position of the B- and C-type CZTS phases is small and only the results of the electron micro probe analyzer and the different defect complexes are leading to distinct cation distributions. All three CZTS phases show some Cu-Zn disorder. In the B-type CZTS Zn_{Cu} dominates and some Zn_{Sn} is present, whereas in the C-type CZTS Cu_{Zn} dominates and some additional Sn_{Zn} can be observed. These observations correspond well with the postulated defect complexes by Lafond et al. [45].

The CZTS compounds analyzed in the following chapters will have an additional off-stoichiometric type influencing the cation distribution.

3.3.4 Cation distribution of Cu-poor / Zn-rich A-B-type CZTS

The results of the A-B type CZTS compounds are especially interesting because the CZTS absorber layer in high efficient solar cells exhibits a Cu-poor / Zn-rich composition (A-type). In total eight CZTS phases will be discussed in this chapter and all were successfully refined. The neutron patterns can be found in the Chapter A.2. One additional CZTS was already discussed in Chapter 3.3.3 and has a pure B-type composition

with a neglectable amount of (1 %) A-type fraction. The eight A-B-type mixture CZTS phases are following a path to stronger off-stoichiometry and are also presented in this order. Figure 3.37 presents only the analyzed A-B-type CZTS compounds in the cation ratio plot. The arrow marks the direction to stronger off-stoichiometry and simultaneous the presentation order in the following figures. Five samples have a single-phase composition and in three samples secondary phases were identified. Coincidentally a cooling rate of $10\,\mathrm{K\,h^{-1}}$ instead of $50\,\mathrm{K\,h^{-1}}$ was applied on these three samples as remarked in Figure 3.37. Tin sulfides and a Cu-Sn-S-compound were detected as secondary phases. The chemical composition changes gradually with a significant gap to the strongest off-stoichiometric CZTS which also has the highest A-type fraction of 47 %.
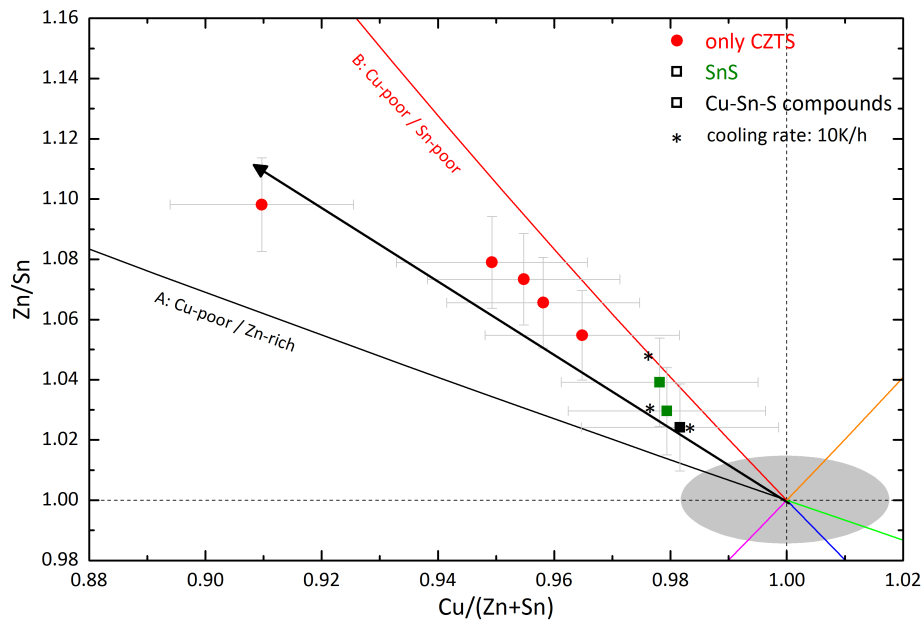
Figure 3.37: Overview of analyzed Cu-rich / Zn-poor (A-B-type mixture) CZTS compounds. The arrow highlights the off-stoichiometric path of the eight CZTS phases.

The results of the average neutron scattering length deduced from the Rietveld refinement results can be seen in Figure 3.38 where the black symbols represent the average neutron scattering length from the Rietveld analysis of the experimental data and the red stars the calculated average neutron scattering length based on the cation distribution model in combination with the chemical composition from the EMPA measurements. This method was described in detail in Chapter 2.2.5 and Chapter 3.1.2. The off-stoichiometry increases from left to right with the $\mathrm{Cu}\,/\,(\mathrm{Zn}+\mathrm{Sn}) = 0.982(17)$ and $\mathrm{Zn}\,/\,\mathrm{Sn} = 1.024(14)$ CZTS on the left and the $\mathrm{Cu}\,/\,(\mathrm{Zn}+\mathrm{Sn}) = 0.910(16)$ and $\mathrm{Zn}\,/\,\mathrm{Sn} = 1.098(16)$ CZTS on the right.

The average neutron scattering lengths calculated from the refinement $(\bar{b}_x^{RR})$ suggest that the 2a(Cu) Wyckoff position is fully occupied by Cu and the 2b(Sn) position fully occupied by Sn. These observations are also reflected by the model (red star = $\bar{b}_x^{calc}$) for both positions which are overlapping with the line of the neutron scattering

length of the observed element. Only in one CZTS phase enough Sn was measured by WDX to fully occupy the 2b(Sn) position, so in the model Zn_{Sn} was introduced to fill the small amount of missing Sn. Vacancies on the Sn position seem not to be realizable because they are not listed in the range of the calculated formation energies by Chen et al. [9] and other authors [33, 38, 63, 99]. Furthermore the Zn_{Sn} antisite has a lower formation energy than Cu_{Sn} and also the Cu-poor / Zn-rich composition supports more the Zn_{Cu} defect [33]. Also Zn_{Cu} has only a small impact on the average neutron scattering length because the difference between the values of Zn and Sn is much smaller than the difference to Cu or the influence of a vacancy.
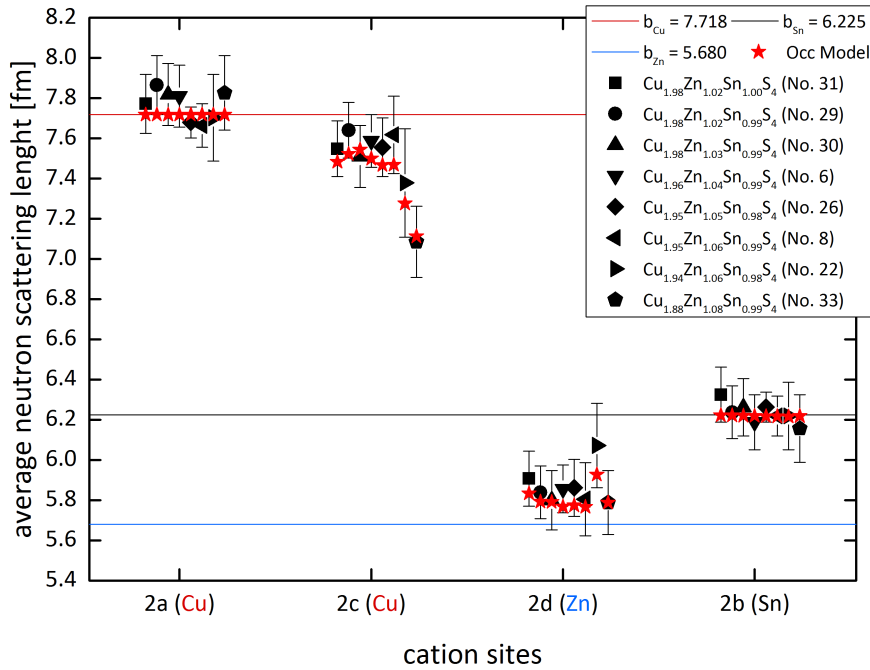
Figure 3.38: Overview of average neutron scattering length vs. the Wyckoff positions: black symbols = average neutron scattering length calculated from the refinement ($\bar{b}_x^{RR}$), red star = calculated average neutron scattering length ($\bar{b}_x^{calc}$), colored lines = neutron scattering length of Cu, Sn and Zn. The off-stoichiometry increases from left to right and is also represented by the formulae and their corresponding symbols.

Significant changes are mostly observed on the 2c(Cu) position which is largely occupied by Cu and the 2d(Zn) position which is almost fully occupied by Zn. The average neutron scattering lengths of the experimental data are slightly above the neutron scattering length of Zn which indicates an incorporation of a stronger scattering element on the 2d(Zn) position. Due to the measured Sn completely bound on the 2b(Sn) position only Cu is left to produce these changes. Neither the A- nor the B-type suggest a Cu_{Zn} antisite. This is no contradiction because the Cu_{Zn} defect belongs to Cu-Zn disorder which was described in Chapter 1.3. The defect complex forming the Cu-Zn disorder ($Cu_{Zn} + Zn_{Cu}$) has such a low formation energy that it was unavoidable with the used synthesis parameters and is present in every CZTS synthesized. The amount
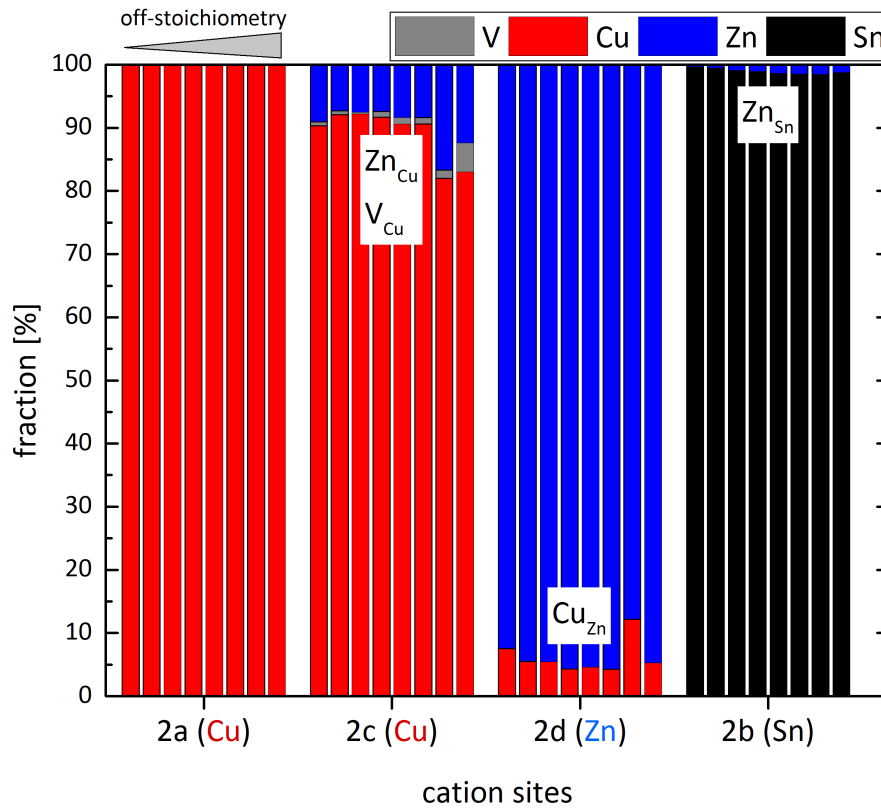
Figure 3.39: Cation distribution of A-B-type CZTS of the Wyckoff sites extracted from the calculated average neutron scattering length in %: vacancies = gray, copper = red, zinc = blue and tin = black. Each column represents a CZTS phase and in total eight CZTS compounds are summarized.

of Cu-Zn disorder can vary due to slightly different formation conditions of the CZTS compounds.

Overall the changes of the average neutron scattering length on the 2c(Cu) position normally occupied by Cu are higher because of the Cu-poor / Zn-rich composition. The first six CZTS compounds exhibit only minor changes of the average neutron scattering length but stronger changes can be observed in the 7th and 8th CZTS. In Figure 3.38 the elements distributing to the calculated average neutron scattering length (red star $= \bar{b}_x^{calc}$) can not be distinguished so that Figure 3.39 was introduced. The elements distributing to the different Wyckoff positions and their fraction on a certain position can be identified. Furthermore it facilitates the comparison between different CZTS phases and also defects like V_{Cu} are visible. On the 2c(Cu) position V_{Cu}, Zn_{Cu} and Cu-Zn disorder have an influence on the average neutron scattering length and occupation.

In Figure 3.39 the already described site occupations are clearly visible with a fully Cu occupied 2a(Cu) position and Sn on the 2b(Sn) position with a small amount of Zn to achieve a full site occupation. Also the Cu_{Zn} on 2d(Zn) and the same amount of Zn_{Cu} on 2c(Cu) must be contributed to the Cu-Zn disorder. The remaining Zn_{Cu} belongs to the A- and B-type Zn_{Cu} point defect. Some further differences are now distinguishable

which could not be identified in Figure 3.38. In the most off-stoichiometric CZTS the deviation from the ideal average neutron scattering length of 2c(Cu) can be mostly attributed to the high amount of vacancies in CZTS due to off-stoichiometry and the highest amount of A-type influence (47 %). Whereas in the CZTS Cu / (Zn + Sn) = 0.949(16) and Zn / Sn = 1.079(15) ($Cu_{1.94}Zn_{1.06}Sn_{0.98}S_4$) the high amount of Zn_{Cu} intrinsic point defects is mainly caused by the higher Cu-Zn disorder. The Cu-Zn disorder is responsible for the deviations from neutron scattering length of 2c(Cu) and 2d(Zn) position and not the vacancies due to the decreased A-type influence of only 17 %. The vacancies have an even lower impact on the less off-stoichiometric CZTS which can mainly be attributed to the low A-type influence.

These results show that neutron diffraction alone is not sensitive enough to observe small chemical changes in the CZTS structure but offers the ability to distinguish fully occupied positions and significant chemical changes and trends on certain Wyckoff positions. Only in combination with the electron micro probe analyzer results it is possible to distinguish detailed changes in the cation distribution.

3.3.5 Cu-rich / Zn-poor CZTS phases and their cation distribution
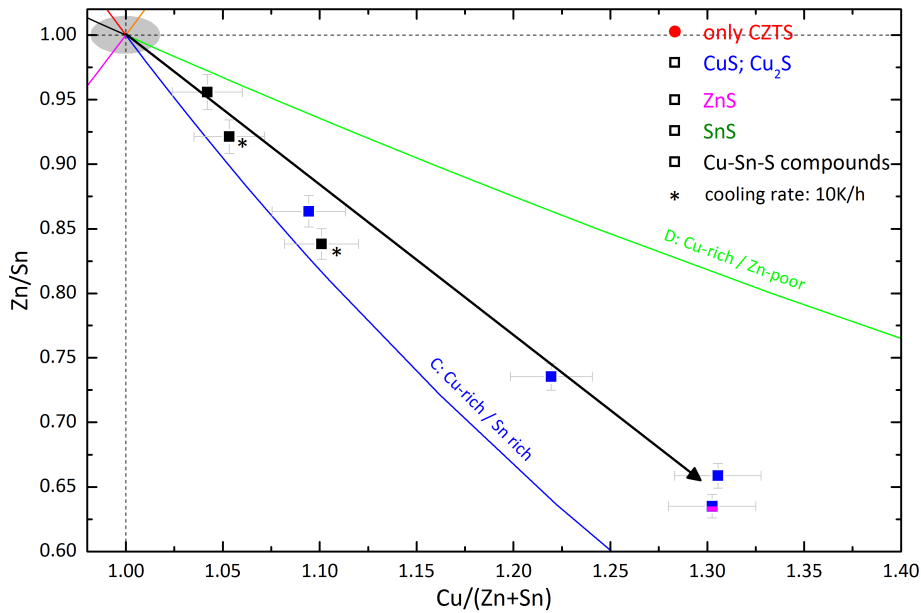
Figure 3.40: Cu-rich / Zn-poor (C-D-type) CZTS compounds analyzed by average neutron scattering length method [73]. The arrow highlights the off-stoichiometric path of the CZTS phases.

From the Cu-poor / Zn-rich CZTS phases (A-B-type), which are more in focus of the kesterite thin film solar cell community, the following chapter concentrates on the equivalent types in the Cu-rich / Zn-poor region (C-D-type). Similar to the A-B-type CZTS compounds a path from almost stoichiometric to off-stoichiometric CZTS was selected and evaluated. In total seven C-D- mixture CZTS phases were chosen and are

highlighted in Figure 3.40. All other CZTS phases with different mixture types or a pure type composition were ignored. In contrast to the A-B-type region no single-phase CZTS with Cu-rich / Zn-poor composition was synthesized. Also two of the analyzed samples were cooled with only $10\,\mathrm{K\,h^{-1}}$ instead of $50\,\mathrm{K\,h^{-1}}$. The most striking difference is the stronger degree of off-stoichiometry of Cu-rich / Zn-poor CZTS compounds which is three times stronger in the Cu / (Zn + Sn) direction and almost four times stronger for Zn / Sn ratio compared to the Cu-poor / Zn-rich CZTS.

The average neutron scattering length results are presented consistent to the A-B-type samples. On the left side the more least off-stoichiometric CZTS with Cu / (Zn + Sn) = 1.042(18) and Zn / Sn = 0.956(14) ratio ($\mathrm{Cu_{2.05}Zn_{0.96}Sn_{1.01}S_4}$) and on the right side the strongest off-stoichiometric CZTS with Cu / (Zn + Sn) = 1.303(23) and Zn / Sn = 0.635(9) ($\mathrm{Cu_{2.30}Zn_{0.69}Sn_{1.08}S_4}$) is located.
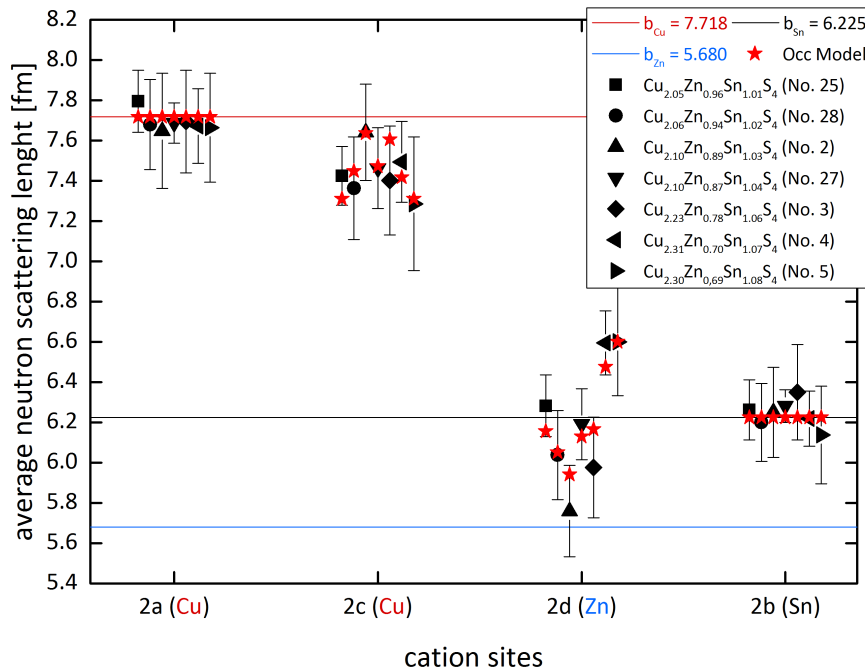
Figure 3.41: Average neutron scattering length vs. the Wyckoff positions of C-D-type CZTS: black symbols = average neutron scattering length calculated from the refinement ($\bar{b}_x^{RR}$), red star = calculated average neutron scattering length ($\bar{b}_x^{calc}$), colored lines = neutron scattering length of Cu, Sn and Zn. The off-stoichiometry increases from left to right and is also represented by the formulae and their corresponding symbols.

Also the results of the average neutron scattering length of the Cu-rich / Zn-poor (C-D-type) CZTS imply a fully Cu occupied 2a(Cu) position and a completely Sn occupied 2b(Sn) position as shown in Figure 3.41. Due to the Cu-rich / Zn-poor / Sn-rich chemistry of the CZTS compounds, fully Cu and Sn occupied Cu(2a) and Sn(2b) positions were expected because already in the Cu-poor / Zn-rich / Sn-poor compounds the same site occupation were observed. So all of the off-stoichiometric type defects of the Cu-rich / Zn-poor CZTS phases are located on the Cu(2c) and Zn(2d) position. In contrast

to the A-B-type CZTS instead of vacancies now Sn as the third element can be distributed because of Sn excess despite of the fully occupied Sn(2b) position. Due to the high formation energy of the Sn_{Cu} over Sn_{Zn} defect and the even lower formation energy of the C-type defect complex $2Cu_{Zn} + Sn_{Zn}$ the occurrence of Sn_{Cu} is very unlikely.

Because of the Cu-rich / Zn-poor characteristic the changes of the site occupation on the 2c(Cu) position are smaller and the majority of changes occur on the 2d(Zn) position. In the A-B-type samples it is contrary due to the opposing Cu-poor / Zn-rich composition. Also stronger diversified values were observed which can be attributed most likely to the occurring secondary phases.

The shift from the neutron scattering length of Cu is caused by the incorporation of Zn on the 2c(Cu) position. Because no type specific defect complexes containing Zn_{Cu} exist for the C- and D-type, the Zn_{Cu} belongs to the Cu-Zn disorder. In CZTS no direct correlation of the Cu-Zn disorder with off-stoichiometry could be observed and the almost stoichiometric and off-stoichiometric CZTS phases possess a similar amount of Cu-Zn disorder. For the cation distribution on the 2d(Zn) position Figure 3.42 improves the accessibility of the calculated site occupation derived from the average neutron scattering length in combination with the EMPA measurements.
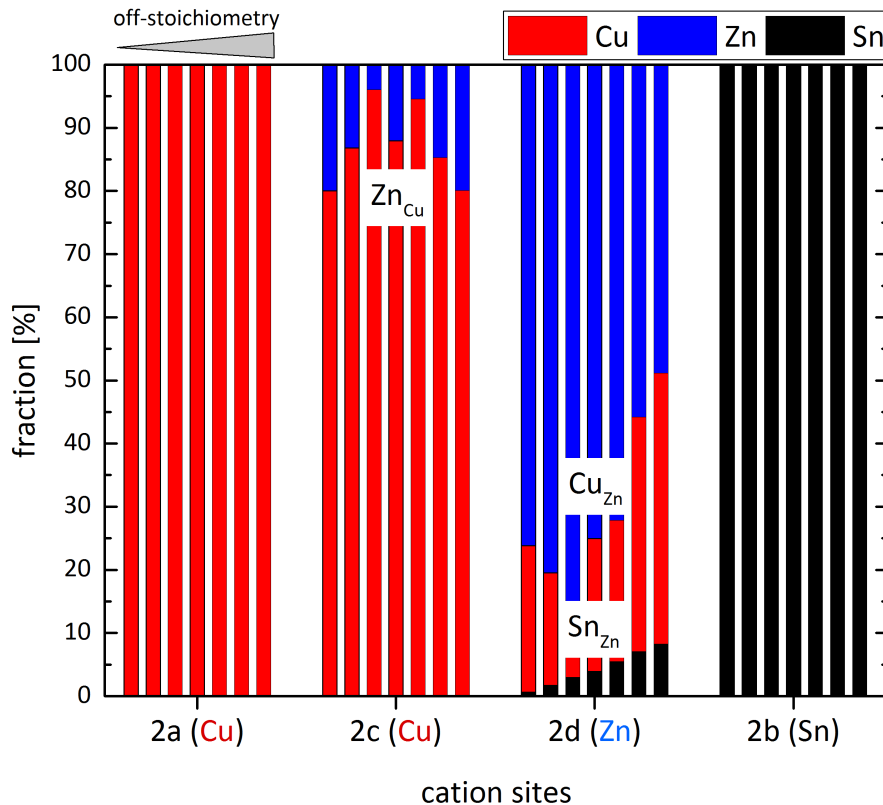
Figure 3.42: Cation distribution of C-D-type CZTS of the Wyckoff sites extracted from the calculated site occupation in %: vacancies = gray, copper = red, zinc = blue and tin = black.

The incorporated Sn_{Zn} on 2d(Zn) position reflects perfectly the increase of Sn within the CZTS structure with stronger off-stoichiometry. This point defect only occurs in the C-type. The corresponding Cu_{Zn} defect, which occurs twice as much and also can be found in the D-type defect complex, increases faster with off-stoichiometry than the Sn_{Zn}. The real Cu_{Zn} defect consists of the remaining Cu_{Zn} after the subtraction of the Cu-Zn disorder. This will be explained in more detail in Chapter 3.4. The Cu_{Zn} and Sn_{Zn} defects complete the C-type defect complex.

A correlation of the defect complexes between the slower cooled samples ($10\,K\,h^{-1}$) and the faster cooled samples ($50\,K\,h^{-1}$) could not be observed which is in agreement to the observation of the A-B-type samples. The samples containing the Cu-Sn-S-compound as secondary phase have the same Cu-Zn disorder as the most off-stoichiometric CZTS. There are also samples in between containing copper sulfides as secondary phases which exhibit a lower Cu-Zn disorder. Further investigations and more samples are necessary to evaluate the influence of the secondary phases on the Cu-Zn disorder.

All CZTS phases have a stronger C-type influence with the D-type fraction mostly limited below 25 % except for one CZTS where the amount of D-type reaches 43 %. The CZTS phase with $Cu\,/\,(Zn+Sn) = 1.042(18)$ and $Zn\,/\,Sn = 0.956(14)$ shows also the highest Cu-Zn disorder of the analyzed C-D-type CZTS compounds This high Cu-Zn disorder could also be related to the influence of the secondary phase or the strong chemical change from an initially weighed Cu-poor / Zn-rich to Cu-rich / Zn-poor composition.

The C-type specific defects were all explained, but to keep the charge balance for the cation substitution reaction of the D-type, Cu_i have to be introduced. Because Cu_i are located on empty positions in the kesterite type structure, they are not included in the cation distribution of the 2a(Cu), 2b(Sn), 2c(Cu) and 2d(Zn) position (see Figure 3.42, page 76). The amount of Cu_i results from the excess of Cu which could not be distributed in the model and would have caused a site occupation higher than 100 % on the Wyckoff positions. If it is possible to identify the location of the Cu_i will be discussed in the following chapter.

3.3.6 Location of the Cu_i point defect in the CZTS structure

In Figure 3.43 the same kesterite type structure as in Chapter 1.3 is shown and additionally the same structure with possible locations of the Cu_i. The 4e (0, 0, ¼), 4f (½, 0, 0) and 8g (¼, ¼, ⅛) Wyckoff positions were identified as possible positions and offer enough space for a Cu atom to enter. Of course further positions might be possible somewhere in between the structure. In the following study the focus lays on the 4e, 4f and 8g Wyckoff positions.

To understand the influence of the Cu_i on a certain position, simulations of neutron diffraction patterns were conducted. Therefore the positions 4e, 4f and 8g were separately introduced in the structural refinement. The site occupation of these Cu_i positions was derived from the CZTS phases with the highest amount of Cu_i. One Cu-rich / Zn-poor CZTS has a fraction of 0.083(2) Cu_i with $Cu\,/\,(Zn+Sn) = 1.305(22)$ and
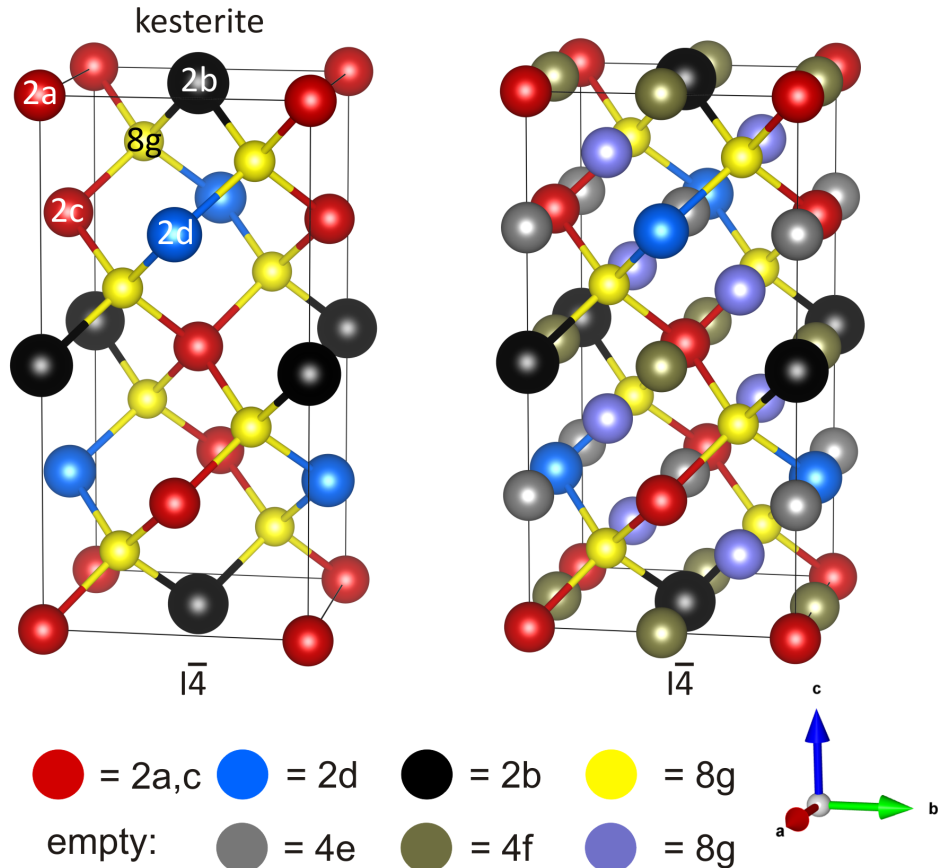
Figure 3.43: Kesterite structure and possible locations of Cu_i (4e, 4f and 8g). Cu = red, Zn = blue, Sn = black and S = yellow.

$Zn/Sn = 0.659(10)$. This amount was raised to 0.1 for the simulations to pronounce the possible changes.

The results of the simulations are shown in Figure 3.44 and all changes are in relation to the stoichiometric CZTS simulation. All three Cu_i positions influence the simulated diffraction patterns and all different Cu_i positions have an impact on the same reflections. There are only slight differences in intensity which separate the various defect positions. These minor changes are not strong enough to distinguish the different Cu_i positions in experimental data. The strongest deviations from the stoichiometric CZTS pattern are observed at the *220* and *228* reflex (see Figure A.71). Even these more significant changes are probably not enough to identify the Cu_i with the current experimental setup because of the background noise and the influence of the temperature parameters. Also the amount of Cu_i was overestimated for the simulations. Furthermore there is a possibility that the Cu_i incorporate at other positions in the crystal structure which generate different intensity changes.

In some CZTS phases, which contain Cu_i, higher intensities at the *220* reflex were measured and these intensity difference could not be refined with the fully ordered kesterite type structure. Unfortunately these changes were not observed in all samples which contain Cu_i. This could be caused by few Cu_i or by Cu_i on another position
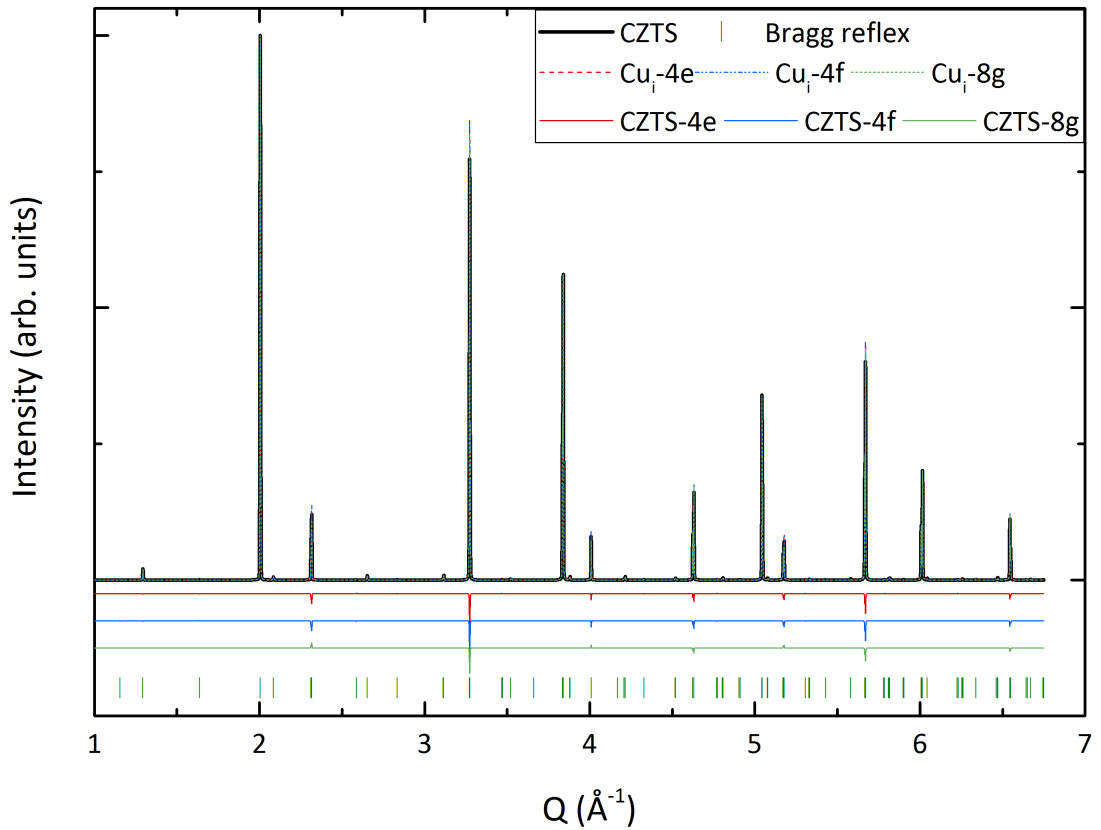
Figure 3.44: Simulation of different Cu_i positions in the kesterite structure: CZTS = black line, Cu_i on 4e = red, Cu_i on 4f = blue, Cu_i on 8g = green and the corresponding difference plot (CZTS-pattern-Cu_i-pattern).

inside the crystal structure. However it shows that some CZTS compounds show a deviation at the expected reflex and that some further investigations are necessary to identify the structural influences of interstitials.

Probably the Cu_i could be identified by improving the experimental setup by measuring at a controlled temperature or low temperatures with a cryostat. Low temperature measurements would only increase the chances of identifying the Cu_i and will certainly not be enough to distinguish the exact Wyckoff position of the Cu_i.

3.3.7 B-F-type CZTS and their cation distribution

The last CZTS compounds analyzed in detail are located in the B-F-type mixture region and can vary from Cu-poor / Zn-rich / Sn-poor to Cu-rich / Zn-rich / Sn-poor composition. The synthesized B-F-type compounds differ from the previous CZTS samples due to stronger changes of the Zn / Sn over the Cu / (Zn + Sn) ratio (see Figure 3.45) whereas the alteration of the A-B- and C-D-type CZTS phases is almost equal in both ratios (see Figure 3.37 and Figure 3.40).

In total seven samples were selected and analyzed. Six of them are single-phase and the last one contains multiple secondary phases. Copper, zinc and tin sulfides were identified by electron micro probe analyzer and X-ray diffraction. The selected CZTS compounds are located parallel to the B-type line. The lesser off-stoichiometric CZTS phases have a stronger F-type influence which decreases with increasing off-stoichiometry and strong B-type influence. Three of the single-phase samples share almost the same chemical composition and so the results of the cation distribution should be comparable.
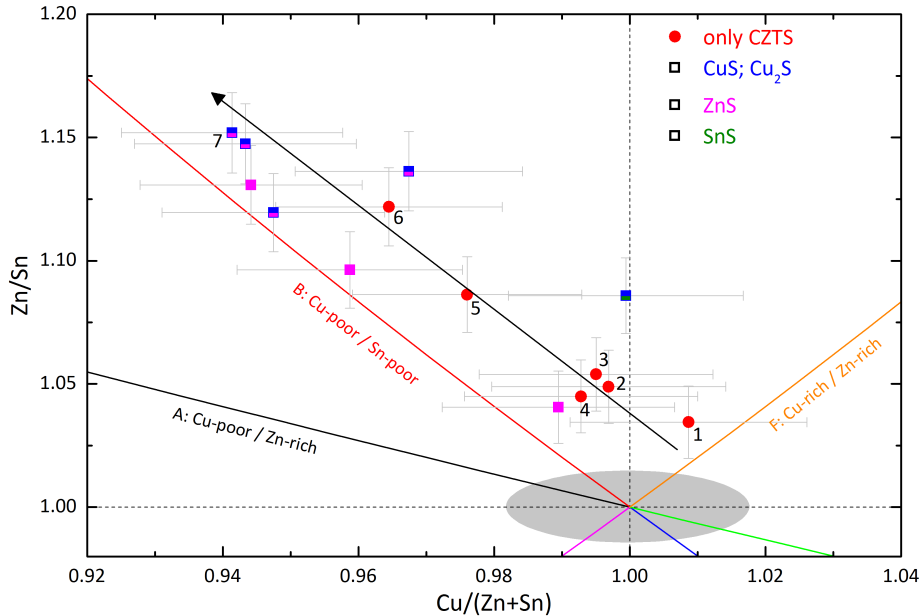
Figure 3.45: Zn-rich / Sn-poor (B-F-type) CZTS analyzed by average neutron scattering length method [73]. The arrow highlights the off-stoichiometric path of the seven samples.

In Figure 3.46 and Figure 3.47 the influence of the chemical composition on the cation distribution can be observed. In agreement with the A-B-type and C-D-type CZTS compounds the changes of the average neutron scattering length are mostly present on the 2c(Cu) and 2d(Zn) position whereas the deviations on the 2a(Cu) and 2b(Sn) are insignificant. These observations support a fully Cu occupied 2a(Cu) and a fully Sn occupied 2b(Sn) position. Due to the slightly Sn-poor composition not enough Sn was identified to fully occupy the 2b(Sn) position and therefore the missing Sn is replaced by Zn_{Sn} defect. The amount of the Zn_{Sn} defect is so small, that it has no impact on the refined and modeled average neutron scattering length (see Figure 3.46, page 81). Because of this the Zn_{Sn} defect can only be seen in Figure 3.47 which presents the cations distributing to the calculated average neutron scattering length in Figure 3.46.

The deviation from the ideal neutron scattering length of the 2c(Cu) and 2d(Zn) position is significant except for one CZTS which indicates a fully occupied 2d(Zn) position. This CZTS is the most off-stoichiometric with Cu / (Zn + Sn) = 0.941(16) and Zn / Sn = 1.152(16) and the only sample containing secondary phases. Zinc sulfide and the
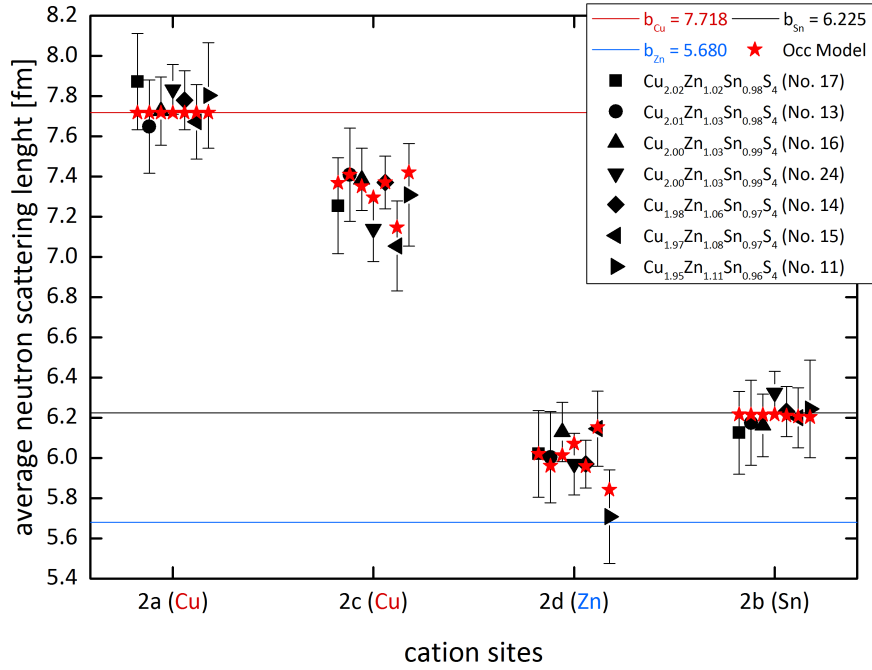
Figure 3.46: Overview of average neutron scattering length vs. the Wyckoff positions of B-F-type CZTS: black symbols = average neutron scattering length calculated from the refinement ($\bar{b}_x^{RR}$), red star = calculated average neutron scattering length ($\bar{b}_x^{calc}$), colored lines = neutron scattering length of Cu, Sn and Zn. The off-stoichiometry increases from left to right and is also represented by the formulae and their corresponding symbols.

low-temperature chalcocite were identified and due to strong reflex overlapping caused by these secondary phases, the results of the refined site occupation and the resulting average neutron scattering length probably possess a larger error than the software calculates. On the 2c(Cu) position all CZTS phases have a lower average neutron scattering length than a fully Cu occupied site. This decrease can be attributed to the Zn_{Cu} intrinsic point defect caused by the B-type. Thereby the B-type defect complex $2Zn_{Cu} + Zn_{Sn}$ is complete.

Distributing the cations in agreement with the F-type defects is more complicated because in principle two different defect complexes are possible to maintain the charge balance like presented in Table 3.2 (page 40) and Figure 3.6 (page 39)b). For the modeled average neutron scattering length and the evaluation of the experimental data the $Zn_{Sn} + 2Cu_i$ defect complex was preferred over the $Cu_{Sn} + Zn_i + Cu_i$ due to the higher formation energy needed to form Cu_{Sn} defects [9, 99]. Furthermore the $Zn_{Sn} + 2Zn_{Cu}$ and $Cu_{Zn} + Cu_i$ have a lower formation energy which supports $Zn_{Sn} + 2Cu_i$ defect complex [9, 99]. Unfortunately there are no calculated and simulated values for the Zn_i point defect. The mentioned arguments and the fact, that Zn also has a slightly higher cation radius and therefore prefers Sn(2b) position, support the used model.
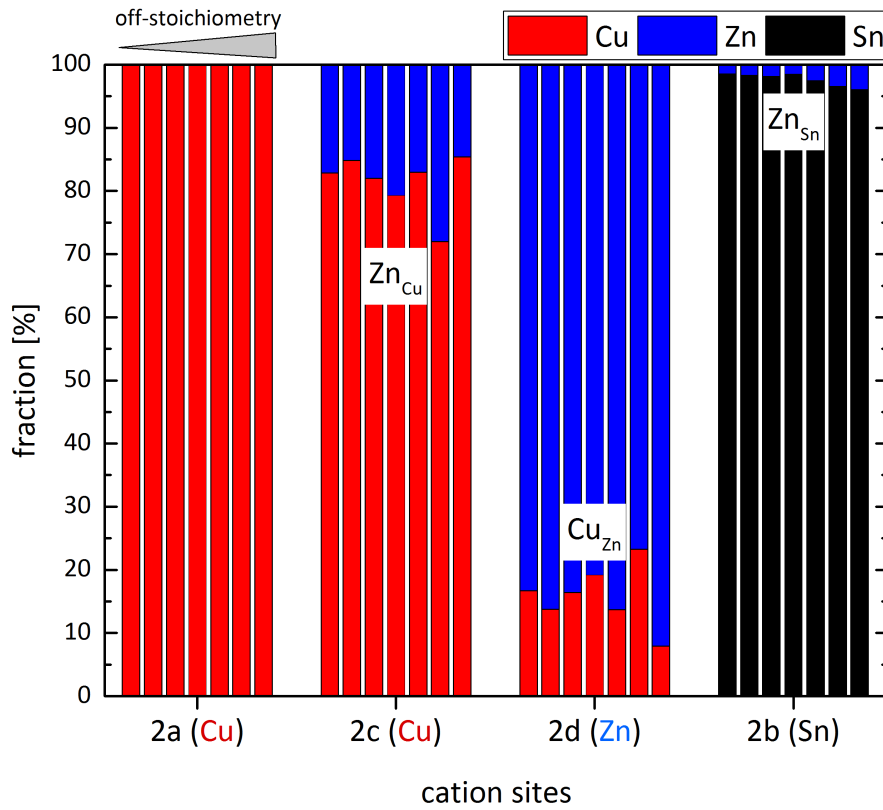
Figure 3.47: Cation distribution of B-F-type CZTS of the Wyckoff sites extracted from the calculated site occupation in %: vacancies = gray, copper = red, zinc = blue and tin = black.

The average neutron scattering length of B-F-type CZTS is not influenced so much by the off-stoichiometry as the A-B-type and C-D-type CZTS compounds. One reason is that the off-stoichiometry is lower in the B-F-type CZTS in comparison to the Cu-rich / Zn-poor C-D-type CZTS. Another reason is the weaker impact of the B-F-type defect complexes on the average neutron scattering length in relation to the strong impact of the V_{Cu} defect of the A-B-type mixture CZTS compounds. Furthermore the changing Cu-Zn disorder exacerbates the identification of clear defect trends and the influence of the intrinsic point defect on the average neutron scattering length.

In Figure 3.47 some trends can be observed after the Cu-Zn disorder was deducted from the site occupation. An increasing Zn_{Cu} defect can be observed with increasing off-stoichiometry. Also for the Zn_{Sn} defect this trend can be observed. The Cu_i are not visible in Figure 3.47 due to their distribution on intermediate positions in the kesterite type structure. A more detailed analyses of the defects follows in the next chapter.

3.3.8 Conclusion

In Chapter 3.3 the cation distributions of various off-stoichiometric CZTS phases were successfully analyzed by the combination of neutron diffraction and the average neu-

tron scattering length method. The kesterite type structure was identified for all off-stoichiometry CZTS types which is in compliance with literature [15, 45, 74]. Furthermore the postulated defect complexes by Lafond et al. [45] and the newly introduced F-type [96] and E-type [29] of the different off-stoichiometric types were identified in accordance to the chemical composition of the synthesized CZTS samples. Also an increase with off-stoichiometry of the intrinsic point defects and the influence of the calculated type fractions on the cation distribution could be observed.

The location of the Cu_i inside the kesterite type structure was analyzed and in simulated patterns an influence on the Bragg reflex intensity could be observed. Unfortunately the small intensity changes disappear in the background noise of the experimental data and the used instrumental setup was not sensitive enough to detect these changes. Probably a different setup, a stronger focus on the identification of the Cu_i defects or another instrument, opens the possibility to identify the location of the Cu_i inside the crystal structure.

As a result of the evaluation of the intrinsic point defects in combination with their influence on the band gap [9] it could be shown why thin film solar cells using an kesterite type absorber with A-type composition produce devices with high efficiencies [1, 43, 97]. The off-stoichiometric Cu-poor / Zn-rich A-type defect complex $V_{Cu} + Zn_{Cu}$ introduced by the substitution of Cu slightly broadens the band gap whereas intrinsic point defects in the Cu-rich / Zn-poor region reduce the band gap. Especially Sn related intrinsic point defects are harmful for device efficiencies.

3.4 Defect concentrations

The defect concentration [defects/cm^3] was introduced to compare the amount of defects in different CZTS compounds. Therefore the defect concentration was derived from the calculated average neutron scattering length based on the cation distribution model. Furthermore the concentration of defects not distributed on a certain Wyckoff position (Cu$_i$) was calculated. Also the Cu-Zn disorder was determined to facilitate the comparison of various CZTS phases by an absolute value. Additionally the separation between the Zn$_{Cu}$ or Cu$_{Zn}$ off-stoichiometric type defects in the Zn-rich or Cu-rich CZTS were easier to discern.
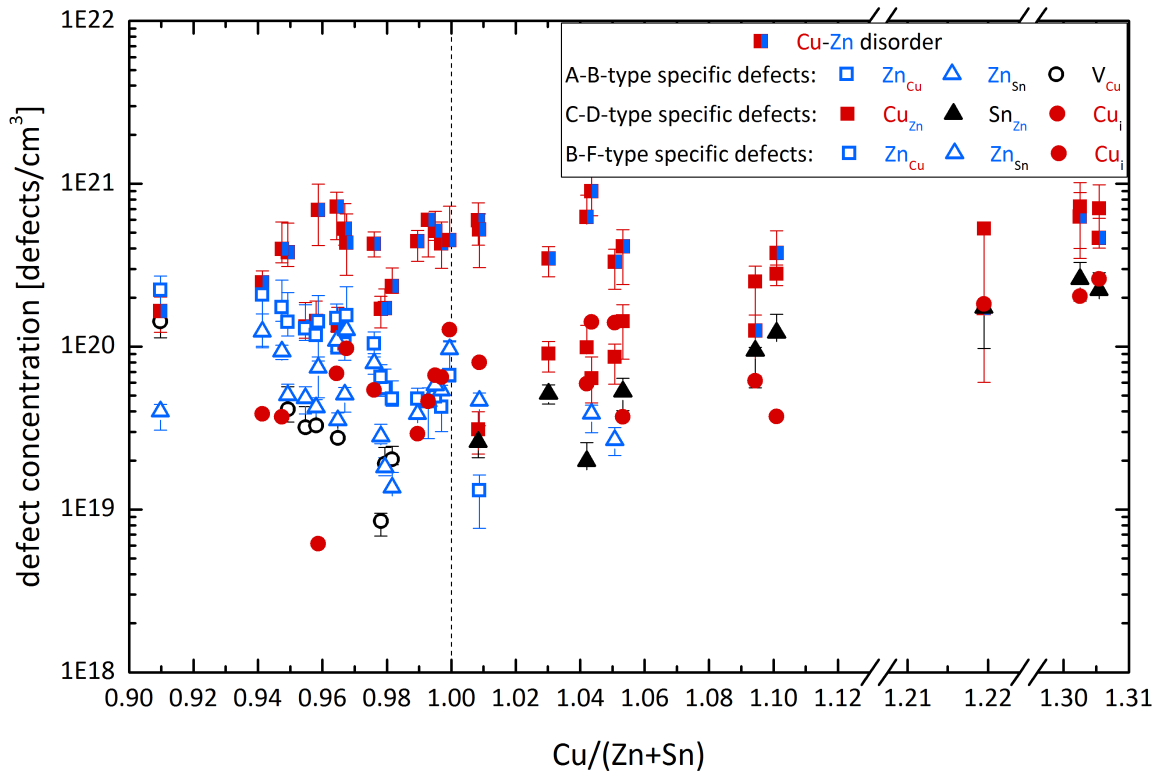
Figure 3.48: Overview of defect concentrations with Cu-Zn disorder = red-blue rectangle and off-stoichiometric type specific defects: A-B-type = Zn$_{Cu}$, Zn$_{Sn}$ and V$_{Cu}$, C-D-type = Cu$_{Zn}$, Sn$_{Zn}$ and Cu$_i$ and B-F-type = Zn$_{Cu}$ Zn$_{Sn}$ and Cu$_i$.

For 32 CZTS compounds a reliable cation distribution could be derived from the Rietveld analysis and the defect concentrations were calculated. Only for two CZTS phases no reliable cation site occupation could be derived due to strong errors mainly caused by the presence of vast amounts of secondary phases and the resulting overlap of reflexes of the CZTS phase.

Figure 3.48 presents an overview of the Cu-Zn disorder defect and off-stoichiometric type specific defects and their corresponding concentrations over the Cu / (Zn + Sn) ratio. Figure A.72 (page 170) shows the results with the Zn / Sn ratio. For the defects/cm^3 a logarithmic scale was used and to further improve the figure two breaks

were introduced in the Cu-rich / Zn-poor region. Due to the amount of CZTS compounds and only small chemical variations of some CZTS phases, especially near in the vicinity of stoichiometry, overlapping of data points is unavoidable.

Therefore the defect concentration will be separated by the synthesized off-stoichiometric types similar to the pattern used in the cation distribution chapter (Chapter 3.3). Furthermore the defects will be distinguished in off-stoichiometric type specific defects and the Cu-Zn disorder which occurs in all CZTS compounds.

3.4.1 Cu-poor / Zn-rich and Cu-rich / Zn-poor defect concentrations
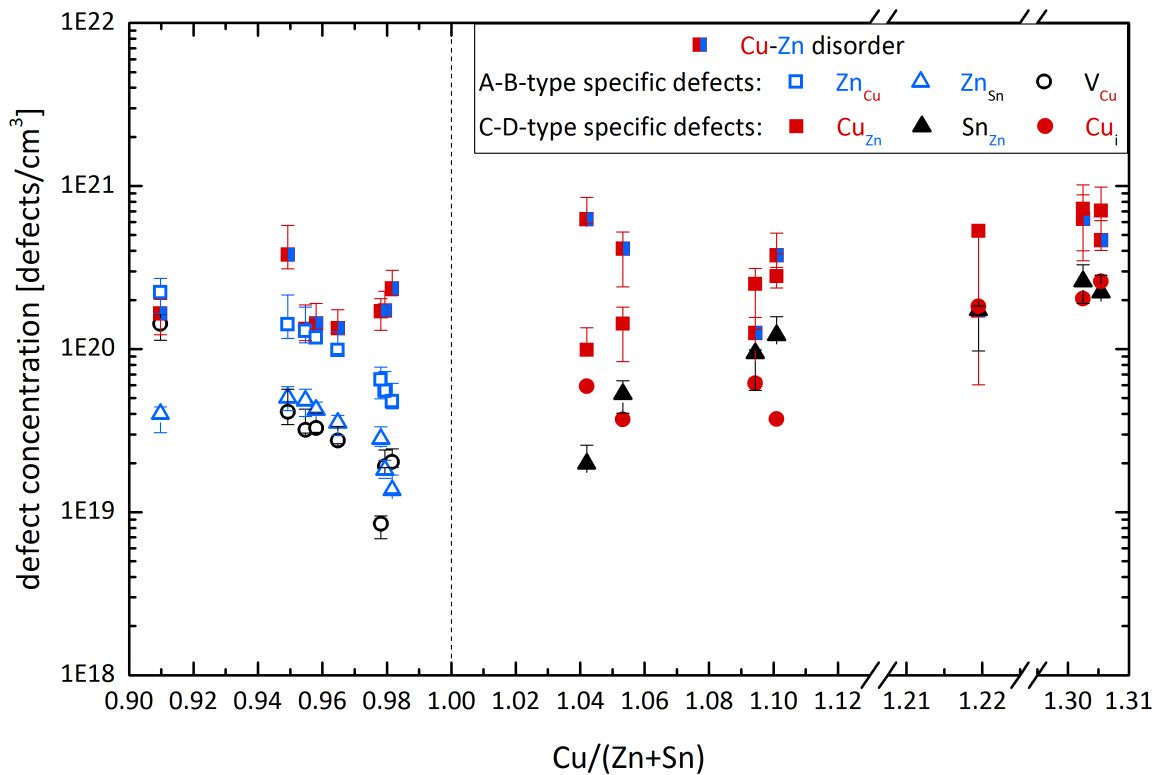
Figure 3.49: A-B- and C-D-type defect concentrations with unspecific Cu-Zn disorder = red-blue rectangle and type specific defects: A-B-type = Zn_{Cu}, Zn_{Sn} and V_{Cu} and C-D-type = Cu_{Zn}, Sn_{Zn} and Cu_i.

In contrast to the cation distribution results the Cu-poor / Zn-rich (A-B-type) and Cu-rich / Zn-poor (C-D-type) CZTS phases are presented together in Figure 3.49 and because of their inverse chemical composition no excessive data overlap was expected. Due to the opposed chemistry also the off-stoichiometric type specific defects are inverse. The A-B-type Cu-poor / Zn-rich CZTS phases are located in the region $Cu / (Zn + Sn)$ < 1 and the Cu-rich / Zn-poor C-D-type CZTS compounds in the region $Cu / (Zn + Sn)$ > 1 and are shown in Figure 3.49.

Zn_{Cu}, Zn_{Sn} and V_{Cu} are the type specific defects of the Cu-poor / Zn-rich CZTS whereas Cu_{Zn}, Sn_{Zn} and Cu_i are the type specific defects of the Cu-rich / Zn-poor CZTS compounds. Furthermore the Cu-Zn disorder is shown which is independent of the different off-stoichiometric types. The errors of the defect concentration were derived from the cation distribution results. Therefore the position of the calculated average neutron scattering length ($\bar{b}_x^{calc}$) in relation to the average neutron scattering length from the Rietveld refinement ($\bar{b}_x^{RR}$) was used and based on this position the error for the defect concentration was calculated.

The Cu-Zn disorder is in the same magnitude for almost all CZTS compounds. In average the Cu-Zn disorder is slightly higher for the Cu-rich / Zn-poor than for Cu-poor / Zn-rich CZTS. Furthermore the Cu-Zn disorder is the dominating defect complex with the highest defect concentration in the majority of the CZTS phases. Only in the most off-stoichiometric CZTS the concentration of the Cu-Zn disorder is below some type specific defects and also in one C-D-type CZTS with Cu / (Zn + Sn) = 1.094(19) and Cu / (Zn + Sn) = 0.864(12) a lower Cu-Zn disorder was observed. Probably slight deviations of parameters like the temperature, vapor pressure or elemental loss during the synthesis of the sample have caused the lower Cu-Zn disorder in comparison to the other CZTS phases. Only the type specific defects Zn_{Cu} of the A-B-type and the Cu_{Zn} of the C-D-type overpower the Cu-Zn disorder in the most off-stoichiometric CZTS. Also there was no direct correlation observed between the concentration of the Cu-Zn disorder and the Cu / (Zn + Sn) and Zn / Sn (see Figure 3.51, page 90) in the presented CZTS compounds.

Table 3.4: Type fractions of the analyzed A-B- and C-D-type compounds. The values of the type fractions are correlating well with the defect concentrations of CZTS.

No.	sample	$\dfrac{Cu}{Zn + Sn}$	err	$\dfrac{Zn}{Sn}$	err	type fraction			
31	A6020	0.982	0.017	1.024	0.014	A	27 %	B	73 %
29	E0030	0.979	0.017	1.030	0.015	A	21 %	B	79 %
30	E0040	0.978	0.017	1.039	0.015	A	7 %	B	93 %
6	A5010	0.965	0.017	1.055	0.015	A	16 %	B	84 %
26	A4050	0.958	0.017	1.066	0.015	A	16 %	B	84 %
8	A3020	0.955	0.017	1.073	0.015	A	14 %	B	86 %
22	A4000	0.949	0.016	1.079	0.015	A	17 %	B	83 %
33	A4020	0.910	0.016	1.098	0.016	A	47 %	B	53 %
25	A4040	1.042	0.018	0.956	0.014	D	43 %	C	57 %
28	E0020	1.053	0.018	0.921	0.013	D	15 %	C	85 %
2	A0100	1.094	0.019	0.864	0.012	D	14 %	C	86 %
27	E0010	1.101	0.019	0.838	0.012	D	7 %	C	93 %
3	A0050	1.220	0.021	0.735	0.010	D	22 %	C	78 %
4	A0025	1.305	0.022	0.659	0.010	D	24 %	C	76 %
5	A0000	1.303	0.023	0.635	0.009	D	18 %	C	82 %

A different trend can be observed for the off-stoichiometric type specific defects in CZTS. These are normally increasing with stronger off-stoichiometry. There seem to be some exceptions like the V_{Cu} which decreases in CZTS with $Cu/(Zn+Sn) = 0.978(17)$ and $Zn/Sn = 1.039(15)$ but this is related to the changing type fractions of the different CZTS phases. The influence of the type fractions (see Table 3.4) can not be seen in Figure 3.49. The mentioned CZTS has the lowest A-type fraction in comparison to the other CZTS phases and due to this small fraction the A-type specific V_{Cu} has a lower concentration. At the same time the B-type defects are stronger represented, especially the Zn_{Sn} defect, in comparison to the almost identical CZTS regarding the chemical composition ($Cu/(Zn+Sn) = 0.979(17)$ and $Cu/(Zn+Sn) = 1.030(15)$) with an A-type fraction of 21 % and the same amount Cu-Zn disorder.

The opposite change of the defect concentrations can be observed in the most off-stoichiometric A-B-type CZTS with $Cu/(Zn+Sn) = 0.910(16)$ and $Zn/Sn = 1.098(16)$. It has the highest fraction of A-type and therefore many V_{Cu} but the Zn_{Sn} B-type defect is lower than in other less off-stoichiometric CZTS phases. This influences off-stoichiometric type defects which belong to only one off-stoichiometric type. In contrast the Zn_{Cu} defect which can be found in the A- and B-type steadily increases with stronger off-stoichiometry. Furthermore the Zn_{Cu} defect has a higher concentration than the Cu-Zn disorder in the most off-stoichiometric A-B-type CZTS and also the V_{Cu} has a similar concentration as the Cu-Zn disorder.

The trend of the type specific defects of the Cu-rich/Zn-poor C-D-type CZTS phases is comparable to the Cu-poor/Zn-rich A-B-type CZTS. The Cu-rich/Zn-poor CZTS are spanning over a wider $Cu/(Zn+Sn)$ range than the Cu-poor/Zn-rich CZTS and are starting further from the stoichiometric composition. The Cu_{Zn}, Sn_{Zn} and Cu_i type defects are increasing with stronger off-stoichiometry. Some small variations are caused by slightly changing type fractions. This can be observed in the two most off-stoichiometric CZTS phases with $Cu/(Zn+Sn) = 1.303(23)$ and $Cu/(Zn+Sn) = 1.305(22)$. If the Zn/Sn ratios 0.635(9) and 0.659(10) are compared the strongest off-stoichiometric CZTS compound changes. The change is caused by the slightly different type fractions which are also reflected in the defect concentrations. The Sn_{Zn} defect dominates in CZTS where the C-type fraction is slightly higher and the Cu_i defect is more pronounced in CZTS where the D-type fraction rises. The deviations of the Cu_i are also correlating in the other CZTS compounds with decreasing or increasing D-type fraction.

In the three most off-stoichiometric CZTS phases the Cu_{Zn} defect has a higher concentration than the Cu-Zn disorder. The amount of CZTS where the type specific defects have a higher concentration is more pronounced for the Cu-rich/Zn-poor C-D-type CZTS due to stronger off-stoichiometry.

3.4.2 Defect concentrations of B-F-type CZTS

In comparison to the A-B- and C-D-type defect concentrations the B-F-type CZTS phases are not as off-stoichiometric and span only over a narrow $Cu/(Zn+Sn)$ ratio. The chemical change in Zn/Sn direction is stronger than the alteration in the $Cu/(Zn+Sn)$ ratio. Because of that the Zn/Sn ratio was used for Figure 3.50. All CZTS compounds have a Zn-rich/Sn-poor composition and are located in the region of $Zn/Sn > 1$.

Similar to A-B- and C-D-type CZTS the concentration of the Cu-Zn disorder is in the same magnitude for all B-F-type CZTS compounds. Due to the weaker off-stoichiometric composition, the type specific defects never overpower the Cu-Zn disorder defect complex. Also the trend of the Cu_i defects is similar to the Cu-Zn disorder and is relative constant over the Zn/Sn ratio. This can be explained by the location of the CZTS phases parallel to the B-type line and due to the path of the B- and F-type line the least off-stoichiometric CZTS with $Cu/(Zn+Sn) = 1.009(17)$ and $Zn/Sn = 1.034(15)$ has the strongest F-type influence (76 %). Whereas in the most off-stoichiometric CZTS with $Cu/(Zn+Sn) = 0.941(16)$ and $Zn/Sn = 1.152(16)$ the influence of the F-type is far smaller (9 %).
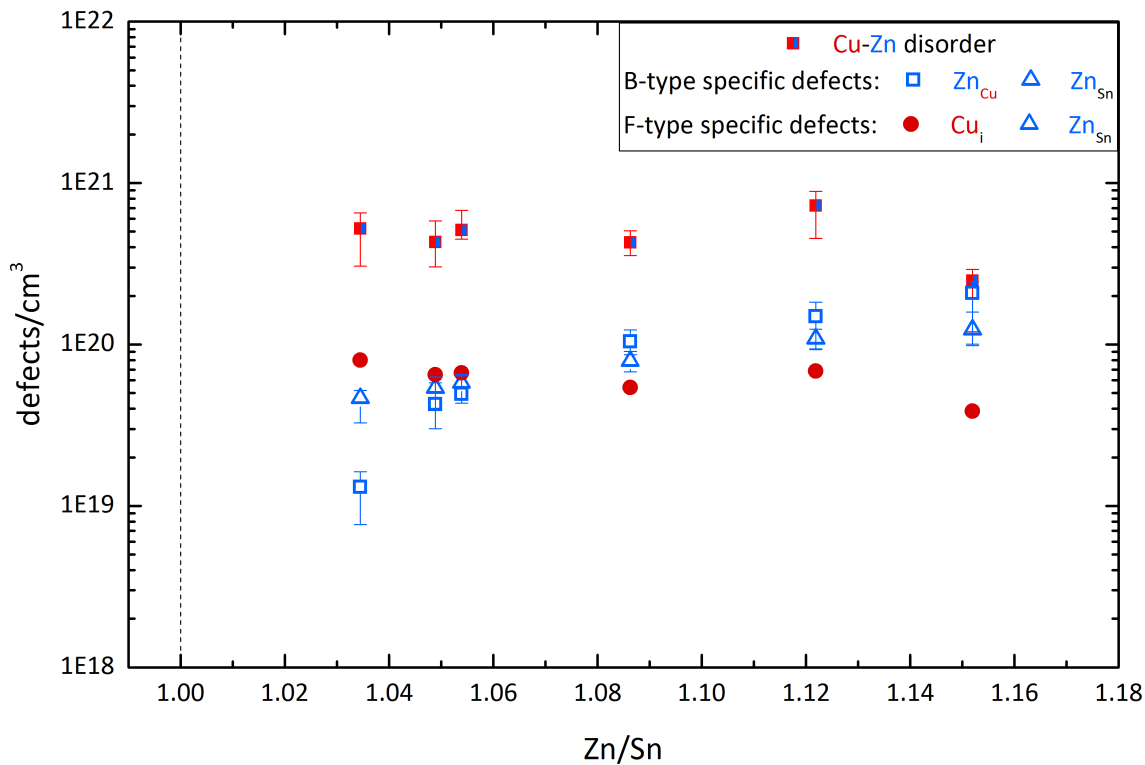
Figure 3.50: B-F-type defect concentrations with unspecific Cu-Zn disorder = red-blue rectangle and type specific B-F- type defects = Zn_{Cu}, Zn_{Sn} and Cu_i.

The path of the CZTS compounds can be seen in Figure 3.45 and the increasing B-type component correlates with the increasing Zn_{Cu} type defect with increasing off-stoichiometry. Also the Zn_{Sn} type defect concentration shows an increase with stronger

Table 3.5: Type fractions of the analyzed B-F-type CZTS.

No.	sample	$\dfrac{\text{Cu}}{\text{Zn} + \text{Sn}}$	err	$\dfrac{\text{Zn}}{\text{Sn}}$	err	type fraction			
17	D0010	1.009	0.017	1.034	0.015	B	24 %	F	76 %
13	B2000	0.997	0.017	1.049	0.015	B	57 %	F	43 %
16	B1000	0.995	0.017	1.054	0.015	B	59 %	F	41 %
24	A4030	0.993	0.017	1.045	0.015	B	66 %	F	34 %
14	B2010	0.976	0.017	1.086	0.015	B	79 %	F	21 %
15	B2020	0.964	0.017	1.122	0.016	B	81 %	F	19 %
11	A2000	0.941	0.016	1.152	0.016	B	91 %	F	9 %

off-stoichiometry. Due to the higher F-type fraction in the less off-stoichiometric CZTS compounds the defect concentration of Zn_{Sn} is higher than the Zn_{Cu} defect. All type fractions and cation ratios are presented in Table 3.5.

3.4.3 Cu-Zn disorder

Until now the Cu-Zn disorder was not analyzed for all CZTS compounds and the defect concentration was given in separated $\text{Cu} / (\text{Zn} + \text{Sn})$ and Zn / Sn plots. To gain more insight on the Cu-Zn disorder distribution over the chemical range, a contour plot as shown for the lattice parameters in Chapter 3.2 was used. Furthermore the Cu-Zn disorder was converted in % and 50 % Cu and 50 % Zn occupying the 2c(Cu) and 2d(Zn) position correspond to a completely disordered CZTS. The maximum value of the Cu-Zn disorder will be given as 50 % and not as 100 % which would sum the values of the 2c(Cu) and 2d(Zn) position.

The range of Cu-Zn disorder reaches in Figure 3.51 from 4 % to 28 %. The results of the Cu-Zn disorder results do not show a distinct trend in correlation with the chemical composition as the tetragonal deformation (see Figure 3.25, page 59) or unit cell volume (see Figure 3.26, page 60). The A-B-type CZTS compounds seem to have the lowest Cu-Zn disorder. B-F-type CZTS phases have a higher Cu-Zn disorder especially near stoichiometry whereas the strongest off-stoichiometric CZTS compounds exhibit a similar Cu-Zn disorder as the A-B-type CZTS. The highest Cu-Zn disorder of all CZTS compound was observed in the F-D-type CZTS, of these only two samples were synthesized which are not enough for reliable conclusions.

In the C-D-type CZTS the Cu-Zn disorder near the stoichiometric composition is similar to the B-F-type CZTS. With increasing off-stoichiometry the Cu-Zn disorder decreases to same level as the A-B-type CZTS only to increase with the two most off-stoichiometric CZTS compounds. In literature [67, 81, 93] the Cu-Zn disorder is strongly connected to the cooling rate and only below the critical temperature the ordering starts, which corresponds to a decrease of the Cu-Zn disorder (see Chapter 1.3). The cooling rates of all samples were $10\,\text{K}\,\text{h}^{-1}$ or $50\,\text{K}\,\text{h}^{-1}$. The results of the CZTS phases with the same cooling rate should be comparable. Unfortunately the Cu-Zn disorder
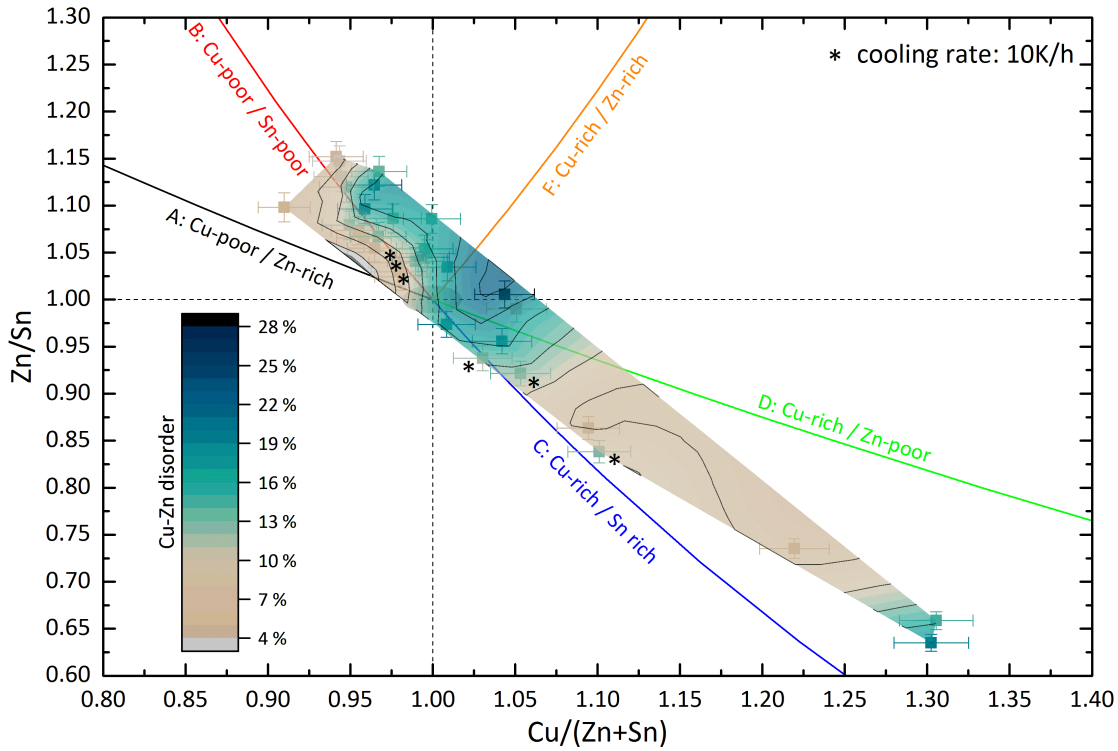
Figure 3.51: Countour plot of the Cu-Zn disorder of the CZTS phase.

does not correlate with cooling rate as presented in Figure 3.51. Hence additional parameters must influence the Cu-Zn disorder. Potential impacts on the Cu-Zn disorder are the secondary phases formed, the varying vapor pressure during the synthesis or the different off-stoichiometric types. There exists no final solution at the moment because also a combination of all parameters could change the Cu-Zn disorder and further investigations are necessary to ascertain the dominating effect.

Rey et al. [67], Scragg et al. [81] and Többens et al. [93] describe a temperature dependency of a structure-based quantitative order-disorder parameter. A lower Cu-Zn disorder can probably achieved if an additional step in the temperature program would be introduced regarding the critical temperature of the order-disorder transition [81, 93].

3.4.4 Conclusion

The results of the off-stoichiometric type defect concentration show a dependence of the chemical composition which is represented by the Cu / (Zn + Sn) or Zn / Sn ratios. Furthermore the defect concentrations [defects/cm^3] of the Cu-Zn disorder were included which are independent of chemical changes but in a similar magnitude in all analyzed CZTS compounds. The Cu-Zn disorder is also the dominating defect complex in the majority of CZTS compounds. Only in the most off-stoichiometric CZTS

phases and in one other exception, the off-stoichiometric type specific defects overpower the defect concentration of the Cu-Zn disorder. Also deviations from increasing off-stoichiometric type defect concentrations with increasing off-stoichiometry are in direct correlation with the varying type fractions of the CZTS compounds. The observed intrinsic point defects in the kesterite type structure and the derived defect concentrations in the CZTS compounds are not directly corresponding to electronic active defects. The average neutron scattering length method can only identify intrinsic point defects and the resulting defect concentrations in the crystal structure, but cannot distinguish electronic active from inactive defects.

3.5 Cu-Zn disorder by anomalous X-ray diffraction

The Cu-Zn disorder is a strongly discussed topic in the kesterite community [67, 81, 92]. Neutron data results of the analyzed CZTS compounds have shown that the Cu-Zn disorder is varying even in CZTS using the same synthesis parameters (temperature and cooling rate). To verify the results from neutron diffraction, anomalous X-ray diffraction experiments were conducted. The evaluation of the anomalous X-ray diffraction data is extensive and therefore limited to two CZTS phases. Currently the method is constricted to analyze only the Cu-Zn disorder. In principle it is expandable to also derive the distribution of Sn.

3.5.1 B-type CZTS $Cu_{1.97}Zn_{1.05}Sn_{0.98}S_4$

For the first analysis a single-phase B-type CZTS with $Cu / (Zn + Sn) = 0.967(17)$ and $Zn / Sn = 1.067(15)$ was selected to exclude as many interfering parameters as possible. In total ten different energies were measured and full pattern Rietveld refinement was conducted. The patterns of the anomalous X-ray diffraction are shown in Figure 3.52 and magnified in Figure 3.53. The signal to noise ratio is excellent due to good measurement conditions which is prerequisite for a reliable data analysis. All patterns of the different energies were normalized to the *112* reflex to be able to compare intensity changes. These intensity changes can be easily observed in Figure 3.53. Furthermore the measured Q-space increases with higher energies or decreasing wavelengths.

Normally an increase of the background noise can be observe behind the Cu-K-edge of 8979 eV due to occurrence of Cu fluorescence. In Figure 3.52 this slight increase can be observed, but due to the normalization the effect is attenuated. The measurements before and after the Cu-K-edge can easily be separated by the start of the patterns. All diffraction patterns before the Cu-K-edge start with a decreasing background and all after the Cu-K-edge with an increasing background.

In Figure 3.53 a zoomed plot of the first three reflexes *002*, *101* and *110* is presented which shows the changing intensities of these reflexes at different energies. These changes are influenced by the Cu and Zn occupations on the 2c(Cu) and 2d(Zn) position. The changes of the *101* reflex are stronger pronounced than for the *002* and *110* reflex. To compare the reflexes from different energies and to see at which energy the intensity is increasing or decreasing Figure 3.54 was introduced. Therefore the reflexes of the different energies were aligned and normalized to the *112* reflex. The *101* reflex exhibits the strongest change and the intensity increases significantly from 8048 eV to 8974 eV which is near the Cu-K-edge, whereas the intensity of the reflexes after the Cu-K-edge are back to the level at 8048 eV. This indicates a strong influence of Cu on the *101* reflex and this observation is supported by energies moving near the Zn-K-edge (9376 eV to 9654 eV) were no intensity changes are observed.

The *110* reflex exhibits different intensity changes. Here the intensity slightly increases near the Cu-K-edge 8979 eV but greatly increases near the Zn-K-edge 9659 eV which indicates a Zn dominated reflex. In further reflexes similar intensity changes were
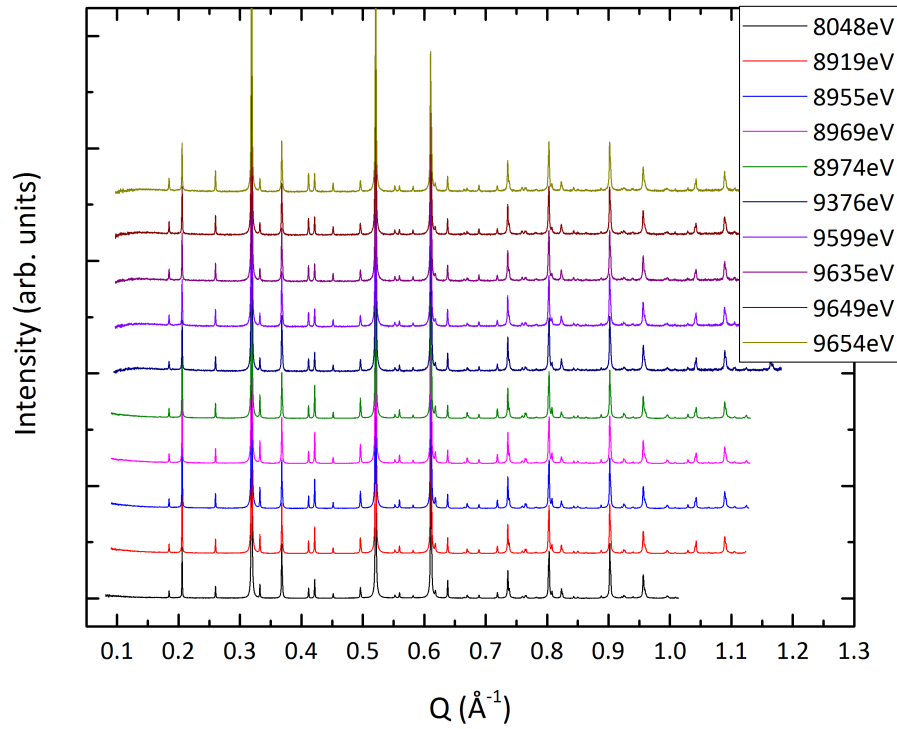
Figure 3.52: Anomalous X-ray diffraction patterns of B-type CZTS with $Cu / (Zn + Sn) = 0.967(17)$ and $Zn / Sn = 1.067(15)$ measured at ten different energies.
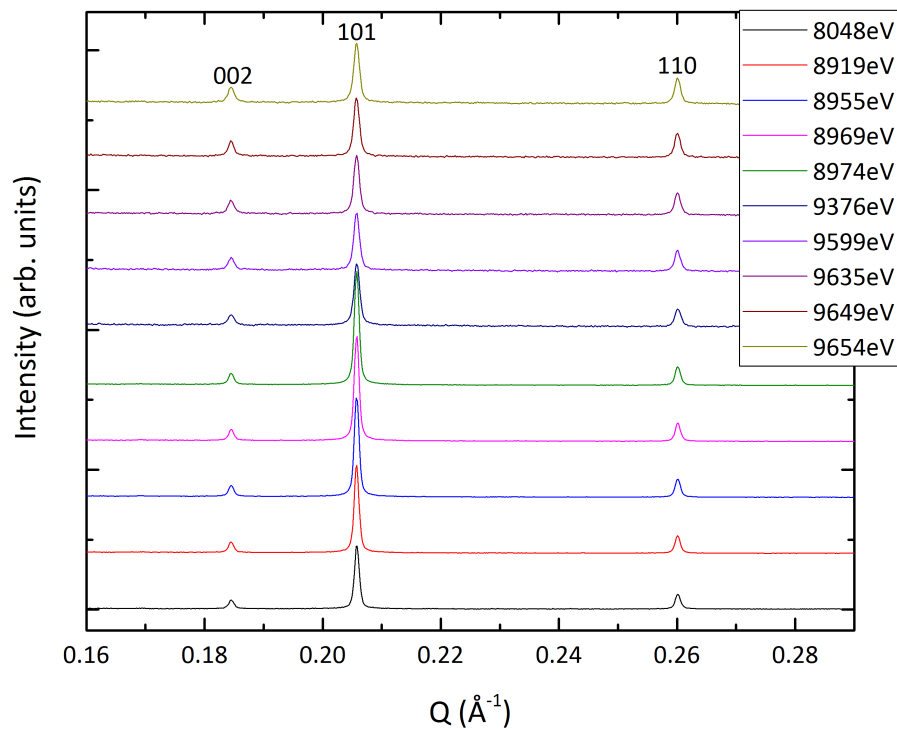
Figure 3.53: Anomalous X-ray diffraction patterns of B-type CZTS (Cu-poor / Zn-rich) with $Cu / (Zn + Sn) = 0.967(17)$ and $Zn / Sn = 1.067(15) = 1.067(15)$ with the region of the *002*, *101* and *110* Bragg reflexes magnified.

observed and by applying the Rietveld refinement, described in Chapter 2.2.4, the Cu
and Zn occupation of the 2c(Cu) and 2d(Zn) position was obtained of these alterations.
The calculations for the relative intensities for the *002* and *101* reflexes were shown
by Nozaki et al. [56] but were used to distinguish kesterite and stannite type structure
and not the Cu-Zn disorder.

a) *002*   **b)** *101*   **c)** *110*
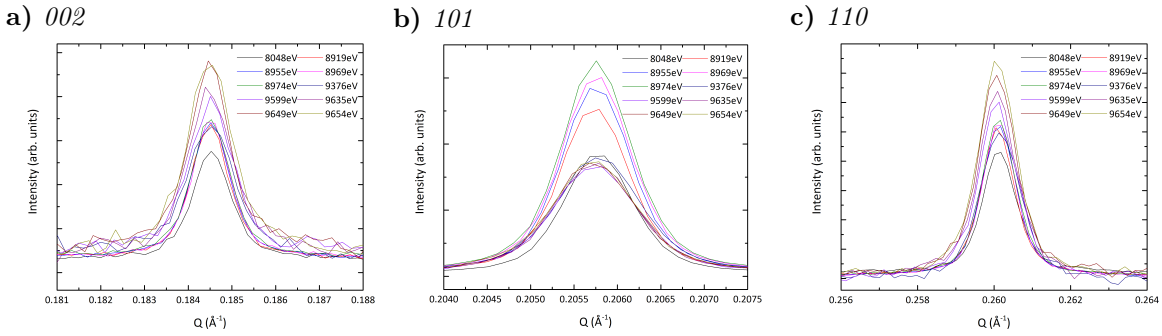
Figure 3.54: Overview of the *002*, *101* and *110* reflexes with all different energies aligned.
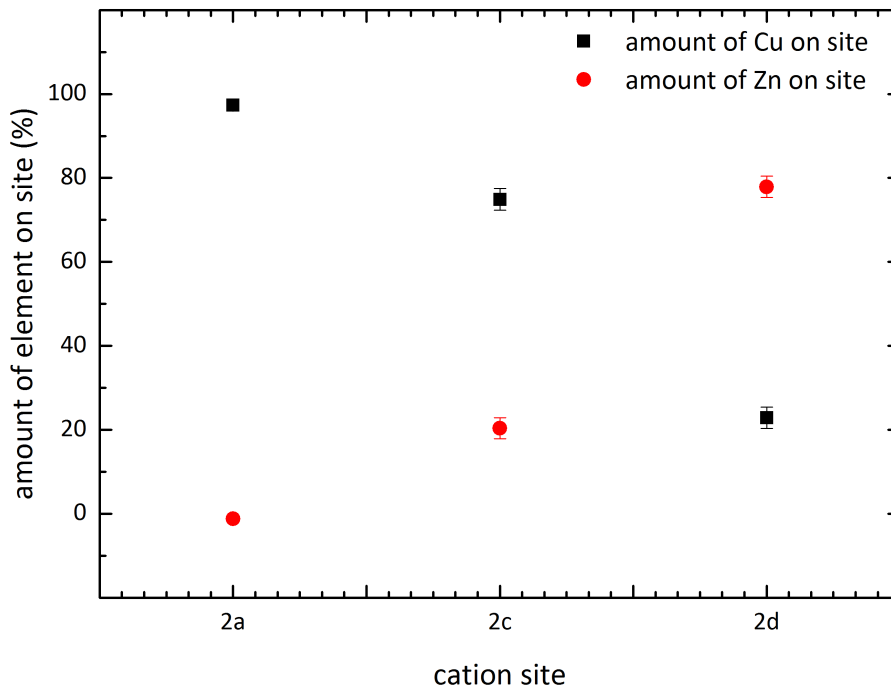
Figure 3.55: B-type CZTS cation distribution anomalous X-ray diffraction following the
layout of the neutron data without the 2b(Sn) position. The black rectan-
gles present the Cu and the red circles the Zn on the corresponding Wyckoff
position.

The Rietveld refinement allows to combine all intensity changes of the Bragg reflexes
and results in occupation values for the 2a(Cu), 2c(Cu) and 2d(Zn) positions. By ap-

plying the described method in Chapter 2.2.3, the final site occupation values for Zn_{Cu} and Cu_{Zn} can be extracted and are presented in Figure 3.55. The cation distribution results of the anomalous X-ray diffraction show a fully Cu occupied 2a(Cu) position which is in perfect agreement with the neutron diffraction results. Furthermore a Cu occupation of 80 % and Zn 20 % on the 2c(Cu) and 80 % Zn and 20 % Cu on the 2d(Zn) position was observed which corresponds to 20 % Cu-Zn disorder. Also this result is in good agreement with the neutron diffraction results which give 17 % Cu-Zn disorder. The CZTS compound is slightly Sn-poor (< 1) therefore a reliable evaluation of 2b(Sn) position was possible because all Sn is located on the 2b(Sn) position. The refined site occupation of all ten measured energies was averaged and the resulting occupation of 0.973 corresponds well to the electron micro probe analyzer results of 0.984 and to the neutron diffraction results of 0.989 considering the error. Also in the neutron diffraction results the Zn_{Sn} contributes to the occupation whereas the other values only give the pure Sn occupation. In conclusion all results are in very good agreement and support the quality of used methods.

3.5.2 B-F-type CZTS $Cu_{1.98}Zn_{1.06}Sn_{0.98}S_4$

A second CZTS exhibiting B-F-type composition with a $Cu / (Zn + Sn) = 0.976(17)$ and $Zn / Sn = 1.086(15)$ ratio was analyzed and compared with the neutron diffraction results. The CZTS compound also shows no secondary phases and has a similar chemical composition as the pure B-type CZTS. The anomalous X-ray diffraction patterns measured for ten different energies are presented in Figure 3.56 and Figure 3.57. Similar intensity changes as in the pure B-type CZTS can be observed which corresponds to the similar chemical composition of the CZTS compounds. Also the Bragg reflexes *002*, *101* and *110* in Figure 3.57 show the same trends as observed in B-type CZTS.

The most pronounced difference between the two CZTS compounds is the peak shape which gives sharp and expected Bragg reflexes for the pure B-type CZTS and slightly tilted reflexes for the B-F-type CZTS. These differences had no real impact on the quality factors of the Rietveld analysis and if the origin of the peak shape was introduced by the sample or the instrument setup could not be resolved.

The cation distribution result of the anomalous X-ray diffraction in Figure 3.58 indicates that the 2a(Cu) Wyckoff position is fully occupied by Cu which is in agreement with the neutron diffraction results, whereas the 2c(Cu) and 2d(Zn) Wyckoff position exhibit a mixed site occupation of Cu and Zn. The 2c(Cu) position shows around 70 % Cu and 30 % Zn and the 2d(Zn) position around 75 % Zn and 25 % Cu. There is a slight deviation between the 2c(Cu) and 2d(Zn) occupation which is mainly caused by the type specific Zn_{Cu} defect. Also the error of the cation distribution can have an influence which is normally around 5 % but often underestimated by the refinement software. The same effect can also be observed in the pure B-type CZTS but is more pronounced in the B-F-type CZTS. Both CZTS phases are strongly B-type influenced and so the Zn occupation is slightly higher on the 2c(Cu) than the Cu occupation on the 2d(Zn) position due to the Zn_{Cu} defect. However the main goal was to estimate the Cu-Zn disorder and therefore the small influence of the Zn_{Cu} defect was neglected. In
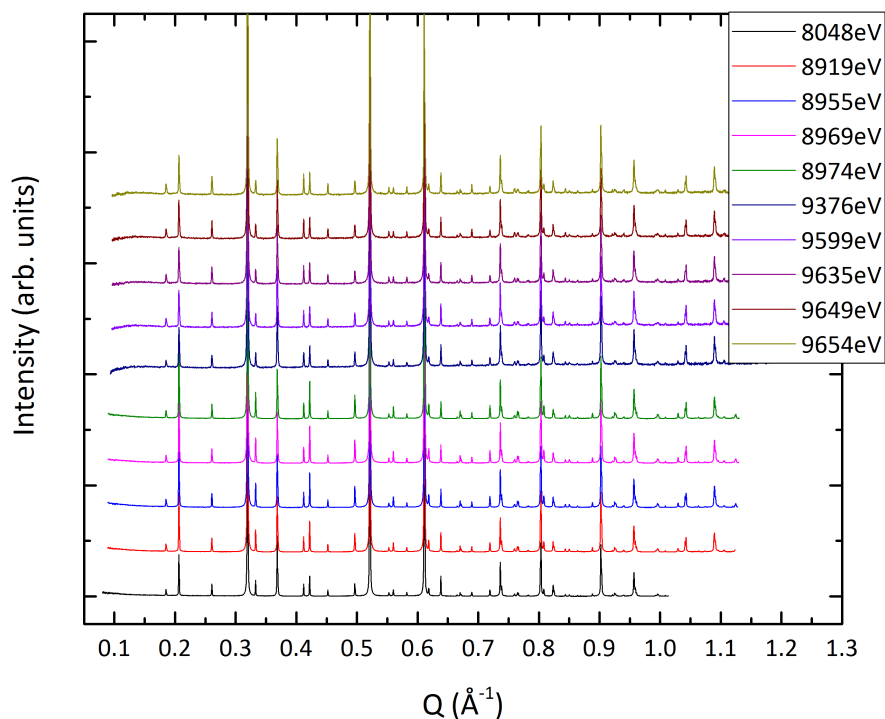
Figure 3.56: Anomalous X-ray diffraction patterns of B-F-type CZTS (Cu-poor / Zn-rich) with Cu / (Zn + Sn) = 0.976(17) and Zn / Sn = 1.086(15) ratio measured at ten different energies.
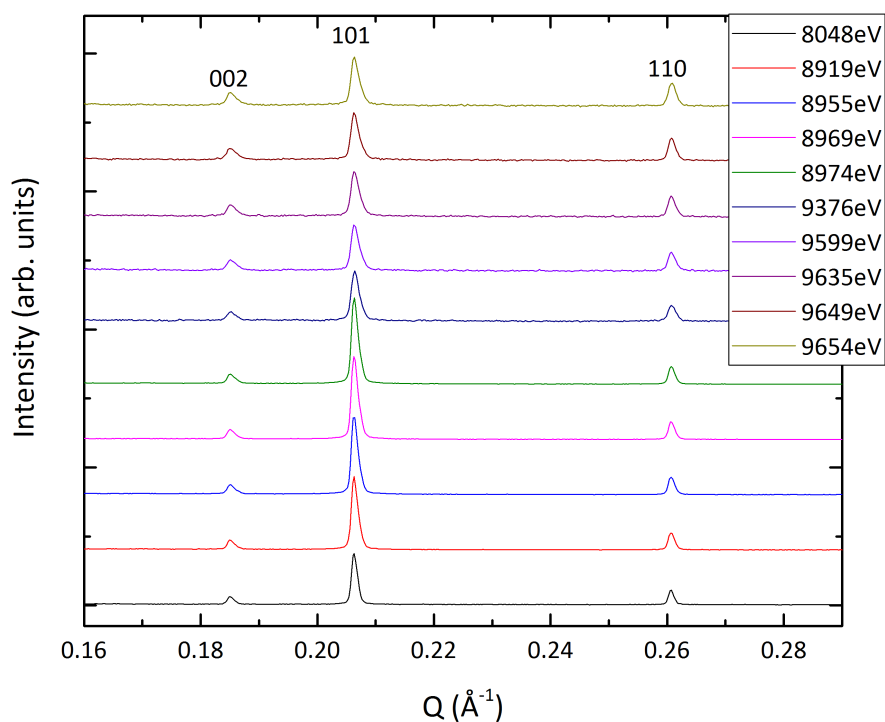
Figure 3.57: Anomalous X-ray diffraction patterns of B-type CZTS (Cu-poor / Zn-rich) with Cu / (Zn + Sn) = 0.976(17) and Zn / Sn = 1.086(15) ratio with the region of the *002*, *101* and *110* Bragg reflexes magnified.

principle it should be possible to deduce the cation distribution for the Cu-Zn disorder and also for off-stoichiometric type specific defects from anomalous X-ray diffraction. Currently the evaluation of the experimental data is more sophisticated and especially when Sn needs to be introduced more unreliable than the combination of neutron diffraction and the average neutron scattering length method [73].
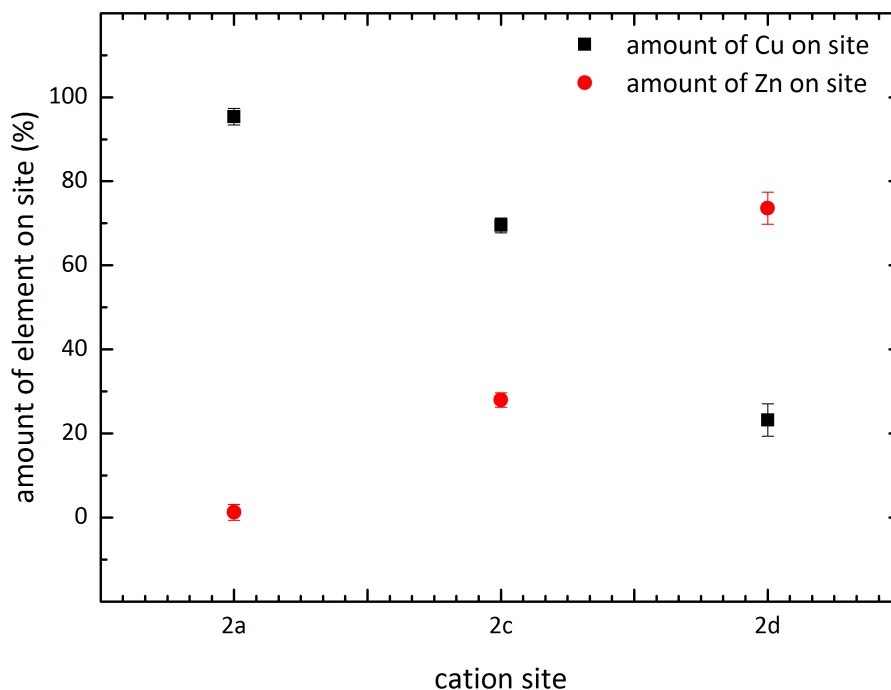
Figure 3.58: Anomalous X-ray diffraction B-F-type CZTS cation distribution following the layout of the neutron data without the 2b(Sn) position. The black rectangles present the Cu and the red circles the Zn on the corresponding Wyckoff position.

When Sn > 1 the additional Sn needs to be distributed on a different Wyckoff position and not only on 2b(Sn) position. As already mentioned in a previous chapter the Sn will normally be incorporated on the 2d(Zn) position. This also influences the Rietveld refinement and the results become more unreliable. Due to the influence of the third element (Sn) on a Wyckoff position the anomalous X-ray diffraction was limited to slightly Sn-poor CZTS compounds.

Around 25 % Cu-Zn disorder were observed by anomalous X-ray diffraction whereas only 15 % were observed by neutron diffraction. Due to the underestimated error of the anomalous X-ray diffraction and the error of the neutron diffraction, the Cu-Zn disorder results are still in good agreement. Probably the tilted peak shape had an influence on the results which was not reflected by the quality factors of the Rietveld refinement. Also the different sample volume analyzed by anomalous X-ray diffraction and neutron diffraction could have an impact on the Cu-Zn disorder results.

The average Sn occupation deduced from the anomalous X-ray diffraction corresponds to 0.978 Sn on the 2b(Sn) position which is in good agreement to the 0.975 amount of Sn measured by electron micro probe analyzer. The neutron diffraction results show a higher occupied position of 1.001 because also the Zn_{Sn} is included. Overall the anomalous X-ray diffraction results of the B-f-type and pure B-type CZTS phases are in good agreement with neutron diffraction.

3.5.3 Conclusion

In the previous chapter the anomalous X-ray diffraction, an alternative to the neutron diffraction, was tested to distinguish the cation distributions in off-stoichiometric CZTS. The anomalous X-ray diffraction allows to distinguish isoelectronic elements like Cu^+ and Zn^{2+} and overcomes the limits of traditional laboratory X-ray powder diffraction. Due to the possibility to differentiate isoelectronic elements, the Cu-Zn disorder was successfully determined in two off-stoichiometric CZTS samples and the results are in good agreement with neutron diffraction results. At the moment there are still limitations if Sn > 1 which prevents anomalous X-ray diffraction to replace neutron diffraction as the preferred method. Currently the evaluation of the experimental data of the neutron diffraction is faster and more accessible compared to the anomalous X-ray diffraction.

3.6 Bond distances and bond angles

From the Rietveld analysis some further parameters are obtainable which allow a deeper insight into the structure, like the bond distance and bond angles. Furthermore the bond distance can also be calculated from the cation distribution model (see Chapter 3.3). In Figure 3.59 the sulfur tetrahedron is illustrated with all four bonds to the 2a(Cu), 2b(Sn), 2c(Cu) and 2d(Zn) Wyckoff position. In total six different bond angles are possible (atom1-sulfur-atom2) which were extracted from the Rietveld refinement and always the obtuse angle, in a tetrahedron also called the tetrahedral angle, was selected.
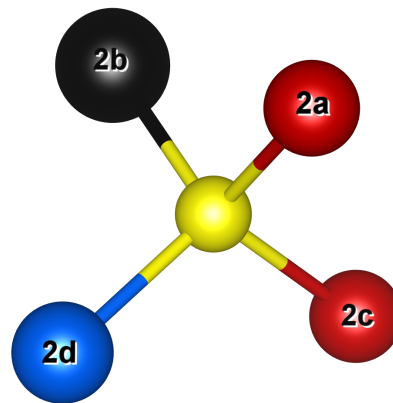
Figure 3.59: Sulfur tetrahedron with 2a(Cu) = red, 2c(Cu) = red, 2d(Zn) = blue, 2b(Sn) = black and in the center 8g(S) = yellow.

3.6.1 Bond distance calculation and experimental correlation

First the focus lies on the evaluation of the bond distances. Therefore only the results of the A-, B-, C- and D-type CZTS compounds are included in Figure 3.60 and Figure 3.61. Figure 3.60 shows the calculated bond distance results of the cation distribution data and average neutron scattering length method whereas Figure 3.61 presents the bond distances extracted from the Rietveld refinement.

The obtained data will be compared to the simulation results by Persson [61] who used the relativistic FPLAPW method and Gürel et al. [28] who used the density functional perturbation theory (DFPT). In contrast to the experimental off-stoichiometric CZTS the calculations were only conducted for stoichiometric CZTS. In Figure 3.60 and Figure 3.61 the simulated data was extended over the whole $Cu / (Zn + Sn)$ range and will be represented by different lines. The difference of the simulation results of Persson [61] and Gürel et al. [28] was considered as the error for the bond distances of the cation distribution and the Rietveld refinement. Therefore no additional errors for the bond distances were used. Especially the error of Rietveld refinement results would be strongly underestimated and would correspond to the size of the data symbols.

Before the calculation of the bond distances from the cation distribution reliable ion radii for the several elements forming CZTS are needed. Shannon [85] provides a comprehensive data source for various elements and their different valence states and all values were gathered for sulfur compounds which coincides well with the bond distance calculation of off-stoichiometric CZTS. The values for $Cu^+ = 0.635\,Å$, $Zn^{2+} = 0.640\,Å$, $Sn^{4+} = 0.690\,Å$ and $S^{2-} = 1.700\,Å$ were used for the calculations.
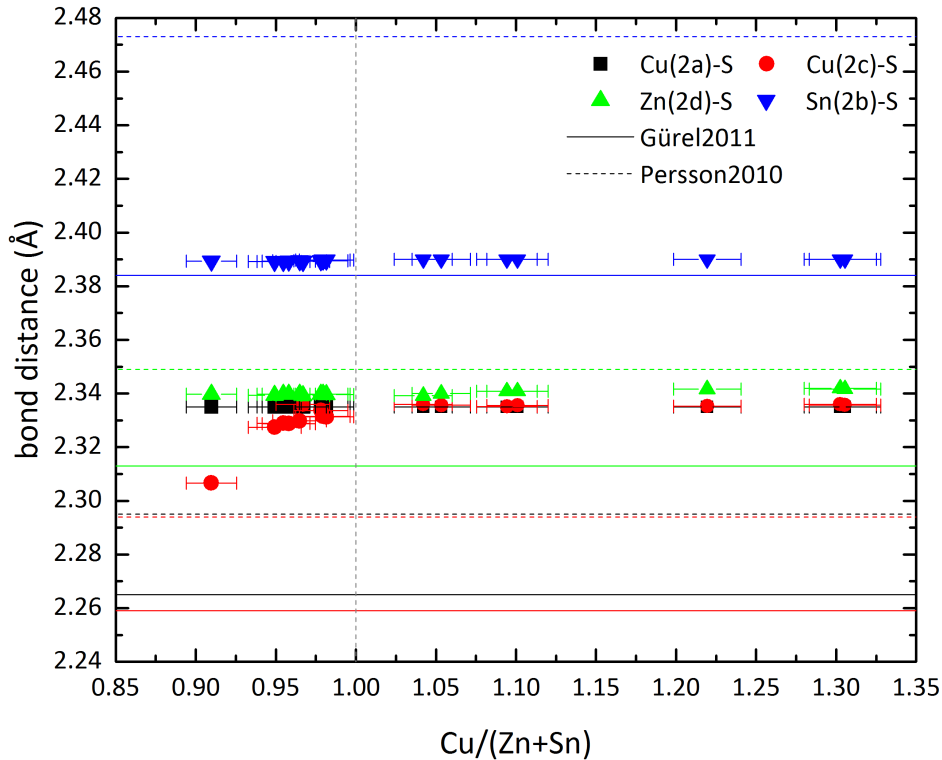
Figure 3.60: Cation-anion bond distances derived from the neutron cation distribution model vs. $Cu\,/\,(Zn + Sn)$. The data points correspond to $2a(Cu)$ = black, $2c(Cu)$ = red, $2d(Zn)$ = green and $2b(Sn)$ = blue and the solid line to Gürel et al. [28] and the dashed line to Persson [61].

The results of the calculation of the bond distances from the cation distribution deviate from the simulated data of Persson [61] and Gürel et al. [28]. There are significant differences between the elements and their correlation with the simulated data. Bond distances to the $2b(Sn)$ position of the CZTS compounds show only slight variations and they are located on a horizontal line. Only minor changes were expected because just small amounts of Zn occupy the $2b(Sn)$ position and the values are located near the simulated value by Gürel et al. [28], whereas Persson [61] results deviate almost $0.1\,Å$. For the $2d(Zn)$ position also no significant changes for the calculated values were expected because of the similar cation radii of $Cu^+ = 0.635\,Å$ and $Zn^{2+} = 0.640\,Å$ [85]. A small increase of the bond distances to Cu-rich / Zn-poor composition can be observed. In contrast to the $2b(Sn)$ position the results of $2d(Zn)$ are in better

agreement with the values of Persson [61]. The calculated bond distances are situated between both simulation results and considering the determined error also Gürel et al. [28] results correlate.

The bond distances of the 2a(Cu) and 2c(Cu) positions show a different progression. Especially in the $Cu / (Zn + Sn) < 1$ region the influence of the V_{Cu} defect identified by the neutron diffraction becomes visible which causes a decreasing bond distance on the 2c(Cu) position with increasing Cu-poor / Zn-rich composition, whereas the fully Cu occupied 2a(Cu) position bond distances are located on a line at $2.335 \, \text{Å}$. Also in the simulated results the 2a(Cu) and 2c(Cu) bond distances are located together similar to the calculated results but have $0.04 \, \text{Å}$ shorter bond distances. The value nearest to the simulated bond distances by Gürel et al. [28] corresponds to the most off-stoichiometric Cu-poor / Zn-rich CZTS.
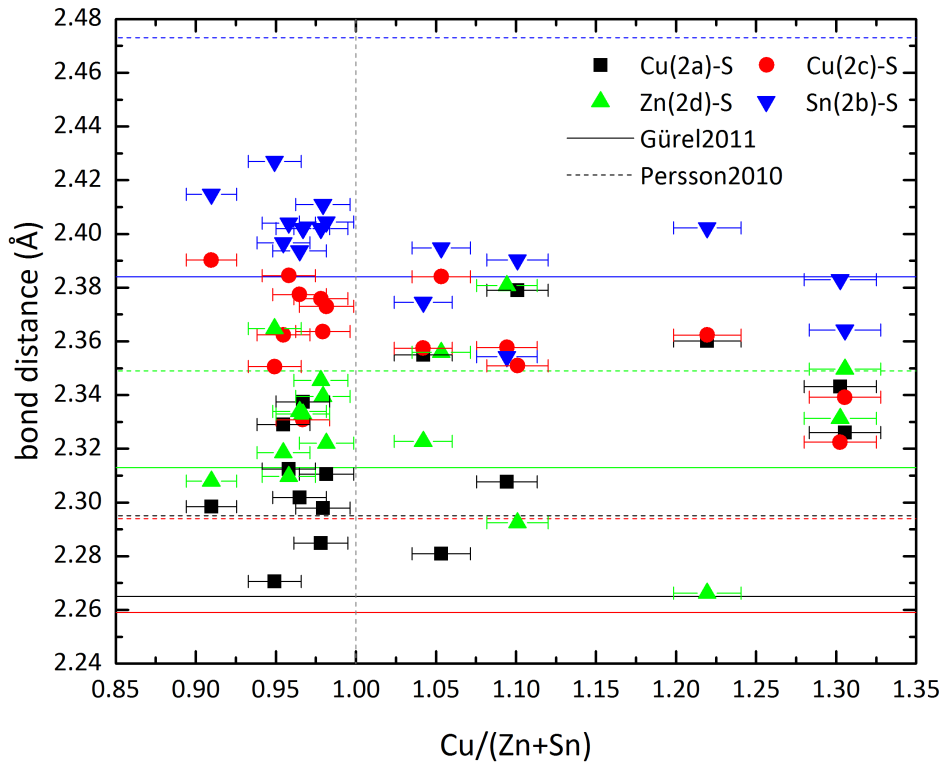
Figure 3.61: Cation-anion bond distances derived from vs. the $Cu / (Zn + Sn)$. The data points correspond to 2a(Cu) = black, 2c(Cu) = red, 2d(Zn) = green and 2b(Sn) = blue and the solid line to Gürel et al. [28] and the dashed line to Persson [61].

Deviations of the simulated and calculated bond distances are probably caused by not considering the chemical environment for the calculated values. Additionally the simulations were only conducted for stoichiometric composition and would change if

off-stoichiometry is introduced. Furthermore the ion radii were published without an error by Shannon [85].

In contrast to the bond distances of the neutron cation distribution the results of the Rietveld refinement consider the chemical environment. In Figure 3.61 the results of the Rietveld analysis are presented and in comparison to Figure 3.60 the values of the 2a(Cu), 2c(Cu), 2d(Zn) and 2b(Sn) position show stronger variations.

The Sn-S bond distances are near the simulated values by Gürel et al. [28] and also correspond well with the bond distances of the neutron cation distribution results. The stronger scattering of the values is caused by the Rietveld refinement due to the refinement of multiple parameters which induce correlations that are reflected by stronger deviations and errors.

Also the majority of the bond distances of the 2d(Zn) position correlates with the simulated data by Gürel et al. [28] and Persson [61] and especially overlaps in slight Cu-poor / Zn-rich conditions with the results of the neutron cation distribution model. Only few values deviate strongly. Unfortunately no real trend or pattern for the cause of the changes can be identified and more investigations are necessary.

The bond distances of the Rietveld results of the 2a(Cu) position are located partly between the simulated values of Gürel et al. [28] and Persson [61] and are lower than the bond distances of the neutron cation distribution. In contrast the bond distances of the 2c(Cu) position are higher and show an opposing trend to the neutron results because the strongest Cu-poor / Zn-rich CZTS has the highest bond distance. Furthermore a trend with decreasing bond distances to Cu-rich / Zn-poor conditions can be observed. If this is caused by the defect complexes and the resulting chemical environment can not be proven. Therefore detailed simulations of off-stoichiometric CZTS samples are needed and further investigations of the influence of off-stoichiometry on the bond distance are necessary.

Furthermore in Figure 3.62 the cation-anion bond distances derived from the Rietveld refinement (colored symbols) are correlated with the results of the neutron cation distribution model (colored lines). The results of the Sn(2b)-S (blue) bond distances of both models are in good agreement. Also for the Zn(2d)-S values near stoichiometry and for the strong off-stoichiometric Cu-rich / Zn-poor CZTS compounds a good agreement with the two models can be observed. The strongest deviations similar to observations in Figure 3.61 are observed for Cu(2a)-S and Cu(2c)-S bond distances. The best agreement between the two models can be observed in the strong off-stoichiometric Cu-rich / Zn-poor region. There Cu(2a)-S and Cu(2c)-S of the cation-anion bond distances derived from the Rietveld refinement and of the neutron cation distribution model are coinciding well. Also two CZTS phases near stoichiometry show similar results. The strong deviation of some bond distances could be connected to the unreliable anion position of the CZTS phase derived from the Rietveld refinement. A shifted anion position has a direct impact on the bond distance.

In Figure 3.63 the bond distances of all evaluated CZTS compounds are introduced in the cation ratio plot. This leads to a better separation of the CZTS phases. In total four different figures for the possible bond distances were introduced. The bond
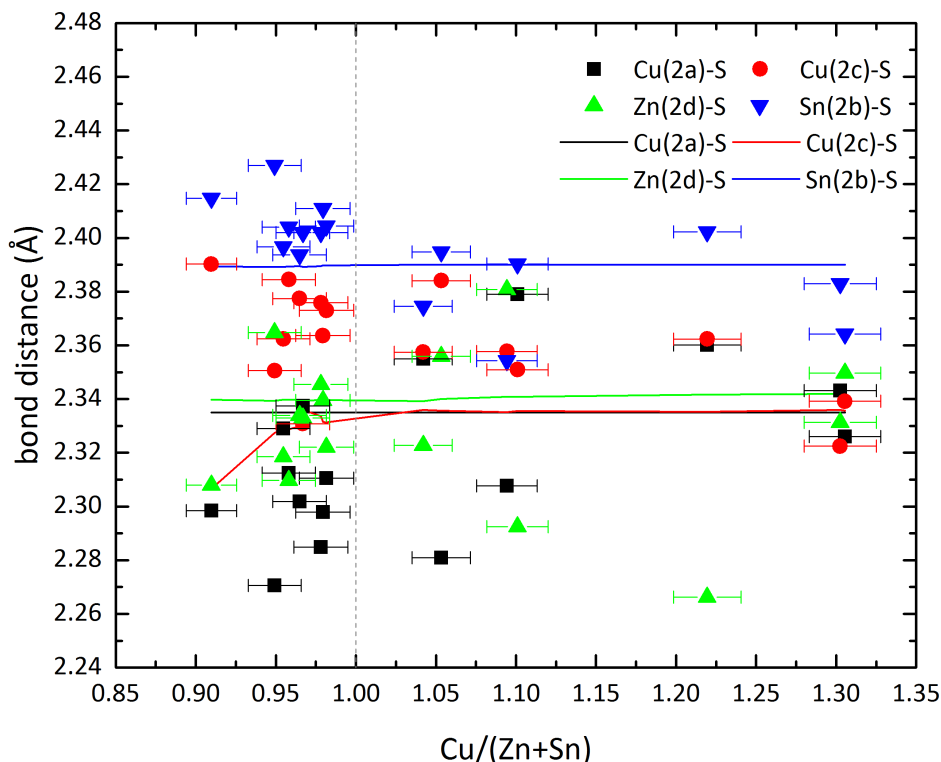
Figure 3.62: Cation-anion bond distances derived from the Rietveld refinement vs. the Cu / (Zn + Sn). The data points correspond to 2a(Cu) = black, 2c(Cu) = red, 2d(Zn) = green and 2b(Sn) = blue and the solid lines to the cation-anion bond distances derived from the neutron cation distribution model.

distances are uniformly distributed with some minima and maxima under all chemical conditions. A clear correlation with the chemical composition as in the tetragonal deformation or unit cell volume is not apparent. This can be mainly ascribed to the varying temperature factors of the Rietveld analysis and can be avoided by applying low temperature measurements.

3.6.2 Bond angles

The last structural parameters more deeply analyzed are the bond angles and in total six different angles of the sulfur tetrahedron can be obtained from the Rietveld refinement: Cu(2a)-S-Cu(2c), Cu(2a)-S-Zn(2d), Cu(2a)-S-Sn(2b), Cu(2c)-S-Zn(2d), Cu(2c)-S-Sn(2b) and Zn(2d)-S-Sn(2b). From these six angles always the obtuse angle was taken which corresponds to the tetrahedral angle in a tetrahedron. In an ideal tetrahedron this angle conforms to 109.4712°, due to structural changes the tetrahedron can be distorted and the tetrahedral angle deviates from the ideal value. Because of the
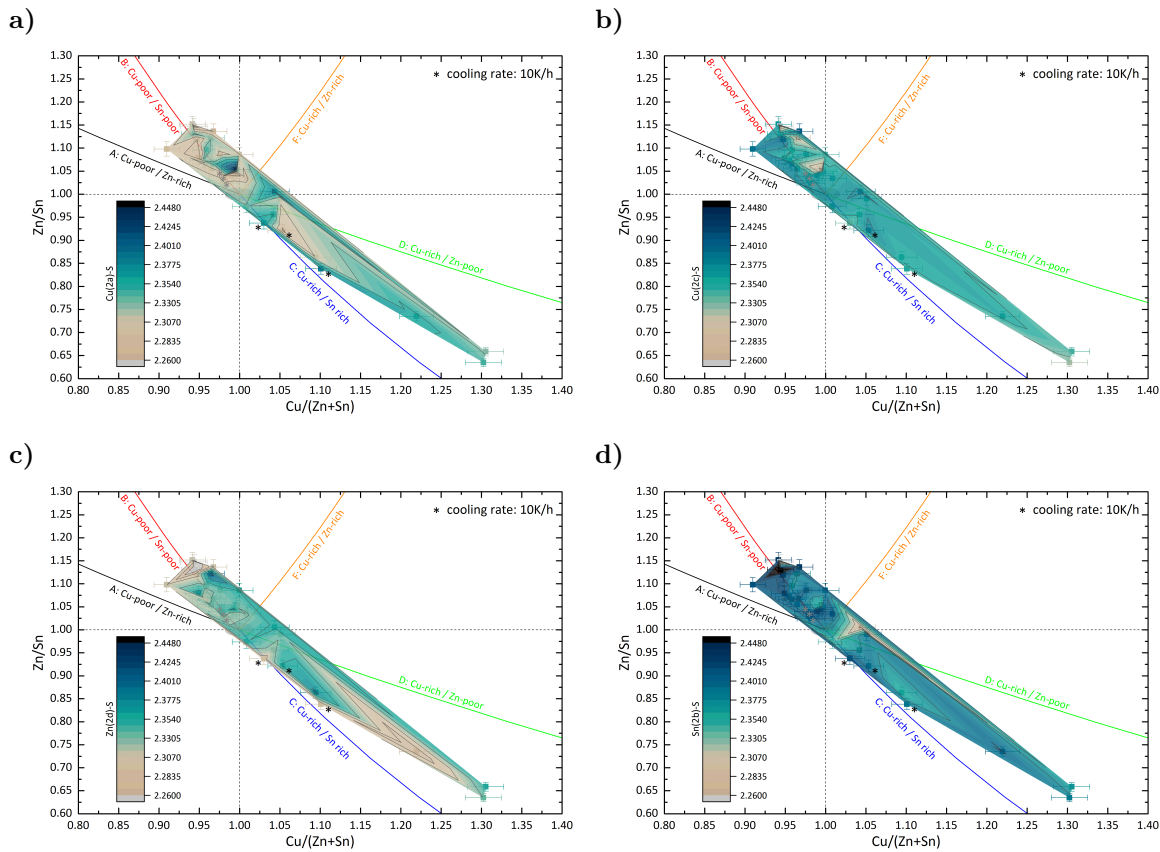
Figure 3.63: Contour plot of bond distances vs. cation ratio plot a) 2a(Cu)–S, b) 2c(Cu)–S, c) 2d(Zn)–S and d) 2b(Sn)–S.

importance of the tetrahedral angle it was included in Figure 3.64 which presents an overview of all six angles for the A-B- and C-D-type CZTS compounds.

In Figure 3.64 the bond angles are marked by different colors and the two off-stoichiometric types by distinct symbols. All analyzed CZTS compounds have a distorted tetrahedron and that the bond angles are similar over the whole $Cu/(Zn+Sn)$ range. Only two exceptions are detectable. The most off-stoichiometric Cu-poor / Zn-rich CZTS seems to have the strongest distorted tetrahedron whereas the most off-stoichiometric Cu-rich / Zn-poor CZTS compounds show the lowest distortion. The maximum deviation from the tetrahedral angle complies to 3° and was found at 113° for the Cu(2a)-S-Zn(2d) and at 106° for the Cu(2c)-S-Sn(2b) angle. These values seem to decrease from Cu-poor / Zn-rich to Cu-rich / Zn-poor conditions. No similar trends can be observed for the other bond angles. In the vicinity of stoichiometric composition the CZTS phases with Cu-poor / Zn-rich composition, the Cu(2a)-S-Sn(2b) and Cu(2c)-S-Zn(2d) angles are close to the ideal value of the tetrahedral angle.

In Figure 3.65 the bond angles were introduced in the cation ratio plot as a contour to check if relations between bond angles and the $Cu/(Zn+Sn)$ or Zn/Sn exist. In contrast to the previous bond angle figures all evaluated samples are present. Figure 3.65 is separated in six figures which represent all possible bond angles. Due to
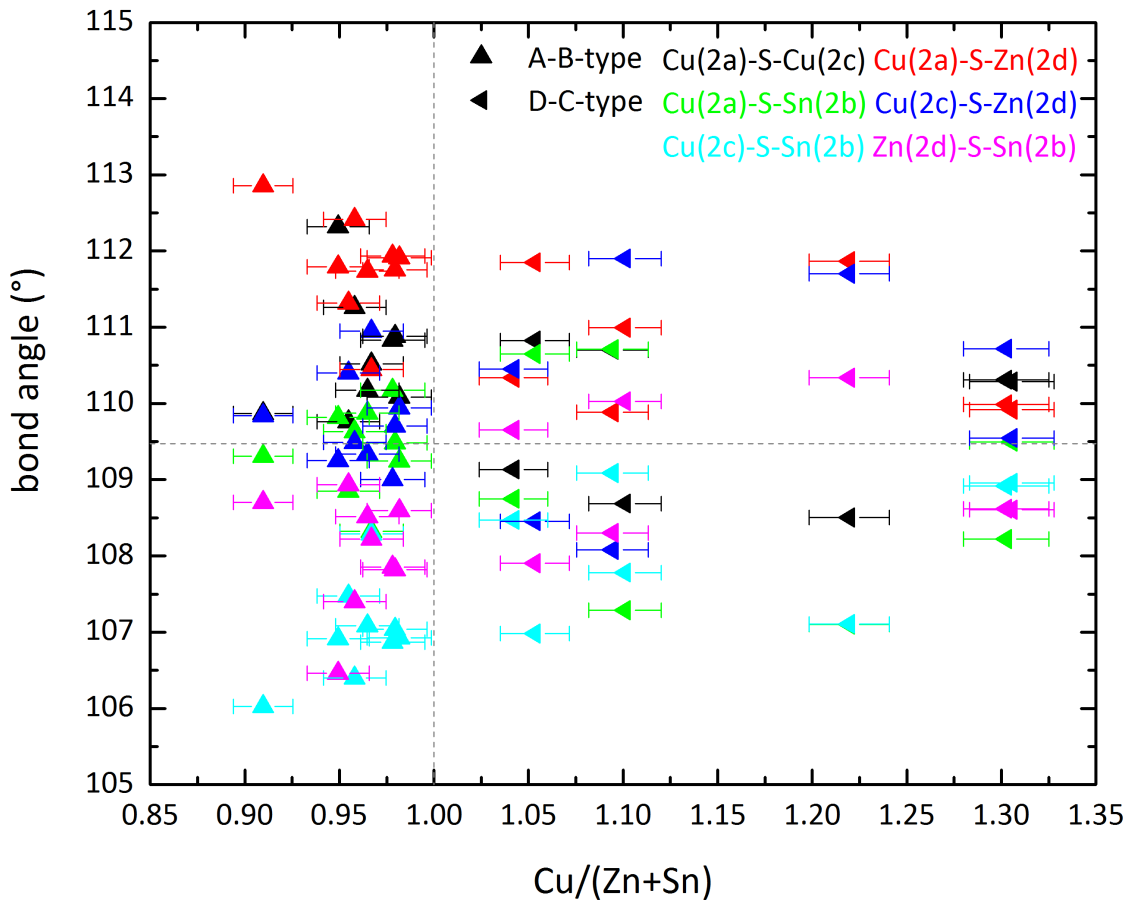
Figure 3.64: Bond angles vs. Cu / (Zn + Sn) of A-B- and C-D-type CZTS phases: Cu(2a)-S-Cu(2c) = black, Cu(2a)-S-Zn(2d) = red, Cu(2a)-S-Sn(2b) = green, Cu(2c)-S-Zn(2d) = blue, Cu(2c)-S-Sn(2b) = cyan and Zn(2d)-S-Sn(2b) = magenta.

the contour plot minima and maxima are easily distinguishable. Unfortunately also this manner of representation does not show any clear trends or correlation with the chemical composition or Cu-Zn disorder Figure 3.51 (page 90).

Overall the results deviate too much to extract reliable trends from the bond angles. Probably due to the six possible bond angles and the resulting correlations during the Rietveld refinement no reliable values are possible. An increase of the evaluated CZTS phases could lead to stronger trends or by measuring at lower temperature the significance of the bond angles could be achieved. Another consideration is, that a direct correlation of the bond angles with the chemical composition does not exist.

3.6.3 Conclusion

The bond distances and angles give a deeper insight in the kesterite type structure. Unfortunately only simulated values of the bond distance of stoichiometric CZTS by Gürel et al. [28] and Persson [61] were published but no values for the bond angles.
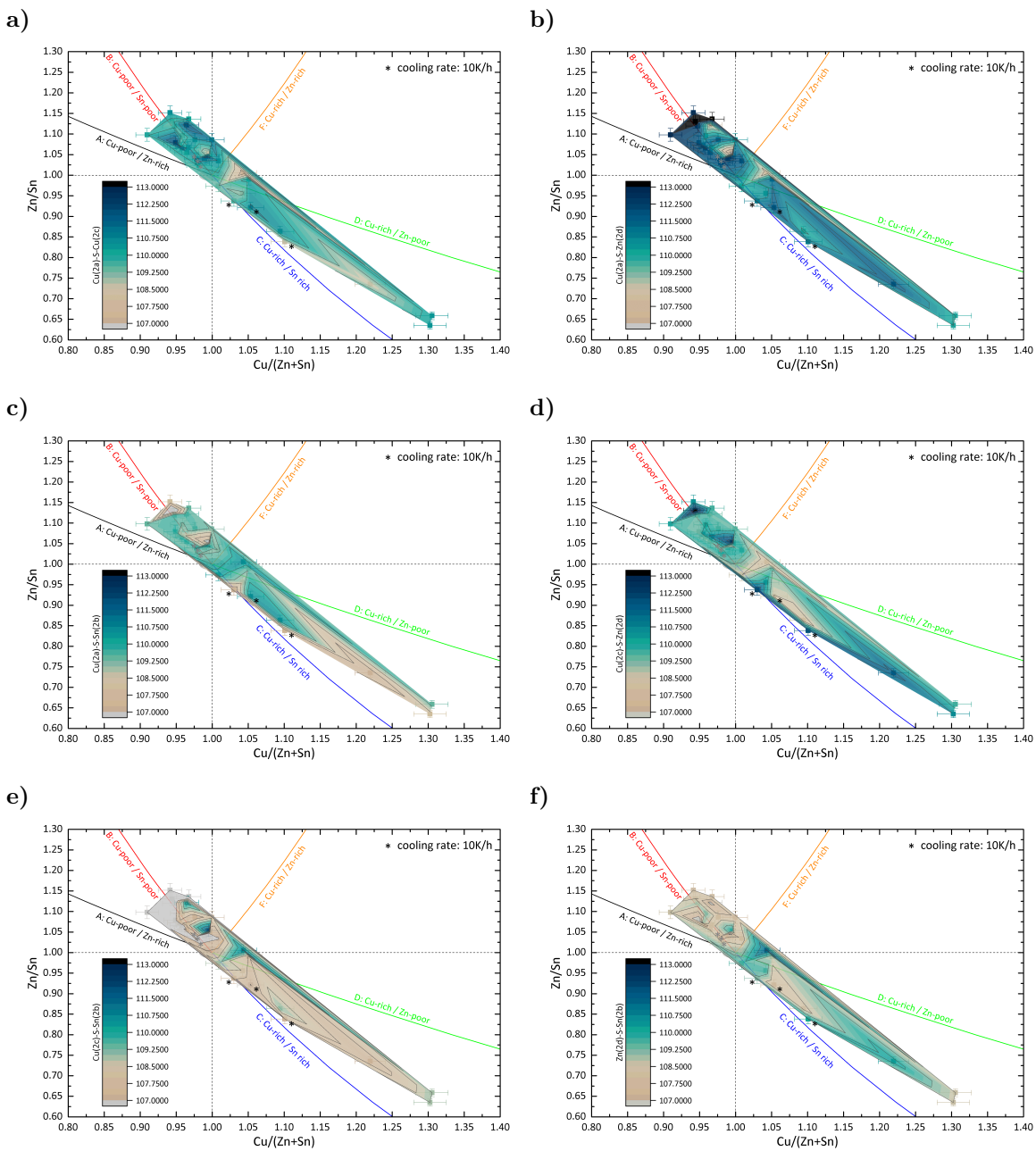
Figure 3.65: Contour plot of bond distances vs. cation ratio plot a) Cu(2a)-S-Cu(2c), b) Cu(2a)-S-Zn(2d), c) Cu(2a)-S-Sn(2b), d) Cu(2c)-S-Zn(2d), e) Cu(2c)-S-Sn(2b) and f) Zn(2d)-S-Sn(2b)

Therefore the tetrahedral angle was used as a comparison for the experimental bond angles. The bond distances of the cation distribution and Rietveld refinement results are in good agreement for the 2b(Sn) and Zn(2d) position. The bond distances of 2a(Cu) and 2c(Cu) deviate stronger which is probably caused by comparing stoichiometric with off-stoichiometric CZTS. Also in the results of the cation distribution no chemical environment is considered. Furthermore the impact of correlating parameters during the refinement can cause deviations. The results of the bond angles are strongly scattered and no clear correlation was observed except that all off-stoichiometric CZTS compounds have distorted S tetrahedrons. Probably a more specialized technique should be applied to increase the understanding of the obtained results.

3.7 Electrical resistivity and conductivity CZTS analyses results
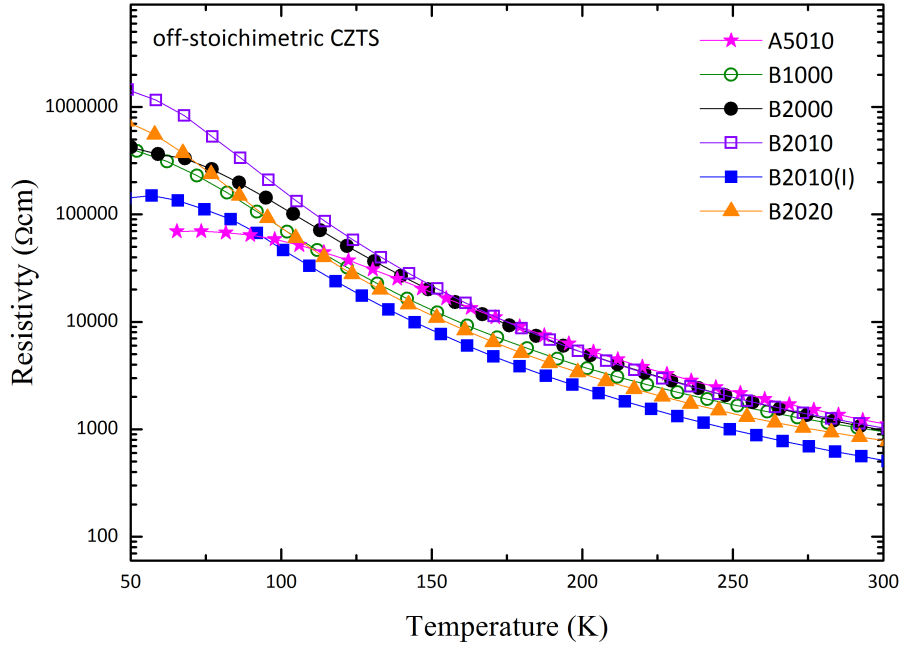
Figure 3.66: Temperature dependence resistivity of CZTS: A5010 = A-B-type and B1000, B2000, B2010, B2010(I) and B2020 = B-F-type [31].

The results of the electrical resistivity and conductivity analyses were conducted by the Institute of Applied Physics at the Academy of Sciences of Moldova. The results are presented in Figure 3.66. More details can be found in literature [31].

Due to very high resistivity at low temperatures of several CZTS compounds, reliable data were only obtained in the range from 50 K to 300 K. In total six CZTS compounds were analyzed, whereas B2010 and B2010(I) are the same CZTS compound, once pressed as a pellet and once as an annealed peace of a pellet after the synthesis [31].

Table 3.6: Overview of obtained electrical resistivity and conductivity parameters [31].

sample	$\dfrac{\text{Cu}}{\text{Zn + Sn}}$	err	$\dfrac{\text{Zn}}{\text{Sn}}$	err	type fraction		dT (K)	T_{04} (K)	W (meV)	N/N_c	a/a_B
A5010	0.965	0.017	1.055	0.015	A 16 %	B 84 %	176 − 265	2.05×10^7	190	0.168	1.201
B2000	0.997	0.017	1.049	0.015	B 57 %	F 43 %	138 − 272	2.42×10^7	202	0.157	1.186
B2010	0.976	0.017	1.086	0.015	B 79 %	F 21 %	118 − 222	3.13×10^7	185	0.124	1.142
B1000	0.995	0.017	1.054	0.015	B 59 %	F 41 %	118 − 212	1.72×10^7	154	0.163	1.195
B2020	0.964	0.017	1.122	0.016	B 81 %	F 19 %	99 − 216	1.91×10^7	161	0.157	1.186
B2010(I)	0.976	0.017	1.086	0.015	B 79 %	F 21 %	138 − 253	1.95×10^7	182	0.168	1.201

Figure 3.66 shows that the values of the resistivity of the CZTS compounds do not change much and the behavior throughout the temperature range is the same for all

investigated CZTS compounds. There are small variations as expected due to the low off-stoichiometry of the CZTS phases with similar chemical compositions. Furthermore it was observed that the resistivity decreases with increasing temperature from 50 K to 300 K. This observation implies that conductivity for the investigated CZTS compounds has an activation character. Also several regions with different slopes can be distinguished. By analyzing the slope of the plotted data it is possible to extract the transport mechanism of the electrons and some further parameters (see Figure 3.67 and Table 3.6) [31].
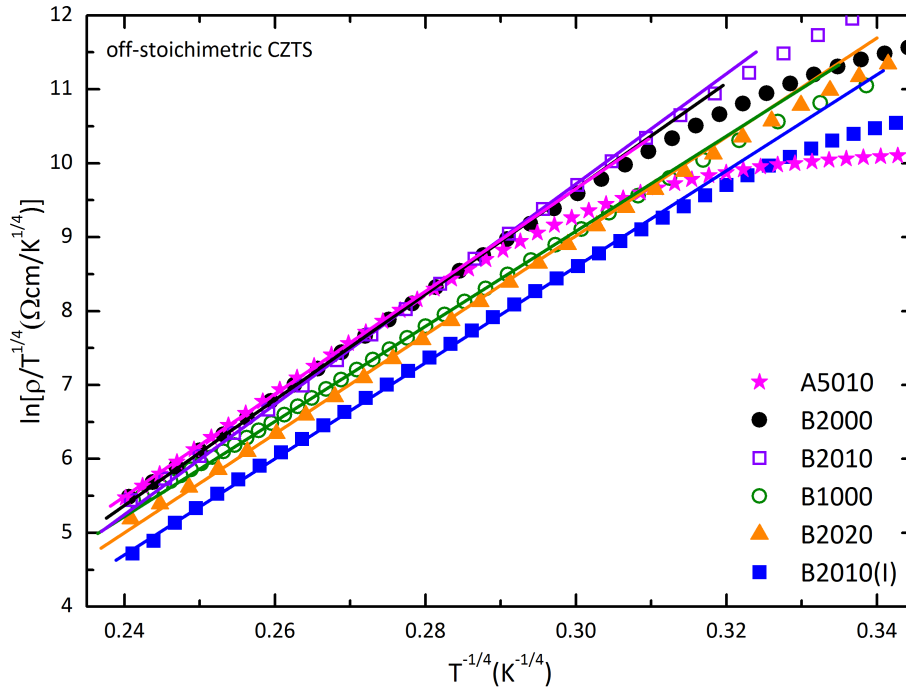
Figure 3.67: Overview of analyzed electrical resistivity and conductivity measurement data: red line = model, magenta star = A5010, black circle = B2000, violet rectangle =B2010, green circle = B1000, orange triangle = B2020 and blue rectangle = B2010(I) [31].

The data in Figure 3.67 could be linear fitted by applying the factor for Mott variable hopping (Mott VRH) in Equation 2.14 [31]. The fitted lines represent the Mott VRH conductivity region. The Mott VRH conductivity region is located at similar temperatures as it was observed for CZTSe samples (between 110 K to 240 K) [27]. The characteristic temperature and width of the acceptor band is greatly increased in CZTS (see Table 3.6). This could be explained by a stronger dispersion of the levels which constitute the acceptor band. Finally the calculation of the relative concentration (N/N_c) and relative localization radius (a/a_B) indicate that all measured CZTS compound are quite far from the metal-insulator transition region (MIT) and that it is not possible to calculate further parameters with an acceptable error. Therefore it was not possible to estimate the acceptor concentration of the CZTS samples. The acceptor concentration could be expected to be similar as in CZTSe but than the critical acceptor concentration should be 5 to 6 times higher in CZTS. Further details can be found in Hajdeu-Chicarosh et al. [31].

The correlation between the electrical resistivity and conductivity results and the defect concentration did not exhibit any significant trend certainly because of the similar chemical composition of the CZTS samples. To correlate the parameters also Cu-rich / Zn-poor CZTS should be analyzed additionally to the already investigated Cu-poor / Zn-rich CZTS compounds.

3.8 Results of the CZTS thin film solar cells fabricated by rapid thermal evaporation

The last step of the characterized homogeneous off-stoichiometric CZTS samples was to actually fabricate a thin film solar cell. Therefore in a corporation with the University Autonoma of Madrid (UAM), by using rapid thermal evaporation the CZTS absorber layer was deposited at UAM. These thin films were completed to a thin film solar cell at UAM and HZB. The completed thin film solar cell was then characterized and efficiency measurements were conducted [22]. Because of the thermal process, the initial composition was partially lost and altered in the fabrication process. More details can be found in Garcia-Llamas et al. [22]. Finally some solar cell devices were produced with an efficiency between 2 % to 3 %. Some selected devices are listed in Table 3.7.

Table 3.7: Overview of solar cell efficencies: D1 = CZTSSe, ZSW = CIGS and R7 = CZTS fabricated by thermal evaporation at UAM.

cell	efficiency %	FF %	V_{OC} mV	J_{SC} mA cm^{-2}	process
D1 (CZTSSe) [97]	12.6	69.8	513.4	35.2	hydrazine pure-solution approach [94]
ZSW (CIGS) [42]	21.7	79.3	746	36.6	co-evaporation & PDT
ZSW (CIGS) [42]	21.7	79.4	748	36.5	co-evaporation & PDT
R7_TT1 (CZTS) [22]	2.2	36.9	551	10.7	thermal evaporation
R7_TT3 (CZTS) [22]	2.7	41.3	544	12	thermal evaporation

In comparison to record efficiencies of thin film solar cells like CZTSSe and CIGS, the solar cells produced by thermal evaporation have lower efficiencies. Considering that the thermal evaporation method is not well tested yet, and the fabrication was one of the first attempts of producing thin film solar cells out of off-stoichiometric CZTS powder, it is a good result. In comparison to CIGS, CZTSSe absorber material and thin film solar cell production have a relative short research history. The fabricated solar cells by rapid thermal evaporation have ¼ of the efficiency than the world record efficiency cell by Wang et al. [97], where a different deposition process and additional Se were used. Nevertheless the V_{OC} is higher than in the CZTSSe record cell (see Table 3.7) and the V_{OC} is assumed to be one of the limiting parameters to reach higher efficiencies in the CZTSSe system. In case of the thermally evaporated thin film solar cell SnS was detected at the back contact which seems to limit efficiency in the fabricated devices. Probably in future experiments the formation of secondary phases can be reduced to achieve higher efficiencies. By adding an anti-reflection coating the efficiency of the fabricated thin film solar cell could be increased above 3 %.

4 Summary and Outlook

In this work a systematic and comprehensive study was conducted on the structural variations and chemical trends in off-stoichiometric kesterite type compound semiconductors. For all examinations the reference powder materials synthesized by solid state reaction in sealed evacuated silica ampules were used.

WDX measurements at an electron micro probe analyzer and X-ray diffraction analyses with Bragg-Brentano geometry were applied in order to obtain the chemical compositions and phase relations of the CZTS powder samples. In total six different off-stoichiometry types have been identified by introducing the E- [29], F-type [96] to the already postulated A-, B-, C- and D-type [45]. In total 34 CZTS samples with different $Cu/(Zn+Sn)$ and Zn/Sn ratios were produced and 12 show single-phase CZTS without the occurrence of secondary phases. All samples exhibiting a single-phase composition were identified in the Cu-poor / Zn-rich region and are located mostly near the B-type line with mixtures of A- and F-type. The majority of samples show several secondary phases like copper, zinc and tin sulfides. Furthermore in few samples a Cu-Sn-S-compound was formed as secondary phase. The formation of secondary phases was mostly in accordance to the chemical composition like under Cu-rich conditions mostly copper sulfide was detected. The quantitative analyses by X-ray diffraction has shown that in the majority of samples CZTS is the main phase.

The shift to B-type compositions, especially of all initially weighted A-type samples, could be ascribed to the loss of Sn during the syntheses. This effect was also described in literature [40, 62, 65, 82, 83] and could not be inhibited throughout the enhancement of the synthesis routine.

Furthermore a calculation was introduced to obtain the off-stoichiometry type fractions of type mixtures and the chemical composition of the different off-stoichiometric CZTS compounds considering the intrinsic point defects and defect complexes.

The evaluation of the lattice parameters obtained by X-ray diffraction has shown that the tetragonal deformation decreases from Cu-poor / Zn-rich to Cu-rich / Zn-poor conditions. One off-stoichiometric Cu-rich sample shows no tetragonal deformation ($c/2a$ = 1) and therefore no Bragg reflex splitting in the obtained powder patterns. Additionally the unit cell volume dependency of the chemical position was analyzed and a decrease from Cu-poor / Zn-rich to Cu-rich / Zn-poor conditions was observed caused by the slightly smaller ion radius of Cu^+ over Zn^{2+}.

For a deeper understanding of the kesterite type structure X-ray diffraction is limited due to the isoelectronic cations Cu^+ and Zn^{2+}, therefore neutron diffraction was applied, which allows the distinction of all three cations of the CZTS compound due to

distinct average neutron scattering lengths. Full pattern Rietveld refinement of neutron diffraction data and the average neutron scattering length method were applied to determine the defect complexes of the different CZTS powder samples. The experimentally observed intrinsic point defects are in perfect agreement with the different off-stoichiometry type specific defect complexes postulated in literature [29, 45, 96]. The Cu-Zn disorder defect complex is not type related and not dependent on off-stoichiometry. Furthermore the Cu-Zn disorder is the only defect complex present in all samples and has a defect concentration with a similar magnitude. In contrast the off-stoichiometry type specific intrinsic point defects are changing according to the chemical composition of the CZTS phase. If the chemical compositions of CZTS were more off-stoichiometric also the corresponding type specific intrinsic point defects were increasing. The defect complexes observed in the off-stoichiometric A-, B-, C- D- and F-type were: $V_{Cu} + Zn_{Cu}$, $2\,Zn_{Cu} + Zn_{Sn}$, $2\,Cu_{Zn} + Sn_{Zn}$, $Cu_{Zn} + Cu_i$ and $Zn_{Sn} + 2\,Cu_i$.

This trend can be seen in the defect concentrations which were extracted from the average neutron scattering length method. Cu-rich samples have more Cu_{Zn} defects whereas Zn-rich conditions show higher Zn_{Cu} concentrations. This also applies to all other defects. Furthermore the off-stoichiometric type fraction of CZTS has to be considered if multiple CZTS phases are evaluated together. The observed defect concentrations are representing the structural defects and not the electronic active defects.

As a result of the evaluation of the intrinsic point defects in combination with their influence on the band gap [9] it can be explained why thin film solar cells using an CZTS absorber with A-type composition produce devices with the highest efficiencies [1, 43, 97]. The off-stoichiometric Cu-poor / Zn-rich A-type defect complex $V_{Cu} + Zn_{Cu}$ introduced by the substitution of Cu slightly broadens the band gap whereas intrinsic point defects in the Cu-rich / Zn-poor region reduce the band gap. Especially Sn related intrinsic point defects are harmful for device efficiencies.

The reliability of the neutron diffraction and average neutron scattering length method was further supported by the results of anomalous X-ray diffraction which overcomes the limits of conventional X-ray powder diffraction by measuring at the absorption edges of the isoelectronic cations Cu^+ and Zn^{2+}. The results of the Cu-Zn disorder obtained by anomalous X-ray diffraction are in good agreement with the average neutron scattering length results. Further intrinsic point defects could not be identified because the method still needs to advance so that the introduction of a third element, in this case Sn, causes no instabilities during the Rietveld analysis.

Also the possibility to identify the Cu_i by applying neutron diffraction was checked but could not accomplished with the used instrumental setup. Low temperature analysis and selective measurements should be applied to achieve higher intensities and reduce the influence of the temperature on the refinement results. Also the results of the cation distribution analysis would benefit from the reduced influence of temperature and minimize the error bar.

For additional investigations of the CZTS system the Sn control of the synthesis needs further improvements to synthesize pure A- and E-type. Also the synthesis of more off-stoichiometric F-type samples should be considered.

This paper provides a summary of a systematic and detailed study on structural variations with changing composition of kesterite type compound semiconductors. A qualitative and quantitative analysis of different off-stoichiometric kesterite types defect complexes and defect concentrations has been performed by applying advanced diffraction techniques and quantitative WDX analyses. This provides an important insight into the structural and chemical relations of CZTS material and could contribute to further push the limits of CZTS thin film solar cell efficiency.

Bibliography

[1] Ahmed, S./ Reuter, K. B./ Gunawan, O./ Guo, L./ Romankiw, L. T./ Deligianni, H. (2012): A High Efficiency Electrodeposited Cu_2ZnSnS_4 Solar Cell, Advanced Energy Materials 2 (2), 253–259.

[2] Ahn, S./ Jung, S./ Gwak, J./ Cho, A./ Shin, K./ Yoon, K./ Park, D./ Cheong, H./ Yun, J. H. (2010): Determination of band gap energy (E_g) of $Cu_2ZnSnSe_4$ thin films: On the discrepancies of reported band gap values, Applied Physics Letters 97 (2), 021905.

[3] Bail, A. L./ Duroy, H./ Fourquet, J. (1988): Ab-initio structure determination of $LiSbWO_6$ by X-ray powder diffraction, Materials Research Bulletin 23 (3), 447–452, URL http://www.sciencedirect.com/science/article/pii/0025540888900190.

[4] Bailey, C. L./ Liborio, L./ Mallia, G./ Tomić, S./ Harrison, N. M. (2010): Defect physics of $CuGaS_2$, Phys. Rev. B 81, 205214.

[5] Barkhouse, D. A. R./ Gunawan, O./ Gokmen, T./ Todorov, T. K./ Mitzi, D. B. (2012): Device characteristics of a 10.1 % hydrazine-processed $Cu_2ZnSn(Se,S)_4$ solar cell, Progress in Photovoltaics: Research and Applications 20 (1), 6–11.

[6] Brennan, S./ Cowan, P. L. (1992): A suite of programs for calculating X-ray absorption, reflection, and diffraction performance for a variety of materials at arbitrary wavelengths, Review of Scientific Instruments 63 (1), 850–853.

[7] Brown, P. J./ Fox, A. G./ Maslen, E. N./ O'Keefe, M. A./ Willis, B. T. M. (2006): Intensity of diffracted intensities, Kapitel 6.1.1, 554–590, John Wiley & Sons, Ltd, URL http://dx.doi.org/10.1107/97809553602060000600.

[8] Centre for Solar Energy and Hydrogen Research Baden-Württemberg, ZSW (2016): CIGS PV's efficiency ratings rising fast, Technischer Report, Centre for Solar Energy and Hydrogen Research Baden-Württemberg, ZSW, URL https://www.zsw-bw.de/en/newsroom/news/news-detail/news/detail/News/zsw-sets-new-world-record-for-thin-film-solar-cells.html.

[9] Chen, S./ Walsh, A./ Gong, X.-G./ Wei, S.-H. (2013): Classification of Lattice Defects in the Kesterite Cu_2ZnSnS_4 and $Cu_2ZnSnSe_4$ Earth-Abundant Solar Cell Absorbers, Advanced Materials 25 (11), 1522–1539.

[10] Chen, S./ Walsh, A./ Luo, Y./ Yang, J.-H./ Gong, X./ Wei, S.-H. (2010): Wurtzite-derived polytypes of kesterite and stannite quaternary chalcogenide

semiconductors, Physical Review B: Condensed Matter and Materials Physics 82 (19), 195203–8.

[11] Chen, S./ Wang, L.-W./ Walsh, A./ Gong, X./ Wei, S.-H. (2012): Abundance of $Cu_{Zn} + Sn_{Zn}$ and $2Cu_{Zn} + Sn_{Zn}$ defect clusters in kesterite solar cells, Applied Physics Letters 101 (22), 223901.

[12] Chen, S./ Yang, J.-H./ Gong, X./ Walsh, A./ Wei, S.-H. (2010): Intrinsic point defects and complexes in the quaternary kesterite semiconductor Cu_2ZnSnS_4, Physical Review B: Condensed Matter and Materials Physics 81 (24), 245204.

[13] Choi, S. G./ Zhao, H. Y./ Persson, C./ Perkins, C. L./ Donohue, A. L./ To, B./ Norman, A. G./ Li, J./ Repins, I. L. (2012): Dielectric function spectra and critical-point energies of $Cu_2ZnSnSe_4$ from 0.5 to 9.0 eV, Journal of Applied Physics 111 (3), 033506.

[14] Choubrac, L./ Lafond, A./ Guillot-Deudon, C./ Moëlo, Y./ Jobic, S. (2012): Structure Flexibility of the Cu_2ZnSnS_4 Absorber in Low-Cost Photovoltaic Cells: From the Stoichiometric to the Copper-Poor Compounds, Inorganic Chemistry 51 (6), 3346–3348.

[15] Choubrac, L./ Paris, M./ Lafond, A./ Guillot-Deudon, C./ Rocquefelte, X./ Jobic, S. (2013): Multinuclear (67Zn, 119Sn and 65Cu) NMR spectroscopy - an ideal technique to probe the cationic ordering in Cu_2ZnSnS_4 photovoltaic materials, Physical Chemistry Chemical Physics 15 (26), 10722–10725.

[16] Cromer, D. T./ Liberman, D. (1970): Relativistic Calculation of Anomalous Scattering Factors for X Rays, The Journal of Chemical Physics 53 (5), 1891–1898.

[17] Cromer, D. T./ Liberman, D. A. (1981): Anomalous dispersion calculations near to and on the long-wavelength side of an absorption edge, Acta Crystallographica Section A 37 (2), 267–268.

[18] Efros, A. L./ Shklovski, B. I. (1984): Electronic Properties of Doped Semiconductors, Springer.

[19] Finger, L. W./ Cox, D. E./ Jephcoat, A. P. (1994): A correction for powder diffraction peak asymmetry due to axial divergence, Journal of Applied Crystallography 27 (6), 892–900.

[20] Fraunhofer ISE (2016): Photovoltaics Report, Technischer Report, Fraunhofer ISE, URL `https://www.ise.fraunhofer.de/en/downloads-englisch/pdf-files-englisch/photovoltaics-report-slides.pdf`.

[21] Furrer, A./ Strässle, T./ Mesot, J. (2009): Neutron Scattering in Condensed Matter Physics, Series on neutron techniques and applications, World Scientific, URL `https://books.google.co.uk/books?id=3epAAQAAIAAJ`.

[22] Garcia-Llamas, E./ Merino, J. M./ Gunder, R./ Neldner, K./ Greiner, D./ Steigert, A./ Giraldo, S./ Izquierdo-Roca, V./ Saucedo, E./ León, M./ Schorr, S./ Caballeroa, R. (2016): Cu_2ZnSnS_4 thin film solar cells grown by fast thermal evaporation and thermal treatment, unpublished .

[23] Grossberg, M./ Krustok, J./ Raudoja, J./ Timmo, K./ Altosaar, M./ Raadik, T. (2011): Photoluminescence and Raman study o$Cu_2ZnSn(Se_xS_{1-x})_4$ monograins for photovoltaic applications, Thin Solid Films 519 (21), 7403–7406, URL `http://www.sciencedirect.com/science/article/pii/S004060901001730X`, proceedings of the {EMRS} 2010 Spring Meeting Symposium M: Thin Film Chalcogenide Photovoltaic Materials.

[24] Grossberg, M./ Krustok, J./ Timmo, K./ Altosaar, M. (2009): Radiative recombination in $Cu_2ZnSnSe_4$ monograins studied by photoluminescence spectroscopy, Thin Solid Films 517 (7), 2489–2492, URL `http://www.sciencedirect.com/science/article/pii/S0040609008014053`, thin Film Chalogenide Photovoltaic Materials (EMRS, Symposium L).

[25] Guc, M./ Caballero, R./ Lisunov, K./ López, N./ Arushanov, E./ Merino, J./ León, M. (2014): Disorder and variable-range hopping conductivity in Cu2ZnSnS4 thin films prepared by flash evaporation and post-thermal treatment, Journal of Alloys and Compounds 596, 140–144, URL `http://www.sciencedirect.com/science/article/pii/S0925838814002412`.

[26] Guc, M./ Lisunov, K./ Hajdeu, E./ Levcenko, S./ Ursaki, V./ Arushanov, E. (2014): Variable-range hopping conductivity in $Cu_2ZnGeSe_4$ single crystals, Solar Energy Materials and Solar Cells 127, 87–91, URL `http://www.sciencedirect.com/science/article/pii/S0927024814001925`.

[27] Guc, M./ Valle Rios, L. E. (2016): Transport properties of $Cu_2ZnSnSe_4$ powder samples, unpublished .

[28] Gürel, T./ Sevik, C./ Cagun, T. (2011): Characterization of vibrational and mechanical properties of quaternary compounds Cu_2ZnSnS_4 and $Cu_2ZnSnSe_4$ in kesterite and stannite structures, Physical Review B: Condensed Matter and Materials Physics 84 (20), 205201.

[29] Gurieva, G./ Dimitrievska, M./ Zander, S./ Pérez-Rodríguez, A./ Izquierdo-Roca, V./ Schorr, S. (2015): Structural characterisation of $Cu_{2.04}Zn_{0.91}Sn_{1.05}S_{2.08}Se_{1.92}$, phys status solidi (c) 12 (6), 588–591.

[30] Haass, S. G./ Diethelm, M./ Werner, M./ Bissig, B./ Romanyuk, Y. E./ Tiwari, A. N. (2015): 11.2% Efficient Solution Processed Kesterite Solar Cell with a Low Voltage Deficit, Advanced Energy Materials 5 (18), 1500712.

[31] Hajdeu-Chicarosh, E./ Guc, M./ Neldner, K./ Gurieva, G./ Schorr, S./ Arushanov, E./ / Lisunov, K. G. (2016): Transport properties of Cu_2ZnSnS_4 powder samples, unpublished .

[32] Hall, S. R./ Szymanski, J. T./ Stewart, J. M. (1978): Kesterite, $Cu_2(Zn,Fe)SnS_4$, and stannite, $Cu_2(Fe,Zn)SnS_4$, structurally similar but distinct minerals, The Canadian Mineralogist 16 (2), 131–137, URL `http://www.canmin.org/content/16/2/131.short`.

[33] Han, D./ Sun, Y. Y./ Bang, J./ Zhang, Y. Y./ Sun, H.-B./ Li, X.-B./ Zhang, S. B. (2013): Deep electron traps and origin of *p*-type conductivity in the earth-abundant solar-cell material Cu_2ZnSnS_4, Physical Review B: Condensed Matter and Materials Physics 87, 155206, URL `http://link.aps.org/doi/10.1103/PhysRevB.87.155206`.

[34] He, B. B. (2009): Two-Dimensional X-Ray Diffraction, John Wiley & Sons, Inc.

[35] Hill, R. J./ Howard, C. J. (1987): Quantitative phase analysis from neutron powder diffraction data using the Rietveld method, Journal of Applied Crystallography 20 (6), 467–474.

[36] Hossain, M. I. (2012): Prospects Of CZTS Solar Cells From The Perspective Of Material Properties, Fabrication Methods And Current Research Challenges, Chalcogenide Letters 9 (6), 231–242.

[37] Htay, M. T./ Hashimoto, Y./ Momose, N./ Sasaki, K./ Ishiguchi, H./ Igarashi, S./ Sakurai, K./ Ito, K. (2011): A Cadmium-Free Cu_2ZnSnS_4/ZnO Hetrojunction Solar Cell Prepared by Practicable Processes, Japanese Journal of Applied Physics 50, 032301.

[38] Huang, D./ Persson, C. (2013): Band gap change induced by defect complexes in Cu_2ZnSnS_4, Thin Solid Films 535, 265–269, URL `http://www.sciencedirect.com/science/article/pii/S0040609012013004`.

[39] Image courtesy of the University of Minnesota Electron Microprobe Lab (2007): URL `http://serc.carleton.edu/research_education/geochemsheets/techniques/EPMA.html`.

[40] Ito, K. (2014): Copper Zinc Tin Sulfide-Based Thin Film Solar Cells, Wiley, URL `https://books.google.de/books?id=h_fWBQAAQBAJ`.

[41] Ito, K./ Nakazawa, T. (1988): Electrical and Optical Properties of Stannite-Type Quaternary Semiconductor Thin Films, Japanese Journal of Applied Physics 27 (Part 1, No. 11), 2094–2097.

[42] Jackson, P./ Hariskos, D./ Wuerz, R./ Kiowski, O./ Bauer, A./ Friedlmeier, T. M./ Powalla, M. (2015): Properties of $Cu(In,Ga)Se_2$ solar cells with new record efficiencies up to 21.7%, physica status solidi (RRL) - Rapid Research Letters 9 (1), 28–31.

[43] Katagiri, H./ Jimbo, K./ Maw, W. S./ Oishi, K./ Yamazaki, M./ Araki, H./ Takeuchi, A. (2009): Development of CZTS-based thin film solar cells, Thin Solid Films 517 (7), 2455–2460, URL `http://www.sciencedirect.com/science/article/pii/S0040609008013953`.

[44] Ki, W./ Hillhouse, H. (2011): Earth-abundant element photovoltaics directly from soluble precursors with high yield using a non-toxic solvent, Advanced Energy Materials 1 (5), 732–735, URL `http://www.scopus.com/inward/record.url?eid=2-s2.0-84858634746&partnerID=40&md5=9e4078677766b37eb3f95480c38c1ca3`.

[45] Lafond, A./ Choubrac, L./ Guillot-Deudon, C./ Deniard, P./ Jobic, S. (2012): Crystal Structures of Photovoltaic Chalcogenides, an Intricate Puzzle to Solve: the Cases of CIGSe and CZTS Materials, Zeitschrift für Anorganische und Allgemeine Chemie 638 (15), 2571–2577.

[46] Lee, Y. S./ Gershon, T./ Gunawan, O./ Todorov, T. K./ Gokmen, T./ Virgus, Y./ Guha, S. (2015): $Cu_2ZnSnSe_4$ Thin-Film Solar Cells by Thermal Co-evaporation with 11.6% Efficiency and Improved Minority Carrier Diffusion Length, Advanced Energy Materials 5 (7).

[47] Lindholm, F. A./ Fossum, J. G./ Burgess, E. L. (1979): Application of the superposition principle to solar-cell analysis, IEEE Transactions on Electron Devices 26 (3), 165–171.

[48] Lisunov, K./ Guc, M./ Levcenko, S./ Dumcenco, D./ Huang, Y./ Gurieva, G./ Schorr, S./ Arushanov, E. (2013): Energy spectrum of near-edge holes and conduction mechanisms in $Cu_2ZnSiSe_4$ single crystals, Journal of Alloys and Compounds 580, 481–486, URL `http://www.sciencedirect.com/science/article/pii/S0925838813015545`.

[49] Lisunov, K./ Guk, M./ Nateprov, A./ Levcenko, S./ Tezlevan, V./ Arushanov, E. (2013): Features of the acceptor band and properties of localized carriers from studies of the variable-range hopping conduction in single crystals of p-Cu_2ZnSnS_4, Solar Energy Materials and Solar Cells 112, 127–133, URL `http://www.sciencedirect.com/science/article/pii/S0927024813000421`.

[50] Luckert, F./ Hamilton, D. I./ Yakushev, M. V./ Beattie, N. S./ Zoppi, G./ Moynihan, M./ Forbes, I./ Karotki, A. V./ Mudryi, A. V./ Grossberg, M./ Krustok, J./ Martin, R. W. (2011): Optical properties of high quality $Cu_2ZnSnSe$ thin films, Applied Physics Letters 99 (6), 062104.

[51] Matsushita, H./ Ichikawa, T./ Katsui, A. (2005): Structural, thermodynamical and optical properties of Cu_2-II-IV-VI_4 quaternary compounds, Journal of Materials Science 40 (8), 2003–2005.

[52] Merritt, E. A. (1996-2012): X-ray Anomalous Scattering, URL `http://skuld.bmsc.washington.edu/scatter/AS_index.html`.

[53] Miller, A./ Abrahams, E. (1960): Impurity Conduction at Low Concentrations, Phys. Rev. 120, 745–755, URL `http://link.aps.org/doi/10.1103/PhysRev.120.745`.

[54] Mott, N./ Davis, E. (2012): Electronic Processes in Non-Crystalline Materials, Electronic Processes in Non-crystalline Materials, OUP Oxford, URL `https://books.google.co.uk/books?id=JKTfZLWEWLIC`.

[55] National Center for Photovoltaics (2016): Research Cell Efficiency Records, URL `http://www.nrel.gov/ncpv/`.

[56] Nozaki, H./ Fukano, T./ Ohta, S./ Seno, Y./ Katagiri, H./ Jimbo, K. (2012): Crystal structure determination of solar cell materials: Cu_2ZnSnS_4 thin films using X-ray anomalous dispersion, Journal of Alloys and Compounds 524 (0), 22–25, URL `http://www.sciencedirect.com/science/article/pii/S0925838812002204`.

[57] Olekseyuk, I. D./ Dudchak, I. V./ Piskach, L. V. (2004): Phase equilibria in the Cu_2S-ZnS-SnS_2 system, Journal of Alloys and Compounds 368 (12), 135–143, URL `http://www.sciencedirect.com/science/article/pii/S0925838803008843`.

[58] Oo, W./ Johnson, J./ Bhatia, A./ Lund, E./ Nowell, M./ Scarpulla, M. (2011): Grain Size and Texture of Cu_2ZnSnS_4 Thin Films Synthesized by Cosputtering Binary Sulfides and Annealing: Effects of Processing Conditions and Sodium, Journal of Electronic Materials 40 (11), 2214–2221.

[59] Park, D./ Nam, D./ Jung, S./ An, S./ Gwak, J./ Yoon, K./ Yun, J. H./ Cheong, H. (2011): Optical characterization of $Cu_2ZnSnSe_4$ grown by thermal co-evaporation, Thin Solid Films 519 (21), 7386–7389, URL `http://www.sciencedirect.com/science/article/pii/S0040609011001854`, proceedings of the {EMRS} 2010 Spring Meeting Symposium M: Thin Film Chalcogenide Photovoltaic Materials.

[60] Van der Pauw, L. J. (1958): A Method of Measuring the Resistivity and Hall Coefficient on Lamellae of Arbitrary Shape, Philips Technical Review 20, 220–224.

[61] Persson, C. (2010): Electronic and optical properties of Cu_2ZnSnS_4 and $Cu_2ZnSnSe_4$, Journal of Applied Physics 107 (5), 053710.

[62] Piacente, V./ Foglia, S./ Scardala, P. (1991): Sublimation study of the tin sulphides SnS_2, Sn_2S_3 and SnS, Journal of Alloys and Compounds 177 (1), 17–30, URL `http://www.sciencedirect.com/science/article/pii/092583889190053X`.

[63] Polizzotti, A./ Repins, I. L./ Noufi, R./ Wei, S.-H./ Mitzi, D. B. (2013): The state and future prospects of kesterite photovoltaics, Energy and Environmental Science 6, 3171–3182.

[64] Rau, U./ Abou-Ras, D./ Kirchartz, T. (2011): Advanced Characterization Techniques for Thin Film Solar Cells, Wiley, URL `https://books.google.de/books?id=dt_5FQUrF24C`.

[65] Redinger, A./ Berg, D. M./ Dale, P. J./ Siebentritt, S. (2011): The Consequences of Kesterite Equilibria for Efficient Solar Cells, Journal of the American Chemical Society 133 (10), 3320–3323, URL `http://dx.doi.org/10.1021/ja111713g`.

[66] Reed, S. (2005): Electron Microprobe Analysis and Scanning Electron Microscopy in Geology Second Edition, Cambridge University Press, URL `http://books.google.de/books?id=9-_v4YgpoVMC`.

[67] Rey, G./ Redinger, A./ Sendler, J./ Weiss, T. P./ Thevenin, M./ Guennou, M./ El Adib, B./ Siebentritt, S. (2014): The band gap of $Cu_2ZnSnSe_4$: Effect of order-disorder, Applied Physics Letters 105 (11), 112106.

[68] Rietveld, H. M. (1967): Line profiles of neutron powder-diffraction peaks for structure refinement, Acta Crystallographica 22 (1), 151–152.

[69] Rietveld, H. M. (1969): A profile refinement method for nuclear and magnetic structures, Journal of Applied Crystallography 2 (2), 65–71.

[70] Ritscher, A./ Hoelzel, M./ Lerch, M. (2016): The order-disorder transition in Cu_2ZnSnS_4 - A neutron scattering investigation, Journal of Solid State Chemistry 238, 68–73, URL `http://www.sciencedirect.com/science/article/pii/S0022459616300846`.

[71] Ritscher, A./ Just, J./ Dolotko, O./ Schorr, S./ Lerch, M. (2016): A mechanochemical route to single phase Cu_2ZnSnS_4 powder, Journal of Alloys and Compounds 670, 289–296, URL `http://www.sciencedirect.com/science/article/pii/S0925838816303280`.

[72] Rodríguez-Carvajal, J. (2001): Recent developments of the program FULLPROF, Commission on powder diffraction (IUCr). Newsletter 26, 12–19.

[73] Schorr, S. (2007): Structural aspects of adamantine like multinary chalcogenides, Thin Solid Films 515 (15), 5985–5991, URL `http://www.sciencedirect.com/science/article/pii/S0040609006016610`.

[74] Schorr, S. (2011): The crystal structure of kesterite type compounds: A neutron and X-ray diffraction study, Solar Energy Materials and Solar Cells 95 (6), 1482–1488.

[75] Schorr, S./ Gonzalez-Aviles, G. (2009): In-situ investigation of the structural phase transition in kesterite, physica status solidi (a) 206 (5), 1054–1058.

[76] Schorr, S./ Hoebler, H.-J./ Tovar, M. (2007): A neutron diffraction study of the stannite-kesterite solid solution series, European Journal of Mineralogy 19 (1), 65–73, URL `http://www.ingentaconnect.com/content/schweiz/ejm/2007/00000019/00000001/art00007`.

[77] Schorr, S./ Mainz, R./ Mönig, H./ Lauermann, I./ Bär, M. (2012): The complex material properties of chalcopyrite and kesterite thin-film solar cell absorbers tackled by synchrotron-based analytics, Progress in Photovoltaics: Research and Applications 20 (5), 557–567.

[78] Schorr, S./ Tovar, M. (2006): Neutron diffraction structural investigation of natural kesterite, BENSC Experimental Report 101, URL `https://www.helmholtz-berlin.de/user/beamtime/reports/ber-reports_en.html`.

[79] Schorr, S./ Tovar, M./ Hoebler, H.-J./ Schock, H.-W. (2009): Structure and phase relations in the 2(CuInS$_2$)-Cu$_2$ZnSnSe$_4$ solid solution system, Thin Solid Films 517 (7), 2508–2510.

[80] Schubert, B.-A./ Marsen, B./ Cinque, S./ Unold, T./ Klenk, R./ Schorr, S./ Schock, H.-W. (2011): Cu$_2$ZnSnS$_4$ thin film solar cells by fast coevaporation, Progress in Photovoltaics: Research and Applications 19 (1), 93–96.

[81] Scragg, J. J. S./ Choubrac, L./ Lafond, A./ Ericson, T./ Platzer-Björkman, C. (2014): A low-temperature order-disorder transition in Cu$_2$ZnSnS$_4$ thin films, Applied Physics Letters 104 (4), 041911.

[82] Scragg, J. J. S./ Dale, P. J./ Colombara, D./ Peter, L. M. (2012): Thermodynamic Aspects of the Synthesis of Thin-Film Materials for Solar Cells, ChemPhysChem 13 (12), 3035–3046, URL `http://dx.doi.org/10.1002/cphc.201200067`.

[83] Scragg, J. J. S./ Ericson, T./ Kubart, T./ Edoff, M./ Platzer-Björkman, C. (2011): Chemical Insights into the Instability of Cu$_2$ZnSnS$_4$ Films during Annealing, Chemistry of Materials 23 (20), 4625–4633, URL `http://dx.doi.org/10.1021/cm202379s`.

[84] Sears, V. F. (1992): Neutron scattering lengths and cross sections, Neutron News 3 (3), 26–37, URL `http://dx.doi.org/10.1080/10448639208218770`.

[85] Shannon, R. (1981): Bond Distances in Sulfides and a Preliminary Table of Sulfide Crystal Radii, Structure and Bonding in Crystals, O'Keeffe, M./ Navrotsky, A., Hrsgs., Bd. 2 von *Industrial Chemistry Library*, 53–70, Elsevier, URL `http://www.sciencedirect.com/science/article/pii/B9780125251020500098`.

[86] Shockley, W./ Queisser, H. J. (1961): Detailed Balance Limit of Efficiency of p-n Junction Solar Cells, Journal of Applied Physics 32 (3), 510–519.

[87] Spieß, L./ Teichert, G./ Schwarzer, R./ Behnken, H./ Genzel, C. (2009): Moderne Röntgenbeugung: Röntgendiffraktometrie für Materialwissenschaftler, Physiker und Chemiker, Vieweg+Teubner Verlag, URL `http://books.google.de/books?id=yKKhuQAACAAJ`.

[88] Stephan, C./ Schorr, S./ Tovar, M./ Schock, H.-W. (2011): Comprehensive insights into point defect and defect cluster formation in CuInSe2, Applied Physics Letters 98 (9), 091906.

[89] Sugimoto, H./ Liao, C./ Hiroi, H./ Sakai, N./ Kato, T. (2013): Lifetime improvement for high efficiency Cu$_2$ZnSnS$_4$ submodules, Photovoltaic Specialists Conference (PVSC), 2013 IEEE 39th, 3208–3211.

[90] Thompson, P./ Cox, D. E./ Hastings, J. B. (1987): Rietveld refinement of Debye–Scherrer synchrotron X-ray data from Al$_2$O$_3$, Journal of Applied Crystallography 20 (2), 79–83, URL `http://dx.doi.org/10.1107/S0021889887087090`.

[91] Timmo, K./ Altosaar, M./ Raudoja, J./ Muska, K./ Pilvet, M./ Kauk, M./ Varema, T./ Danilson, M./ Volobujeva, O./ Mellikov, E. (2010): Sulfur-containing $Cu_2ZnSnSe_4$ monograin powders for solar cells, Solar Energy Materials and Solar Cells 94 (11), 1889–1892, URL http://www.sciencedirect.com/science/article/pii/S0927024810004332.

[92] Többens, D. M./ Gunder, R./ Gurieva, G./ Marquardt, J./ Neldner, K./ Valle-Rios, L. E./ Zander, S./ Schorr, S. (2016): Quantitative anomalous powder diffraction analysis of cation disorder in kesterite semiconductors, Powder Diffraction FirstView, 1–8, URL http://journals.cambridge.org/article_S0885715616000191.

[93] Többens, D. M./ Gurieva, G./ Levcenko, S./ Unold, T./ Schorr, S. (2016 submitted): Thermal Dependence of Cu/Zn Ordering in CZTSe Kesterites by Anomalous Diffraction, Physica Status Solidi B .

[94] Todorov, T. K./ Reuter, K. B./ Mitzi, D. B. (2010): High-Efficiency Solar Cell with Earth-Abundant Liquid-Processed Absorber, Advanced Materials 22 (20), E156–E159.

[95] Valakh, M. Y./ Kolomys, O. F./ Ponomaryov, S. S./ Yukhymchuk, V. O./ Babichuk, I. S./ Izquierdo-Roca, V./ Saucedo, E./ Perez-Rodriguez, A./ Morante, J. R./ Schorr, S./ Bodnar, I. V. (2013): Raman scattering and disorder effect in Cu_2ZnSnS_4, physica status solidi (RRL) 7 (4), 258–261.

[96] Valle Rios, L. E./ Neldner, K./ Gurieva, G./ Schorr, S. (2016): Existence of off-stoichiometric single phase kesterite, Journal of Alloys and Compounds 657, 408–413, URL http://www.sciencedirect.com/science/article/pii/S0925838815311750.

[97] Wang, W./ Winkler, M. T./ Gunawan, O./ Gokmen, T./ Todorov, T. K./ Zhu, Y./ Mitzi, D. B. (2014): Device Characteristics of CZTSSe Thin-Film Solar Cells with 12.6 % Efficiency, Advanced Energy Materials 4 (7), 1301465.

[98] Würfel, P. (2005): Physics of Solar Cells: From Basic Principles to Advanced Concepts, Physics textbook, Wiley, URL https://books.google.de/books?id=w6Ii4r7FuskC.

[99] Xiao, W./ Wang, J./ Zhao, X./ Wang, J./ Huang, G./ Cheng, L./ Jiang, L./ Wang, L. (2015): Intrinsic defects and Na doping in Cu_2ZnSnS_4: A density-functional theory study, Solar Energy 116 (0), 125–132, URL http://www.sciencedirect.com/science/article/pii/S0038092X15001802.

[100] Xin, H./ Katahara, J. K./ Braly, I. L./ Hillhouse, H. W. (2014): 8% Efficient $Cu_2ZnSn(S,Se)_4$ Solar Cells from Redox Equilibrated Simple Precursors in DMSO, Advanced Energy Materials 4 (11), 1301823.

[101] Xinkun, W./ Wei, L./ Shuying, C./ Yunfeng, L./ Hongjie, J. (2012): Photoelectric properties of Cu_2ZnSnS_4 thin films deposited by thermal evaporation, Journal of Semiconductors 33 (2), 022002, URL http://stacks.iop.org/1674-4926/33/i=2/a=022002.

[102] Young, R. (1995): The Rietveld Method, International Union of Crystallography Monographs on Crystallography, Oxford University Press, URL `http://books.google.de/books?id=k4EvAQAAIAAJ`.

Acknowledgment

Appendix

A.1 Tables of obtained data

Table A.1: Sample overview of CZTS cation ratios, type fractions, formulae and the corresponding secondary phases.

No.	sample	Cu/(Zn+Sn)	err	Zn/Sn	err	types fraction type	%	type	%	err	kesterite Cu	Zn	Sn	S	secondary phases (neutron %)
1	A0125	1.008	0.017	0.974	0.014	C	81%	E	19%	4%	2.006	0.981	1.008	4	$Cu_{0.92}S$ (9 %); $Zn_{0.88}(Cu_{0.02}Sn_{0.01})S$
2	A0100	1.094	0.019	0.864	0.012	D	14%	C	86%	4%	2.100	0.890	1.030	4	$Cu_{0.92}S$ (18 %)
3	A0050	1.220	0.021	0.735	0.010	D	22%	C	78%	4%	2.227	0.776	1.055	4	$Cu_{0.98}S$ (4 %); $Cu_{1.70}S$ (4 %)
4	A0025	1.305	0.022	0.659	0.010	D	24%	C	76%	4%	2.307	0.705	1.071	4	$Cu_{0.92}S$ (3 %) $Cu_{2-x}S$ (1 %)
5	A0000	1.303	0.023	0.635	0.009	D	18%	C	82%	4%	2.295	0.687	1.083	4	$Cu_{0.92}S$ (9 %); $Cu_{1.63}S$; $Zn_{0.91}(Cu_{0.01})S$
6	A5010	0.965	0.017	1.055	0.015	A	16%	B	84%	3%	1.960	1.043	0.989	4	-
7	A3010	0.967	0.017	1.067	0.015	A	1%	B	99%	3%	1.966	1.050	0.984	4	-
8	A3020	0.955	0.017	1.073	0.015	A	14%	B	86%	3%	1.949	1.057	0.985	4	-
9	B1010	0.959	0.017	1.096	0.016	B	95%	F	5%	3%	1.956	1.069	0.976	4	$Zn_{0.92}(Cu_{0.05}Sn_{0.02})S$
10	B1020	0.944	0.016	1.131	0.016	B	95%	F	5%	3%	1.946	1.094	0.966	4	$Zn_{0.95}(Cu_{0.04}Sn_{0.01})S$
11	A2000	0.941	0.016	1.152	0.016	B	91%	F	9%	2%	1.946	1.106	0.960	4	$Zn_{0.96}(Cu_{0.04}Sn_{0.01})S$; $Sn_{0.97}(Cu_{0.02}Zn_{0.01})S$ (11 %); $Cu_{1.85}S$ (12 %)
12	C0025	0.943	0.016	1.147	0.016	B	91%	F	9%	2%	1.948	1.103	0.961	4	$Zn_{0.96}(Cu_{0.04}Sn_{0.01})S$; $Sn_{0.97}(Cu_{0.02}Zn_{0.01})S$ (33 %), $Cu_{1.86}S$
13	B2000	0.997	0.017	1.049	0.015	B	57%	F	43%	1%	2.007	1.031	0.983	4	-
14	B2010	0.976	0.017	1.086	0.015	B	79%	F	21%	2%	1.984	1.059	0.975	4	-
15	B2020	0.964	0.017	1.122	0.016	B	81%	F	19%	2%	1.974	1.083	0.965	4	-
16	B1000	0.995	0.017	1.054	0.015	B	59%	F	41%	2%	2.005	1.034	0.981	4	-
17	D0010	1.009	0.017	1.034	0.015	B	24%	F	76%	2%	2.021	1.019	0.985	4	-
18	D0040	1.044	0.018	1.006	0.014	F	29%	D	71%	3%	2.066	0.992	0.988	4	$Cu_{0.95}(Zn_{0.01})S$
19	D0050	1.051	0.018	0.990	0.014	F	17%	D	83%	4%	2.072	0.981	0.991	4	$Cu_{0.96}S$, SnS
20	D0020R	0.999	0.017	1.086	0.015	B	51%	F	49%	2%	2.019	1.052	0.969	4	$Cu_{1.84}(Sn_{0.02})S$, $Sn_{0.96}(Cu_{0.08}Zn_{0.02})S$
21	D0000	0.967	0.017	1.136	0.016	B	76%	F	24%	2%	1.981	1.090	0.959	4	$Cu_{1.90}(Sn_{0.01})S$, $Sn_{0.98}(Cu_{0.03}Zn_{0.01})S$ (3 %), $Zn_{0.98}(Cu_{0.03}Sn_{0.01})S$
22	A4000	0.949	0.016	1.079	0.015	A	17%	B	83%	3%	1.941	1.062	0.984	4	-
23	A4010	0.989	0.017	1.041	0.015	B	76%	F	24%	2%	1.994	1.028	0.988	4	$Zn_{0.95}(Cu_{0.03}Sn_{0.01})S$
24	A4030	0.993	0.017	1.045	0.015	B	66%	F	34%	2%	2.000	1.030	0.985	4	-
25	A4040	1.042	0.018	0.956	0.014	C	43%	D	57%	3%	2.051	0.962	1.006	4	$Cu_{0.41}Zn_{0.13}Sn_{1.31}S_3$
26	A4050	0.958	0.017	1.066	0.015	A	16%	B	84%	3%	1.952	1.051	0.986	4	-
27	E0010	1.101	0.019	0.838	0.012	D	7%	C	93%	5%	2.102	0.871	1.039	4	$Cu_{0.69}Zn_{0.08}Sn_{1.26}S_3$
28	E0020	1.053	0.018	0.921	0.013	D	15%	C	85%	4%	2.058	0.937	1.017	4	$Cu_{0.59}Zn_{0.11}Sn_{1.26}S_3$
29	E0030	0.979	0.017	1.030	0.015	A	21%	B	79%	3%	1.976	1.024	0.994	4	$Sn_{0.97}(Cu_{0.04}Zn_{0.02})S_2$
30	E0040	0.978	0.017	1.039	0.015	A	7%	B	93%	3%	1.977	1.030	0.991	4	$Sn_{2.82}(Cu_{0.08}Zn_{0.05})S_4$
31	A6020	0.982	0.017	1.024	0.014	A	27%	B	73%	2%	1.978	1.020	0.996	4	$Cu_{0.33}Zn_{0.14}Sn_{1.34}S_3$
32	A6030	1.030	0.018	0.938	0.013	C	97%	E	3%	5%	2.029	0.953	1.016	4	$Cu_{0.56}Zn_{0.12}Sn_{1.28}S_3$
33	A4020	0.910	0.016	1.098	0.016	A	47%	B	53%	2%	1.883	1.084	0.987	4	-
34	D0030	0.947	0.016	1.120	0.016	B	97%	F	3%	3%	1.948	1.086	0.970	4	$Cu_{1.80}(Sn_{0.02})S$, $Sn_{0.96}(Cu_{0.05}Zn_{0.01})S$, $Zn_{0.98}(Cu_{0.03}Sn_{0.01})S$

Table A.2: Sample overview of CZTS lattice parameters, cell volume, density and occupation factors of neutron diffraction.

No.	sample	XRD a	XRD c	Volume Å	neutrons a	neutrons c	Volume Å	density g/cm3	Occ (neutrons) Cu(2a)	err	Cu(2c)	err	Zn(2d)	err	Sn(2b)	err
1	A0125	5.435	10.845	320.377	5.426	10.866	319.880	4.653	0.980	0.030	0.947	0.027	1.073	0.035	0.997	0.029
2	A0100	5.431	10.840	319.731	5.424	10.864	319.627	4.609	0.991	0.037	0.990	0.031	1.014	0.040	1.004	0.036
3	A0050	5.423	10.838	318.783	5.418	10.846	318.337	4.629	0.997	0.033	0.958	0.035	1.053	0.044	1.021	0.038
4	A0025	5.418	10.832	317.935	5.417	10.822	317.524	4.709	0.994	0.024	0.972	0.026	1.161	0.028	0.999	0.022
5	A0000	5.418	10.836	318.100	5.415	10.831	317.584	4.684	0.992	0.035	0.942	0.043	1.163	0.047	0.987	0.039
6	A5010	5.439	10.841	320.721	5.436	10.835	320.161	4.517	1.012	0.020	0.983	0.017	1.031	0.021	0.994	0.022
7	A3010	5.439	10.840	320.672	5.434	10.833	319.850	4.607	0.990	0.025	0.966	0.030	1.061	0.034	0.989	0.026
8	A3020	5.439	10.840	320.644	5.436	10.836	320.205	4.557	0.993	0.014	0.987	0.025	1.022	0.032	0.999	0.016
9	B1010	5.438	10.844	320.714	5.435	10.837	320.122	4.522	1.005	0.036	0.933	0.041	1.079	0.048	0.977	0.036
10	B1020	5.439	10.845	320.776	5.435	10.840	320.228	4.563	0.944	0.059	0.983	0.039	1.050	0.045	1.029	0.066
11	A2000	5.439	10.844	320.725	5.426	10.875	320.193	4.475	1.016	0.033	0.943	0.032	1.003	0.040	1.006	0.038
12	C0025	5.440	10.847	320.972	5.424	10.877	319.997	4.560								
13	B2000	5.439	10.844	320.798	5.439	10.843	320.763	4.550	0.991	0.030	0.960	0.030	1.057	0.040	0.992	0.034
14	B2010	5.439	10.843	320.748	5.436	10.839	320.344	4.534	1.008	0.019	0.955	0.017	1.051	0.021	1.001	0.020
15	B2020	5.438	10.845	320.770	5.438	10.846	320.695	4.569	0.994	0.024	0.914	0.029	1.082	0.033	0.996	0.024
16	B1000	5.439	10.843	320.790	5.435	10.836	320.099	4.570	1.001	0.022	0.957	0.020	1.079	0.026	0.990	0.025
17	D0010	5.438	10.844	320.610	5.434	10.835	319.917	4.467	1.020	0.031	0.940	0.031	1.060	0.038	0.984	0.033
18	D0040	5.434	10.842	320.185	5.424	10.865	319.659	4.625	0.989	0.029	0.924	0.032	1.120	0.038	0.989	0.029
19	D0050	5.435	10.842	320.253	5.425	10.869	319.899	4.540	1.006	0.029	0.972	0.024	1.031	0.029	0.999	0.031
20	D0020R	5.440	10.844	320.882	5.426	10.876	320.236	4.504	1.019	0.036	0.985	0.035	1.077	0.039	0.981	0.036
21	D0000	5.439	10.843	320.825	5.438	10.838	320.486	4.553	0.999	0.018	0.950	0.040	1.067	0.053	1.011	0.020
22	A4000	5.439	10.843	320.799	5.437	10.839	320.463	4.570	0.998	0.028	0.956	0.035	1.069	0.037	0.999	0.027
23	A4010	5.439	10.841	320.704	5.438	10.839	320.504	4.565	1.000	0.017	0.951	0.019	1.051	0.024	1.013	0.018
24	A4030	5.438	10.838	320.519	5.436	10.834	320.175	4.503	1.015	0.016	0.925	0.021	1.051	0.027	1.016	0.017
25	A4040	5.438	10.85	320.808	5.437	10.847	320.631	4.567	1.010	0.020	0.962	0.019	1.106	0.027	1.006	0.024
26	A4050	5.440	10.841	320.774	5.438	10.838	320.461	4.590	0.994	0.010	0.978	0.019	1.033	0.025	1.006	0.012
27	E0010	5.437	10.852	320.755	5.437	10.851	320.738	4.615	0.996	0.013	0.967	0.026	1.090	0.031	1.009	0.013
28	E0020	5.437	10.849	320.767	5.439	10.851	320.963	4.575	0.995	0.029	0.954	0.033	1.063	0.039	0.996	0.031
29	E0030	5.439	10.841	320.674	5.439	10.840	320.624	4.552	1.019	0.019	0.990	0.018	1.028	0.023	1.002	0.021
30	E0040	5.439	10.841	320.662	5.436	10.835	320.190	4.513	1.013	0.020	0.973	0.020	1.021	0.026	1.006	0.023
31	A6020	5.439	10.843	320.724	5.437	10.840	320.478	4.554	1.007	0.019	0.978	0.018	1.040	0.024	1.016	0.022
32	A6030	5.437	10.848	320.696	5.439	10.851	321.030	4.575	0.999	0.022	0.967	0.020	1.052	0.024	1.011	0.023
33	A4020	5.438	10.836	320.424	5.438	10.836	320.407	4.446	1.014	0.022	0.918	0.023	1.019	0.029	0.989	0.024
34	D0030	5.439	10.845	320.844	5.439	10.842	320.722	4.550	0.991	0.014	0.962	0.030	1.067	0.039	0.996	0.016

Table A.3: Bragg factors of CZTS, average weighted Bragg factors, Chi-square and isotropic temperature factors (Biso).

No.	sample	CZTS Bragg R	CZTS RF-factor	average Bragg R	average RF-factor	Chi-square	Cu(2a)	Cu(2c)	Biso Zn(2d)	Sn(2b)	S
1	A0125	2.310	3.680	3.190	4.090	1.790	2.110	1.715	1.715	0.144	0.852
2	A0100	2.240	3.630	3.260	4.040	1.840	2.236	1.588	1.274	0.165	1.034
3	A0050	2.480	5.020	3.890	5.890	1.670	2.194	2.074	0.823	0.642	1.025
4	A0025	1.360	3.390	2.070	3.720	1.490	2.991	1.089	1.089	0.431	1.306
5	A0000	4.270	42.000	4.270	42.000	4.618	1.427	1.478	0.737	0.781	0.858
6	A5010	2.700	6.010	2.700	6.010	1.180	2.905	0.757	0.757	1.040	0.850
7	A3010	3.760	43.400	3.760	43.400	5.260	1.098	1.522	0.690	0.654	0.662
8	A3020	2.240	5.070	2.240	5.070	1.850	1.550	1.966	1.849	0.726	0.981
9	B1010	4.640	7.790	4.640	7.790	1.370	2.587	2.157	2.157	1.031	1.490
10	B1020	5.180	7.77	5.180	7.770	1.710	1.299	1.562	0.651	0.620	0.710
11	A2000	2.330	2.84	4.340	3.890	1.840	2.959	0.820	0.820	0.368	0.821
12	C0025	2.770	3.01	7.030	4.530	3.210					
13	B2000	2.370	5.540	2.370	5.540	1.630	1.813	1.873	1.756	0.990	1.191
14	B2010	2.580	5.260	2.580	5.260	1.340	2.720	0.621	0.621	0.919	0.939
15	B2020	3.170	5.480	3.170	5.480	1.520	1.266	2.031	0.714	0.126	0.762
16	B1000	2.750	5.220	2.750	5.220	1.300	1.763	1.389	1.389	0.608	0.718
17	D0010	2.200	5.190	2.200	5.190	1.140	2.724	1.018	1.018	0.469	0.925
18	D0040	2.580	6.610	2.580	6.610	1.650	2.594	0.759	0.759	0.494	0.803
19	D0050	2.640	6.830	2.640	6.830	1.780	2.481	0.594	0.594	0.815	0.850
20	D0020R	2.450	6.190	2.450	6.190	2.210	3.154	1.108	1.108	0.541	0.797
21	D0000	4.680	9.84	4.680	9.840	4.370	1.341	1.576	1.576	0.517	0.497
22	A4000	2.870	4.81	2.870	4.810	1.660	2.523	1.491	0.207	0.748	0.697
23	A4010	2.830	4.49	2.830	4.490	1.730	1.483	1.516	1.100	0.191	0.558
24	A4030	2.780	5.56	2.780	5.560	1.480	1.848	1.679	1.299	0.197	0.696
25	A4040	4.160	7.76	4.160	7.760	1.810	2.438	0.692	0.692	0.603	0.836
26	A4050	3.020	5.17	3.020	5.170	1.670	1.428	1.469	1.352	0.605	0.809
27	E0010	3.620	5.88	3.620	5.880	1.690	2.308	1.422	0.902	0.191	0.846
28	E0020	2.390	4.97	2.390	4.970	1.430	2.309	2.299	0.433	0.439	1.019
29	E0030	3.640	5.18	3.640	5.180	2.140	1.424	1.424	1.269	0.203	0.618
30	E0040	2.660	5.16	2.660	5.160	1.590	1.325	1.515	1.398	0.501	0.840
31	A6020	3.360	5.33	3.360	5.330	1.560	1.329	1.510	1.393	0.502	0.768
32	A6030	3.000	5.63	3.000	5.630	1.590	2.304	2.107	0.518	0.183	0.821
33	A4020	2.750	4.93	2.750	4.930	1.860	1.559	1.238	1.121	0.736	0.789
34	D0030	3.750	7.05	3.750	7.050	2.530	1.243	1.483	1.366	0.420	0.747

Table A.4: Defect concentration part 1: Cu-Zn disorder, Zn_{Cu} and Cu_{Zn}.

No.	sample	Cu-Zn disorder			Zn_{Cu}			Cu_{Zn}		
		dc	err +	err -	dc	err +	err -	dc	err +	err -
1	A0125	5.98E+20	1.67E+20	1.77E+20				3.11E+19	8.70E+18	9.22E+18
2	A0100	1.25E+20	3.10E+19	5.90E+19				2.51E+20	6.21E+19	1.18E+20
3	A0050	1.72E+20	1.52E+19	1.11E+20				5.30E+20	4.69E+19	3.43E+20
4	A0025	4.64E+20	1.82E+20	6.06E+19				7.06E+20	2.77E+20	9.21E+19
5	A0000	6.28E+20	2.55E+20	2.80E+20				7.24E+20	2.94E+20	3.23E+20
6	A5010	1.34E+20	4.05E+19	7.08E+18	9.83E+19	2.97E+19	4.23E+18			
7	A3010	5.30E+20	2.27E+20	1.10E+20	1.04E+20	4.46E+19	2.17E+19			
8	A3020	1.33E+20	5.39E+19	1.99E+19	1.29E+20	5.24E+19	1.93E+19			
9	B1010	6.88E+20	3.05E+20	2.71E+20	1.43E+20	6.31E+19	5.62E+19			
10	B1020									
11	A2000	2.48E+20	4.34E+19	1.28E+20	2.09E+20	3.64E+19	1.08E+20			
12	C0025									
13	B2000	4.31E+20	1.53E+20	1.28E+20	4.26E+19	1.52E+19	1.26E+19			
14	B2010	4.28E+20	7.89E+19	7.30E+19	1.04E+20	1.92E+19	1.78E+19			
15	B2020	7.25E+20	1.61E+20	2.69E+20	1.49E+20	3.32E+19	5.55E+19			
16	B1000	5.12E+20	1.66E+20	6.37E+19	4.94E+19	1.60E+19	6.14E+18			
17	D0010	5.23E+20	1.31E+20	2.16E+20	1.31E+20	3.26E+18	5.41E+18			
18	D0040	9.00E+20	3.21E+20	2.63E+20				6.38E+19	2.27E+19	1.87E+19
19	D0050	3.32E+20	6.55E+19	1.06E+20				8.67E+19	1.71E+19	2.77E+19
20	D0020R	4.52E+20	2.77E+20	3.85E+19	6.65E+19	4.07E+19	5.67E+18			
21	D0000	4.35E+20	2.19E+20	1.61E+20	1.55E+20	7.82E+19	5.76E+19			
22	A4000	3.79E+20	1.95E+20	6.81E+19	1.42E+20	7.30E+19	2.55E+19			
23	A4010	4.43E+20	7.23E+19	1.09E+20	4.79E+19	7.81E+18	1.17E+19			
24	A4030	6.00E+20	3.10E+20	2.45E+20	4.61E+19	2.38E+18	1.88E+19			
25	A4040	6.24E+20	2.29E+20	3.15E+19				9.90E+19	3.63E+19	5.00E+18
26	A4050	1.44E+20	4.73E+19	1.13E+19	1.17E+20	3.86E+19	9.24E+18			
27	E0010	3.75E+20	1.40E+20	5.77E+19				2.81E+20	1.05E+20	4.31E+19
28	E0020	4.11E+20	1.10E+20	1.70E+20				1.43E+20	3.83E+19	5.93E+19
29	E0030	1.72E+20	5.39E+19	1.49E+19	5.55E+19	1.73E+19	4.80E+18			
30	E0040	1.71E+20	3.36E+19	4.00E+19	6.49E+19	1.28E+19	1.52E+19			
31	A6020	2.35E+20	6.88E+19	2.27E+19	4.77E+19	1.40E+19	4.61E+18			
32	A6030	3.47E+20	6.46E+19	7.89E+19				9.06E+19	1.69E+19	2.06E+19
33	A4020	1.65E+20	3.62E+19	4.28E+19	2.22E+20	4.87E+19	5.77E+19			
34	D0030	3.99E+20	1.85E+20	7.22E+19	1.75E+20	8.10E+19	3.17E+19			

Table A.5: Defect concentration part 2: V_{Cu}, Zn_{Sn}, Sn_{Zn} and Cu_i.

No.	sample	V_{Cu} dc	err +	err -	Zn_{Sn} dc	err +	err -	Sn_{Zn} dc	err +	err -	Cu_i dc	err
1	A0125							2.60E+19	5.17E+18	5.17E+18		
2	A0100							9.45E+19	4.29E+18	3.87E+19	6.17E+19	1.23E+18
3	A0050							1.74E+20	1.04E+19	7.64E+19	1.83E+20	3.65E+18
4	A0025							2.23E+20	6.18E+19	8.97E+18	2.60E+20	5.21E+18
5	A0000							2.60E+20	6.94E+19	6.94E+19	2.04E+20	4.08E+18
6	A5010	2.75E+19	6.02E+18	1.18E+18	3.54E+19	3.75E+18	5.95E+18					
7	A3010				5.10E+19	5.21E+18	1.13E+19					
8	A3020	3.19E+19	1.09E+19	1.40E+18	4.84E+19	8.24E+18	9.84E+18					
9	B1010				7.44E+19	7.45E+18	2.59E+19				6.16E+18	1.23E+17
10	B1020											
11	A2000				1.24E+20	3.50E+19	2.50E+19				3.86E+19	7.73E+17
12	C0025											
13	B2000				5.38E+19	9.21E+18	1.36E+19				6.49E+19	1.30E+18
14	B2010				7.92E+19	1.14E+19	1.14E+19				5.43E+19	1.09E+18
15	B2020				1.09E+20	1.56E+19	1.56E+19				6.84E+19	1.37E+18
16	B1000				5.79E+19	5.99E+18	1.20E+19				6.65E+19	1.33E+18
17	D0010				4.65E+19	5.30E+18	1.38E+19				8.01E+19	1.60E+18
18	D0040				3.89E+19	4.86E+18	9.17E+18				1.42E+20	2.83E+18
19	D0050				2.67E+19	5.11E+18	5.19E+18				1.40E+20	2.80E+18
20	D0020R				9.66E+19	1.18E+19	3.14E+19				1.27E+20	2.53E+18
21	D0000				1.26E+20	2.72E+19	4.29E+18				9.75E+19	1.95E+18
22	A4000	4.13E+19	1.54E+19	6.91E+18	5.03E+19	8.58E+18	8.33E+18					
23	A4010				3.85E+19	7.70E+18	9.40E+17				2.92E+19	5.84E+17
24	A4030				4.61E+19	9.83E+18	8.45E+16				4.62E+19	9.23E+17
25	A4040							1.98E+19	5.95E+18	1.32E+17	5.93E+19	1.19E+18
26	A4050	3.27E+19	7.72E+18	1.88E+18	4.23E+19	5.05E+18	1.27E+18					
27	E0010							1.22E+20	3.65E+19	5.00E+18	3.72E+19	7.45E+17
28	E0020							5.30E+19	1.10E+19	1.25E+19	3.70E+19	7.41E+17
29	E0030	1.91E+19	4.92E+18	3.82E+17	1.82E+19	2.66E+18	2.09E+18					
30	E0040	8.46E+18	1.02E+19	1.59E+18	2.82E+19	5.22E+18	2.84E+18					
31	A6020	2.03E+19	4.15E+18	1.50E+18	1.37E+19	3.27E+18	4.78E+17					
32	A6030							5.13E+19	7.00E+18	7.00E+18		
33	A4020	1.43E+20	2.14E+19	2.92E+19	3.99E+19	4.26E+18	9.17E+18					
34	D0030				9.34E+19	8.50E+18	1.01E+19				3.70E+19	7.41E+17

Table A.6: Defect concentration of V_{Cu}, Cu-Zn disorder, Zn_{Cu}, Cu_{Zn}, Zn_{Sn}, Sn_{Zn} and Cu_i calculated in %.

No.	sample	V_{Cu}	Cu-Zn disorder	Zn_{Cu}	Cu_{Zn}	Zn_{Sn}	Sn_{Zn}	Cu_i
1	A0125		19%		1%		1%	
2	A0100		4%		8%		3%	2%
3	A0050		5%		17%		6%	6%
4	A0025		15%		22%		7%	8%
5	A0000		20%		23%		8%	6%
6	A5010	1%	4%	3%		1%		
7	A3010		17%	3%		2%		
8	A3020	1%	4%	4%		2%		
9	B1010		22%	5%		2%		0%
10	B1020							
11	A2000		8%	7%		4%		1%
12	C0025							
13	B2000		14%	1%		2%		2%
14	B2010		14%	3%		3%		2%
15	B2020		23%	5%		3%		2%
16	B1000		16%	2%		2%		2%
17	D0010		17%	0%		1%		3%
18	D0040		29%		2%	1%		5%
19	D0050		11%		3%	1%		4%
20	D0020R		14%	2%		3%		4%
21	D0000		14%	5%		4%		3%
22	A4000	1%	12%	5%		2%		
23	A4010		14%	2%		1%		1%
24	A4030		19%	1%		1%		1%
25	A4040		20%		3%		1%	2%
26	A4050	1%	5%	4%		1%		
27	E0010		12%		9%		4%	1%
28	E0020		13%		5%		2%	1%
29	E0030	1%	6%	2%		1%		
30	E0040	0%	5%	2%		1%		
31	A6020	1%	8%	2%		0%		
32	A6030		11%		3%		2%	
33	A4020	5%	5%	7%		1%		
34	D0030		13%	6%		3%		0%

Table A.7: Sample overview of bond distances of the Rietveld refinement and calculated bond distances of the neutron cation distribution.

No.	sample	Bond distance (RR)								Bond distance (Calc)							
		Cu(2a)-S	err	Cu(2c)-S	err	Zn(2d)-S	err	Sn(2b)-S	err	Cu(2a)-S	err	Cu(2c)-S	err	Zn(2d)-S	err	Sn(2b)-S	err
1	A0125	2.3329	0.0233	2.3737	0.0237	2.3531	0.0235	2.3426	0.0234	2.3350	0.0234	2.3360	0.0234	2.3394	0.0234	2.3900	0.0239
2	A0100	2.3077	0.0231	2.3577	0.0236	2.3808	0.0238	2.3543	0.0235	2.3350	0.0234	2.3352	0.0234	2.3409	0.0234	2.3900	0.0239
3	A0050	2.3602	0.0236	2.3623	0.0236	2.2662	0.0227	2.4022	0.0240	2.3350	0.0234	2.3353	0.0234	2.3416	0.0234	2.3900	0.0239
4	A0025	2.3260	0.0233	2.3392	0.0234	2.3496	0.0235	2.3642	0.0236	2.3350	0.0234	2.3357	0.0234	2.3417	0.0234	2.3900	0.0239
5	A0000	2.3431	0.0234	2.3225	0.0232	2.3313	0.0233	2.3830	0.0238	2.3350	0.0234	2.3360	0.0234	2.3420	0.0234	2.3900	0.0239
6	A5010	2.3018	0.0230	2.3774	0.0238	2.3340	0.0233	2.3936	0.0239	2.3350	0.0234	2.3298	0.0233	2.3398	0.0234	2.3894	0.0239
7	A3010	2.3375	0.0234	2.3308	0.0233	2.3329	0.0233	2.4019	0.0240	2.3350	0.0234	2.3360	0.0234	2.3392	0.0234	2.3892	0.0239
8	A3020	2.3290	0.0233	2.3624	0.0236	2.3186	0.0232	2.3967	0.0240	2.3350	0.0234	2.3289	0.0233	2.3398	0.0234	2.3892	0.0239
9	B1010	2.3424	0.0234	2.3551	0.0236	2.3340	0.0236	2.3731	0.0237	2.3350	0.0234	2.3363	0.0234	2.3389	0.0234	2.3888	0.0239
10	B1020	2.3331	0.0233	2.3615	0.0236	2.2341	0.0236	2.4911	0.0249								
11	A2000	2.3088	0.0231	2.3627	0.0236	2.3084	0.0236	2.4294	0.0243	2.3350	0.0234	2.3357	0.0234	2.3396	0.0234	2.3880	0.0239
12	C0025																
13	B2000	2.3194	0.0232	2.3669	0.0237	2.3311	0.0233	2.3947	0.0239	2.3350	0.0234	2.3358	0.0234	2.3393	0.0234	2.3891	0.0239
14	B2010	2.3012	0.0230	2.3666	0.0237	2.3377	0.0234	2.4033	0.0240	2.3350	0.0234	2.3359	0.0234	2.3393	0.0234	2.3887	0.0239
15	B2020	2.3287	0.0233	2.3011	0.0230	2.4074	0.0241	2.3755	0.0238	2.3350	0.0234	2.3364	0.0234	2.3388	0.0234	2.3883	0.0239
16	B1000	2.4472	0.0245	2.2776	0.0228	2.3387	0.0234	2.3469	0.0235	2.3350	0.0234	2.3359	0.0234	2.3392	0.0234	2.3891	0.0239
17	D0010	2.3026	0.0230	2.3632	0.0236	2.3276	0.0233	2.4118	0.0241	2.3350	0.0234	2.3359	0.0234	2.3392	0.0234	2.3893	0.0239
18	D0040	2.3824	0.0238	2.3810	0.0238	2.3596	0.0236	2.2797	0.0228	2.3350	0.0234	2.3364	0.0234	2.3385	0.0234	2.3894	0.0239
19	D0050	2.3130	0.0231	2.3673	0.0237	2.3349	0.0233	2.3882	0.0239	2.3350	0.0234	2.3355	0.0234	2.3393	0.0234	2.3896	0.0239
20	D0020R	2.3123	0.0231	2.3438	0.0234	2.3559	0.0236	2.3949	0.0239	2.3350	0.0234	2.3358	0.0234	2.3393	0.0234	2.3885	0.0239
21	D0000	2.2837	0.0228	2.4013	0.0240	2.3017	0.0230	2.4276	0.0243	2.3350	0.0234	2.3359	0.0234	2.3393	0.0234	2.3880	0.0239
22	A4000	2.2706	0.0227	2.3506	0.0235	2.3647	0.0235	2.4269	0.0243	2.3350	0.0234	2.3274	0.0233	2.3394	0.0234	2.3892	0.0239
23	A4010	2.2826	0.0228	2.3702	0.0237	2.3320	0.0237	2.4280	0.0243	2.3350	0.0234	2.3358	0.0234	2.3393	0.0234	2.3894	0.0239
24	A4030	2.2614	0.0226	2.3700	0.0237	2.3586	0.0237	2.4201	0.0242	2.3350	0.0234	2.3360	0.0234	2.3390	0.0234	2.3893	0.0239
25	A4040	2.3550	0.0236	2.3575	0.0236	2.3227	0.0236	2.3745	0.0232	2.3350	0.0234	2.3360	0.0234	2.3392	0.0234	2.3900	0.0239
26	A4050	2.3124	0.0231	2.3845	0.0238	2.3097	0.0238	2.4040	0.0240	2.3350	0.0234	2.3288	0.0233	2.3398	0.0234	2.3893	0.0239
27	E0010	2.3791	0.0238	2.3509	0.0235	2.2925	0.0235	2.3902	0.0229	2.3350	0.0234	2.3356	0.0234	2.3409	0.0234	2.3900	0.0239
28	E0020	2.2810	0.0228	2.3841	0.0238	2.3559	0.0238	2.3947	0.0236	2.3350	0.0234	2.3357	0.0234	2.3400	0.0234	2.3900	0.0239
29	E0030	2.2979	0.0230	2.3636	0.0236	2.3395	0.0236	2.4110	0.0234	2.3350	0.0234	2.3315	0.0233	2.3397	0.0234	2.3897	0.0239
30	E0040	2.2848	0.0228	2.3758	0.0238	2.3455	0.0238	2.4019	0.0235	2.3350	0.0234	2.3337	0.0233	2.3397	0.0234	2.3895	0.0239
31	A6020	2.3105	0.0231	2.3730	0.0237	2.3222	0.0237	2.4045	0.0232	2.3350	0.0234	2.3313	0.0233	2.3396	0.0234	2.3898	0.0239
32	A6030	2.3665	0.0237	2.3360	0.0234	2.2982	0.0234	2.4156	0.0230	2.3350	0.0234	2.3356	0.0234	2.3401	0.0234	2.3900	0.0239
33	A4020	2.2985	0.0230	2.3903	0.0239	2.3079	0.0239	2.4147	0.0231	2.3350	0.0234	2.3066	0.0231	2.3397	0.0231	2.3894	0.0239
34	D0030	2.2837	0.0228	2.4013	0.0240	2.3017	0.0240	2.4276	0.0230	2.3350	0.0234	2.3359	0.0234	2.3394	0.0234	2.3885	0.0239

Table A.8: Sample overview of the bond angles (tetrahedral angles).

No.	sample	Bond angle									
		Cu(2a)-S-Zn(2d)	err	Cu(2a)-S-Sn(2b)	err	Cu(2c)-S-Zn(2d)	err	Cu(2c)-S-Sn(2b)	err	Zn(2d)-S-Sn(2b)	err
1	A0125	110.0270	1.1003	110.2790	1.1028	108.5160	1.0852	108.9820	1.0898	109.6920	1.0969
2	A0100	109.8850	1.0989	110.7100	1.1071	108.0790	1.0808	109.0850	1.0909	108.3030	1.0830
3	A0050	111.8660	1.1187	107.1010	1.0710	111.7010	1.1170	107.1090	1.0711	110.3370	1.1034
4	A0025	109.9180	1.0992	109.4975	1.0950	109.5468	1.0955	108.9580	1.0896	108.6040	1.0860
5	A0000	109.9900	1.0999	108.2200	1.0822	110.7200	1.1072	108.9200	1.0892	108.6200	1.0862
6	A5010	111.7359	1.1174	109.8736	1.0987	109.3355	1.0934	107.0822	1.0708	108.5143	1.0851
7	A3010	110.4448	1.1044	108.3251	1.0833	110.9495	1.1095	108.2890	1.0829	108.2196	1.0822
8	A3020	111.3186	1.1132	108.8513	1.0885	110.3993	1.1040	107.4769	1.0748	108.9343	1.0893
9	B1010	110.2835	1.1028	109.1716	1.0917	110.0858	1.1009	108.5026	1.0850	109.2151	1.0922
10	B1020	114.3263	1.1433	105.5778	1.0558	113.4714	1.1347	104.5080	1.0451	108.5040	1.0850
11	A2000	112.5867	1.1259	108.1177	1.0812	110.4448	1.1044	106.5408	1.0654	108.3020	1.0830
12	C0025										
13	B2000	111.3631	1.1136	109.3821	1.0938	109.8381	1.0984	107.4428	1.0744	108.5583	1.0856
14	B2010	111.6578	1.1166	109.5766	1.0958	109.6021	1.0960	107.1534	1.0715	108.1000	1.0810
15	B2020	108.3260	1.0833	109.6380	1.0964	109.4740	1.0947	110.3760	1.1038	106.7980	1.0680
16	B1000	106.5747	1.0657	106.5593	1.0656	112.7119	1.1271	112.1342	1.1213	109.9520	1.0995
17	D0010	111.9079	1.1191	109.1547	1.0915	109.9886	1.0999	106.9228	1.0692	108.0827	1.0808
18	D0040	108.0870	1.0809	110.6860	1.1069	108.0080	1.0801	110.8710	1.1087	111.6490	1.1165
19	D0050	111.3920	1.1139	109.3570	1.0936	109.3320	1.0933	107.6810	1.0768	108.7580	1.0876
20	D0020R	110.7350	1.1074	109.1870	1.0919	109.4600	1.0946	108.3010	1.0830	107.9000	1.0790
21	D0000	113.6720	1.1367	109.3631	1.0936	109.6703	1.0967	105.2920	1.0529	108.4830	1.0848
22	A4000	111.7943	1.1179	109.8195	1.0982	109.2497	1.0925	106.9144	1.0691	106.4619	1.0646
23	A4010	112.5738	1.1257	109.3864	1.0939	109.7120	1.0971	106.2570	1.0626	107.4823	1.0748
24	A4030	112.2932	1.1229	110.3424	1.1034	108.7638	1.0876	106.4582	1.0646	106.8217	1.0682
25	A4040	110.3370	1.1034	108.7489	1.0875	110.4514	1.1045	108.4725	1.0847	109.6532	1.0965
26	A4050	112.4133	1.1241	109.6294	1.0963	109.4898	1.0949	106.3966	1.0640	107.4026	1.0740
27	E0010	110.9920	1.1099	107.2854	1.0729	111.9023	1.1190	107.7822	1.0778	110.0295	1.1003
28	E0020	111.8519	1.1185	110.6492	1.1065	108.4536	1.0845	106.9806	1.0698	107.9023	1.0790
29	E0030	111.7553	1.1176	109.4838	1.0948	109.7026	1.0970	107.0362	1.0704	107.8203	1.0782
30	E0040	111.9339	1.1193	110.1753	1.1018	109.0053	1.0901	106.8669	1.0687	107.8559	1.0786
31	A6020	111.9089	1.1191	109.2459	1.0925	109.9415	1.0994	106.9254	1.0693	108.5962	1.0860
32	A6030	110.8615	1.1086	107.0739	1.0707	112.1828	1.1218	107.8721	1.0787	109.1300	1.0913
33	A4020	112.8577	1.1286	109.3099	1.0931	109.8402	1.0984	106.0260	1.0603	108.7005	1.0870
34	D0030	112.5190	1.1252	109.6595	1.0966	109.4877	1.0949	106.3611	1.0636	108.8956	1.0890

A.2 BSE micrographs and neutron diffraction patterns

1 - A0125 - $Cu_{2.01}Zn_{0.98}Sn_{1.01}S_4$ - C 81 % E 19 %
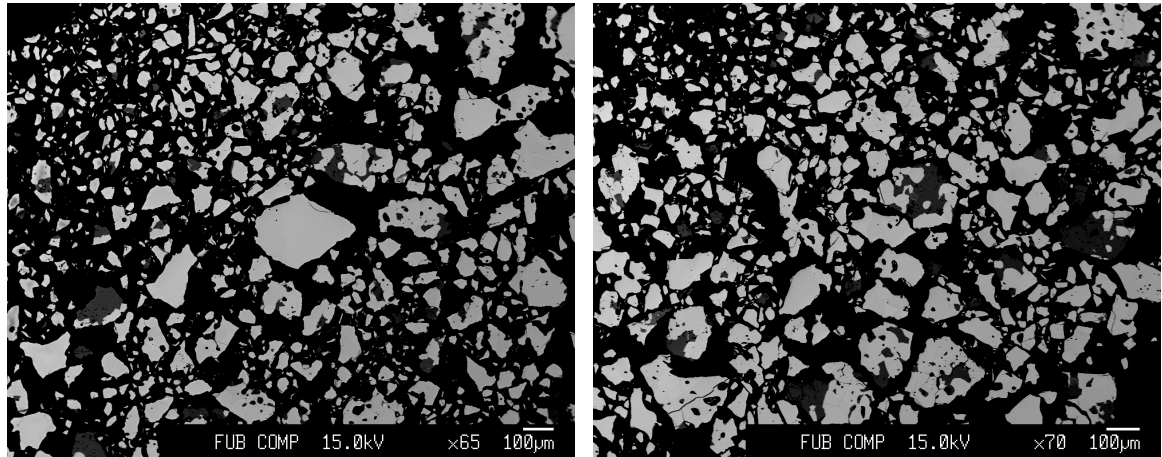
Figure A.1: BSE micrographs: 1 - A0125

$Cu / (Zn + Sn) = 1.008(17)$, $Zn / Sn = 0.974(14)$
Secondary phases: $Cu_{0.92}S$ (9 %); $Zn_{0.88}(Cu_{0.02}Sn_{0.01})S$
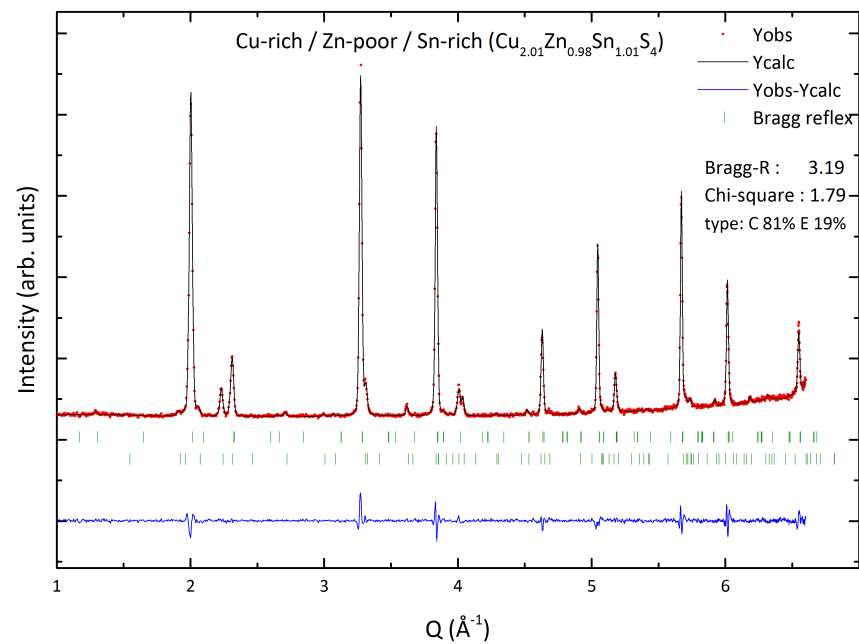
Figure A.2: Neutron diffraction pattern: 1 - A0125

2 - **A0100** - **Cu$_{2.10}$Zn$_{0.89}$Sn$_{1.03}$S$_4$** - **C 86 % E 14 %**
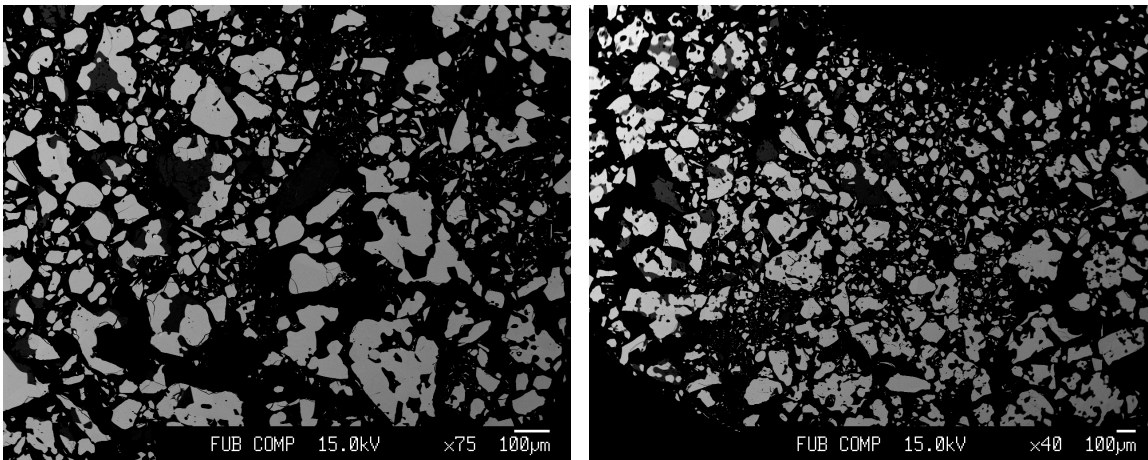
Figure A.3: BSE micrographs: 2 - A0100

Cu / (Zn + Sn) = 1.094(19), Zn / Sn = 0.864(12)
Secondary phases: Cu$_{0.92}$S (18 %)
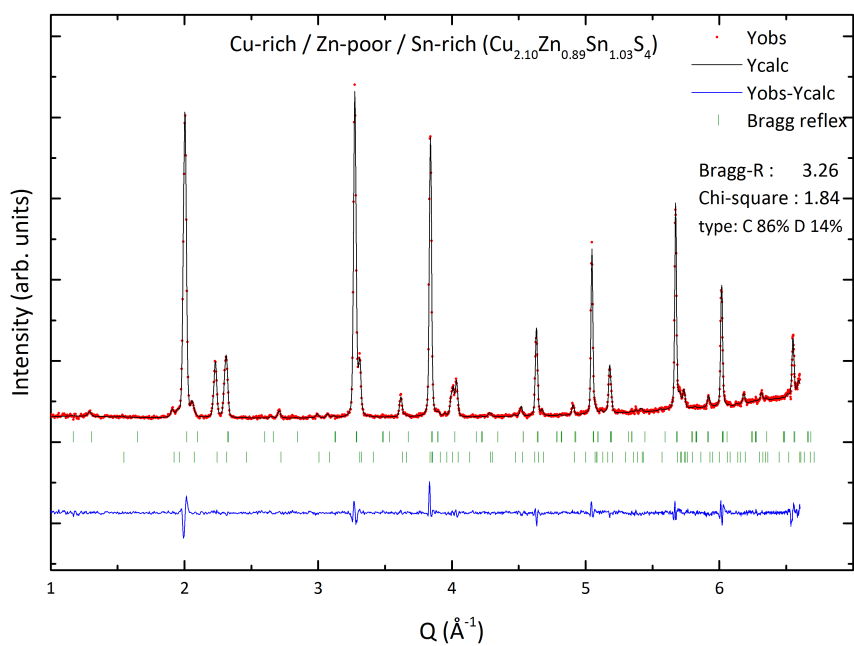
Figure A.4: Neutron diffraction pattern: 2 - A0100

3 - **A0050** - **Cu$_{2.23}$Zn$_{0.78}$Sn$_{1.06}$S$_4$** - **C 78 % E 22 %**
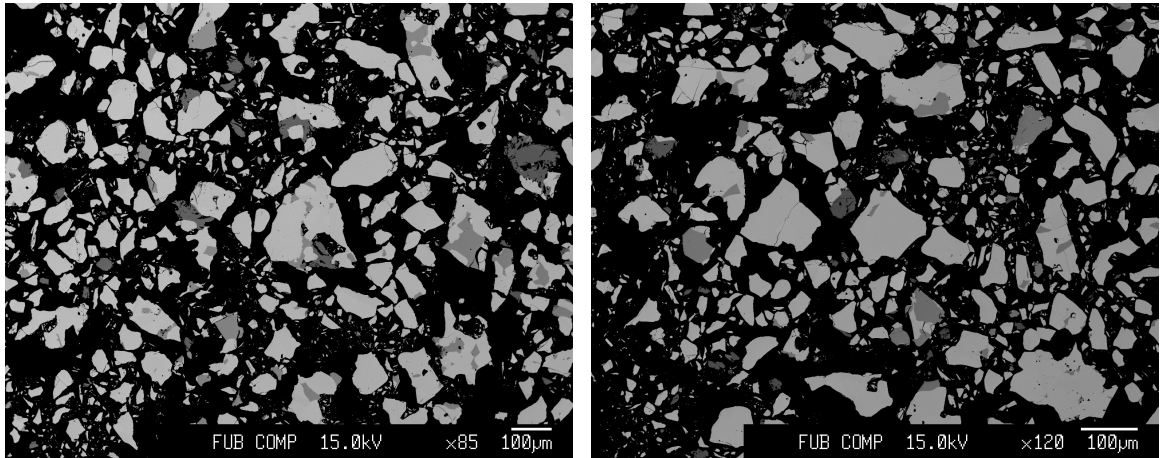
Figure A.5: BSE micrographs: 3 - A0050

$Cu / (Zn + Sn) = 1.220(21)$, $Zn / Sn = 0.735(10)$
Secondary phases: $Cu_{0.98}S$ (4 %); $Cu_{1.70}S$ (4 %)
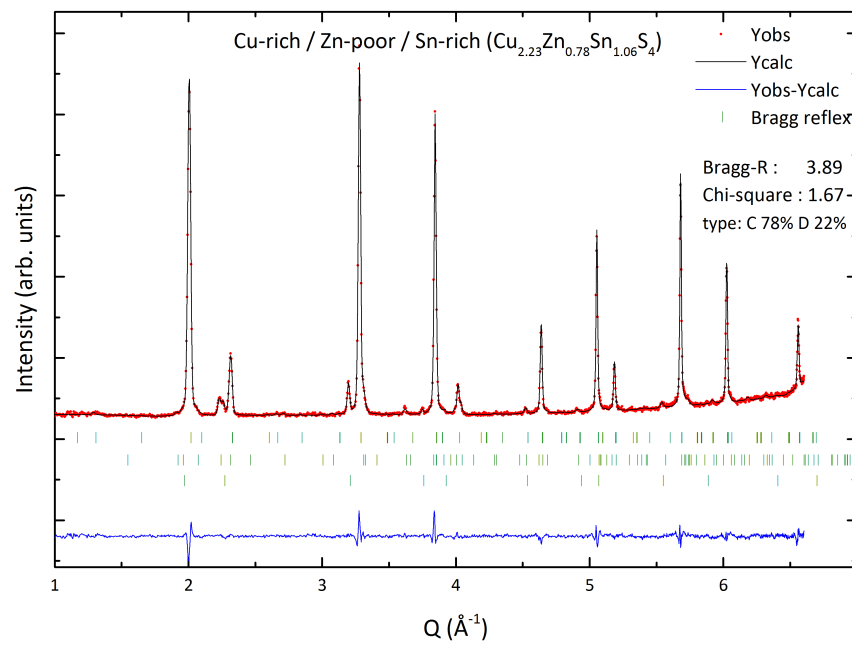
Figure A.6: Neutron diffraction pattern: 3 - A0050

4 - **A0025** - **Cu$_{2.31}$Zn$_{0.71}$Sn$_{1.07}$S$_4$** - **C 76 % E 24 %**
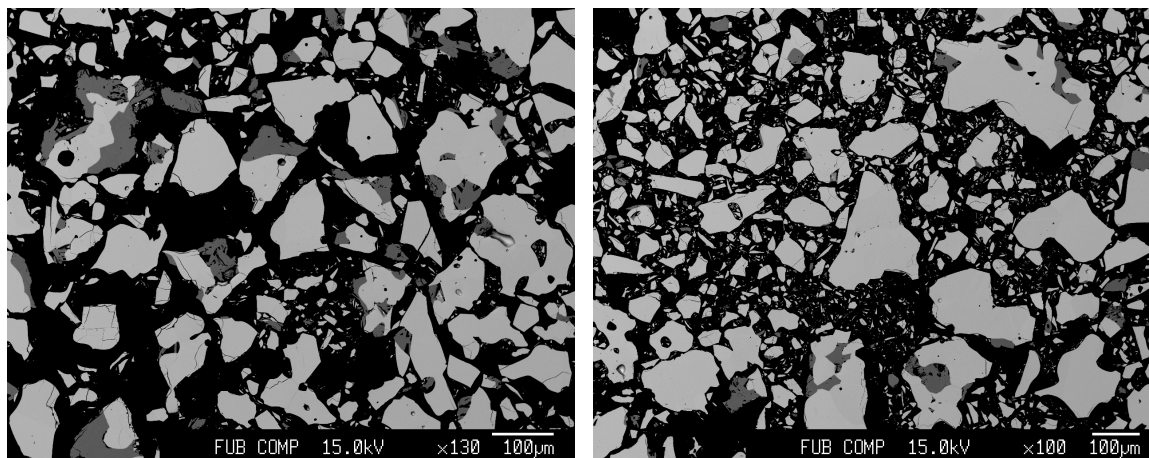
Figure A.7: BSE micrographs: 4 - A0025

Cu / (Zn + Sn) = 1.305(22), Zn / Sn = 0.659(10)
Secondary phases: Cu$_{0.92}$S (3 %) (Cu$_{2-x}$S (1 %))
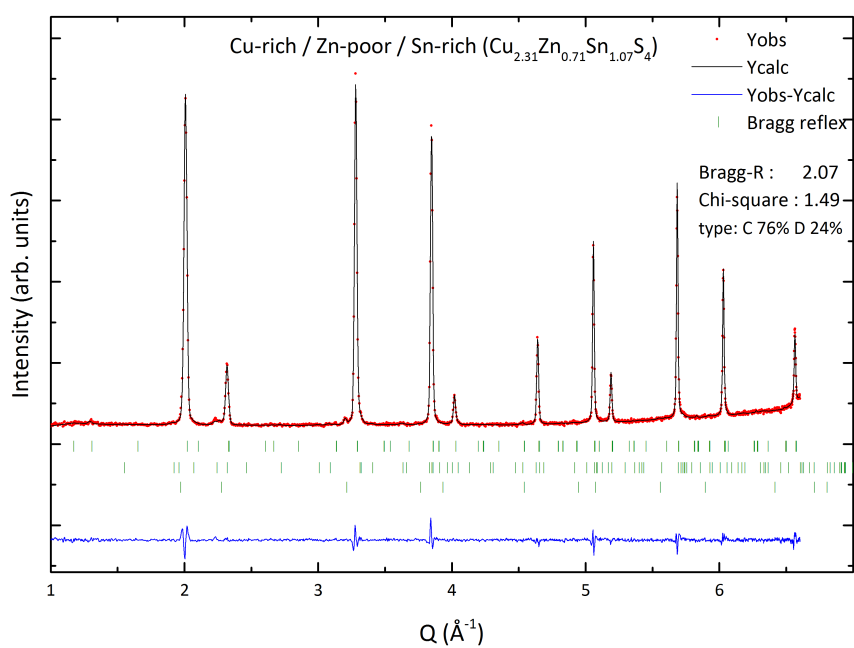
Figure A.8: Neutron diffraction pattern: 4 - A0025

5 - **A0000** - $Cu_{2.30}Zn_{0.69}Sn_{1.08}S_4$ - **C 82 % E 18 %**
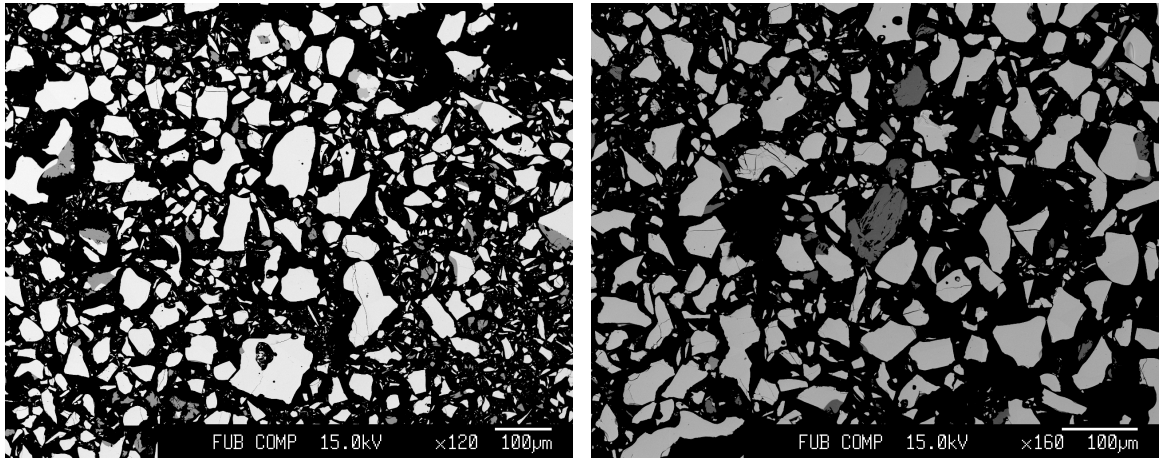
Figure A.9: BSE micrographs: 5 - A0000

$Cu / (Zn + Sn) = 1.303(23)$, $Zn / Sn = 0.635(9)$
Secondary phases: $Cu_{0.92}S$ (9%); $Cu_{1.63}S$; $Zn_{0.91}(Cu_{0.01})S$
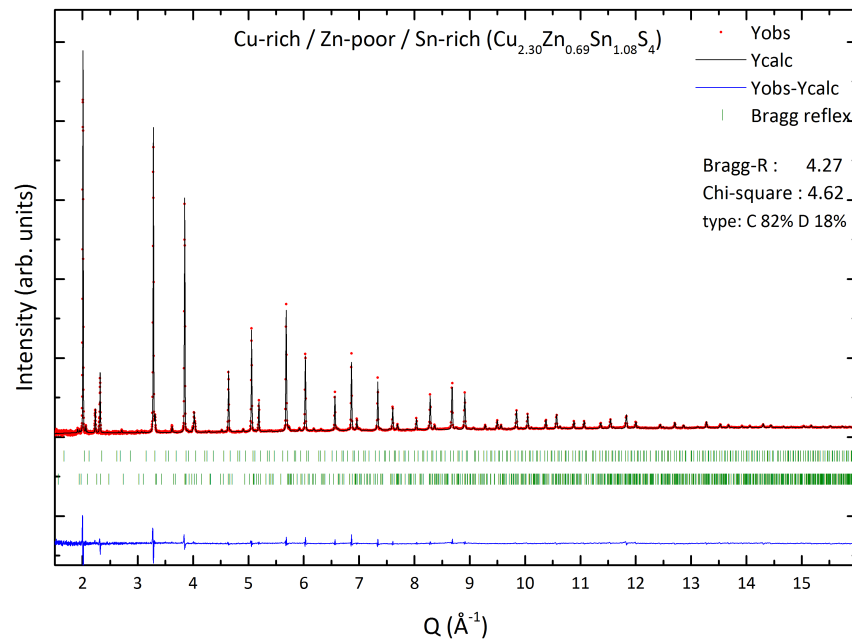
Figure A.10: Neutron diffraction pattern: 5 - A0000

6 - **A5010** - **Cu$_{1.96}$Zn$_{1.04}$Sn$_{0.99}$S$_4$** - **A 16 % B 84 %**
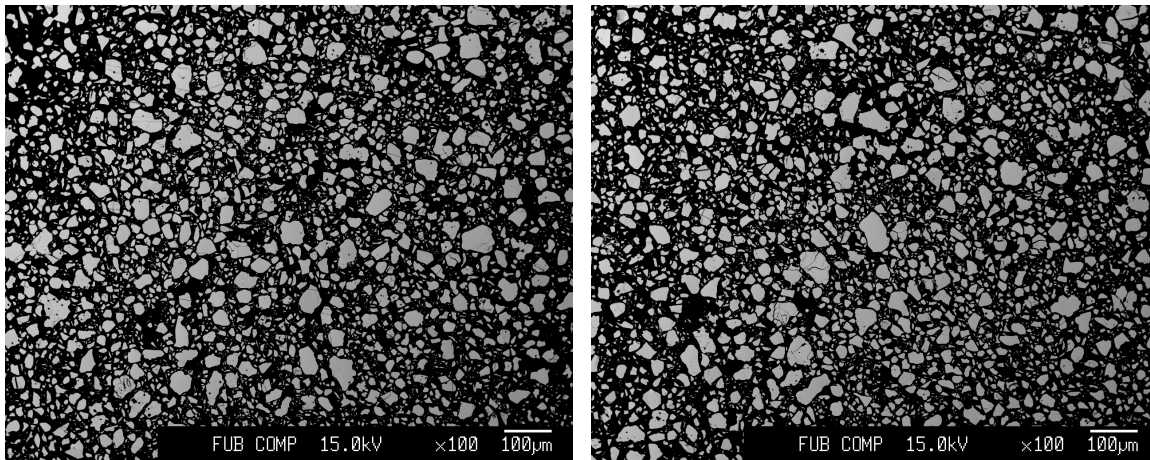
Figure A.11: BSE micrographs: 6 - A5010

$Cu / (Zn + Sn) = 0.965(17)$, $Zn / Sn = 1.055(15)$
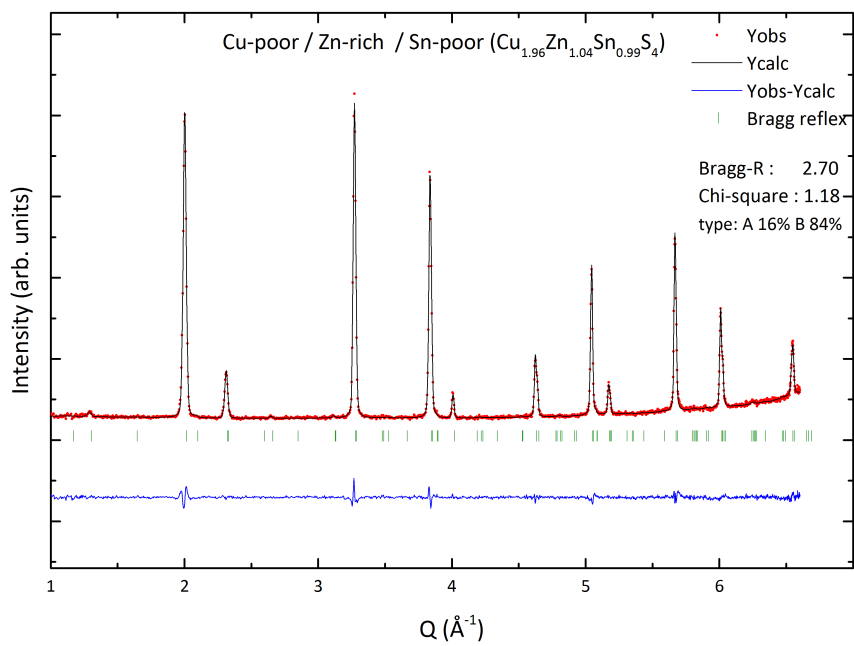
Figure A.12: Neutron diffraction pattern: 6 - A5010

7 - **A3010** - **Cu$_{1.97}$Zn$_{1.05}$Sn$_{0.98}$S$_4$** - **A 1 % B 99 %**
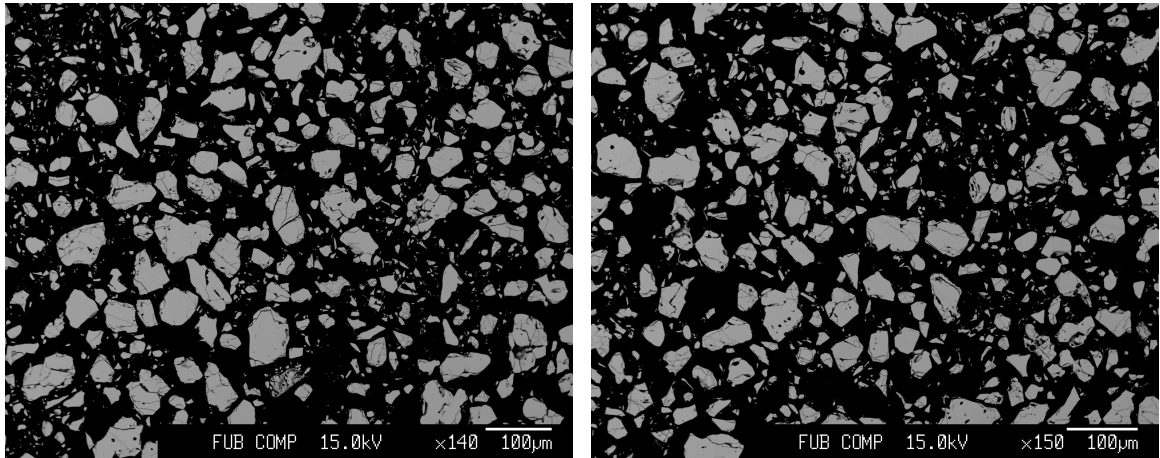
Figure A.13: BSE micrographs: 7 - A3010

$Cu / (Zn + Sn) = 0.967(17)$, $Zn / Sn = 1.067(15)$
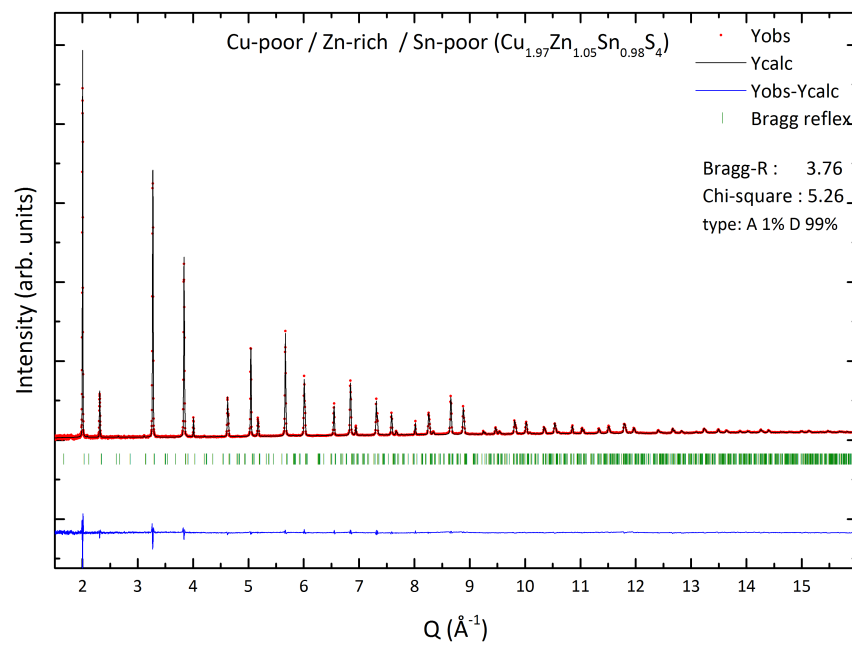
Figure A.14: Neutron diffraction pattern: 7 - A3010

8 - **A3020** - **Cu$_{1.95}$Zn$_{1.06}$Sn$_{0.99}$S$_4$** - **A 14 % B 86 %**
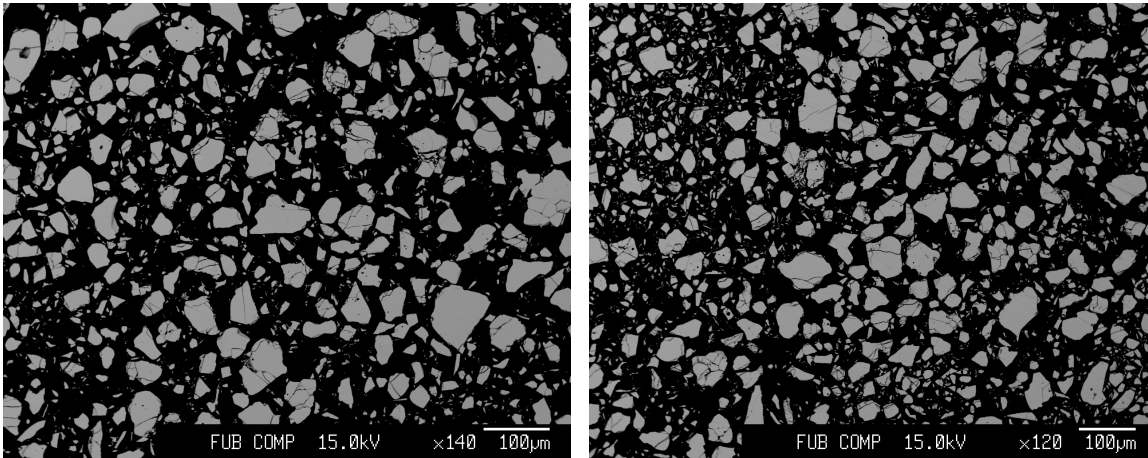
Figure A.15: BSE micrographs: 8 - A3020

Cu $/$ (Zn $+$ Sn) $= 0.955(17)$, Zn $/$ Sn $= 1.073(15)$
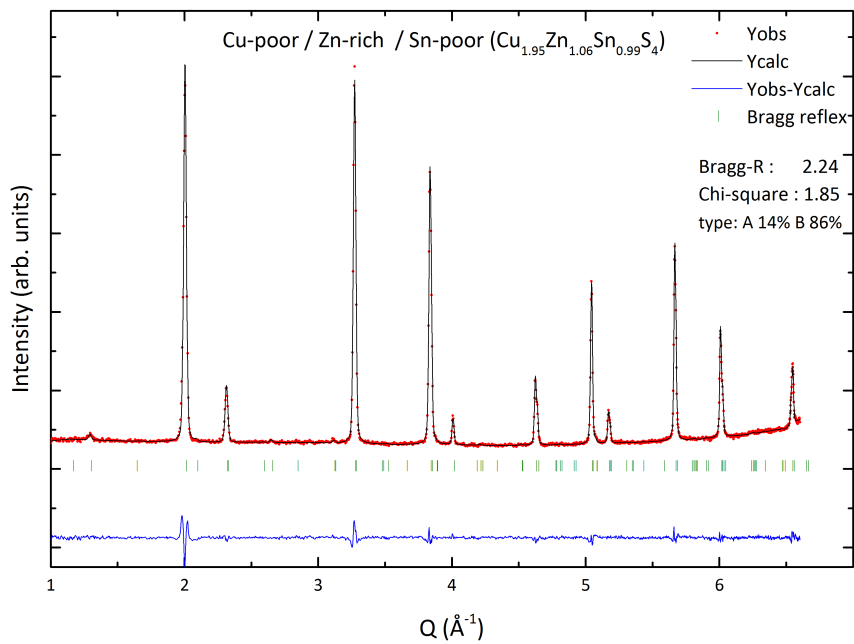
Figure A.16: Neutron diffraction pattern: 8 - A3020

9 - B1010 - $Cu_{1.96}Zn_{1.07}Sn_{0.98}S_4$ - B 95 % F 5 %
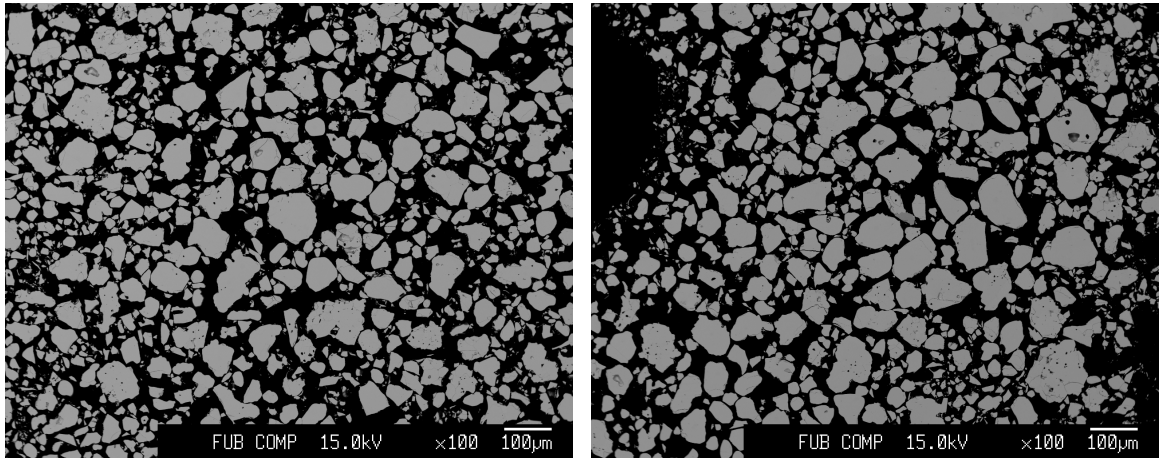
Figure A.17: BSE micrographs: 9 - B1010

$Cu / (Zn + Sn) = 0.959(17)$, $Zn / Sn = 1.096(16)$
Secondary phases: $Zn_{0.92}(Cu_{0.05}Sn_{0.02})S$
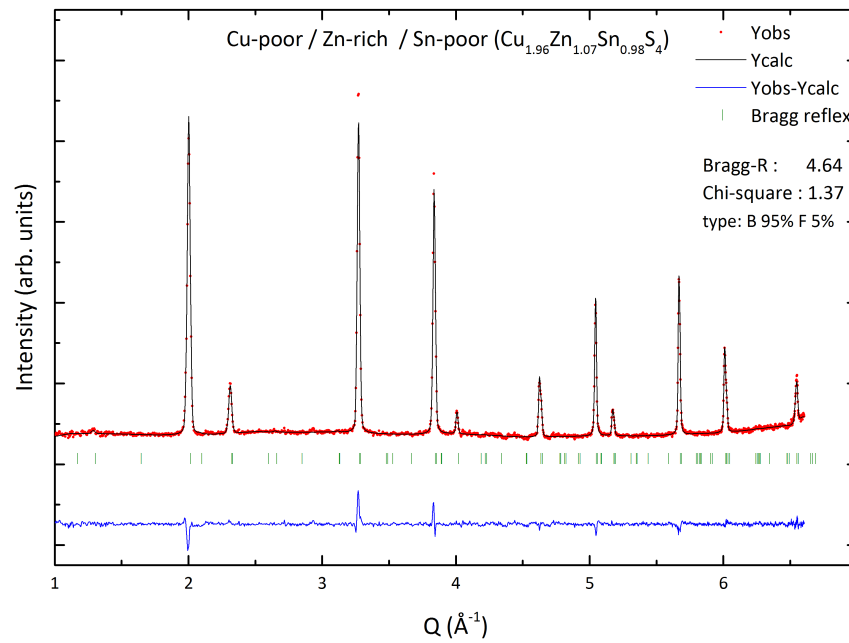
Figure A.18: Neutron diffraction pattern: 9 - B1010

10 - B1020 - Cu$_{1.95}$Zn$_{1.09}$Sn$_{0.97}$S$_4$ - B 95 % F 5 %
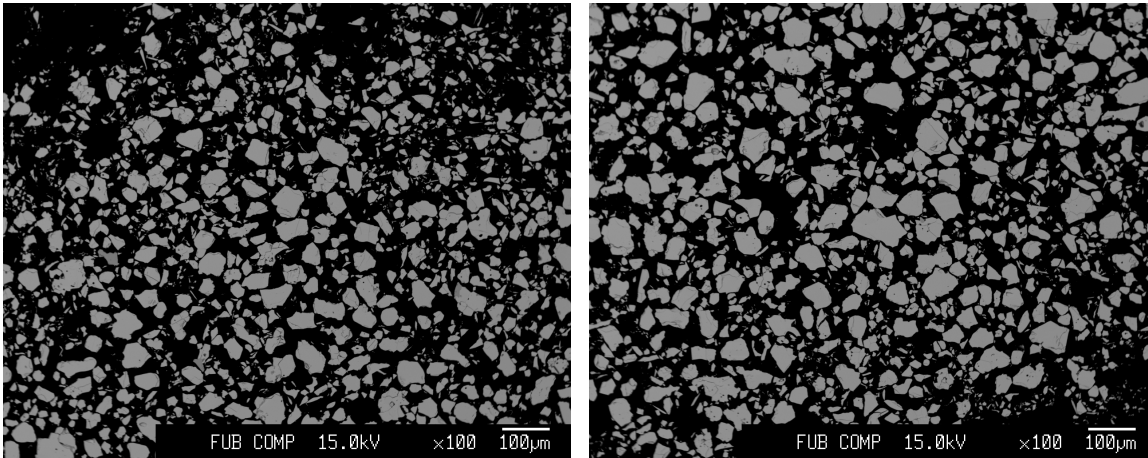
Figure A.19: BSE micrographs: 10 - B1020

$Cu/(Zn+Sn) = 0.944(16)$, $Zn/Sn = 1.131(16)$
Secondary phases: $Zn_{0.95}(Cu_{0.04}Sn_{0.01})S$
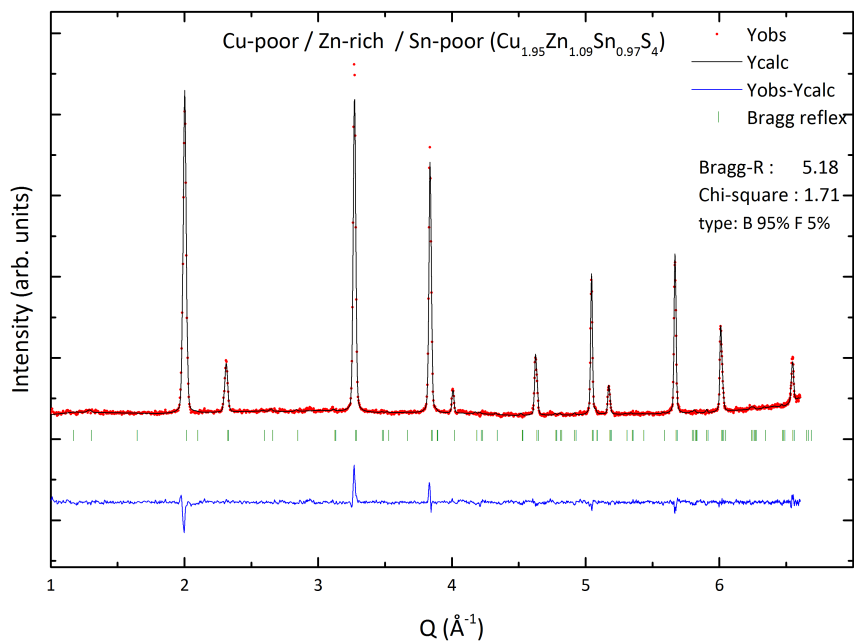
Figure A.20: Neutron diffraction pattern: 10 - B1020

11 - **A2000** - $\mathbf{Cu_{1.95}Zn_{1.11}Sn_{0.96}S_4}$ - **B 91 % F 9 %**
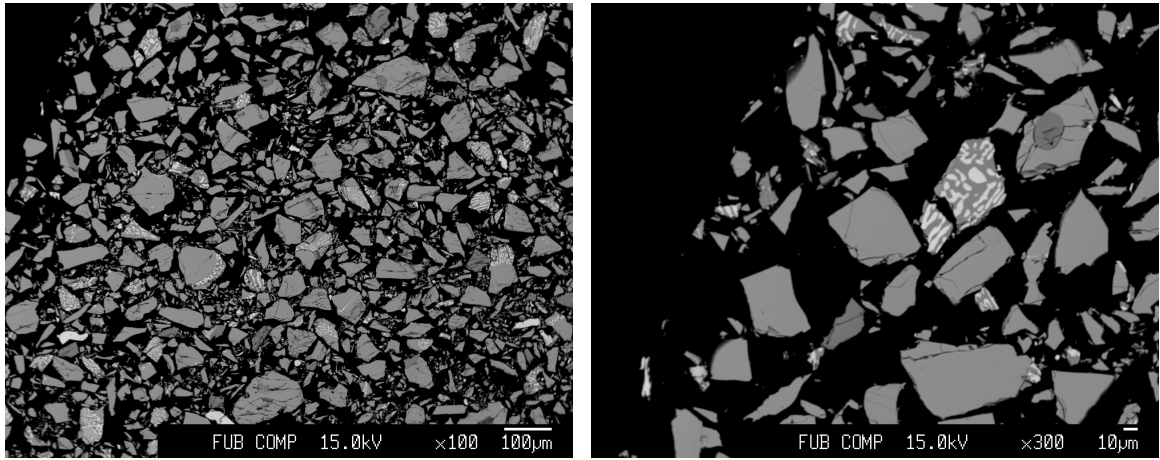
Figure A.21: BSE micrographs: 11 - A2000

$Cu / (Zn + Sn) = 0.941(16)$, $Zn / Sn = 1.152(16)$
Secondary phases: $Zn_{0.96}(Cu_{0.04}Sn_{0.01})S$; $Sn_{0.97}(Cu_{0.02}Zn_{0.01})S$ (11 %); $Cu_{1.85}S$ (12 %)
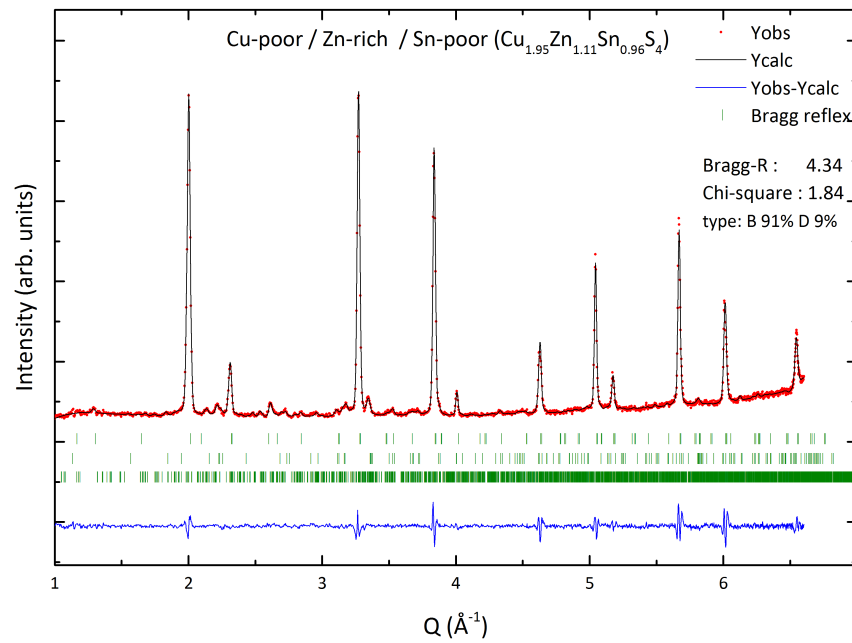
Figure A.22: Neutron diffraction pattern: 11 - A2000

12 - C0025 - $Cu_{1.95}Zn_{1.10}Sn_{0.96}S_4$ - B 91 % F 9 %
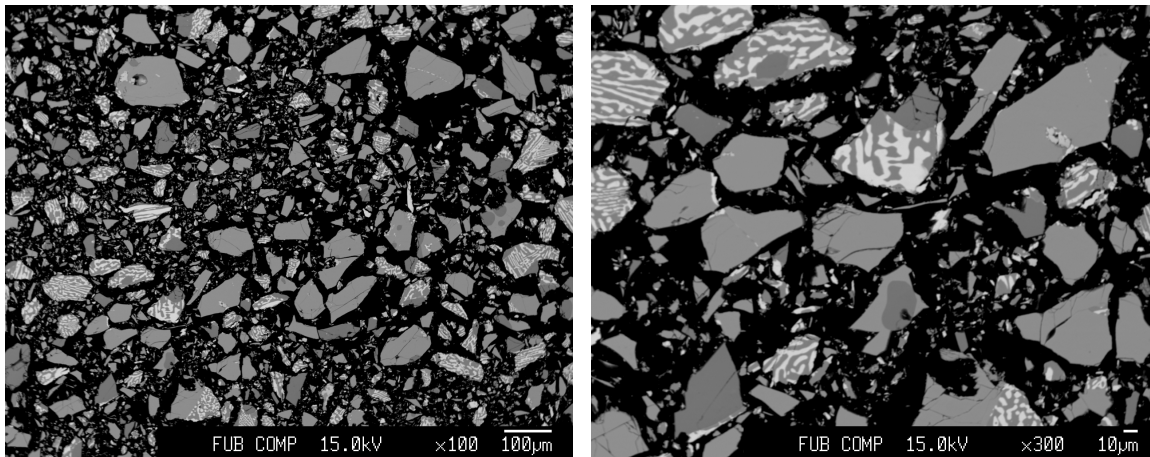
Figure A.23: BSE micrographs: 12 - C0025

$Cu / (Zn + Sn) = 0.943(16)$, $Zn / Sn = 1.147(16)$
Secondary phases: $Zn_{0.96}(Cu_{0.04}Sn_{0.01})S$; $Sn_{0.97}(Cu_{0.02}Zn_{0.01})S$ (33 %), $Cu_{1.86}S$
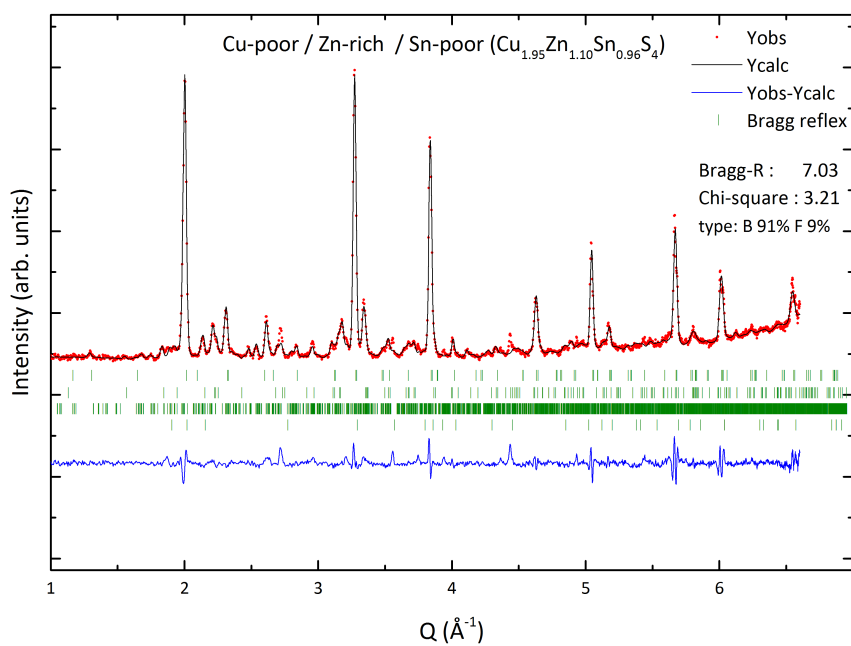
Figure A.24: Neutron diffraction pattern: 12 - C0025

13 - B2000 - $Cu_{2.01}Zn_{1.03}Sn_{0.98}S_4$ - B 57 % F 43 %
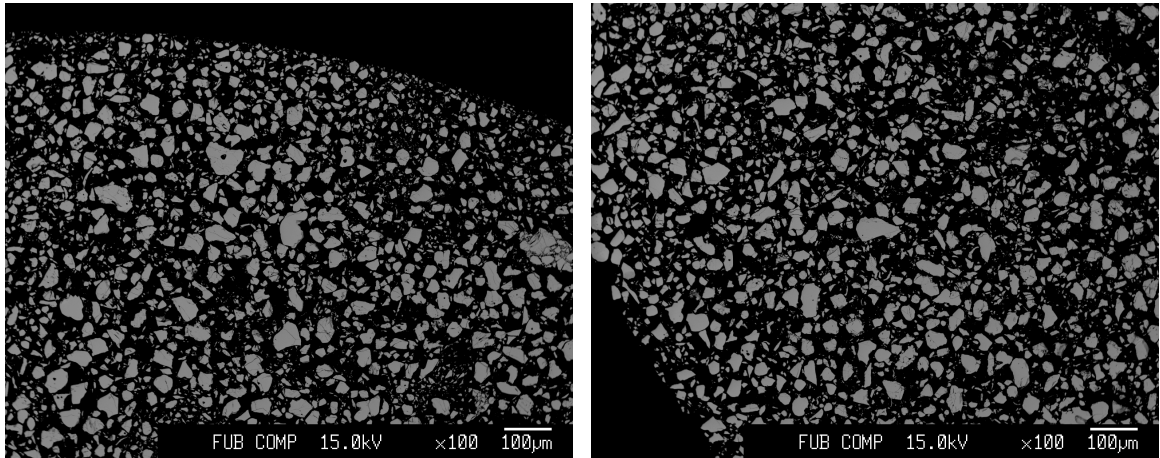
Figure A.25: BSE micrographs: 13 - B2000

$Cu / (Zn + Sn) = 0.997(17)$, $Zn / Sn = 1.049(15)$
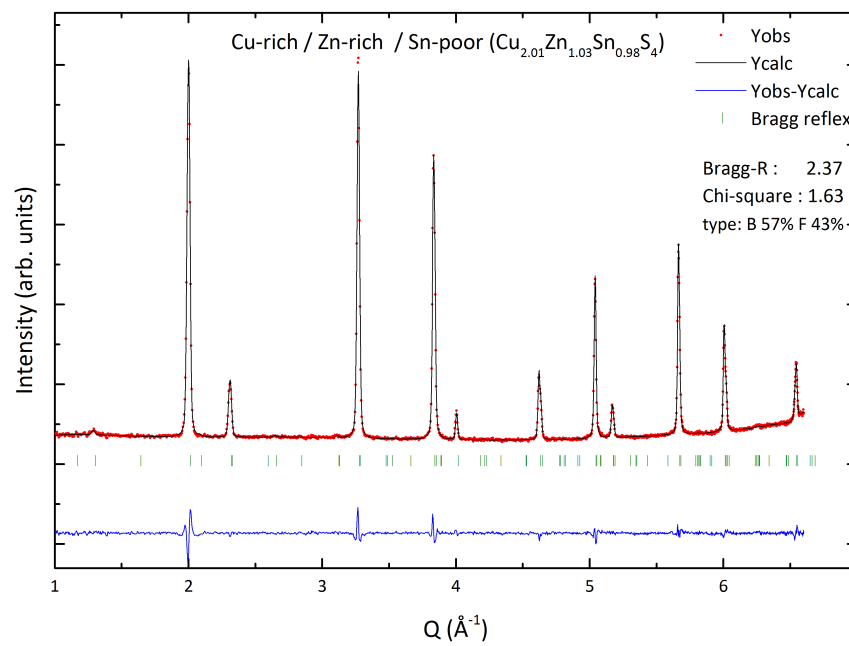
Figure A.26: Neutron diffraction pattern: 13 - B2000

14 - B2010 - Cu$_{1.98}$Zn$_{1.06}$Sn$_{0.98}$S$_4$ - B 79 % F 21 %
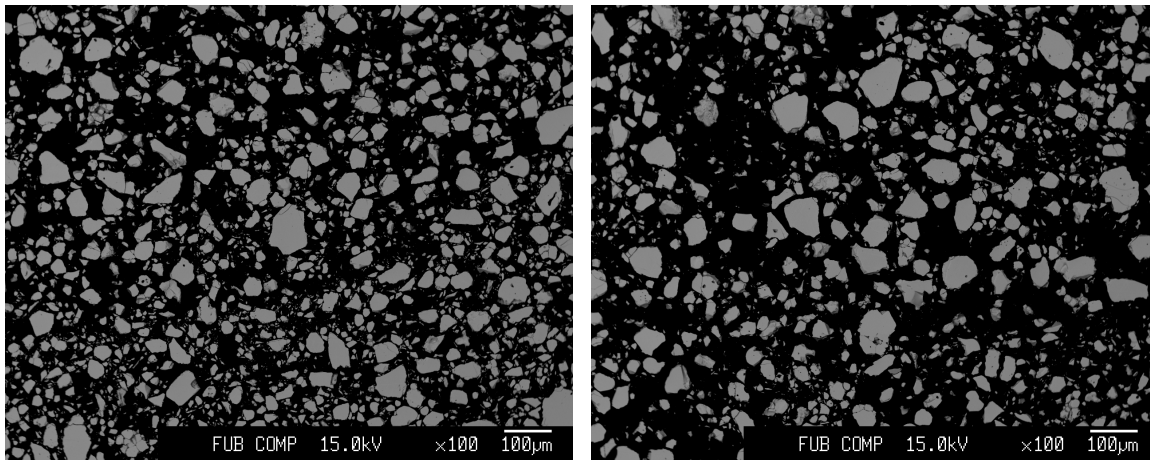
Figure A.27: BSE micrographs: 14 - B2010

Cu / (Zn + Sn) = 0.976(17), Zn / Sn = 1.086(15)
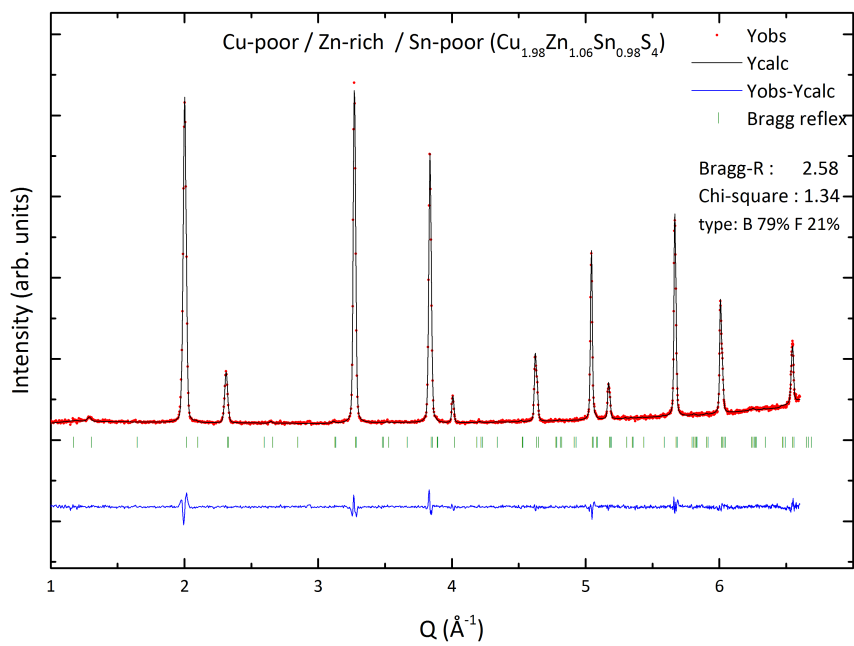
Figure A.28: Neutron diffraction pattern: 14 - B2010

15 - B2020 - $Cu_{1.97}Zn_{1.08}Sn_{0.97}S_4$ - B 81 % F 19 %
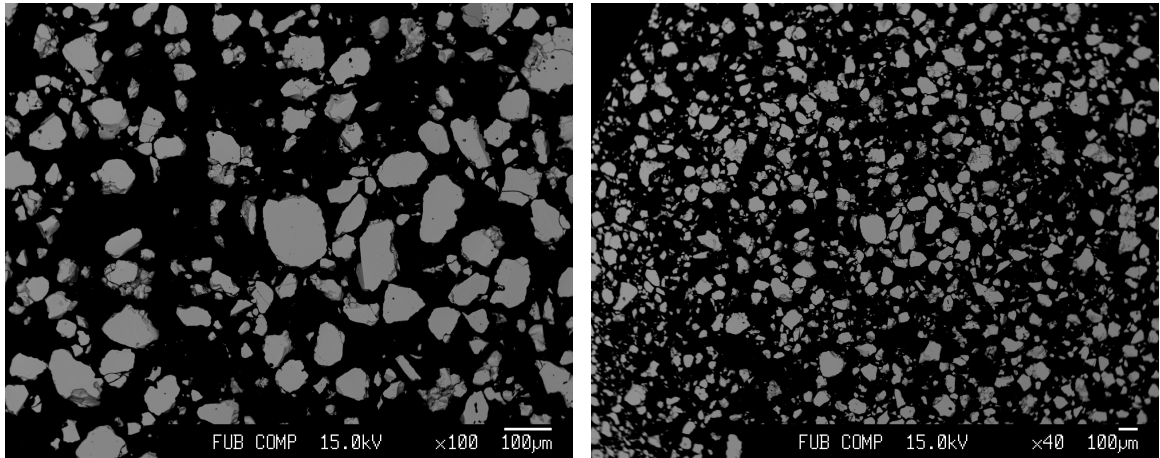
Figure A.29: BSE micrographs: 15 - B2020

$Cu \,/\, (Zn + Sn) = 0.964(17), \; Zn \,/\, Sn = 1.122(16)$
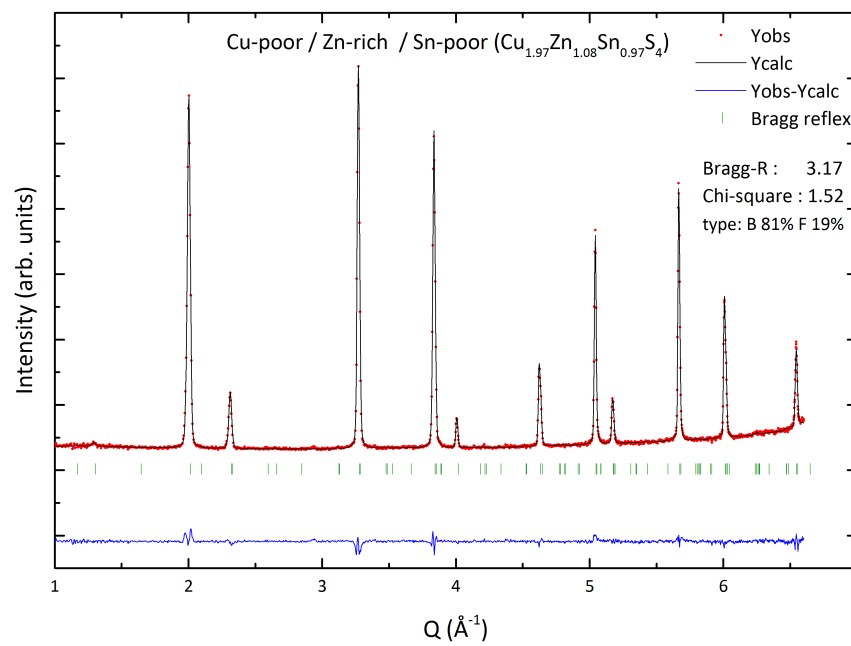
Figure A.30: Neutron diffraction pattern: 15 - B2020

16 - B1000 - $Cu_{2.01}Zn_{1.03}Sn_{0.98}S_4$ - B 59 % F 41 %
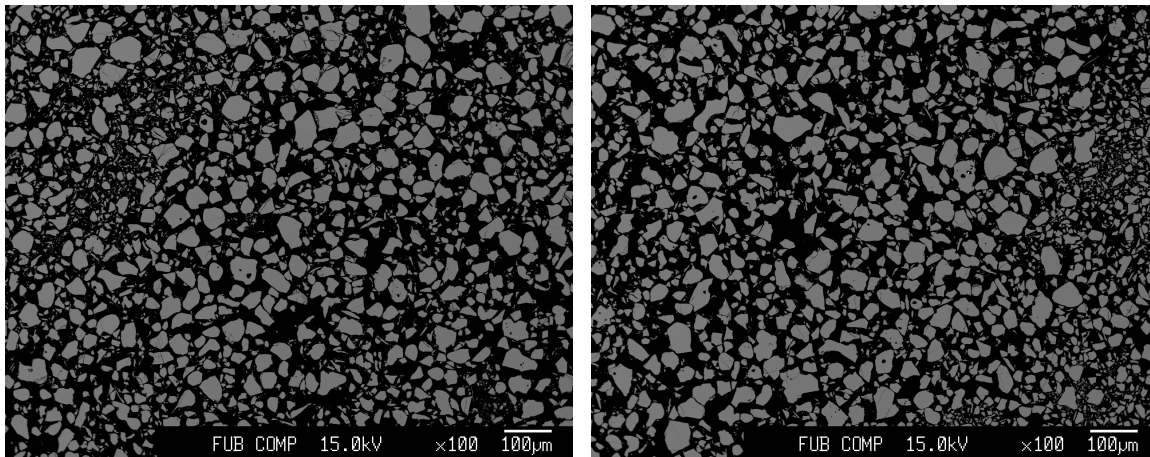
Figure A.31: BSE micrographs: 16 - B1000

$Cu / (Zn + Sn) = 0.995(17), Zn / Sn = 1.054(15)$
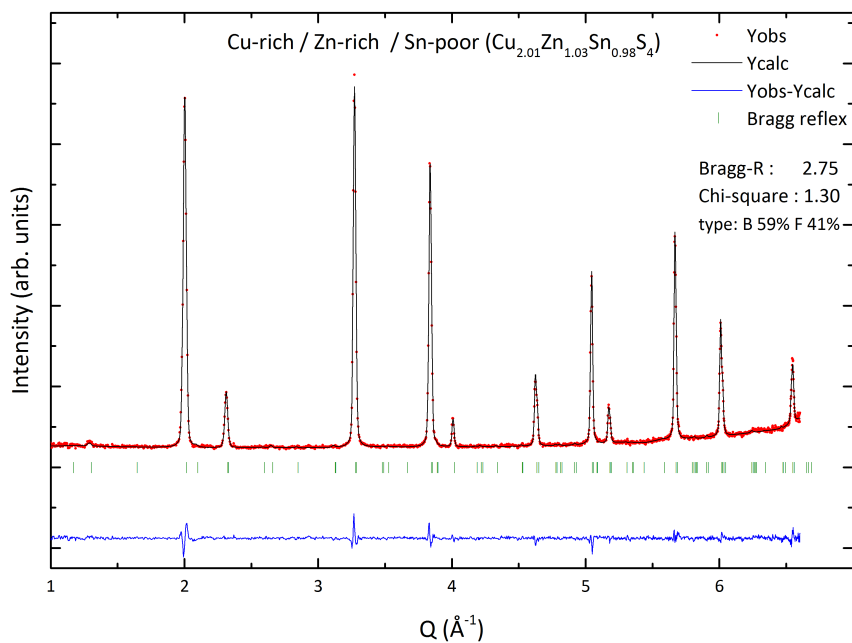
Figure A.32: Neutron diffraction pattern: 16 - B1000

17 - D0010 - $Cu_{2.02}Zn_{1.02}Sn_{0.99}S_4$ - B 24 % F 76 %
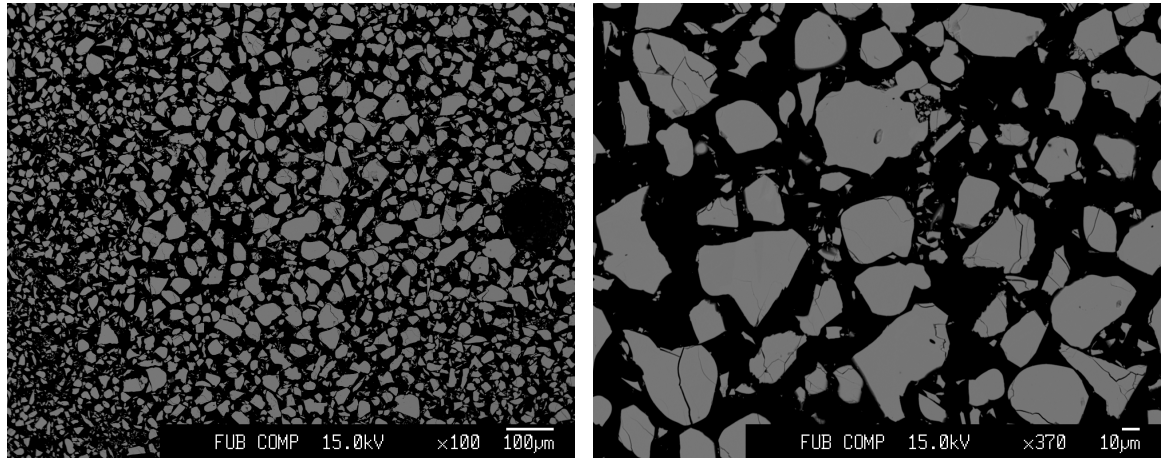
Figure A.33: BSE micrographs: 17 - D0010

$Cu / (Zn + Sn) = 1.009(17)$, $Zn / Sn = 1.034(15)$
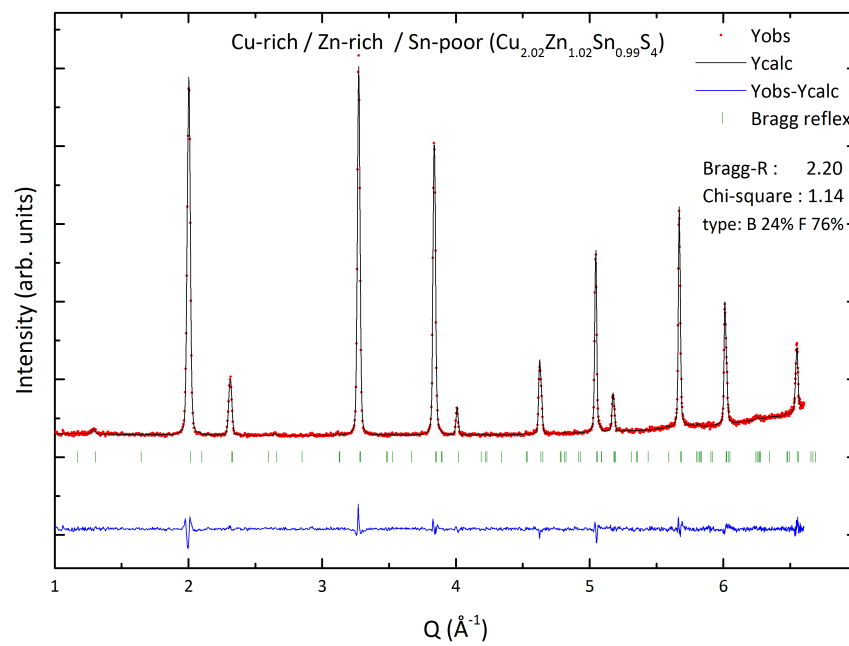
Figure A.34: Neutron diffraction pattern: 17 - D0010

18 - D0040 - $Cu_{2.07}Zn_{0.99}Sn_{0.99}S_4$ - D 71 % F 29 %
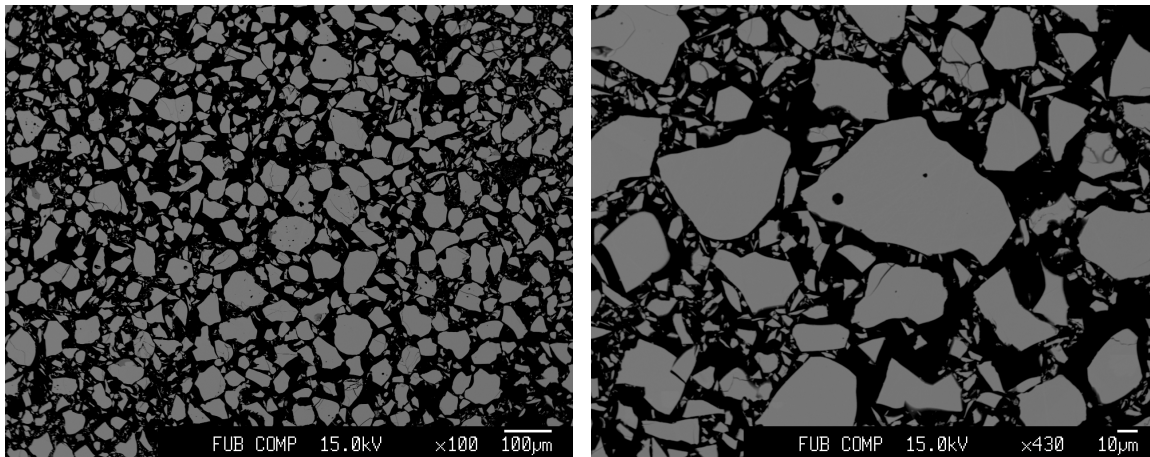
Figure A.35: BSE micrographs: 18 - D0040

$Cu / (Zn + Sn) = 1.044(18)$, $Zn / Sn = 1.006(14)$
Secondary phases: $Cu_{0.95}(Zn_{0.01})S$
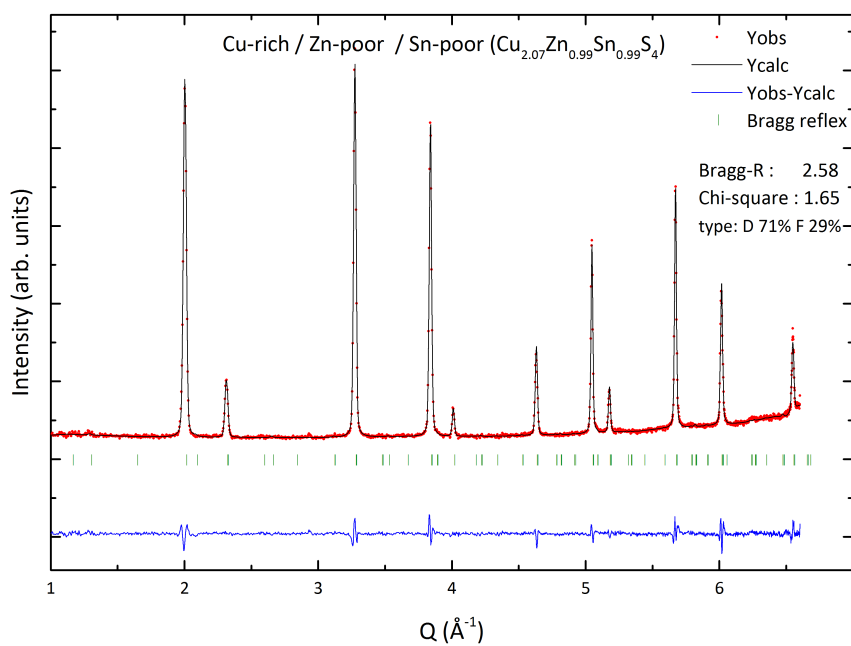
Figure A.36: Neutron diffraction pattern: 18 - D0040

19 - D0050 - Cu$_{2.07}$Zn$_{0.98}$Sn$_{0.99}$S$_4$ - D 83 % F 17 %
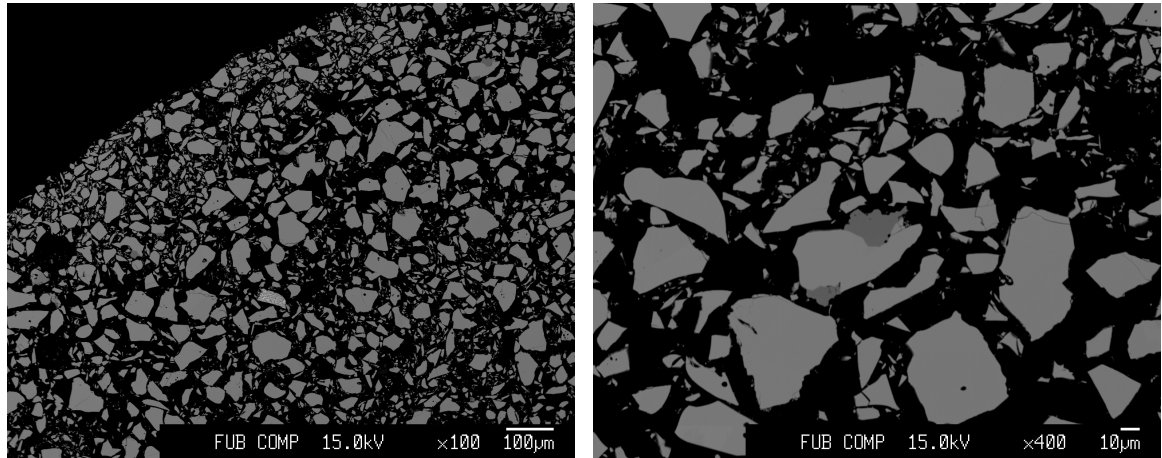
Figure A.37: BSE micrographs: 19 - D0050

Cu / (Zn + Sn) = 1.051(18), Zn / Sn = 0.990(14)
Secondary phases: Cu$_{0.96}$S, SnS
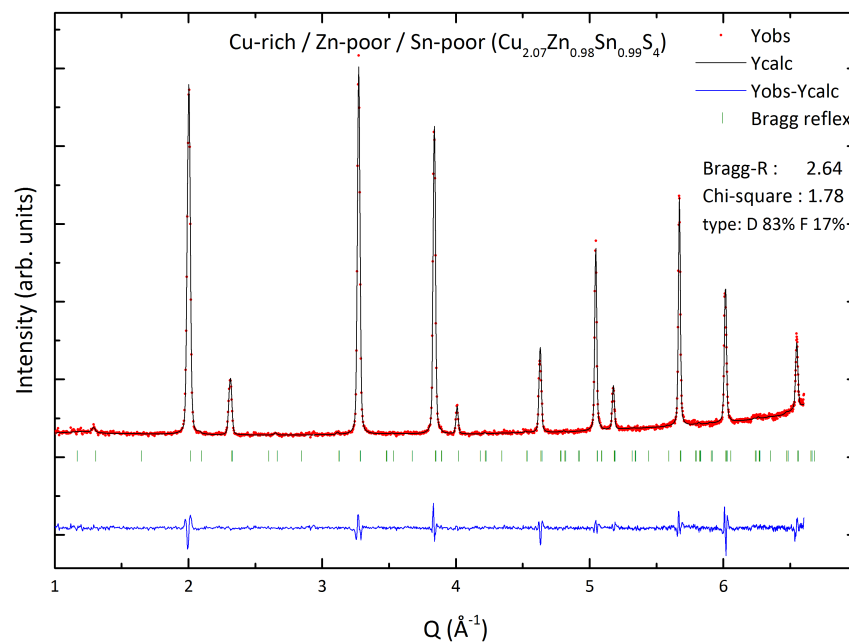
Figure A.38: Neutron diffraction pattern: 19 - D0050

20 - D0020 - Cu$_{2.02}$Zn$_{1.05}$Sn$_{0.97}$S$_4$ - B 51 % F 49 %
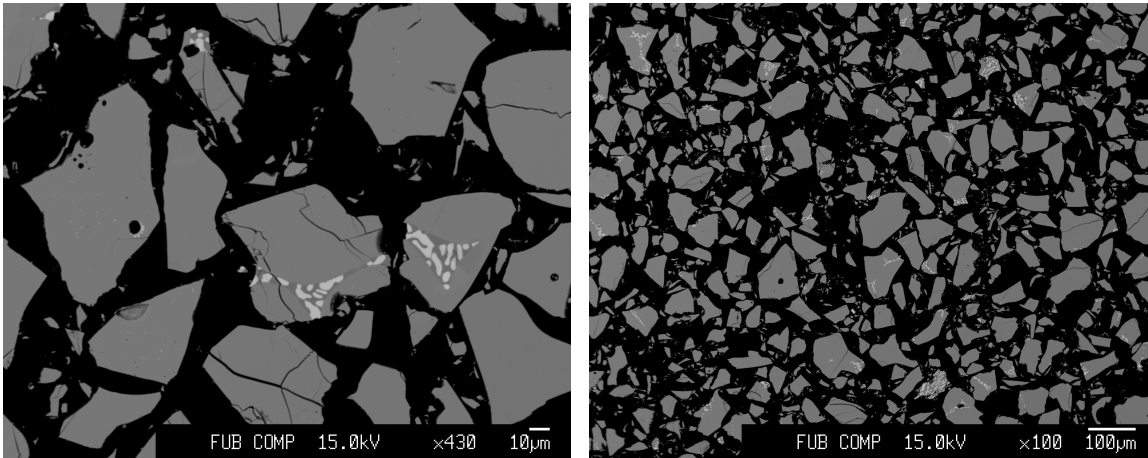
Figure A.39: BSE micrographs: 20 - D0020

Cu / (Zn + Sn) = 0.999(17), Zn / Sn = 1.086(15)
Secondary phases: Cu$_{1.84}$(Sn$_{0.02}$)S, Sn$_{0.96}$(Cu$_{0.08}$Zn$_{0.02}$)S
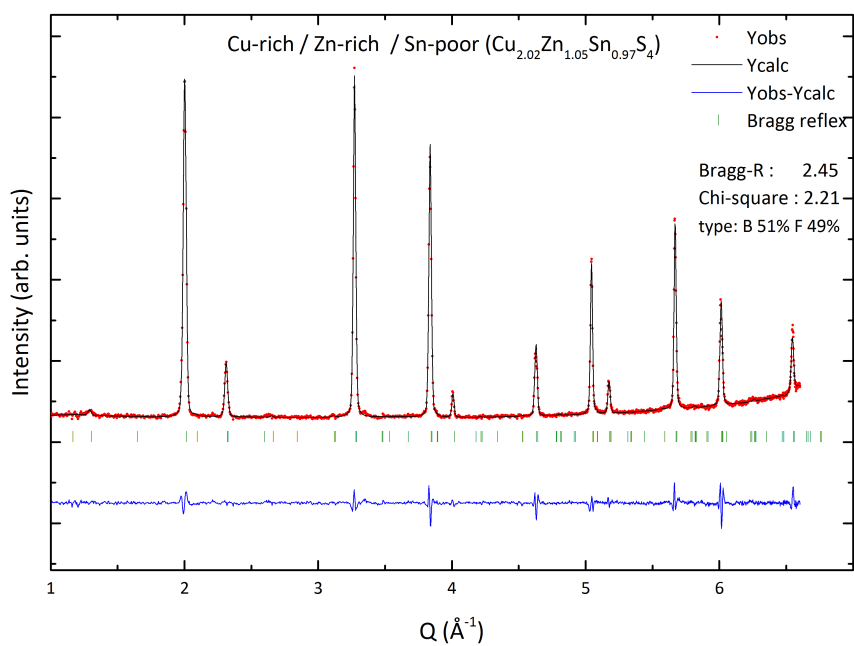
Figure A.40: Neutron diffraction pattern: 20 - D0020

21 - D0000 - $Cu_{1.98}Zn_{1.09}Sn_{0.96}S_4$ - B 76 % F 24 %
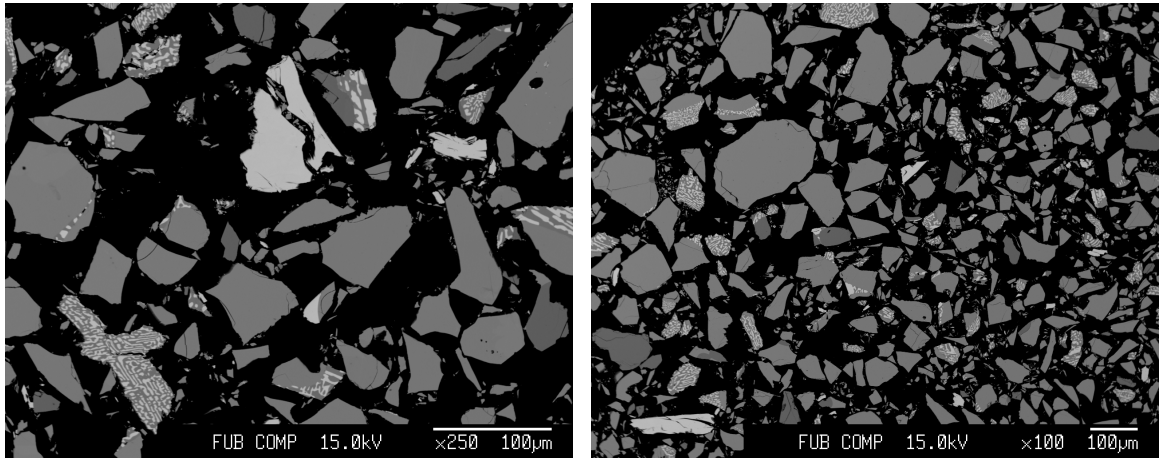
Figure A.41: BSE micrographs: 21 - D0000

$Cu / (Zn + Sn) = 0.967(17)$, $Zn / Sn = 1.136(16)$
Secondary phases: $Cu_{1.90}(Sn_{0.01})S$, $Sn_{0.98}(Cu_{0.03}Zn_{0.01})S$ (3 %), $Zn_{0.98}(Cu_{0.03}Sn_{0.01})S$
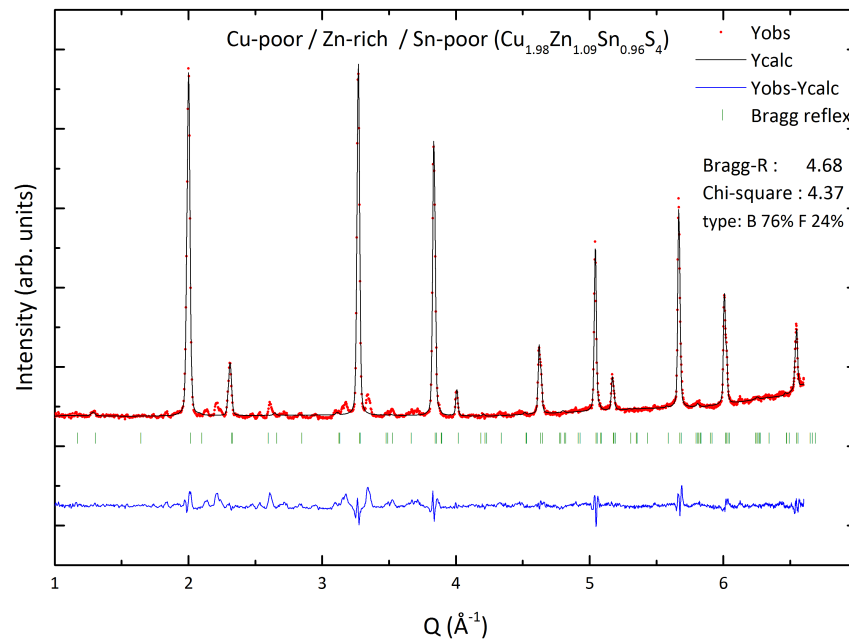
Figure A.42: Neutron diffraction pattern: 21 - D0000

22 - **A4000** - **Cu$_{1.94}$Zn$_{1.06}$Sn$_{0.98}$S$_4$** - **A 17 % B 83 %**
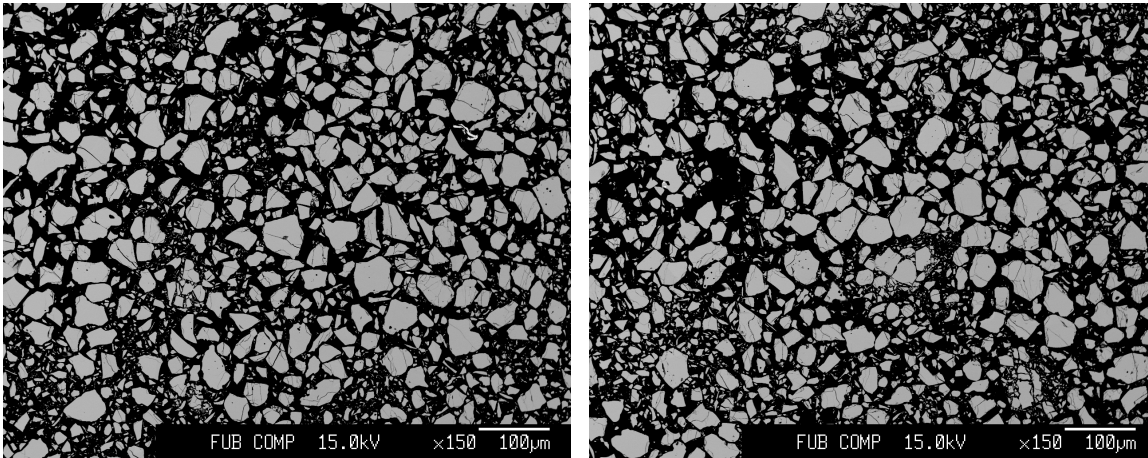
Figure A.43: BSE micrographs: 22 - A4000

$Cu / (Zn + Sn) = 0.949(16)$, $Zn / Sn = 1.079(15)$
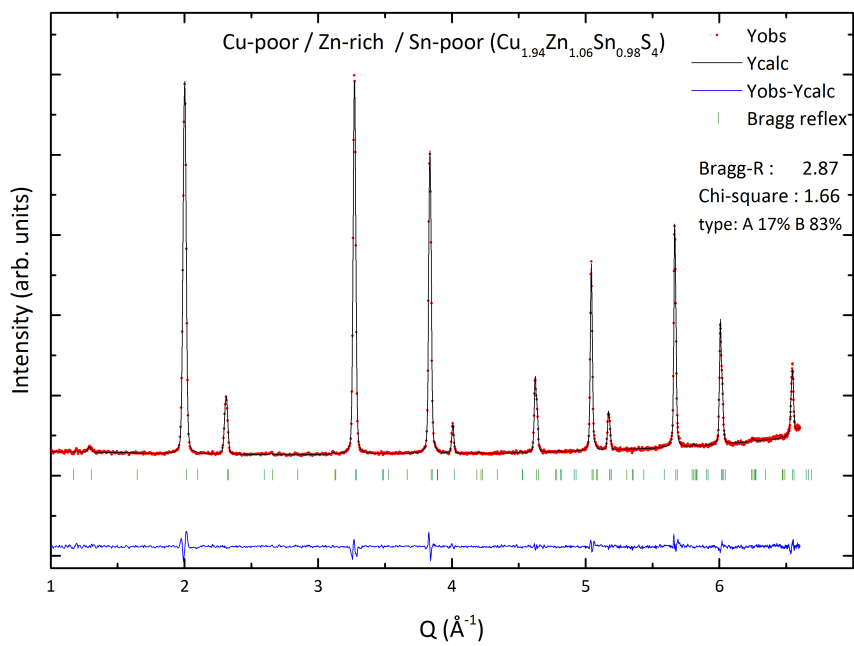
Figure A.44: Neutron diffraction pattern: 22 - A4000

23 - **A4010** - **$Cu_{1.99}Zn_{1.03}Sn_{0.99}S_4$** - **B 76 % F 24 %**
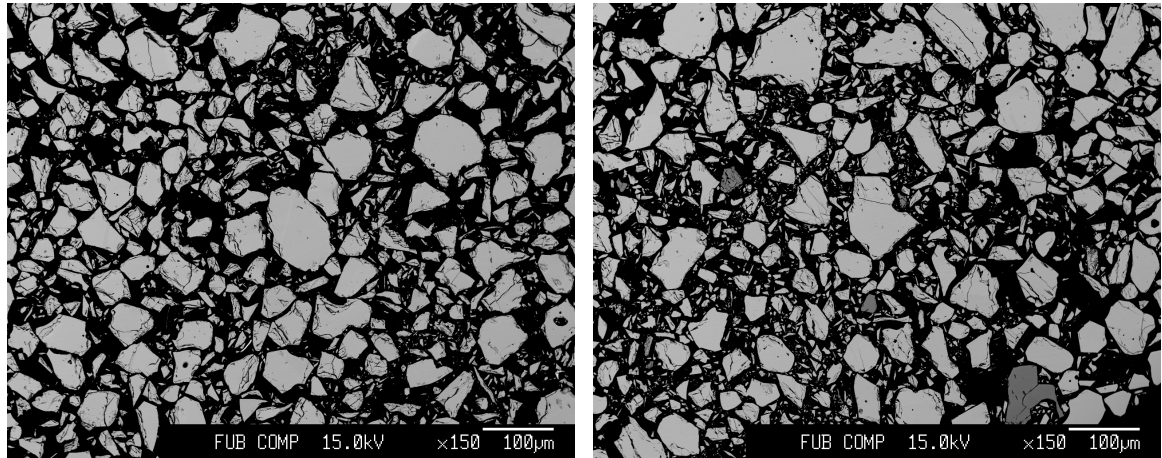
Figure A.45: BSE micrographs: 23 - A4010

$Cu / (Zn + Sn) = 0.989(17)$, $Zn / Sn = 1.041(15)$
Secondary phases: $Zn_{0.95}(Cu_{0.03}Sn_{0.01})S$
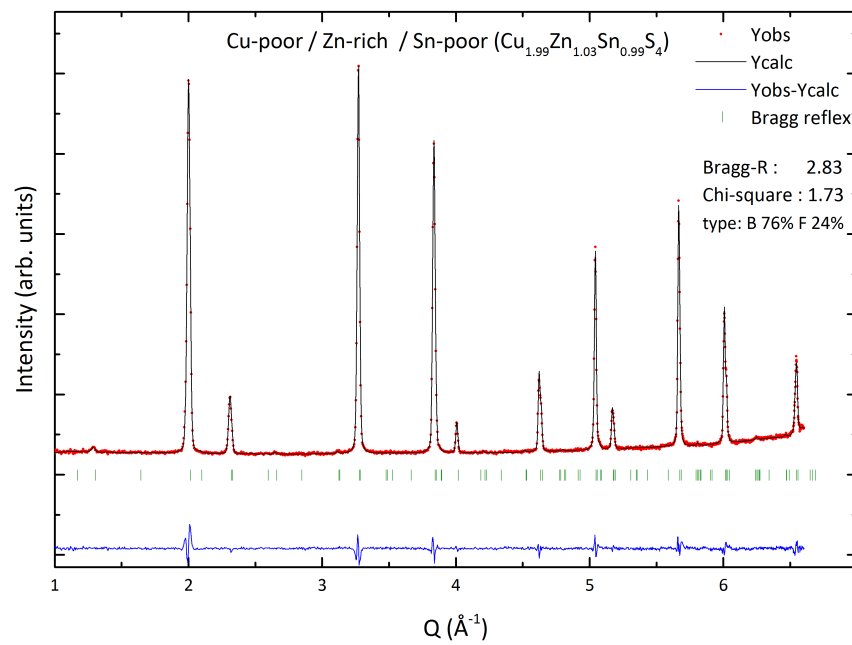
Figure A.46: Neutron diffraction pattern: 23 - A4010

24 - **A4030** - **Cu$_{2.00}$Zn$_{1.03}$Sn$_{0.99}$S$_4$** - **B 66 % F 34 %**
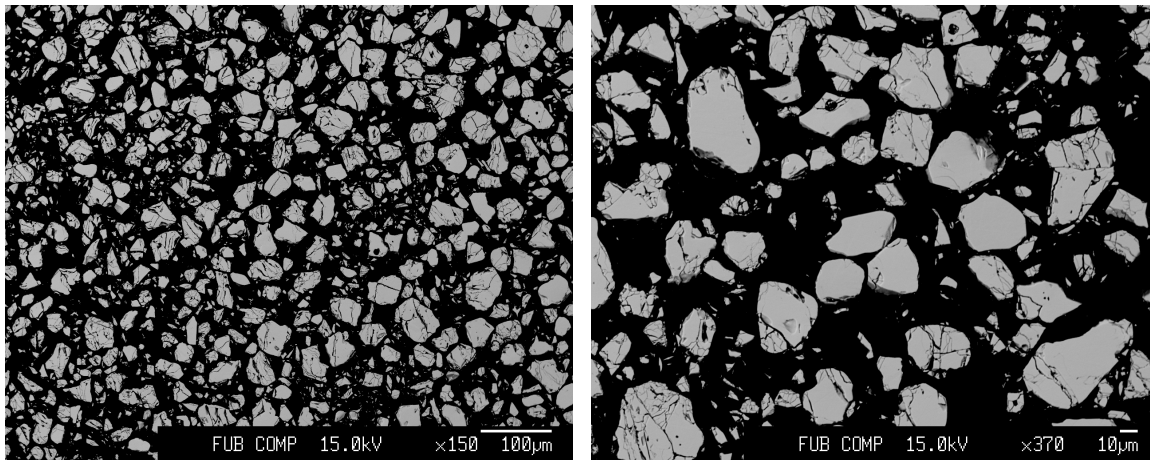
Figure A.47: BSE micrographs: 24 - A4030

$Cu \, / \, (Zn + Sn) = 0.993(17)$, $Zn \, / \, Sn = 1.045(15)$
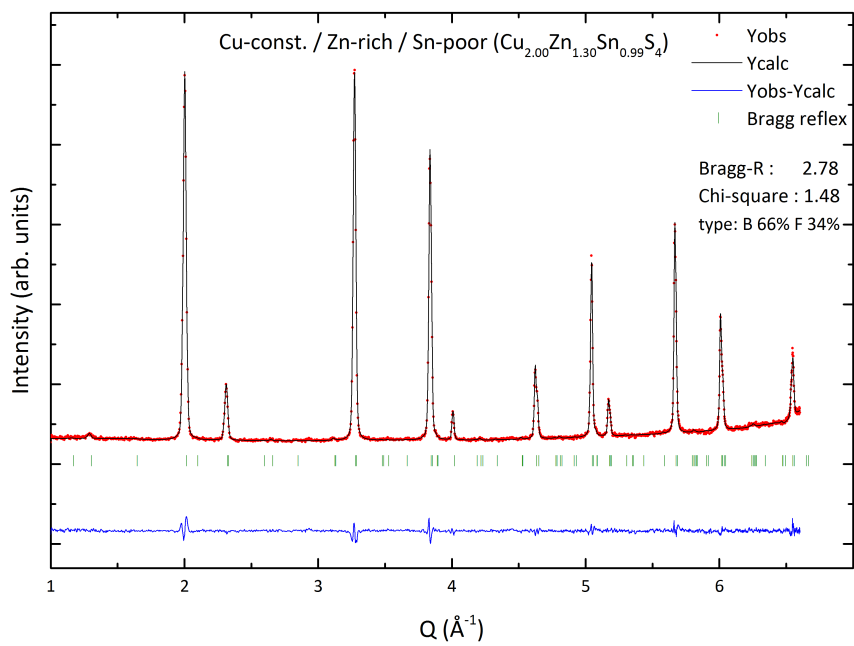
Figure A.48: Neutron diffraction pattern: 24 - A4030

25 - **A4040** - $Cu_{2.05}Zn_{0.96}Sn_{1.01}S_4$ - **C 57 % D 43 %**
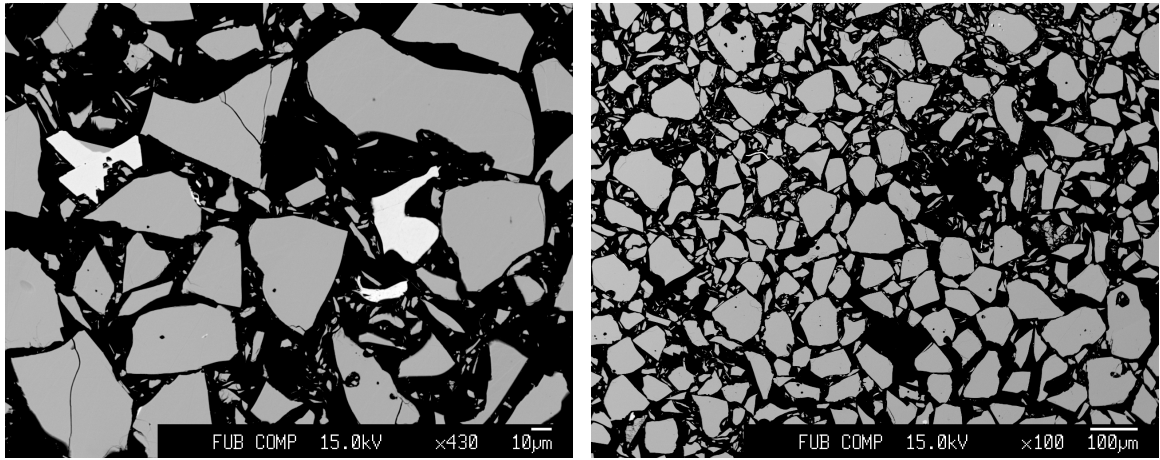
Figure A.49: BSE micrographs: 25 - A4040

$Cu / (Zn + Sn) = 1.042(18)$, $Zn / Sn = 0.956(14)$
Secondary phases: $Cu_{0.41}Zn_{0.13}Sn_{1.31}S_3$
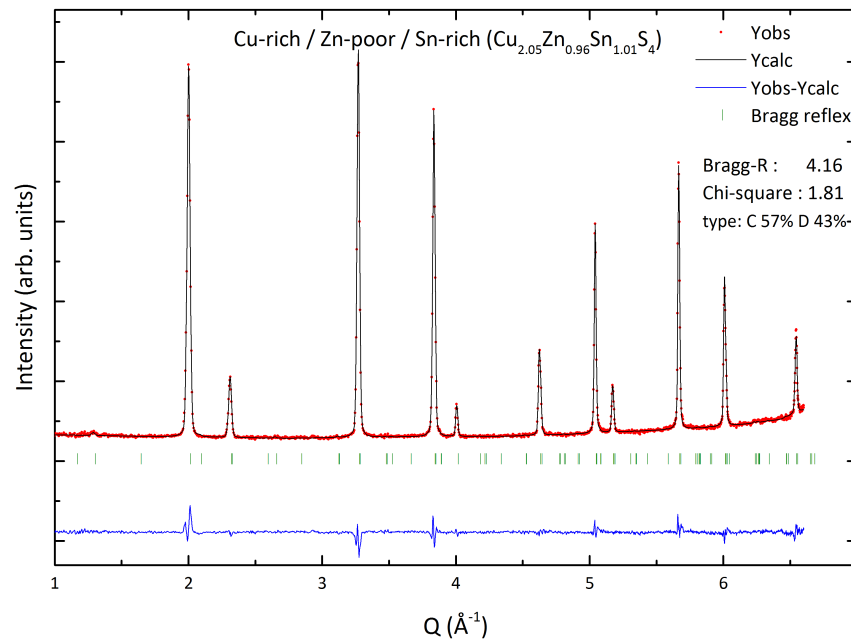
Figure A.50: Neutron diffraction pattern: 25 - A4040

26 - **A4050** - **Cu$_{1.95}$Zn$_{1.05}$Sn$_{0.99}$S$_4$** - **A 16 % B 84 %**
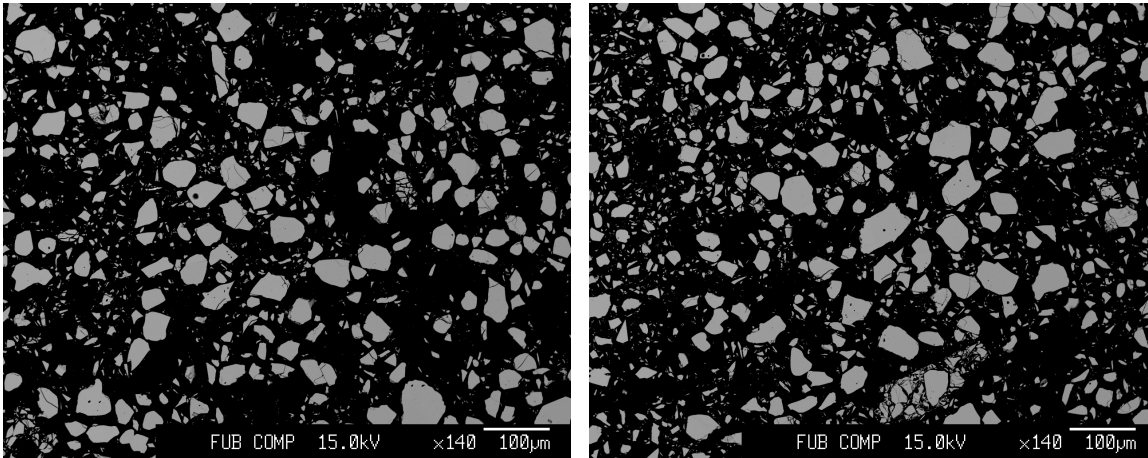
Figure A.51: BSE micrographs: 26 - A4050

$Cu / (Zn + Sn) = 0.958(17)$, $Zn / Sn = 1.066(15)$
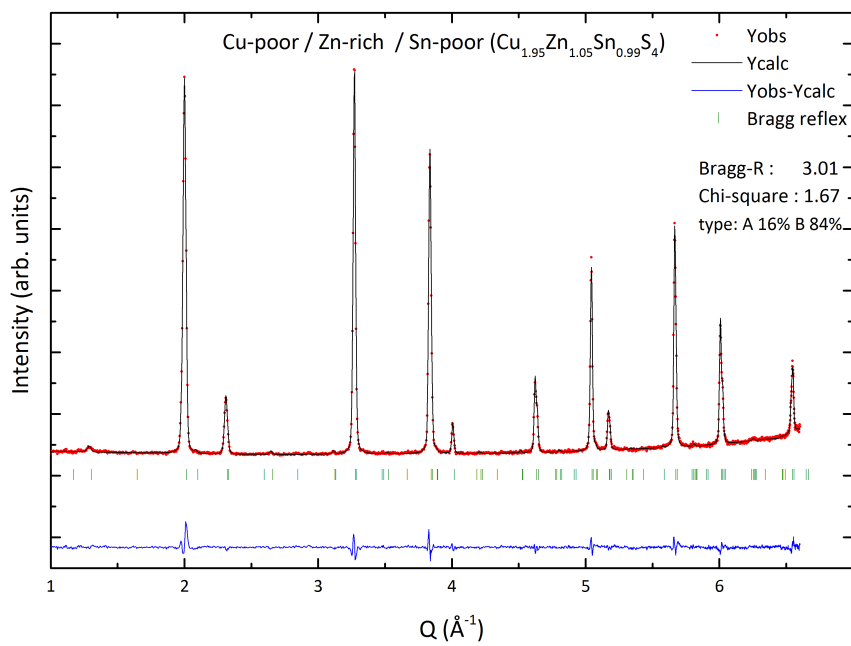
Figure A.52: Neutron diffraction pattern: 26 - A4050

27 - **E0010** - **Cu$_{2.10}$Zn$_{0.87}$Sn$_{1.04}$S$_4$** - **C 93 % D 7 %**
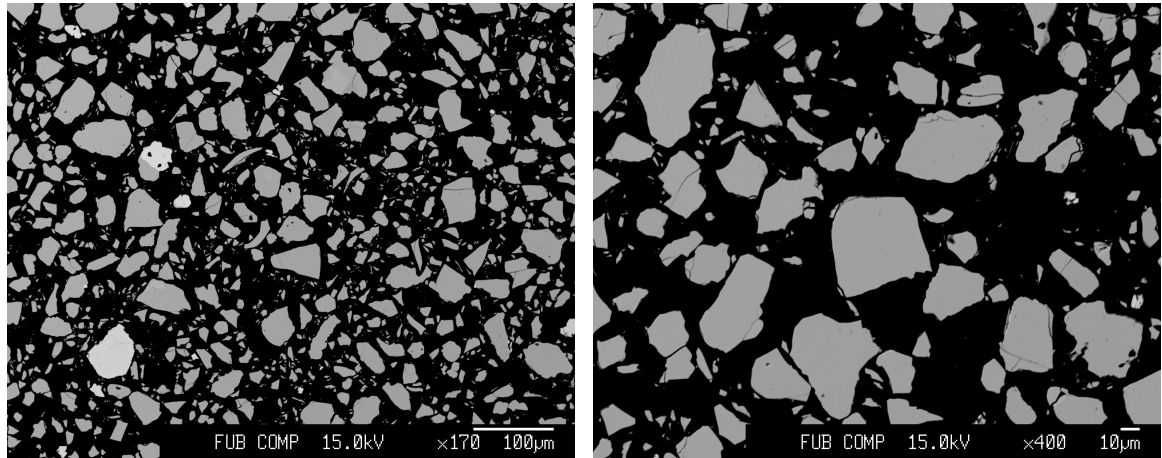
Figure A.53: BSE micrographs: 27 - E0010

$Cu / (Zn + Sn) = 1.101(19)$, $Zn / Sn = 0.838(12)$
Secondary phases: $Cu_{0.69}Zn_{0.08}Sn_{1.26}S_3$
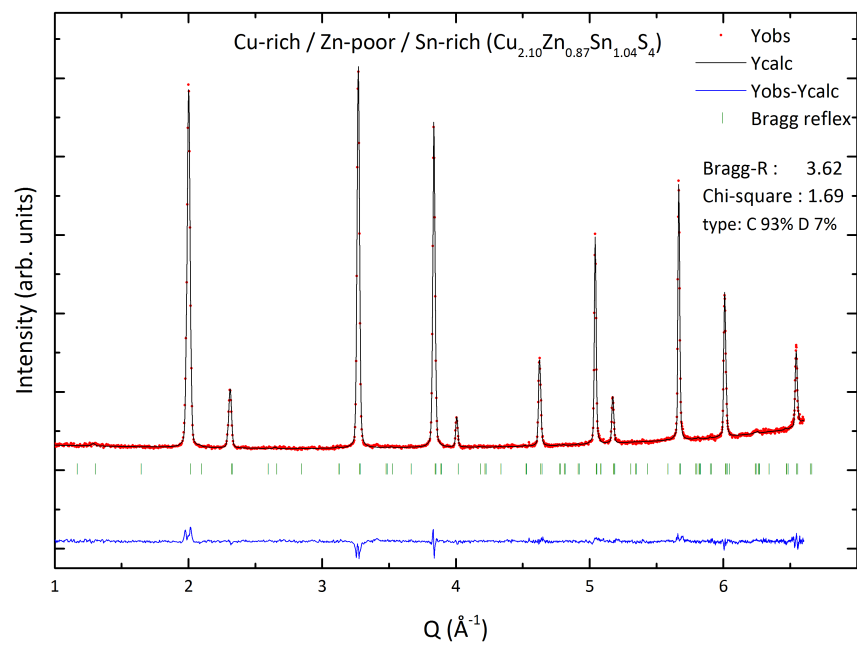
Figure A.54: Neutron diffraction pattern: 27 - E0010

28 - **E0020** - **Cu$_{2.06}$Zn$_{0.94}$Sn$_{1.02}$S$_4$** - **C 85 % F 15 %**
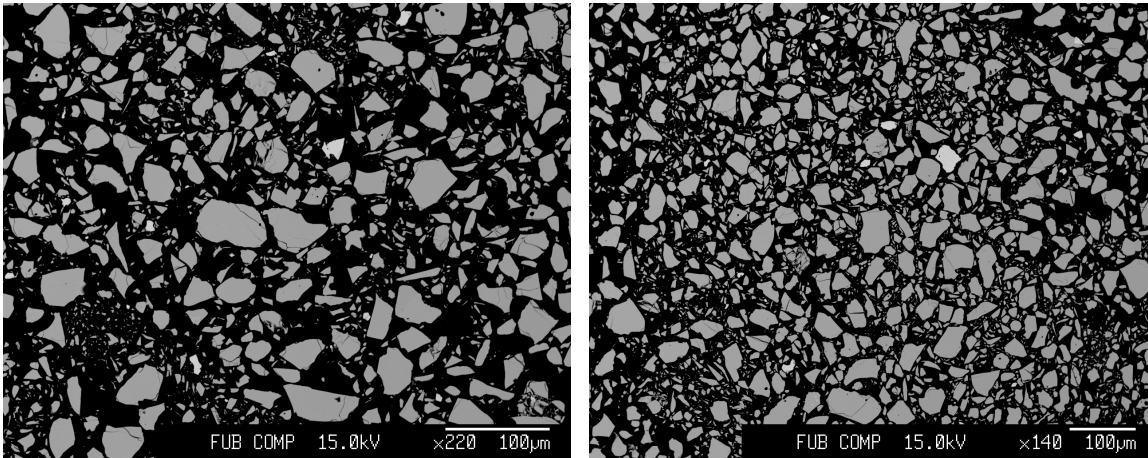
Figure A.55: BSE micrographs: 28 - E0020

$Cu / (Zn + Sn) = 1.053(18)$, $Zn / Sn = 0.921(13)$
Secondary phases: $Cu_{0.59}Zn_{0.11}Sn_{1.26}S_3$
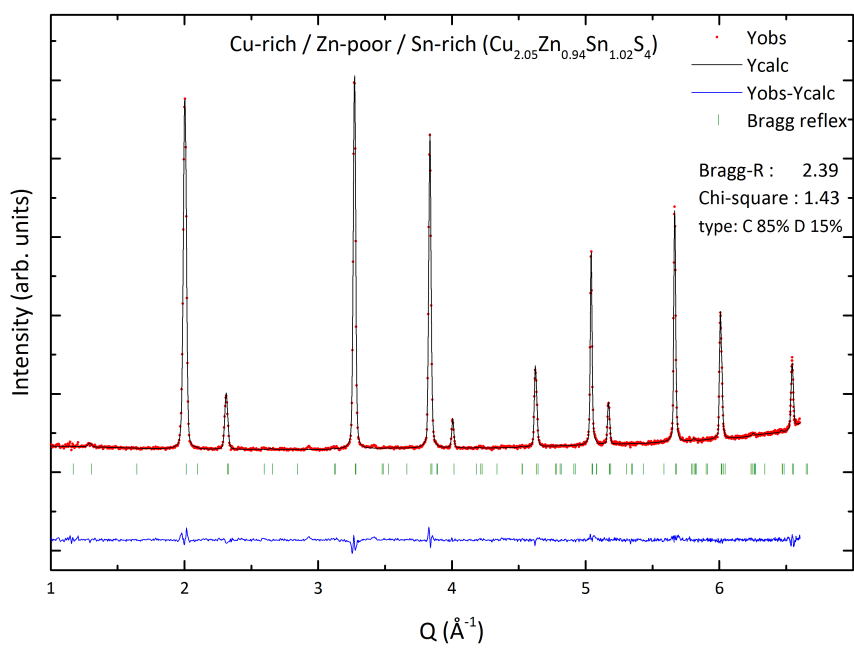
Figure A.56: Neutron diffraction pattern: 28 - E0020

29 - E0030 - $Cu_{1.98}Zn_{1.02}Sn_{0.99}S_4$ - A 21 % B 79 %
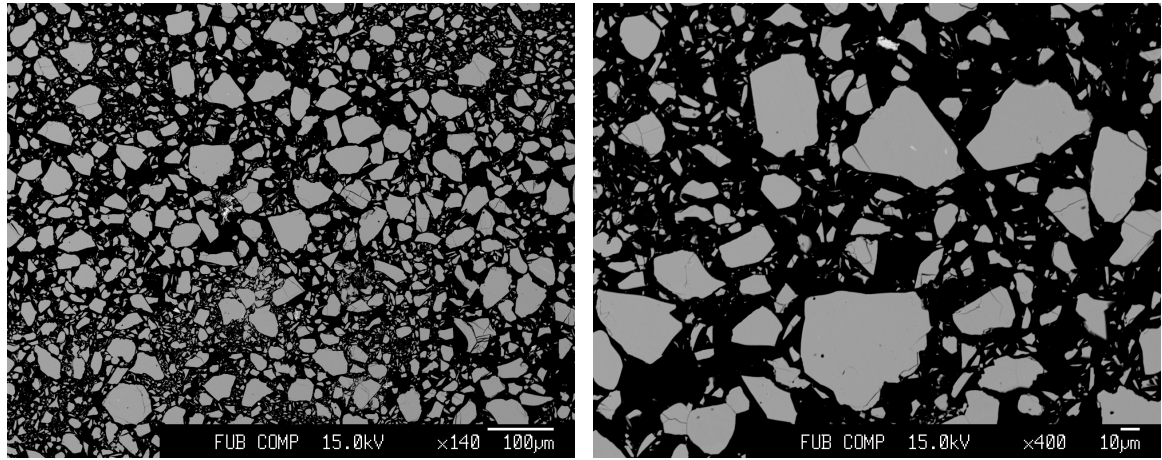
Figure A.57: BSE micrographs: 29 - E0030

$Cu / (Zn + Sn) = 0.979(17)$, $Zn / Sn = 1.030(15)$
Secondary phases: $Sn_{0.97}(Cu_{0.04}Zn_{0.02})S_2$
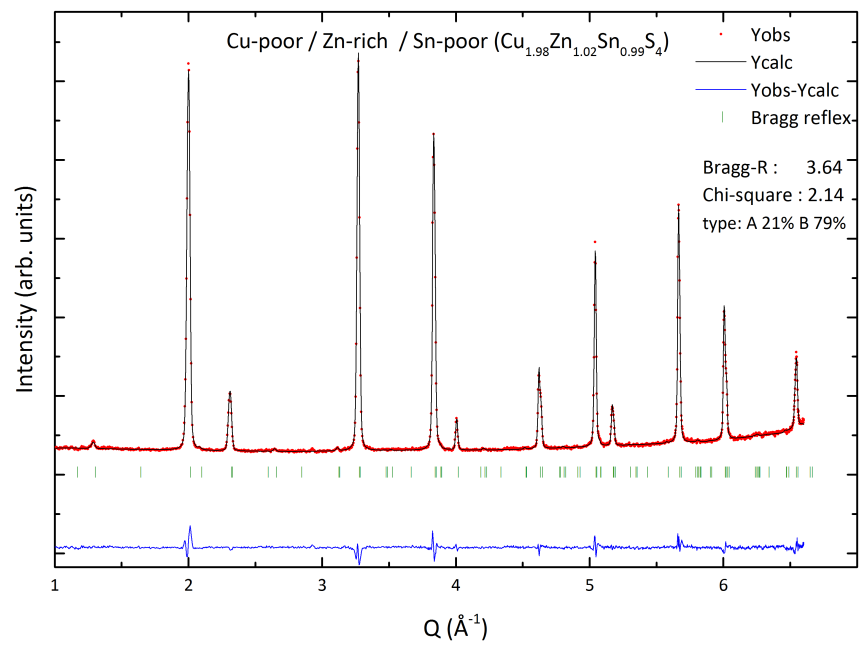
Figure A.58: Neutron diffraction pattern: 29 - E0030

30 - **E0040** - **Cu$_{1.98}$Zn$_{1.03}$Sn$_{0.99}$S$_4$** - **A 7 % B 93 %**
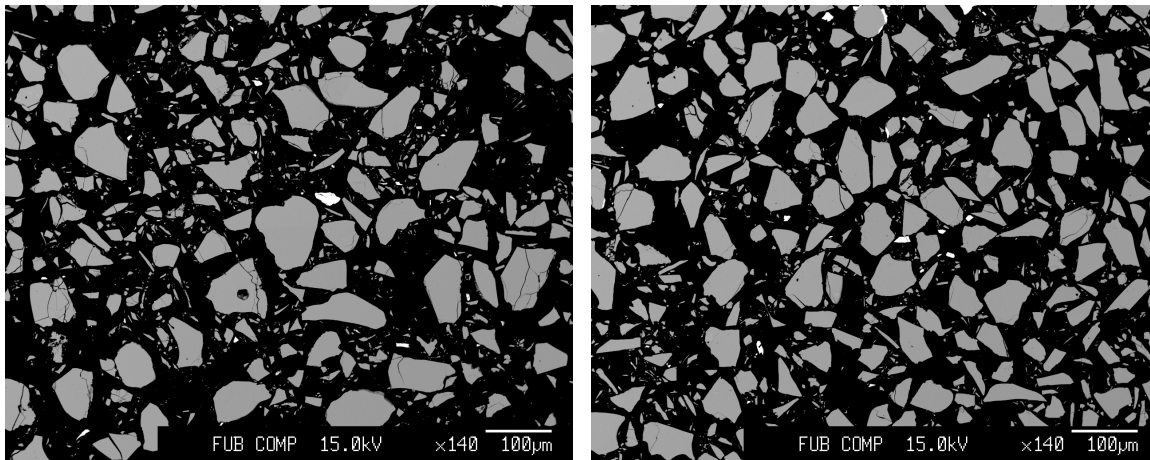
Figure A.59: BSE micrographs: 30 - E0040

$Cu / (Zn + Sn) = 0.978(17)$, $Zn / Sn = 1.039(15)$
Secondary phases: $Sn_{2.82}(Cu_{0.08}Zn_{0.05})S_4$
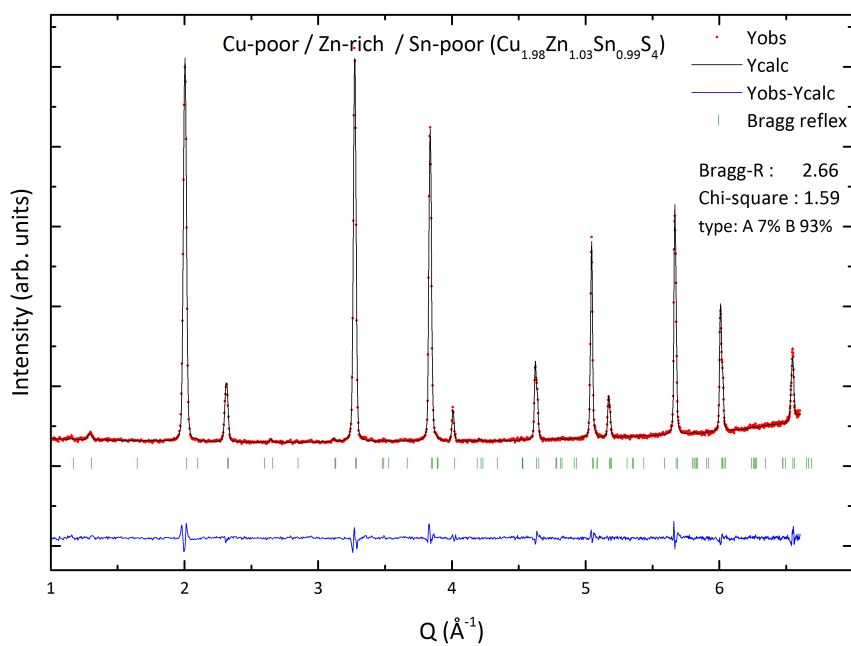
Figure A.60: Neutron diffraction pattern: 30 - E0040

31 - **A6020** - **Cu$_{1.98}$Zn$_{1.02}$Sn$_{1.00}$S$_4$** - **A 27 % B 73 %**
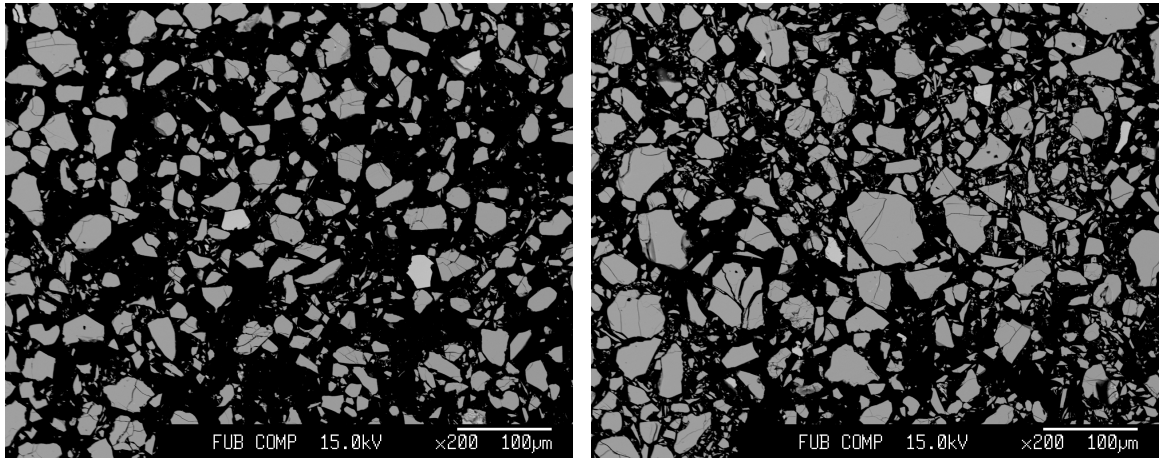
Figure A.61: BSE micrographs: 31 - A6020

Cu / (Zn + Sn) = 0.982(17), Zn / Sn = 1.024(14)
Secondary phases: Cu$_{0.33}$Zn$_{0.14}$Sn$_{1.34}$S$_3$
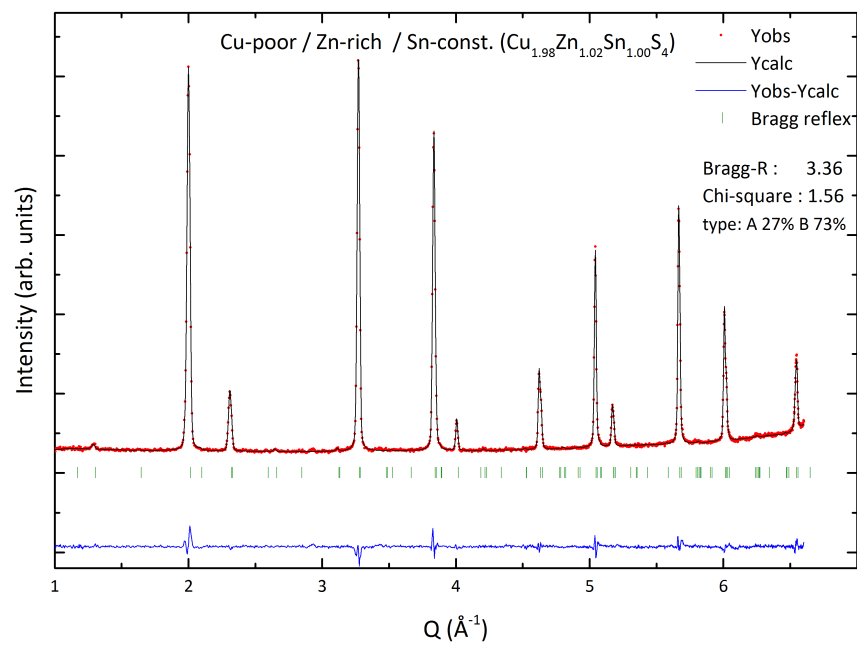
Figure A.62: Neutron diffraction pattern: 31 - A6020

32 - **A6030** - **Cu$_{2.03}$Zn$_{0.95}$Sn$_{1.02}$S$_4$** - **C 97 % E 3 %**
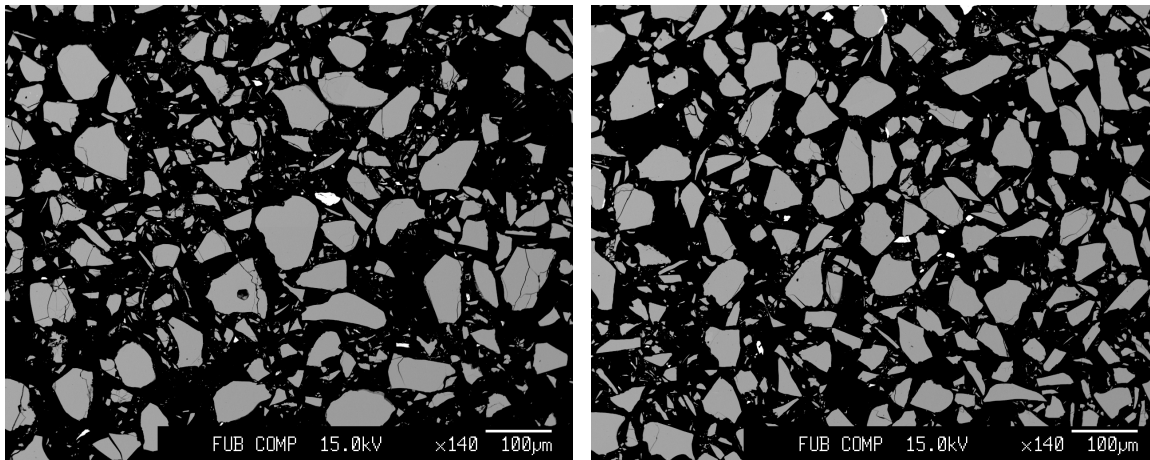
Figure A.63: BSE micrographs: 32 - A6030

Cu / (Zn + Sn) = 1.030(18), Zn / Sn = 0.938(13)
Secondary phases: Cu$_{0.56}$Zn$_{0.12}$Sn$_{1.28}$S$_3$
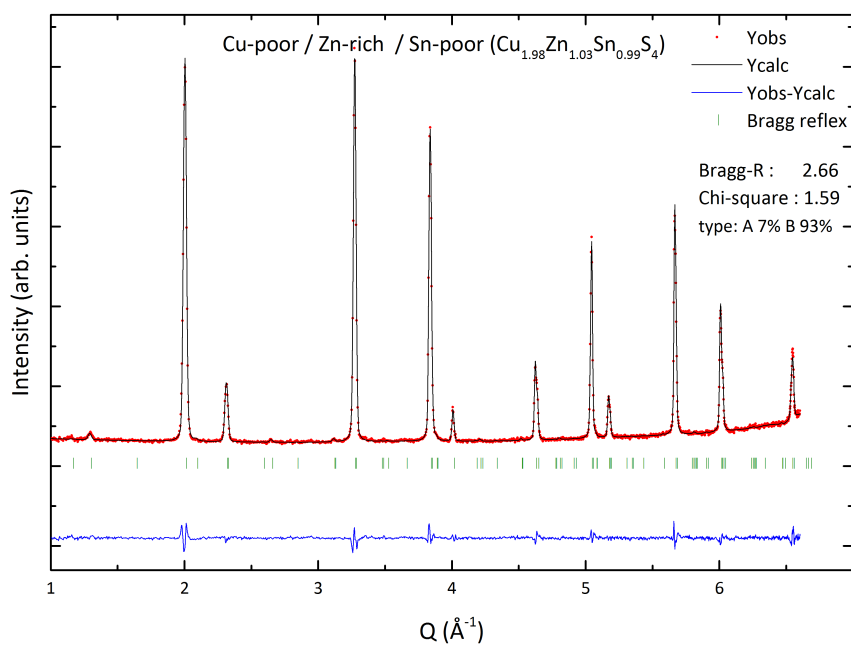
Figure A.64: Neutron diffraction pattern: 32 - A6030

33 - **A4020** - **Cu$_{1.88}$Zn$_{1.08}$Sn$_{0.99}$S$_4$** - **A 47 % B 53 %**
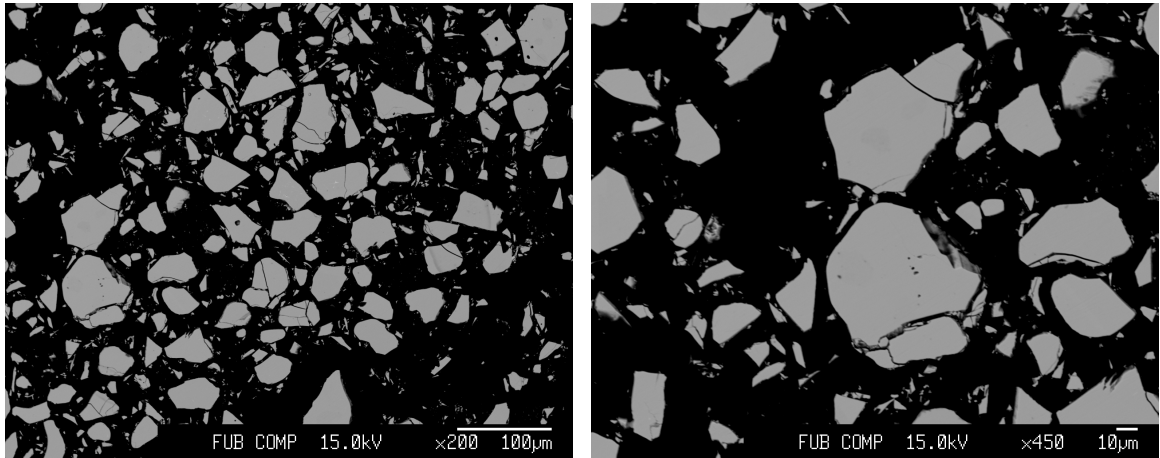
Figure A.65: BSE micrographs: 33 - A4020

Cu $/$ (Zn $+$ Sn) $= 0.910(16)$, Zn $/$ Sn $= 1.098(16)$
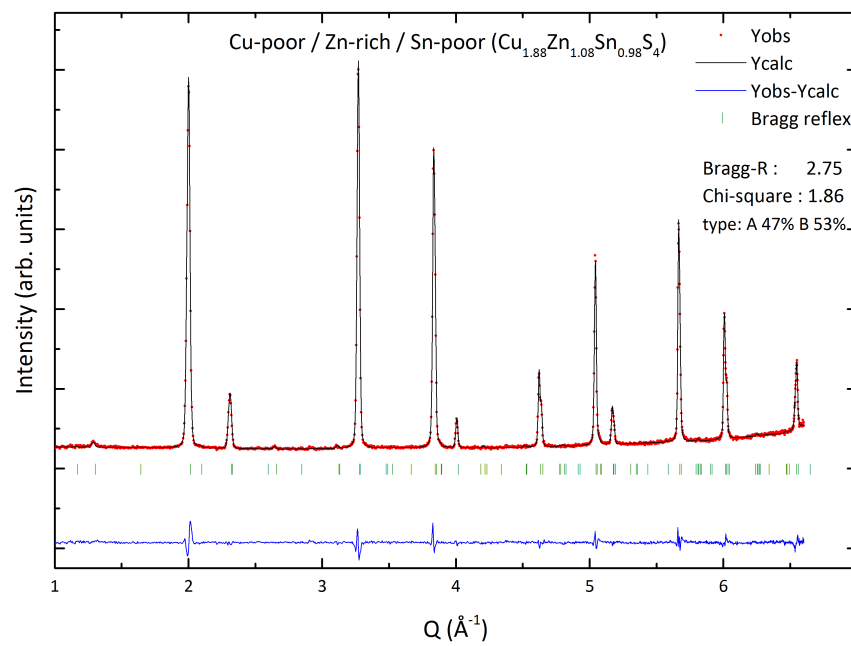
Figure A.66: Neutron diffraction pattern: 33 - A4020

34 - **D0030** - $\mathbf{Cu_{1.95}Zn_{1.09}Sn_{0.97}S_4}$ - **B 97 % F 3 %**
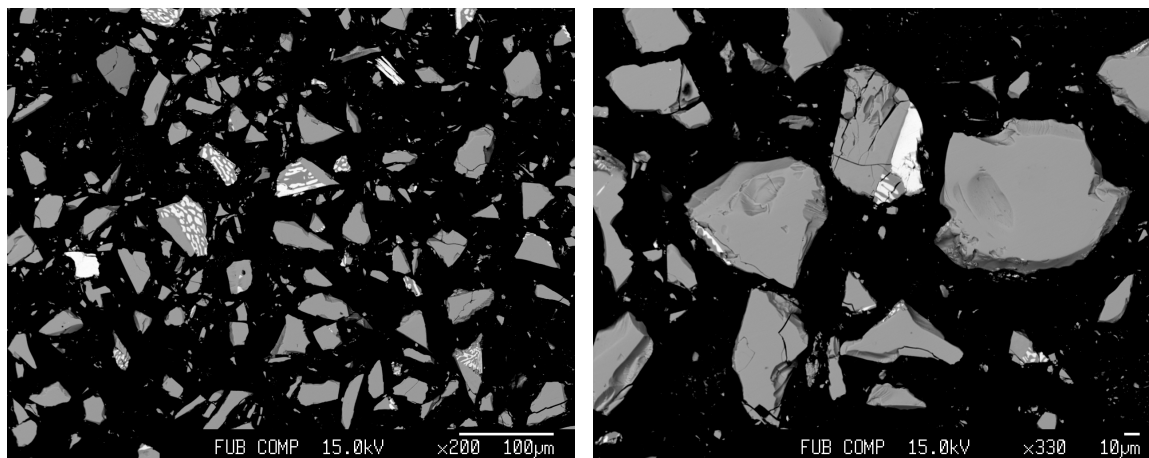
Figure A.67: BSE micrographs: 34 - D0030

$Cu / (Zn + Sn) = 0.947(16)$, $Zn / Sn = 1.120(16)$
Secondary phases: $Cu_{1.80}(Sn_{0.02})S$, $Sn_{0.96}(Cu_{0.05}Zn_{0.01})S$, $Zn_{0.98}(Cu_{0.03}Sn_{0.01})S$
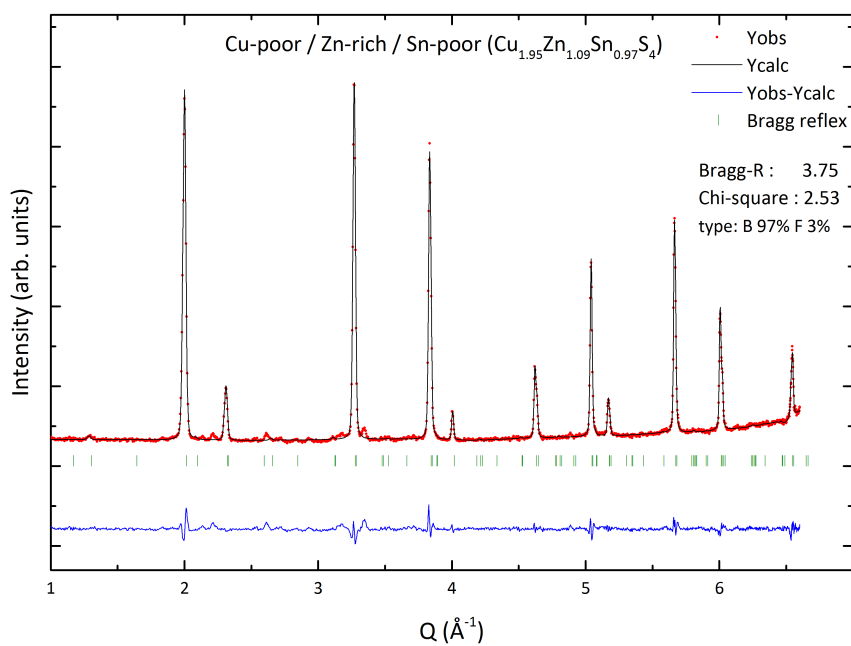
Figure A.68: Neutron diffraction pattern: 34 - D0030

A.3 Additional figures
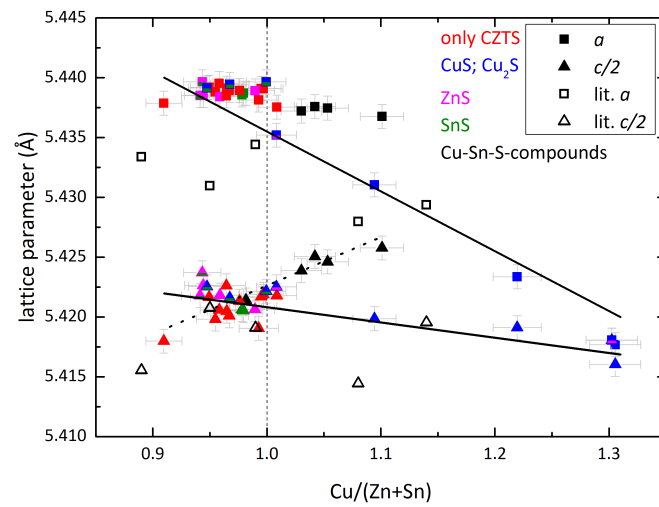
Figure A.69: Lattice parameters vs. Zn / Sn: single phase = red, copper sulfides = blue, zinc sulfides = magenta, tin sulfides = green, Cu-Sn-S-compound = black, rectangle = a, triangle = $c/2$ and open symbols = literature [45].
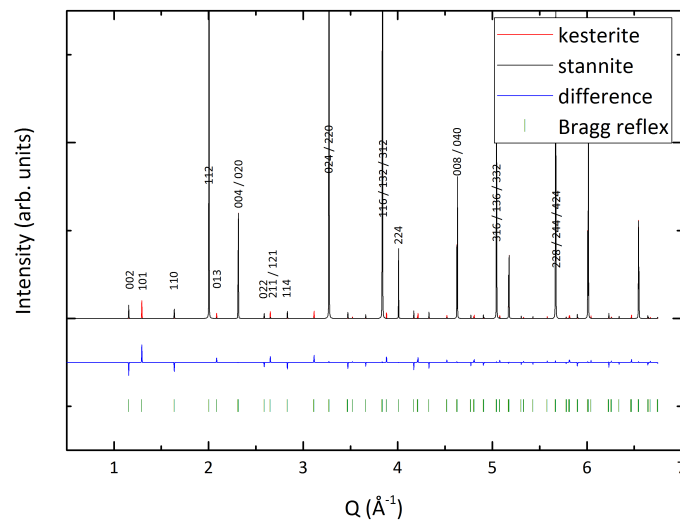
Figure A.70: A comparison of simulated kesterite and stannite structure neutron patterns and their difference plot.

a)

b)
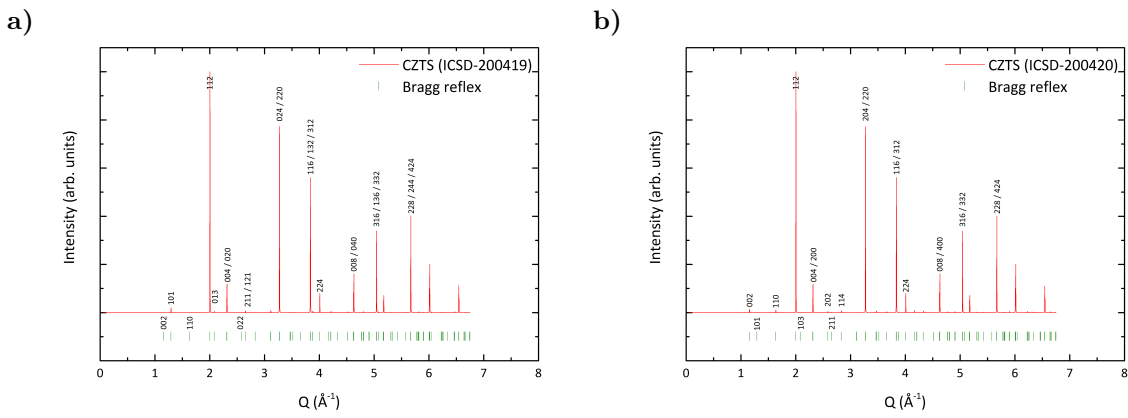
Figure A.71: Simulated neutron patterns of kesterite and stannite.
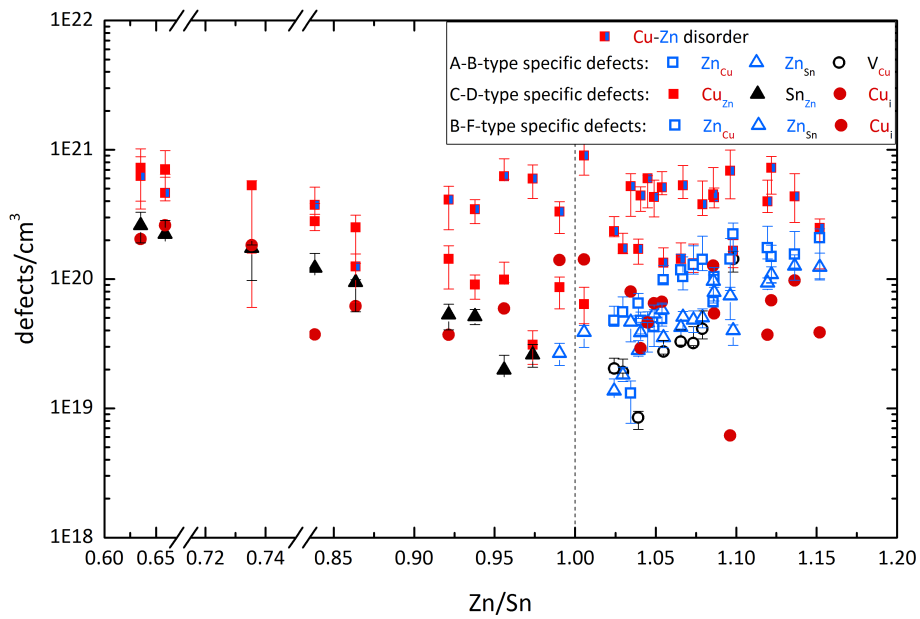
Figure A.72: Overview of defect concentrations vs. Zn / Sn with Cu-Zn disorder = red-blue rectangle and off-stoichiometric type specific defects: A-B-type = Zn_{Cu}, Zn_{Sn} and V_{Cu}, C-D-type = Cu_{Zn}, Sn_{Zn} and Cu_i and B-F-type = Zn_{Cu} Zn_{Sn} and Cu_i.
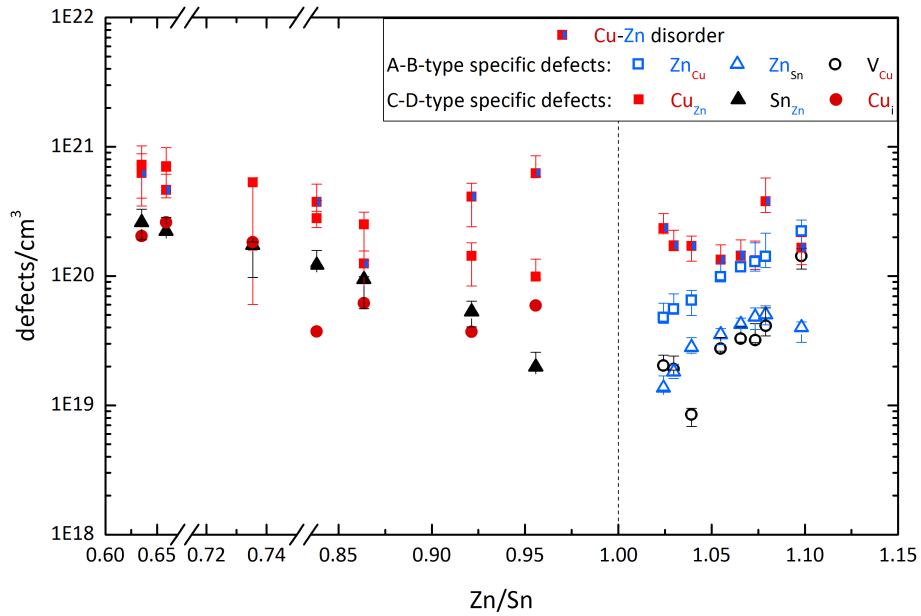
Figure A.73: A-B- and C-D-type defect concentrations vs. Zn_{Sn} with unspecific Cu-Zn disorder = red-blue rectangle and type specific defects: A-B-type = Zn_{Cu}, Zn_{Sn} and V_{Cu} and C-D-type = Cu_{Zn}, Sn_{Zn} and Cu_i.
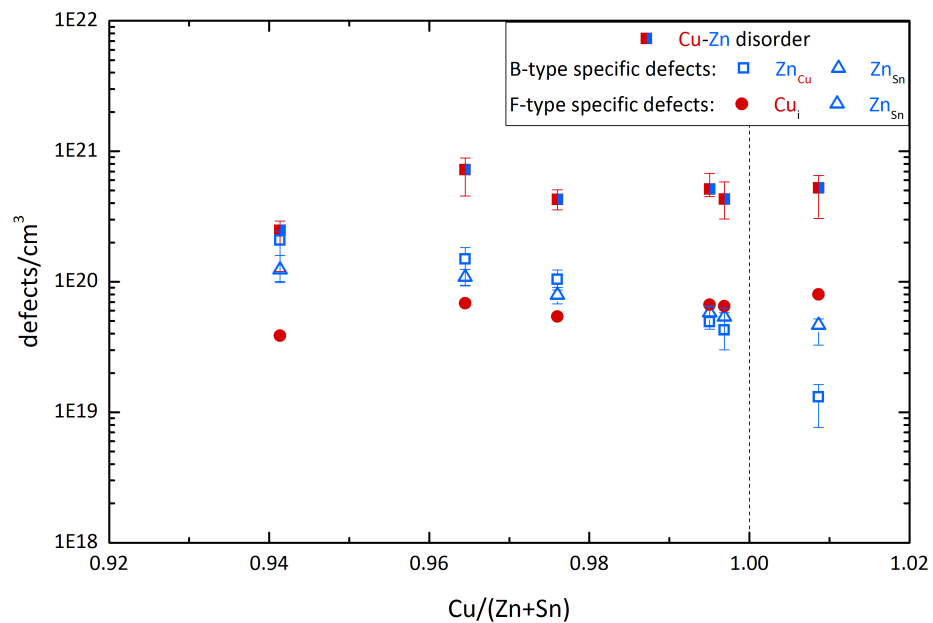
Figure A.74: B-F-type defect concentrations vs. $Cu/(Zn+Sn)$ with unspecific Cu-Zn disorder = red-blue rectangle and type specific B-F- type defects = Zn_{Cu}, Zn_{Sn} and Cu_i.

Dissertation (treatise):

The author (Kai Neldner) has done the following work:

syntheses of samples, chemical analysis of CZTS samples by electron micro probe analyzer, X-ray diffraction, evaluation of collected data (Rietveld refinement etc.), neutron diffraction (BER II) and anomalous X-ray diffraction (BESSY II) experiments, presentation of evaluated data in figures

Valle Rios, L. E./ Neldner, K./ Gurieva, G./ Schorr, S. (2016): Existence of off-stoichiometric single phase kesterite, Journal of Alloys and Compounds 657, 408–413, URL http://www.sciencedirect.com/science/article/pii/ S0925838815311750.

Kai Neldner prepared the CZTS powders, conducted X-ray diffraction and electron micro probe analysis of CZTS powders, Rietveld refinement of X-ray pattern, plotted the obtained data, contributed to the publication text

Garcia-Llamas, E./ Merino, J. M./ Gunder, R./ Neldner, K./ Greiner, D./ Steigert, A./ Giraldo, S./ Izquierdo-Roca, V./ Saucedo, E./ León, M./ Schorr, S./ Caballeroa, R. (2017): Cu2ZnSnS4 thin film solar cells grown by fast thermal evaporation and thermal treatment, Solar Energy 141, 236-241,
URL http://www.sciencedirect.com/science/article/pii/S0038092X16305758.

Kai Neldner prepared the CZTS powders used for the fabrication of the thin film solar cells

Többens, D. M./ Gunder, R./ Gurieva, G./ Marquardt, J./ Neldner, K./ Valle- Rios, L. E./ Zander, S./ Schorr, S. (2016): Quantitative anomalous powder diffraction analysis of cation disorder in kesterite semiconductors, Powder Diffraction FirstView, 1–8, URL http://journals.cambridge.org/article_ S0885715616000191.

Kai Neldner conducted measurements of samples and helped improving the presented method

Hajdeu-Chicarosh, E./ Guc, M./ Neldner, K./ Gurieva, G./ Schorr, S./ Arushanov, E./ Lisunov, K. G. (2016): Transport properties of Cu2ZnSnS4 powder samples, submitted

Kai Neldner prepared the samples for the analysis

Eidesstattliche Erklärung

Ich, Kai Neldner, Matrikel-Nr. 4142760, versichere hiermit, dass ich die vorgelegte Dissertation mit dem Thema:

Structural trends and phase relations in off-stoichiometric kesterite type compound semiconductors

selbständig und ohne unzulässige fremde Hilfe angefertigt und verfasst habe, dass alle Hilfsmittel und sonstigen Hilfen angegeben und dass alle Stellen, die ich wörtlich oder dem Sinne nach aus anderen Veröffentlichungen entnommen habe, kenntlich gemacht worden sind. Des Weiteren, dass die Dissertation in der vorgelegten oder einer ähnlichen Fassung noch nicht zu einem früheren Zeitpunkt an der Freien Universität oder einer anderen in- oder ausländischen Hochschule als Dissertation eingereicht worden ist.

Berlin, den 9. Dezember 2016

_____

Kai Neldner